DYNAMIC MODELLING AND SIMULATION OF THE MULTI-PHASE FLOW IN BUBBLE COLUMNS

by

SHANSHAN LONG

A thesis submitted to the University of Nottingham in partial fulfilment of the requirements for the degree of

Doctor of Philosophy

Under the supervision of

Prof Xiaogang Yang

Dr Jie Yang

FEBRUARY 2022

DECICATION

To my parents for their endless love, support and encouragement.

ACKNOWLEDGEMENT

It is now the final time to put pen to paper and express my thanks, a moment I had rehearsed in my mind countless times. The acknowledgement is an extremely symbolic point for me, it means that another turning point in my life has indeed arrived.

For the past three and a half years, the person who I would most like to express my sincere thanks is my PhD supervisor, Prof. Xiaogang Yang. My association with Prof. Yang dates back to the time when I first returned from the exchange programme in the UK and was lucky enough to have him as my supervisor for my final year project. After the meeting with Prof. Yang at my undergraduate graduation ceremony in 2017, I wrote: "How can I describe my teacher? Think of being outside in the hot sun, with the wind whistling in my ears and the rain pouring down, and he made me come out of such a place; I had probably never seen someone so calm in introspection." I remember that when I was sometimes studying late into the midnight in my senior year, I found finding the light in his office to be surprisingly still on. Having known Prof. Yang for six years now, the calm strength he imparted to me, the rigour in his studies and the diligence to work harder than students have not diminished in any way. He not only helped me tremendously with my dissertation but also guided me along the way. Whenever I told him about my confusion, he always gave me tolerance and understanding, and poured out his experience to help me.

Also, my thanks go to the thesis' two examiners, Professor Bin Chen, Xi'an Jiaotong University and Dr Yong Ren, the University of Nottingham Ningbo China. Thank you for taking time out of your busy schedules to review my PhD thesis.

This work was financially supported by the National Natural Science Foundation of China and the Deutsche Forschungsgemeinschaft (DFG, German Research Foundation) (Grant Nos. 91534118, 21761132026). I would also like to acknowledge the full Ph.D. scholarship of the University of Nottingham Ningbo China.

I would like to thank the FAST group members, Dr. Guang Li, Dr. Jie Yang, Dr. Weibin Shi, Dr. Xiani Huang, Dr. Chenyang Xue, Dr. Lu Liu, Dr. Yanqing Guo, Dr. Bin Li, Ms. Xinyue Cai, Ms. Lulu Wang, Ms. Jiaying Lu and Ms. Rui Jiang for their assistance and pleasurable discussion. I wish to express my thanks to Dr. Zhuang Dong and Dr. Chendi Zhu for all the help and support.

Special thanks are given to my parents for their continued support and encouragement, and for their unfailingly gentle treatment. Thank you to my brother and sister-in-law for your accompany to our parents. And my warm thanks to my lovely nieces and nephews for bringing me the joy and lighting up the countless dark nights when I was depressed.

Gratitude is a constant in life, while the mentality of a twenties is no longer present in life. I have had more twists and turns in my life than my peers. The doctoral life has not only broadened my academic horizons, but also precipitated a lot of understanding of life. Life is about resilience, and resilience means the future. I will tirelessly continue to explore and always remember“凭借这份光，我便能把黑夜变成白天”.

Finally, I wish all the people I love in this world all the best.

SYNOPSIS

Bubble column reactors are commonly used in petrochemical, energy, environmental and bioengineering industries, due to their simple structure and high mass and heat transfer efficiency. An in-depth study of the hydrodynamic behaviour of gas-liquid two-phase flow and gas-liquid-solid three-phase flow in bubble column reactors can provide a basis for optimizing reactor performance, designing efficient reactor structures and expanding the scope of application of bubble columns. In recent years, with the development of computational fluid dynamics and the improvement of relevant physical models, numerical simulations have become an important tool in the study of bubble columns. The strong interactions between phases, resulting in a very complex coupling of mass and momentum transfer cause many difficulties to be solved. The Eulerian/Eulerian LES is adopted throughout this PhD project to investigate bubble column bubbly flow and bubble column three-phase flow, focusing on LES sub-grid-scale (SGS) modelling which implements the modifications of the dynamic responses of the rising bubbles and solid particles to their surrounding turbulent eddies into the SGS models for modelling the gas-liquid two-phase and gas-solid-liquid three-phase flows in bubble column reactors. Furthermore, the interfacial forces closures based on spatial-filtering are concerned.

The current status of LES modelling of two or three-phase flows in bubble columns together with the corresponding experimental studies has been comprehensively reviewed in Chapter 1. A fundamental understanding of the complicated mechanisms of multiphase flow in bubble columns has been shaped through the overview of numerical and experimental studies.

A modified LES SGS eddy viscosity model is proposed in Chapter 2, with the introduction of a dynamic SGS Stokes number to include the effect of bubble dynamic responses to surrounding eddies. The proposed model is successfully implemented into Euler/Euler LES bubbly flow and compared with the use of the standard Smagorinsky model in bubble column simulation. The simulation results demonstrate improvements in the estimations of gas holdup, liquid velocity, and bubble size distribution, as well as uniform enhancements in mass transfer prediction. The importance of taking into account the additional SGS eddy viscosity caused by bubble response to turbulent eddies is revealed, which has been ignored in all previous studies on multiphase flow LES modeling.

Unlike the ensemble-averaged interfacial force closures used in RANS modeling, the SGS spatial filtering process introduces two additional terms into the interfacial momentum exchange terms in the filtered momentum equation for the Euler/Euler LES approach: SGS turbulent dispersion force and SGS added mass stress force. Chapter 3 introduces a spatially filtered SGS turbulent dispersion force model (SGS-TDF) that implicitly accounts for bubble deformation due to local shear caused by grid-scale eddies and sub-grid scale fluctuations. It was proved unequivocally that by employing Euler/Euler large-eddy simulations (LES) and accounting for the influence of bubble-eddy interaction on the SGS turbulent dispersion model, the bubble dynamics in bubble column bubbly flow can be represented without using Euler/Lagrange LES modeling. This implies that when the modified SGS tur-

bulent dispersion model is used, Euler/Euler LES modeling plays an identical function in revealing the bubble fluctuation motion indicated by the Euler/Lagrange LES modeling approach, but with the stochastic dispersion model.

As a result of the LES spatial filtering process, an additional term, SGS added mass stress (SGS-AMS) term in the interfacial momentum exchanges is formed, which may have a significant effect on bubble dynamics or bubble transport in the bubble column, as presented in detail in Chapter 4. On the basis of bubble axial velocity and bubble volume fraction profiles, the improvement in bubble dynamics prediction was evident. This may imply that employing the modified SGS-TDF model in conjunction with the SGS-AMS model in Euler/Euler LES simulations effectively mimics the bubble fluctuation motion predicted by the Euler/Lagrange LES modeling approach.

Because the turbulent eddies located in the front of the rising bubbles interact strongly with bubbles (added mass) and generate local fluctuation, it is reasonable to expect that considering the SGS-AMS and SGS-TDF will have a significant effect on the interfacial mass transfer occurring in the bubble column. Chapter 5 assesses and discusses the impact of including the suggested SGS-AMS and SGS-TDF models in the Euler/Euler LES modeling on the mass transfer of CO2 chemisorption in a reactive bubble column reactor. When compared to the LES simulation using only conventional models, the proposed models show obvious advantages in predicting the time evaluation of species concentrations in the CO2 chemisorption process and pH curve. Additionally, the predicted species concen-

tration spectrum clearly demonstrates the reaction mechanism of CO2 chemisorption in the bubble column. The predicted species concentration spectrum revealed that the slope shift in the spectrum retains a typical -5/3 scaling followed by an approximate -1 scaling.

The modified SGS eddy viscosity model, which considers bubble and solid particle dynamic responses to SGS turbulent eddies through the introduction of the Stokes numbers for bubbles and solid particles, is proposed in Chapter 6. With consideration of the bubble and solid particle responses to the eddies, an Eulerian-Eulerian LES of gas-liquid-solid three-phase flow in a slurry column is conducted. Based on the simulation results using different SGS models, the hydrodynamics and bubble dynamics can be better predicted by using the modified SGS model. The use of the modified SGS eddy viscosity model in three phase flow in bubble column is found to be able to deliver a better performance in predicting the shear turbulence in the near wall region, especially for the gas hold-up gradient and liquid shear strain rate. The typical -5/3 Kolmogorov and -3 scaling laws for bubbly column bubbly flows can be still identified in the turbulent kinetic energy spectrum obtained for gas-liquid-solid particle three-phase slurry flow in bubble columns, but the turbulent kinetic energy corresponding to the higher wave number region was found to be enhanced due to the modulation caused by particle-eddy interactions. This finding further demonstrates the necessity of considering the SGS relative velocity fluctuations in the modified Smagorinsky's SGS model in Euler/Euler LES modelling.

To sum up, bubble column bubbly flow and bubble column three-phase flow using the Euler/Euler LES approach are investigated. A particular emphasis on LES sub-

grid-scale (SGS) modeling and the effects of the dynamic responses of rising bubbles and solid particles to their surrounding turbulent eddies on the SGS eddy viscosity model are successfully reinforced. The critical importance of including the SGS-TDF and SGS-AMS in Euler/Euler LES modeling of bubble column bubbly flows is highlighted, particularly when interfacial mass transfer is involved.

TABLE OF CONTENTS

CHAPTER 2: LARGE-EDDY SIMULATION OF GAS-LIQUID TWO-PHASE FLOW IN A BUBBLE COLUMN REACTOR USING A MODIFIED SUB-GRID SCALE MODEL WITH THE CONSIDERATION OF BUBBLE-EDDY INTERACTION

CHAPTER 3: LARGE EDDY SIMULATION OF BUBBLE COLUMN BUBBLY FLOWS BY CONSIDERING SUB-GRID SCALE TURBULENT DISPERSION EFFECT ON MODULATING BUBBLE TRANSPORT

CHAPTER 4: LARGE EDDY SIMULATION OF BUBBLE FLOW IN BUBBLE COLUMN REACTOR BY CONSIDERING SUB-GRID SCALE TURBULENT DIFFUSION EFFECT AND BUBBLE OSCILLATION

CHAPTER 5: EULER/EULER LARGE EDDY SIMULATION OF BUBBLY FLOW IN BUBBLE COLUMNS UNDER CO_2 CHEMISORPTION CONDITIONS

CHAPTER 7: RECAPITULATION AND RECOMMENDATIONS

LIST OF FIGURES

CHAPTER 1: CURRENT STATUS OF DYNAMIC MODELLING AND SIMULATION OF THE MULTIPHASE FLOWS IN BUBBLE COLUMNS – LITERATUE REVIEW

CHAPTER 2 LARGE-EDDY SIMULATION OF GAS-LIQUID TWO-PHASE FLOW IN A BUBBLE COLUMN REACTOR USING A MODIFIED SUB-GRID SCALE MODEL WITH THE CONSIDERATION OF BUBBLE-EDDY INTERACTION

CHAPTER 5: EULER/EULER LARGE EDDY SIMULATION OF BUBBLY FLOW IN BUBBLE COLUMNS UNDER CO_2 CHEMISORPTION CONDITIONS

CHAPTER 6: EFFECTS OF SUB-GRID SCALE BUBBLE-EDDY AND PARTICLE-EDDY INTERACTIONS ON GAS-SOLID-LIQUID THREE-PHASE FLOW IN A SLURRY BUBBLE COLUMN

LIST OF TABLES

CHAPTER 1: CURRENT STATUS OF DYNAMIC MODELLING AND SIMULATION OF THE MULTIPHASE FLOWS IN BUBBLE COLUMNS – LITERATUE REVIEW

CHAPTER 2: LARGE-EDDY SIMULATION OF GAS-LIQUID TWO-PHASE FLOW IN A BUBBLE COLUMN REACTOR USING A MODIFIED SUB-GRID SCALE MODEL WITH THE CONSIDERATION OF BUBBLE-EDDY INTERACTION

CHAPTER 3 LARGE EDDY SIMULATION OF BUBBLE COLUMN BUBBLY FLOWS BY CONSIDERING SUB-GRID SCALE TURBULENT DISPERSION EFFECT ON MODULATING BUBBLE TRANSPORT

NOMENCLATURE

a	[m $^{-1}$]	Interfacial area concentration
A	$[m^2]/[-]$	Area/ pre-exponential factor
c	[-]	Coefficient
	/[kmol m^{-3}]	/Molar concentration
C_{AM}	[-]	Virtual mass coefficient
C_D	[-]	Drag coefficient
C_L	[-]	Lift force model constant
C_S	[-]	Sub-grid scale model constant
C_{TD}	[-]	Turbulent dispersion coefficient
D	$[m^2/s]$	Diffusion coefficient
	/[m]	Depth of the reactor
d_B	[m]	Bubble diameter
$\bar{D}$	$[m^2/s]$	Mass diffusivity
d	[m]	Bubble diameter
E	[-]	Enhancement factor
E_0	[-]	Eötvös number
f	[Hz]	Frequency
$\dot{m}$	[kg/s]	Mass transfer from gas (single bubble)
m	[kg]	Mass
$\mathbf{M_L}$	$[N/m^3$	Lift force
$\mathbf{M_{AM}}$	$[N/m^3]$	Added mass force

$\mathbf{M_{TD}}$	$[\mathrm{N/m^3}]$	Turbulence dispersion force
$\mathbf{g}$	$[\mathrm{m/s^2}]$	Gravity acceleration
H	[-]/[m]	Henry constant/Distance from the bottom surface
I	[kmol/m^3]	Ionic concentration
k_{1+} / k_{2+}	$[\mathrm{m^3/}$ $(kmol\ s)]$	Forward reaction rate constant
k_{1-} / k_{2-}	[s^{-1}]	Backward reaction rate constant
K	[-]	Equilibrium constants
K_L	[m/s]	Convective mass transfer film coefficient
n	[m^{-3}]	Bubble number density
p	[N/m^2]	Pressure of continuous phase
Q	$[\mathrm{s^{-2}}]$	Invariant Q-criterion
R	[m]	Radius of the reactor
Re	[-]	Reynolds number
S	$[\mathrm{s^{-1}}]$ /$[\mathrm{kg\ m^{-3}}s^{-1}]$	Characteristic filtered rate of strain /Source term in the species transport equation
St	[-]	Stokes number
Sc	[-]	Schmidt number
Sh	[-]	Sherwood number
$\mathbf{u}$	[m/s]	Grid scale velocity vector
$\tilde{\mathbf{u}}$	[m/s]	Instantaneous velocity
$\mathbf{u}'$	[m/s]	Fluctuation velocity
t	[s]	Time

T	[K]	Temperature
U_{Slip}	[m/s]	Slip velocity
W	[m]	Width of the reactor
Y	[-]	Mass fraction
z	[-]	Ionic charge

Greek letters

α	[-]	Volume fraction
ε	$[m^2/s^3]$	Turbulence dissipation rate
ρ	$[kg/m^3]$	Fluid density
κ	$[m^{-1}]$	Wave number
λ	[m]	Characteristic length scale of eddy
μ	[Pa · s]	Liquid dynamic viscosity
μ_{eff}	[Pa · s]	Effective viscosity of the liquid phase
μ_L	[Pa · s]	Kinematic viscosity
μ_{BI}	[Pa · s]	Bubble induced viscosity
τ	Pa	Shear stress
ν_t	$[m^2/s]$	Turbulent kinematic viscosity
σ_{TD}	[-]	Turbulent Schmidt number of gas phase
ω	$[s^{-1}]$	Water vorticity
Δ	[m]	Filtering width
Δ_i	[m]	Grid spacing in radial direction
Δ_j	[m]	Grid spacing in axial direction

Δ_k	[m]	Grid spacing in lateral direction
κ	[m^{-1}]	Wave number
γ	[-]	Volume increment ratio
σ	[N/m]	Surface tension

CHAPTER 1: CURRENT STATUS OF DYNAMIC MODELLING AND SIMULATION OF THE MULTIPHASE FLOWS IN BUBBLE COLUMNS – LITERATUE REVIEW

SUMMARY

Significant development has been achieved experimentally and numerically in the investigation of multiphase flow in bubble column reactors over the past few decades. Initially, early studies concentrated on experimental exploration of global properties and time-averaged parameters. A fundamental understanding of gas-liquid two-phase flow and gas-liquid solid three-phase flow in bubble columns has been shaped through these studies. As new experimental equipment has been developed since the 90s of last century, it has become possible to capture the dynamic structure and behaviour of the local flow field much more precisely. In recent years, because of the urgent demand for carbon neutrality, there has been an increasing interest in bubble columns as its high efficiency in heat and mass transfer. This allows a more comprehensive study of the multiphase structure of the bubble columns. Numerous correlations and phenomenal models have been developed and applied in CFD modelling on the basis of the experimental discoveries, which speeds the development of mathematical understanding of the turbulent mechanisms in bubble columns. The fluid dynamics in the bubble columns, on the other hand, are extremely complex. The multi-scale behaviour of the multiphase flow in

bubble column reactors, particularly the gas-liquid two-phase interactions and some interfacial phase closures, have not been fully elucidated, which has become a critical challenge in their design and scaling up. As such, this chapter summarizes some of the efforts according to the available literatures, both experimentally and through CFD modelling, to gain a better understanding of the turbulent flow characteristics of bubble column multiphase flow.

1. INTRODUCTION

The bubble column reactor is a multiphase reaction device in which bubbles ascend as a driving force for mixing and dispersion. After passing through the distributor located at the bottom of the reactor, the gas rises in the form of bubbles in the continuous liquid phase to enhance interphase contact and transfer. Compared to other multiphase reactors (e.g. stirred tanks, trickle beds, fixed beds, drip beds, packed beds, etc.), bubble columns are capable of: i) simpler structure, no moving parts and easy to maintain; ii) relatively high liquid retention allowing the reactions with long residence time required (Lier et al., 2018); iii) high inter-phase mass transfer capacity with relative low energy consumption (Taborda et al., 2021); iv) compared with above mentioned three-phase reactors, less prone to corrosion and blockage when solid phase is present (Rollbusch et al., 2015); v) low cost; vi) can withstand high temperature and pressure with better sealing (Shu et al., 2019).

Due to the above advantages, bubble column reactors are widely used in petrochemical, coal chemical, nuclear power engineering, metallurgical engineering, biochemical and environmental engineering, i.e., Fischer-Tropsch synthesis, ozone catalytic oxidation and biological fermentation (Chen et al., 2008, Chen et al., 2005a, Manjrekar et al., 2017, Manjrekar et al., 2019, Schmidt and Velten, 2016, Kantarci et al., 2005, Shah et al., 1982). In the advanced oxidation section of wastewater treatment, the advanced oxidation reactor for ozone is a gas-liquid-solid three-phase bubble column reactor, which is a large industrial unit with a very complex flow pattern in the reactor (Lucas et al., 2010, Besagni and Inzoli, 2016). More research on bubble column reactor has been conducted by academics, including experimental measurements and numerical simulations. However, the complex fluid dynamics of multiphase flow in bubble column reactors and the presence of dispersed bubbles or solid phase particles in the reactor make it difficult to accurately predict the phase composition. Due to measurement techniques constraints, early experimental studies focused on the overall performance parameters of the bubble column reactor, such as the overall gas volume fraction. Although continuous advances in measurement methods have made it possible to quantitatively investigate the time-averaged characteristics of the bubble column in recent years, it still does not reflect the multi-scale flow conditions of the bubbly flow, and the hydrodynamic behaviour of the bubbly flow is not sufficiently understood. In addition, certain study achievements have recently been obtained in the numerical simulation of bubble column bubbly flow. Especially for large eddy simulation

(LES) model, which can resolve a larger range of turbulent scale motions comparing with Reynolds-averaged Navier-Storkes (RANS) models and less computational cost comparing with direct numerical simulation (DNS) (Bouffanais, 2010), is becoming a more promising tool in capturing the turbulence in bubble column bubbly flow. However, further research is still needed on the accuracy of the computational model and its applicability to different turbulent eddy scales. This chapter aims to give a state-of-art review of the published literature on multiscale multiphase phenomena in bubble column reactor in order to better understand the flow characteristics. An overview of the flow regime, flow pattern and mass transfer in bubble column is presented in Section 2. Section 3 focuses on the numerical modelling of the bubbly flow including the simulation approach, turbulent models, and interfacial forces.

2. OVERVIEW OF FLOW BEHAVIOUR IN BUBBLING COLUMNS

The bubble column reactor is a typical multi-scale system consisting of: macroscale or reactor-scale structures, such as large-scale liquid circulation; mesoscale interactions, such as bubble-bubble or bubble-eddy collisions, and microscale behaviour such as mass or momentum transfer at the bubble surface, as shown in Figure 1-1. Although the complex multiphase and multi-scale nature has not yet been fully and completely revealed, due to the limitations of experimental equipment and techniques, and the development of turbulence theory, a fundamental understanding of turbulence in bubble columns (e.g. transitions in flow structure and

flow regime, as well as bubble deformation and interfacial mass transfer) has been established and generally accepted on the basis of experimental studies.

2.1 Macroscale phenomena- flow regime

The flow regime in bubble column is depended on the gas superficial velocity and the bubble column size, as illustrated by Figure 1-2. When using a narrow opening inlet, Ong (2003) observed a homogeneous (bubbly) flow regime at low gas superficial velocity and atmospheric pressure, which is characterised by a narrow bubble size distribution, with zero or limited interactions between bubbles, a near uniform radial gas volume fraction distribution, and a low liquid phase turbulence intensity (Mudde, 2005). Depending on the observed bubble size distribution, bubble flow regimes can be divided into mono-disperse or poly-disperse. Churn turbulent regime is observed at higher gas superficial velocity and is characterised by the existence of a broad bubble size distribution, frequent interaction between bubbles (break-up and coalescence), parabolic gas void fraction distributions and high liquid phase turbulence intensity. A transition flow regime is observed between the bubbly flow and the churn regime. This flow regime is not always observed and is not as well characterized as the previous two turbulent flow regimes (Groen, 2004). Slug flow regime is characterised by large sized bubbles, equivalent to the length scale of the column diameter, which are not frequently observed in the bubble column. This regime will not be discussed further in this chapter due to these large bubbles' instability in large diameter bubble columns.

A considerable amount of effort has been done over the last three decades to describe the characteristic flow structures observed in each flow regime. Individual bubbles migrate upwards from the central region of the column in the bubbly flow regime, according to Chen et al. (1994). The increased gas velocity will finally result in the generation of bubble cluster or bubble coalescence in the center of the column. These bubble clusters or coalescing bubbles spiral upwards from the column's center and downwards in the near-wall region as shown in Figure 1-3. As the gas superficial velocity increasing until the flow regime reaches turbulence, bubble coalescence becomes dominant and creates huge bubbles. The vortex and spiral structure are eventually disrupted by the local chaotic motion of the liquid induced by the bubble motion, leading to turbulence. The intensity of turbulence is much higher in churn turbulent regimes, leading to much higher values of eddy diffusion of mass, heat and momentum (Degaleesan et al., 1996). The rates of heat and mass transmission and mixing in homogeneous and heterogeneous systems are considerably different (Thorat and Joshi, 2004). As a result, in order to effectively forecast these values, it is of vital importance to understand the nature of the flow regimes in bubble column.

The flow regime in a bubble column is complex and is determined by the fluid and gas phase physical properties, the column geometry, the configuration of gas aerators and internals as well as the operating pressure (Azzopardi et al., 2011, Manjrekar and Dudukovic, 2019). Furthermore, the transition point between bubbly and turbulent churn flow regimes varies with operating pressure and the extra liquid

phase compositions (e.g. organic solvents, surfactants), which makes 'a priori' prediction of the flow regime difficult (Joshi et al., 1998). Furthermore, due to the opaque nature of industrial equipment, classifying flow regimes is challenging, and even the techniques available to quantify the gas volume fraction under these conditions are restricted. As a result, it is necessary to create a methodology for detecting the flow condition in bubble columns that is simple to use even in opaque reactors.

Many strategies for predicting flow regimes have been proposed over the last two decades. The existing methods for determining flow regimes are summarized by Shaikh and Al-Dahhan (2007), Manjrekar and Dudukovic (2019). Finally, these strategies rely on tracking the time history of each system parameter throughout a range of gas superficial velocity, i.e., bubble volume fraction, bubble swarm stream-wise velocity, the pressure fluctuation signals standard deviation, Kolmogorov entropy and so on. There are even more complex signal analysis approaches, including chaos analysis and fractal analysis pressure variations that are utilized to classify the flow regime ((Ruzicka et al., 2003, Olmos et al., 2003, Lucas and Ziegenhein, 2019, Medjiade et al., 2017, Besagni and Inzoli, 2016, Besagni and Inzoli, 2017b, Vandu et al., 2004b, Krishna and Ellenberger, 1996, Li et al., 2013, Krishna et al., 1991, Kantarci et al., 2005, Shiea et al., 2013). As physical properties and system design evolve, the transition points in the experimentally predicted flow regime maps may shift. It is not always possible to produce such flow diagrams in industrial processes by undertaking extensive experimental work under different

operating conditions to get such transition points. Thus, computational fluid dynamics (CFD) and linear stability analysis have been applied, and these methods have been successful in forecasting the flow regime of gas-liquid two-phase systems (Chen et al., 2009; Joshi et al., 2001). According to Monahan and Fox (2007), in order to accurately estimate the flow diagrams, all factors operating on the bubble and the bubble motion must be addressed. The numerical predictions present a significant obstacle because validating the closure forms and interfacial forces utilized under industrial situations is a continuous issue for the modelling community. Detailed review on numerical modelling of the multiphase flow in bubble column reactors will be presented in Section 3.

2.2 Microscale phenomena- mass transfer

When the bubble rises in the liquid, the mass transfer is mainly determined by two factors: the area of the interfacial surface and the rate of mass transfer between phases. Due to the fact that the gas is typically dispersed in a bubble column, the interfacial mass transfer mainly happens at the bubbles' surfaces. Thus, the size and shape of the bubbles can be used to determine the interfacial area. As illustrated in Figure 1-2, the overall flow structure is relatively uniform, with bubbles rising in ascending order once sparged into the system in the homogeneous flow region. As turbulence intensity is low at this point, the bubble coalescence and breakage phenomena are relatively uncommon. An acceptable approximation in this scenario would be spherical bubbles of the same size. Increasing gas superficial velocity

brings the flow into the transition regime where bubble coalescence and breakage may occur locally. The collisions between bubbles and bubble-eddy occur regularly throughout the column once the flow enters the churn-turbulent regime or heterogeneous regime. If the turbulent kinetic energy in the colliding eddies and bubbles is sufficient, they will rapidly change shape and diameter. At the transition and heterogeneous regimes, ellipsoidal and spherical-cap bubbles with a considerably bigger surface area are commonly presented, facilitating interfacial mass transfer. Bubble column design often avoids slug flow regimes due to the restricted contact surface between the bubble slug and the carrier fluid, which may weaken the interfacial mass transfer.

Additionally, bubbles' size and shape are also influenced by the physical properties of liquid phase including dynamic viscosity and surface tension. Despite the fact that bubbles oscillate in turbulent flows, Clift et al. (1976) summarised the bubble shape regime based on extensive experimental findings, as illustrated in Figure 1-4. Three dimensionless parameters, Reynolds number Re, Eötvös number Eo, and Morton number Mo, were used to classify bubbles into spherical, elliptical, and capped bubbles. Wobbling, skirted or crown bubbles can also be formed in the bubble column due to surface oscillations. The physical significance of these dimensionless quantities shows that inertial forces, viscous forces, gravity, and surface tension are the most important variables impacting the system. In the following section, we'll go over some of the dimensionless figures in the previous work.

When bubbles rise in a liquid, the resistance to mass transfer is mainly on the continuous phase side. According to the literature, there are a number of different theoretical models for calculating mass transfer coefficients, such as two-film theory, surface renewal theory, etc. and these are summarised in Table 1-1.

Table 1- 1 Different mass transfer theories

Two-film model	Lewis and Whitman(1924)	$k_l = Sh\ D_l/d_b$
Penetration model	Higbie(1935)	$k_l = \frac{2}{\sqrt{\pi}}\sqrt{\frac{D_l}{t_c}}$
Surface renewal model	Danckwerts(1951)	$k_l = c_r\sqrt{\frac{D_l}{t_r}}$

Two-film model

The two-film theory claims that molecular diffusion governs the gas transporting from one layer to another when it comes into contact with the liquid, creating a gaseous and a liquid interface. In the two-film theory, both films show stagnant flow, with the thickness of the film varying with the flow rate of the fluid. In the mass transfer process, the solute generally passes through these two films in a continuous molecular diffusion manner into the main body of the liquid phase. One of the things to note is that the concentrations of the gas and liquid phases at the phase interface balance each other. In the gas-liquid two-phase flow, the concentration is uniform due to the turbulent flow of the fluid and there is no concentration difference, i.e. there is no absorption resistance. In contrast, when solutes are transferred from the gas phase body to the liquid phase body, all resistance exists only in the

two stagnant films. The mass transfer rate coefficient can be related to the diffusivity and dynamic Sherwood number. In terms of each bubble, The Sherwood correlation under forced convection can be expressed as below,

$$\mathrm{Sh} = 2 + \mathrm{a} \cdot Re^{b} \cdot Sc^{c} \tag{1-1}$$

According to the open literature, different coefficients a, b, c were proposed under different conditions, as shown in Table 1-2. The model proposed by Bird et al. (2006) is more suitable in contaminated system, while the fitted model between numerical and experiments proposed by Brauer (1981) is appropriate for the non-spherical bubbles with stochastic deformation shape in partly contaminated system. The two models proposed by Henket (2007) are empirical correlation in partly contaminated system with small and rigid bubble shape and large and deformable bubble shapes respectively.

Table 1- 2 Coefficients of Sherwood number in mass transfer model

a	b	c	Mass transfer model
0.6415	0.5	0.5	Bird (Hlawitschka et al., 2017)
0.015	0.89	0.7	Brauer (Darmana et al., 2007)
1.25	0.5	0.33	Henket(Jain et al., 2015)
0.43	0.58	0.33	Henket (Jain et al., 2015)

In terms of the reactive bubbly flow in bubble column reactor, lots of numerical simulation work of the heated topic, CO2 absorption, have been conducted. As illustrated in Figure 1-5, the concentration difference between the bubbles and surrounding liquid causes the fast reaction period. This forced convection is always

described by two-film mass transfer model in the available work. Darmana et al. (2005) used LES with Eulerian-Lagrangian method to simulate the flow, mass transfer and chemical reactions in a squared bubble column. They considered the mass transfer rate in the liquid phase momentum equation and the reaction interface forces in the bubble equation of motion. Also, the presence of various chemical species was considered through the transport equation for each species. Darmana et al. estimated mass transfer rates directly from the information of individual bubbles. They used the model to simulate the reversible two-step reaction found during chemisorption of CO2 in aqueous NaOH solutions in a laboratory-scale pseudo-2D bubble column reactor. They found good agreement between simulations and measurements in the absence of mass transfer. In the absence of an accurate mass transfer closure, the authors found a lower overall mass transfer rate compared to the measured results. However, after considering the effect of mass transfer on flow, the predicted results agree well with the experimental data.

The procedure used by Zhang et al. (2009) is similar to the one used by Darmana et al. (2007) but using the Eulerian-Eulerian method. The physical and chemical absorption of carbon dioxide bubbles in aqueous solutions of water and sodium hydroxide was studied. They employed the bubble number density equation to couple the effect of mass transfer, hydrodynamics and chemical reaction among the system. The authors demonstrate the effects of mass transfer and chemical reactions on hydrodynamics, bubble size distribution and gas retention, as shown in Figure 1-6.

However, from the equation shown in Table 1-1, the mass transfer coefficient is proportional to the diffusivity D. However, based on the extensive experimental findings, $k \propto D^n, n \in (0.5,1)$. This may indicate that the proposed model is not only associated with the hydrodynamics, but also related to the liquid phase composition.

Penetration model

As shown in Table 1-1, mass transport is also described by Higbie's penetration theory (Higbie, 1935) and its extension (the surface renewal theory), suggesting that surface renewal controls the mass transfer coefficient. In the gas-liquid mass transfer processes carried out in industrial devices, the fluid at the phase interface is always constantly mixing with the mainstream and exposing new contact surfaces. Higbie argues that the exposure time of the fluid at the phase interface is very short that it is impossible for the solute to establish a stable concentration distribution within the film as assumed by the two-film theory. He proposed that solutes permeate continuously from the surface to the liquid by molecular diffusion, with each instant having a different instantaneous concentration distribution and corresponding instantaneous diffusion rate at the interface (proportional to the concentration gradient at the interface). The longer the fluid surface is exposed, the more the concentration distribution curve in the membrane tends to flatten out and the rate of solute diffusion at the interface decreases. Mass transfer takes place by unsteady molecular diffusion in the various elements of the liquid surface. The penetration model is associated with the contact time t_c, as expressed by Equation 1-2,

$$t_c = d_b/U_b \quad (1\text{-}2)$$

Where U_b is the bubble rising velocity. The theory, which states that the mass transfer coefficient k_l is proportional to the 0.5th power of diffusivity, is closer to the experimental value than the two-film theory, indicating that its analysis of the mass transfer mechanism is closer to reality. Furthermore, the theory takes into account the transition time for the formation of a stable concentration gradient, during which there is a gradual penetration of solute from the phase interface towards the depth of the liquid film. However, the proposed model is still fundamentally based on the mode model, only with non-stable diffusion and an emphasis on the transition of the liquid phase, mainly for liquid film-controlled absorption processes of refractory gases.

Surface renewal model

Surface Renewal Theory is based on the concept that the liquid elements do not stay the same time at the phase interface surface. Danckwerts (1951) discarded the concept of stagnant films and argued that gas-liquid contact surfaces are continuously renewed, rather than occurring only at certain intervals t_c. He proposed that certain turbulent eddies could move directly between the interface and the turbulent body, allowing the liquid surface to be continuously renewed by individual liquid units moving in from the turbulent zone. Moreover, fluid units at the interface can be renewed at any time, regardless of the length of time they remain on the surface, and the small units have an equal chance of being renewed. In this model, the mass transfer coefficient is proportional to the square root of mean time between renewal

events t_r . This time scale is estimated based on Kolmogorov time scale $t\sim(\nu/\varepsilon)\hat{}(1/2)$, where ν and ε stand for the kinematic viscosity of the liquid phase, and turbulent dissipation rate respectively.

Although molecular diffusion still affects the transfer between the film and gaseous phase between these periodic replacements, the overall transfer velocity is a function of the time interval between film renewal events in the penetration and surface renewal models. There are no effects of film thickness due to the relatively short timescale than diffusion across this distance. In many cases, the difference between predictions based on different models will be less than the uncertainties about the physical properties utilized in the calculation. The models can thus be interchangeable for many applications, and it is only a matter of convenience which one is utilized.

3. NUMERICAL SIMULATION OF MULTIPHASE FLOWS IN BUBBLE COLUMN REACTORS

Vorticity with rotational energy axis is carried by turbulent motions in all directions. As a result, turbulent flows can be quite irregular, unstable, and three-dimensional, whereas laminar flows can be regular, two-dimensional, or one-dimensional. There is a wide range of different eddy sizes in turbulence, interacting with each other. Big eddies are associated with low frequency fluctuations with the size of the entire domain, such as the pipe diameter or jet width, while small eddies are associated with high frequency fluctuations where viscous forces act and dissipate. Flow quantities including velocity, temperature, and concentration, fluctuate greatly in space and time accordingly. Momentum, heat and mass transfer are affected as a result of these turbulent fluctuations. Therefore, accurate CFD modelling is of vital importance in predicting the two-phase turbulent bubbly flow in the bubble column and can be challenging for the community.

3.1 Simulation approaches

A multiphase flow is defined as a flow with two or more phases that are separated by an interface. Different modeling methodologies are needed for different flow regimes, so classifying the flow is critical before making a modeling decision. Examples of different multiphase flows are shown in Table 1-3.

Table 1- 3 Classification of multiphase flow regimes

Flow regime	Dispersed	Mixed	Separated
	Bubbly flow	Droplet annular flow	Film flow
	Particle laden flow	Bubbly annular flow	Annular flow
	Droplet flow	Slug/Cap/Churn flow	Jet flow

The flow structure and macroscopic properties of gas-liquid two-phase flows are related to the gas-liquid phase interface, and knowledge of the distribution properties of the gas-liquid phase interface is the key to understanding gas-liquid two-phase flows. Therefore, the numerical simulation of gas-liquid two-phase flow is mainly concerned with the simulation of the distribution of the gas-liquid phase interface and its motion characteristics. The direct numerical simulations for gas-liquid two-phase flows solve the governing equations for the liquid phase flow and the gas flow field in every single bubble. The interface between two phases should be represented explicitly with sharp interfacial properties and should be free to move, deform, breakup and coalesce as an actual interface would behave. Therefore, the two-phase coupling and the momentum exchange rely on the interface-tracking methods. The interface-tracking methods that have been developed mainly include Particle-In-Cell (PIC) (Harlow, 1988), Marker-and-Cell (MAC) (Harlow and Welch, 1965, Amsden and Harlow), volume of fluid (VOF) (Hirt and Nichols, 1981a, Hirt and Nichols, 1981b), level-set method (Osher et al., 2004), boundary-fitted grid method and front tracking method (Tryggvason et al., 2001). It is one of the greatest advantages of the DNS method for gas-liquid two-phase flow simulations that the changes at the bubble interface can be clearly illustrated, such as

Krishna and van Baten (1999c). Also, the DNS method for two-phase flow can be used as a tool to study liquid phase turbulence under the influence of gas bubbles, as in Metrailler et al. (2017). Although there are no interphase force model or turbulence models required as model closure, the computational demand is so high that DNS is limited to low Reynolds numbers and few bubbles, which makes the simulation of real industrial processes almost impossible. In the next step, Eulerian-Lagrangian and Eulerian-Eulerian methods would be mainly discussed.

Reference frames, such as Eulerian or Lagrangian, are used for formulating the governing equations. Observers in Eulerian and Lagrangian frames of reference are both stationary, but in a Lagrangian frame of reference, the observer moves along with the flow. The Eulerian-Lagrangian approach treats the continuous fluid in an Eulerian frame of reference, while the dispersed phase is treated in a Lagrangian frame of reference. The continuous and dispersed phases are regarded as interpenetrating continua in the frame of Eulerian-Eulerian approach.

Eulerian-Lagrangian approach

The Eulerian-Lagrangian method is a more promising approach. This method considers the dispersed phase as discrete particles, and the appropriate equation of motion is solved for each particle in a Lagrangian frame of reference. The particle-particle interactions can be clearly described, such as hard-sphere models or soft-ball models for bubble collision and coalescence. The continuous phase is calculated as time-averaged flow field using a grid-based Eulerian method. When the dispersed phase particles are very small in size and low in concentration, it can be

assumed that the movement of the dispersed phase particles does not change the flow field of the continuous phase. However, when the particle concentration can no longer be ignored, the discrete particles and the continuous phase can be coupled by using a source term in interphase momentum exchange equations. Some researchers have used this method to study the gas-liquid two-phase flow in the bubble columns and have shown more promising results, such as Delnoij et al. (2000), Sokolichin et al. (1997), Lain and Sommerfeld (2003), Deen et al.(2004) and Buwa et al. (2006). The continuous phase motion is obtained by solving the NS equation in the Eulerian coordinate system; the particle is coupled to the continuous phase by the interphase force model. The Eulerian-Lagrangian technique is well-suited for fundamental research because it enables direct study of a variety of phenomena associated with bubble-bubble and bubble-liquid interactions. The use of this method is often limited not only by the spatial resolution of the meshes but also by the number of tracked bubbles. Although the computational cost is still very high for industrial-scale simulations, the physical interpretations still make sense while the considered models in this method are simpler than DNS method.

Eulerian-Eulerian approach

Three different Euler-Euler multiphase models are available in CFD: the volume of fluid (VOF) model, the mixing model, and the Eulerian model. The VOF model is a surface tracking technique applied to a fixed Eulerian mesh. It is designed for two or more immiscible fluids where the position of the interface between the fluids is of interest. In the VOF model, the fluids have a single set of momentum equations

and the volume fraction of each fluid in each computational cell is tracked over the entire domain. Applications of the VOF model include stratified flow, free surface flow, filling, sloshing, the motion of large bubbles in a fluid, the motion of fluids after dam failure, prediction of nozzle breakup (surface tension), and steady-state or transient tracking of any fluid-gas interface. The mixture model is designed for two or more phases (liquid or particulate). As in the Eulerian model, the phases are treated as interpenetrating continua. The mixture model solves the momentum equation for the mixture and specifies relative velocities to describe the dispersed phases. Applications of the mixing model include particle-laden flows with low loading, bubbly flows, sedimentation, and cyclone separators. The mixing model can also be used without relative velocities for the dispersed phases to model homogeneous multiphase flows. The Eulerian model is the most complex of the multiphase models and is employed in each chapter of this PhD thesis. It solves a set of momentum and continuity equations for each phase. The coupling is achieved through the pressure and interphase exchange coefficients. The way this coupling is handled depends on the type of phases involved. Granular (fluid-solid) flows are handled differently than non-granular (fluid-fluid) flows. For granular flows, the properties are determined by applying kinetic theory. The momentum exchange between phases also depends on the type of mixture modeled. Applications of the Eulerian multiphase model include bubble columns, particle suspensions, and fluidized beds. Details of the Eulerian-Eulerian approach used in bubble column bubbly flow is shown as follows.

The Eulerian-Eulerian method, also known as two-fluid model, is the most widely

used approach in numerical simulations of multiphase flow. Not only the continuous phase is considered statistically continuous, but also the dispersed phase. The two-fluid model is created to macroscopically represent the movements of each phase. As there are two 'fluids' present, the void fraction is used to represent the concentration of each phase. Because it cannot be resolved at each point in time and space, the void fraction must be averaged across a period of time and space. The mass and momentum conservations are expressed as

$$\frac{\partial}{\partial t}(\rho_k \alpha_k) + \nabla(\rho_k \alpha_k \boldsymbol{u_k}) = 0 \qquad (1-3)$$

$$\frac{\partial}{\partial t}(\rho_k \alpha_k \boldsymbol{u_k}) + +\nabla(\rho_k \alpha_k \boldsymbol{u_k u_k}) = -\alpha_k \nabla p + \nabla \cdot \alpha_k \bar{\bar{\boldsymbol{\tau}}}_k + \alpha_k \rho_k \boldsymbol{g} + \boldsymbol{F_k} \qquad (1-4)$$

where $\rho_k, \alpha_k, u_k, \bar{\bar{\tau}}_k, g$ and F_k represent the density, volume fraction, velocity, viscous stress tensor, gravity and the inter-phase momentum exchange term for the k=L, k=G for continuous and dispersed phase respectively. The sum of the volume fractions for both phases is equal to 1. The governing equations of the two-fluid model can be treated based on averaging methods. For example, the most commonly used averaging method that has been accepted by many commercial CFD codes is the Reynolds (ensemble) averaging, which decomposes instantaneous flow variable into the time-averaged mean component and the fluctuating component. After ensemble averaging, the two-fluid model can no longer describe all scales of flow in the flow field. Nevertheless, it contains a large amount of flow information on a scale larger than that of the ensemble averaging, and the direct discretization of these equations is still very computationally intensive for the numerical simula-

tion of bubble columns. The Reynolds averaging method is often used to time-average Equations 1-3 and 1-4, and a detailed derivation can be found in the literature. The two-fluid model after Reynolds averaging is as follows,

$$\frac{\partial}{\partial t}(\overline{\alpha_k}) + \nabla(\overline{\alpha_k \boldsymbol{u_k}}) = -\nabla \cdot \left(\overline{\alpha'_k \boldsymbol{u'_k}}\right) \quad (1-5)$$

$$\frac{\partial}{\partial t}\left(\rho_k\left(\overline{\alpha_k \boldsymbol{u_k}} + \overline{\alpha'_k \boldsymbol{u'_k}}\right)\right) + \nabla(\rho_k \overline{\alpha_k \boldsymbol{u_k} \boldsymbol{u_k}}) = -\overline{\alpha_k}\nabla\bar{p} - \overline{\alpha'_k \nabla p'} + \nabla \cdot \left(\overline{\alpha_k \bar{\bar{\tau}}_k} + \overline{\alpha'_k \bar{\bar{\tau}}'_k}\right) + \alpha_k \rho_k \boldsymbol{g} + \overline{\boldsymbol{F_k}} + \overline{\boldsymbol{F'_k}} - \boldsymbol{\nabla} \cdot \left[\rho_k\left(\overline{\alpha_k \boldsymbol{u'_k} \boldsymbol{u'_k}}\right) + \boldsymbol{2}\overline{\boldsymbol{u_k}\alpha'_k \boldsymbol{u'_k}} + \overline{\alpha'_k \boldsymbol{u'_k} \boldsymbol{u'_k}}\right] \quad (1-6)$$

Equations 1-5 and 1-6 contain a number of fluctuation correlation terms. For example, the fluctuation velocity second-order correlation $\overline{\boldsymbol{u'_k}\boldsymbol{u'_k}}$, which represents the turbulent transfer of momentum, i.e. Reynolds stress; the fluctuation velocity-phase volume fraction correlation $\overline{\alpha'_k \boldsymbol{u'_k}}$, which represents the turbulent fluctuation mass transport, i.e. turbulent diffusion term; the fluctuation pressure-phase volume fraction correlation $\overline{\alpha'_k \nabla p'}$; the fluctuation phase volume fraction - effective stress correlation $\overline{\alpha'_k \bar{\bar{\tau}}'_k}$; the fluctuation of interphase force $\overline{\boldsymbol{F'_k}}$; and the fluctuation velocity-velocity-phase volume fraction third-order correlation $\overline{\alpha'_k \boldsymbol{u'_k} \boldsymbol{u'_k}}$. Obviously, the above fluctuation phase terms must be closed in order to solve the model equations numerically, as discussed in detail by Joshi (2001). However, with the exception of the fluctuation velocity second-order correlation term, no suitable closure model or model parameters have been found for the other correlation terms containing the fluctuation volume fraction, which is a difficult problem for multiphase flow simulations. Despite the importance of volume fraction fluctuation correlation term, the effect of α'has been mostly ignored due to the lack of suitable models.

Therefore, the above equation can be simplified as,

$$\frac{\partial}{\partial t}(\overline{\alpha_k}) + \nabla(\overline{\alpha_k \boldsymbol{u_k}}) = 0 \qquad (1-7)$$

$$\frac{\partial}{\partial t}(\rho_k \overline{\alpha_k \boldsymbol{u_k}}) + \nabla(\rho_k \overline{\alpha_k \boldsymbol{u_k} \boldsymbol{u_k}}) = -\overline{\alpha_k}\nabla\bar{p} + \nabla \cdot \left(\overline{\alpha_k \bar{\bar{\tau}}_k} - \rho_k(\overline{\alpha_k \boldsymbol{u'_k} \boldsymbol{u'_k}})\right) + \alpha_k \rho_k \boldsymbol{g} + \overline{\boldsymbol{F_k}} \quad (1-8)$$

As can be seen from Equations 1-7 and 1-8, solving the two-fluid model requires closure of the interphase forces $\overline{\boldsymbol{F_k}}$ as well as the Reynolds stress $\overline{\boldsymbol{u'_k} \boldsymbol{u'_k}}$. Since the interphase drag and lift coefficients are functions of the bubble diameter, a suitable bubble model is also required to predict the bubble diameter. The interphase force model, the turbulence model and the bubble model are described separately in Section 3.2 and 3.3. For convenience, the time homogenization superscript "I" will not appear in the above equations.

When the bubble column is operated at the homogeneous regime with the bubble size distribution being very narrow, using a volume averaged bubble diameter seems to be acceptable. However, in most industrial processes when the bubble columns are operated at the churn-turbulent flow regime, the bubble sizes are broadly distributed due to intensive bubble coalescence and breakage phenomenon. In this case, the uniform bubble diameter assumption is no longer appropriate, and the local bubble sizes can be calculated with the use of bubble population balance equations.

3.2 Turbulent models

Turbulent flow is one of the most difficult and therefore the most promising areas in computational fluid dynamics (CFD). Turbulence is a widespread phenomenon in industrial reactors and its behaviour is quite complex, especially in multiphase

turbulence. As bubble column reactors are usually operated under highly turbulent conditions, multi-phase turbulence is an unavoidable part of the numerical simulation of bubble column reactors. Turbulence simulations can be divided into direct and non-direct numerical simulations. Theoretically, direct numerical simulations which has been already discussed in the previous section can predict the turbulent structure at all scales with sufficiently fine meshes and time steps. However, the Kolmogorov (1991) theory shows that the minimum turbulent eddy scale is inversely proportional to $Re^{\frac{3}{4}}$. Obviously, it is not possible at this stage to use simulations for industrial problems due to the large computational costs. At present, direct numerical simulations can only simulate low Reynolds number flows, such as DNS simulations of individual bubbles. In terms of non-direct simulations, the numerical calculation methods currently can be roughly divided into three types (Figure 1-7): Direct Simulation (DNS), Large Eddy Simulation (LES), and Reynolds-averaged Navier-Stokes (RANS) etc. The Reynolds stress term, which results from Reynolds aver-aging, is the key subject of concern. In order to get appropriate results, the Reynolds stress term must be modeled accurately. Different models have been developed to model the Reynolds stress term, such as one equation Spalart-Allmaras model, two-equation models, and Reynolds stress models. The details of k-ε, Reynolds stress model and large eddy simulation model will be addressed in the following paragraphs.

Two-equation k- ε model

The eddy-viscosity model in k- ε model can be described by,

$$\mu_t = \rho v_t, \text{ where } v_t = C_\mu \frac{k^2}{\varepsilon} \quad (1\text{-}9)$$

C_μ is set as a constant value of 0.09, k stands for the turbulent kinetic energy and is defined as the variance of velocity fluctuations; and ε is the turbulent dissipation rate.

The standard k -ε model for the liquid phase can be defined by

$$\frac{\partial}{\partial \mathrm{t}}(\alpha_L \rho_L k_L) + \nabla \cdot (\alpha_L \rho_L k_L u_L) = \nabla \cdot \left[\alpha_L \Gamma^{(k)} \nabla k_L\right] + \alpha_L (G_{k.L} - \rho_L \varepsilon_L) + S^k \quad (1\text{-}10)$$

$$\frac{\partial}{\partial \mathrm{t}}(\alpha_L \rho_L \varepsilon_L) + \nabla \cdot (\alpha_L \rho_L \varepsilon_L u_L) = \nabla \cdot \left[\alpha_L \Gamma^{(\varepsilon)} \nabla \varepsilon_L\right] + \alpha_L \frac{\varepsilon_L}{k_L} (C_{1\varepsilon} G_{k.L} - C_{2\varepsilon} \rho_L \varepsilon_L) + S^\varepsilon \quad (1\text{-}11)$$

k and ε are determined by solving above transport equations. The diffusivities of k and ε are related to the physical properties of phase k:

$$\Gamma^{(k)} = \mu_L + \frac{\mu_t}{\sigma_k}, \quad \Gamma^{(\varepsilon)} = \mu_L + \frac{\mu_t}{\sigma_\varepsilon} \quad (1\text{-}12)$$

S^k and S^εrepresent the source terms for the turbulence generated in the wakes of bubbles. It may indicate that only the liquid shear turbulence is considered without

these two source terms. This turbulence model can partially present the effects of the bubble induced turbulence by adding the source terms.

The term G_k is described by:

$$G_k = -\rho\overline{\mathbf{u}'\mathbf{v}'}\frac{\partial U}{\partial y} = v_t\left(\frac{\partial U}{\partial y}\right)^2 \tag{1-13}$$

or, in general, by

$$G_k = -\overline{u_i' u_j'}\frac{\partial U_i}{\partial x_j} \tag{1-14}$$

with implied summation over the repeated indices. Under the model assumptions, G_k is always positive and proportional to the square of the mean velocity gradient. A flow is considered to be in local equilibrium if $G_k = \varepsilon$ (production equals dissipation).The Reynolds stress terms are new unknowns that are introduced into the averaged equations by the Reynolds averaging, which inevitably leads to the closure problem. The Reynolds stress terms are not solved directly in the two-equation model but are approximated by using the Boussinesq's turbulent viscosity hypothesis, which can be described by,

$$-\rho\overline{u_i' u_j'} = 2\mu_t \boldsymbol{S_{ij}} - \frac{2}{3}\rho k\delta_{ij} \tag{1-15}$$

Where S_{ij} is the shear strain rate tensor, expressed by $S_{ij} = \frac{1}{2}\left(\frac{\partial U_i}{\partial x_j} + \frac{\partial U_j}{\partial x_i}\right)$, and δ_{ij} stands for the Kronecker delta. Then, the production of turbulent kinetic energy can be defined as,

$$G_k = 2\mu_t S_{ij} S_{ij} \quad (1\text{-}16)$$

In terms of the consistency with the log law, and assuming viscous stresses to be negligible in the log-law region, equation 1-16 can be rewritten as $G_k = \frac{u_\tau^3}{ky}$, with further assumption of local equilibrium, $G_k = \varepsilon$, then $v_t = u_\tau^4/\varepsilon$.

The standard k-e model is based on the assumption of anisotropy, whereas experimental measurements of the flow in a bubble column show that the axial fluctuations are significantly stronger than the radial and tangential fluctuations (Degaleesan et al., 2001), i.e. the liquid phase in the column is anisotropic. Therefore, the Reynolds stress model and the LES model, which can deal with anisotropic turbulence, are more suitable for accurate simulation of bubble columns (See Figure 1-8).

Reynolds stress model

The use of the isotropic principal equation for viscous Newtonian fluids and the concept of turbulent viscosity to model Reynolds stresses is contrary to physical fact. Eddy viscosity model does not reflect the anisotropy of Reynolds stress due to the distribution of turbulent flow in each principal axis direction, as it ignores the effect of the pressure-strain term. Fundamentally, the concept of υ_t should be avoided and the transport equation for Reynolds stress should be solved directly by modelling the fluctuation correlation term in it. In the RSM model, the Reynolds

stress terms $\overline{\mathrm{u_i}u_j}$ are computed via a differential transport equation. Reynolds stress transport equations are derived by considering the moments of the exact momentum equation. Accordingly, the turbulent dissipation rate equation can be solved. The exact transport equation for Reynolds stresses $\rho\overline{\mathrm{u_i}'u_j'}$ is expressed by:

$$\frac{\partial}{\partial \mathrm{t}}\left(\alpha_L\rho_L\overline{\mathbf{u_i}'\boldsymbol{u_j}'}\right)+\frac{\partial}{\partial x_k}\left(\alpha_L\rho_L\boldsymbol{u_k}\overline{\mathbf{u_i}'\boldsymbol{u_j}'}\right)=\alpha_{\mathrm{L}}P'_{ij}+\alpha_L\phi_{ij}+\frac{\partial}{\partial x_k}\Big(\alpha_L\Big(\mu_L+\frac{2}{3}C'_s\rho\frac{k^2}{\varepsilon}\Big)\frac{\partial\overline{\mathbf{u_i}'\boldsymbol{u_j}'}}{\partial x_k}\Big)-\frac{2}{3}\delta_{ij}\alpha_L\rho_L\varepsilon \quad (1\text{-}17)$$

where ϕ_{ij} is the pressure-strain correlation, and P' stands for the exact production term, expressed as:

$$\mathrm{P}'=-\rho_{\mathrm{L}}\left(\overline{\mathbf{u_i}'\boldsymbol{u_j}'}(\boldsymbol{\nabla u})^{\boldsymbol{T}}+(\nabla\boldsymbol{u})\overline{\mathbf{u_i}'\boldsymbol{u_j}'}\right) \quad (1\text{-}18)$$

Turbulence dissipation appeared in Equation 1-17, the related transport equation is provided as,

$$\frac{\partial}{\partial \mathrm{t}}(\alpha_L\rho_L\varepsilon)+\frac{\partial}{\partial x_i}(\alpha_L\rho_L\boldsymbol{u}_i\varepsilon)=\frac{\partial}{\partial x_j}\left(\alpha_L\left(\mu_L+\frac{\mu_{t,L}}{\sigma_\varepsilon}\right)\frac{\partial\varepsilon}{\partial x_j}\right)+\alpha_L C_{1\varepsilon}\rho_L\left(\overline{\boldsymbol{u}'_{\boldsymbol{i}}\boldsymbol{u}'_{\boldsymbol{k}}}\frac{\partial\boldsymbol{u_i}}{\partial x_k}\right)\frac{\varepsilon}{k}-\alpha_L C_{2\varepsilon}\rho_L\frac{\varepsilon^2}{k} \quad (1\text{-}19)$$

And k can be obtained from the solved values of normal stress using the Reynolds stress transport equation, as

$$k = \frac{1}{2}\left(\sum_{i=1,2,3} u_i' u_i'\right) \quad (1\text{-}20)$$

Based on the Reynolds stress transport equation, which incorporates the Reynolds stress development process, global effects such as streamline curvature and rotating systems and therefore provides a better prediction of complex turbulent flows (Gupta and Roy, 2013, Tabib et al., 2008). While the Reynolds stress dissipation near the wall is strongly anisotropic, the dissipation model needs to be improved. Equation 1-19 is basically reasonable, but the anisotropic diffusion should be considered. The deficiencies of the Reynolds stress model are particularly pronounced in near-wall turbulence and strongly rotating turbulence. Its resolution for small-scale turbulent eddies in bubble column should be improved due to limitations in computational accuracy.

Large eddy simulation

RANS has been developed over a long period of time and is very mature. However, RANS does not capture the small eddy structures in turbulent flows by averaging out the velocities. At the same time, these small eddies are essentially isotropic. On the other hand, the large vortices, which extract energy from the main flow, are anisotropic and are highly correlated with the geometry, boundaries of the computational domain and volumetric forces. When using RANS, the same turbulence model must be used for the whole flow field to resolve the turbulence at various scales, but usually the large and small eddies behave differently. Researchers have

therefore explored a more refined model. Unlike RANS, LES believes that large eddies are directly affected by boundary conditions and therefore need to be resolved, but small eddies are isotropic, so they behave the same and can be modeled. Hence, the smallest grid unit needs to be larger than the Kolmogorov scale, otherwise it may play the equivalent role with DNS. The most important part in LES is the modelling of the sub-grid scale (SGS) structures. The development of SGS models requires consideration of how information that is smaller than the grid scale is handled. Because the sub-grid scale is much larger than the Kolmogorov scale, the computational resource consumption of LES is much smaller than that of DNS and therefore, for a given computational resource, LES has more flexibility than DNS to compute cases with larger Reynolds numbers. In addition, unlike the concept of averaging in RANS, LES uses a spatial filtering technique. The concept of the LES model is as follows:

1. First filter function and appropriate SGS model have to be determined. In this way, transient calculations can be performed for all eddies larger than the sub-grid scale.

2. Apply the spatial filtering operation on time-dependent variables by using filter function. In this step, the eddies smaller than the cutoff scale are filtered out.

3. During the operation of solving large eddies and modeling small eddies, a sub-grid scale stress (SGS) is generated, and the sub-grid scale stress needs to be modeled by the SGS model. Thus, the entire flow field is decomposed into a large-scale component needs to be resolved and a sub-grid scale component needs to be modelled.

Filter Function

There are currently different filter functions available. The simplest filter function is box filter (top-hat filter).

$$G(x-x') = \begin{cases} \frac{1}{\Delta^3} & |x-x'| < \frac{\Delta}{2} \\ 0 & otherwise \end{cases} \quad (1\text{-}21)$$

Other filter functions include the Gaussian filter function developed by Stanford University and the Laplacian filter function. Using different filter functions, the flow field variables may have different profiles, as shown in Figure 1-9 (a) and Figure 1 (b).

Cutoff Length

The cutoff length Δ in Equation 1-21is a concept used to indicate how big an eddy is considered to be a large eddy, which can be of any size, but it is meaningless to choose a cutoff length smaller than the grid. Based on the Cartesian grid, the simplest cutoff length is calculated like,

$$\Delta = \sqrt[3]{\Delta_i \Delta_j \Delta_k} \quad (1\text{-}22)$$

where $\Delta_i, \Delta_j, \Delta_k$ stand for the length of the computational grid in i, j, k direction. There are also many other calculation methods including the maximum length method and the Prandtl mixed length method, which are not commonly used.

N-S Equation

For phase k simulation, according to Equation 1-3, after filtering, the continuous equation can be expressed by,

$$\frac{\partial}{\partial t}(\rho_k \alpha_k) + \nabla \cdot (\alpha_k \rho_k \bar{u}_k) = 0 \quad (1\text{-}23)$$

In LES, the velocity in Equation 1-23

$$\mathrm{u_k} = \bar{u}_k + u'_k \quad (1\text{-}24)$$

where $\bar{u}_k$ is the velocity that needs to be resolved in filtering, while $\mathrm{u_k}$ represents the instantaneous velocity and $\boldsymbol{u}'_k$ stands for the unresolved part that requires the closure from the use of the SGS model in the LES simulations. It needs to be noted that the equations of mass and momentum are derived by time-averaging in RANS models. In LES modelling, these equations are solved by spatial filtering, hence, $\widetilde{\boldsymbol{u}}_k$ and $\boldsymbol{u}'_k$ are referred to grid scale and sub-grid scale velocity, respectively. When either ensemble averaging or filtering is used, unclosed parts occur in the stress term and the interface forces.

Additionally, in terms of the momentum equation for incompressible flow,

$$\frac{\partial}{\partial \mathrm{t}}(\alpha_\mathrm{k}\rho_\mathrm{k}\bar{\mathbf{u}}_\mathbf{k}) + \nabla \cdot (\alpha_\mathrm{k}\rho_\mathrm{k}\overline{\mathbf{u}_\mathbf{k}\mathbf{u}_\mathbf{k}}) = -\nabla \cdot (\alpha_\mathrm{k}\bar{\boldsymbol{\tau}}_\mathbf{k}) - \alpha_\mathrm{k}\nabla\bar{\mathrm{p}} + \alpha_k\rho_k\boldsymbol{g} + \bar{\mathbf{M}}_{\mathrm{F,k}} \quad (1\text{-}25)$$

In Equation 1-25, apart from the unresolved $\bar{u}_k$ and $\bar{\mathrm{p}}$, the unknown $\overline{\mathrm{u_k u_k}}$term is added. In order to simplify the problem, the second term in Equation 1-25 can be written as follow,

$$\nabla \cdot (\overline{\mathbf{u_k} \mathbf{u_k}}) = \nabla \cdot (\overline{\mathbf{u}}_\mathbf{k} \overline{\mathbf{u}}_\mathbf{k}) + \left(\nabla \cdot (\overline{\mathbf{u_k} \mathbf{u_k}}) - \nabla \cdot (\overline{\mathbf{u}}_\mathbf{k} \overline{\mathbf{u}}_\mathbf{k})\right) \tag{1-26}$$

Substituting above equation into Equation 1-25,

$$\frac{\partial}{\partial \mathrm{t}} (\rho_\mathrm{k} \overline{\mathbf{u}}_\mathbf{k}) + \nabla \cdot (\rho_\mathrm{k} \overline{\mathbf{u}}_\mathbf{k} \overline{\mathbf{u}}_\mathbf{k}) = -\nabla \bar{\mathrm{p}} + \nabla \cdot (\nu \nabla \overline{\boldsymbol{u}}_{\boldsymbol{k}}) - \left(\nabla \cdot (\overline{\mathbf{u_k} \mathbf{u_k}}) - \nabla \cdot (\overline{\mathbf{u}}_\mathbf{k} \overline{\mathbf{u}}_\mathbf{k})\right) \tag{1-27}$$

Comparing with original NS equation, the last term is the special term due to filter operation, and it can be expanded as,

$$\nabla \cdot \overline{\mathbf{u}}_\mathbf{k} \overline{\mathbf{u}}_\mathbf{k} = \nabla \cdot \begin{bmatrix} \overline{\mathbf{u}}_\mathbf{i} \\ \overline{\mathbf{u}}_\mathbf{j} \\ \overline{\mathbf{u}}_\mathbf{k} \end{bmatrix} [\overline{\mathbf{u}}_\mathbf{i} \quad \overline{\mathbf{u}}_\mathbf{j} \quad \overline{\mathbf{u}}_\mathbf{k}] = \nabla \cdot \begin{bmatrix} \bar{\mathrm{u}}_\mathrm{i} \bar{\mathrm{u}}_\mathrm{i} & \bar{\mathrm{u}}_\mathrm{i} \bar{\mathrm{u}}_\mathrm{j} & \bar{\mathrm{u}}_\mathrm{i} \bar{\mathrm{u}}_\mathrm{k} \\ \bar{\mathrm{u}}_\mathrm{j} \bar{\mathrm{u}}_\mathrm{i} & \bar{\mathrm{u}}_\mathrm{j} \bar{\mathrm{u}}_\mathrm{j} & \bar{\mathrm{u}}_\mathrm{j} \bar{\mathrm{u}}_\mathrm{k} \\ \bar{\mathrm{u}}_\mathrm{k} \bar{\mathrm{u}}_\mathrm{i} & \bar{\mathrm{u}}_\mathrm{k} \bar{\mathrm{u}}_\mathrm{j} & \bar{\mathrm{u}}_\mathrm{k} \bar{\mathrm{u}}_\mathrm{k} \end{bmatrix} \tag{1-28}$$

$$\nabla \cdot \overline{\mathbf{u_k} \mathbf{u_k}} = \nabla \cdot \overline{\begin{bmatrix} \boldsymbol{u}_\iota \\ \mathbf{u}_\jmath \\ \mathbf{u}_\mathbf{k} \end{bmatrix} [\boldsymbol{u}_\iota \quad \mathbf{u}_\jmath \quad \mathbf{u}_\mathbf{k}]} \tag{1-29}$$

Substitute above Eqns. (1-28) and (1-29) to $-\left(\nabla \cdot (\overline{\mathrm{u_k u_k}}) - \nabla \cdot (\bar{\mathrm{u}}_\mathrm{k} \bar{\mathrm{u}}_\mathrm{k})\right)$,

$$-\left(\nabla \cdot (\overline{\mathrm{u_k u_k}}) - \nabla \cdot (\bar{\mathrm{u}}_\mathrm{k} \bar{\mathrm{u}}_\mathrm{k})\right) = \nabla \cdot \begin{bmatrix} \overline{u_\iota u_\iota} - \bar{\mathrm{u}}_\mathrm{i} \bar{\mathrm{u}}_\mathrm{i} & \overline{\mathrm{u}_\imath u_\jmath} - \bar{\mathrm{u}}_\mathrm{i} \bar{\mathrm{u}}_\mathrm{j} & \overline{\mathrm{u}_\imath u_k} - \bar{\mathrm{u}}_\mathrm{i} \bar{\mathrm{u}}_\mathrm{k} \\ \overline{\mathrm{u}_\mathrm{j} u_\iota} - \bar{\mathrm{u}}_\mathrm{j} \bar{\mathrm{u}}_\mathrm{i} & \overline{\mathrm{u}_\jmath u_\jmath} - \bar{\mathrm{u}}_\mathrm{j} \bar{\mathrm{u}}_\mathrm{j} & \overline{\mathrm{u}_\mathrm{j} u_k} - \bar{\mathrm{u}}_\mathrm{j} \bar{\mathrm{u}}_\mathrm{k} \\ \overline{\mathrm{u}_\mathrm{k} u_\iota} - \bar{\mathrm{u}}_\mathrm{k} \bar{\mathrm{u}}_\mathrm{i} & \overline{\mathrm{u}_\mathrm{k} u_\jmath} - \bar{\mathrm{u}}_\mathrm{k} \bar{\mathrm{u}}_\mathrm{j} & \overline{\mathrm{u}_\mathrm{k} u_k} - \bar{\mathrm{u}}_\mathrm{k} \bar{\mathrm{u}}_\mathrm{k} \end{bmatrix}. \tag{1-30}$$

And stress can be defined as,

$$\tau = \begin{bmatrix} \overline{u_\iota u_\iota} - \bar{\mathrm{u}}_\mathrm{i}\bar{\mathrm{u}}_\mathrm{i} & \overline{\mathrm{u}_\mathrm{i} u_J} - \bar{\mathrm{u}}_\mathrm{i}\bar{\mathrm{u}}_\mathrm{j} & \overline{\mathrm{u}_\mathrm{i} u_k} - \bar{\mathrm{u}}_\mathrm{i}\bar{\mathrm{u}}_\mathrm{k} \\ \overline{\mathrm{u}_\mathrm{j} u_\iota} - \bar{\mathrm{u}}_\mathrm{j}\bar{\mathrm{u}}_\mathrm{i} & \overline{\mathrm{u}_\mathrm{j} u_J} - \bar{\mathrm{u}}_\mathrm{j}\bar{\mathrm{u}}_\mathrm{j} & \overline{\mathrm{u}_\mathrm{j} u_k} - \bar{\mathrm{u}}_\mathrm{j}\bar{\mathrm{u}}_\mathrm{k} \\ \overline{\mathrm{u}_\mathrm{k} u_\iota} - \bar{\mathrm{u}}_\mathrm{k}\bar{\mathrm{u}}_\mathrm{i} & \overline{\mathrm{u}_\mathrm{k} u_J} - \bar{\mathrm{u}}_\mathrm{k}\bar{\mathrm{u}}_\mathrm{j} & \overline{\mathrm{u}_\mathrm{k} u_k} - \bar{\mathrm{u}}_\mathrm{k}\bar{\mathrm{u}}_\mathrm{k} \end{bmatrix} \quad (1\text{-}31)$$

The definition of Equation 1-31 is the sub-grid-scale stress (SGS) in LES, which represents the effect of the modeled velocity component on the resolved velocity component. The simple version could be written as,

$$\tau_{ij} = \rho\overline{\boldsymbol{u_\iota u_J}} - \rho\bar{\boldsymbol{u}}_\boldsymbol{i}\bar{\boldsymbol{u}}_\boldsymbol{j} = \left(\rho\overline{\bar{\boldsymbol{u}}_\boldsymbol{\iota}\bar{\boldsymbol{u}}_\boldsymbol{J}} - \rho\bar{\boldsymbol{u}}_\boldsymbol{i}\bar{\boldsymbol{u}}_\boldsymbol{j}\right) + \rho\overline{\bar{\boldsymbol{u}}_\boldsymbol{\iota}\boldsymbol{u}_\boldsymbol{J}'} + \rho\overline{\bar{\boldsymbol{u}}_\boldsymbol{J}\boldsymbol{u}_\boldsymbol{\iota}'} + \rho\overline{\boldsymbol{u}_\boldsymbol{\iota}'\boldsymbol{u}_\boldsymbol{J}'} \quad (1\text{-}32)$$

(I) (II) (III)

From the mathematical perspective, it originated in the process of filtering nonlinear convection terms. Leonard (1975) further divides the sub-grid-scale stress (SGS) into three parts: (I) Leonard stress, (II) cross-stresses and (III) LES Reynolds stresses. The Leonard stress is due to the effects at resolved scale. The cross-stress term is due to the interactions between the eddies at SGS scale and resolved scale. Furthermore, the LES Reynolds stress is referring to the eddies in SGS scale and can be divided into partial stress and normal stress. When referring to the incompressible fluid or very small turbulent Mach number, the normal stress is usually negligible. Substitute Equation 1-32 into Equation 1-27,

$$\frac{\partial}{\partial \mathrm{t}}(\rho_\mathrm{k}\bar{\mathrm{u}}_\mathrm{k}) + \nabla\cdot(\rho_\mathrm{k}\bar{\mathrm{u}}_\mathrm{k}\bar{\mathrm{u}}_\mathrm{k}) = -\nabla\bar{\mathrm{p}} + \nabla\cdot(\nu\nabla\bar{u}_k) - \nabla\cdot\tau \quad (1\text{-}33)$$

Next step, τ needs to be modeled. It should be noted that $\bar{u}_k$ mentioned above is time-dependent, so LES is a kind of transient calculation. Also, due to the inherent nature of turbulence itself, LES is usually three-dimensional (except in very special cases). At the same time, it can be noticed that when the cutoff length $\Delta \rightarrow 0$, $\bar{u}_k \rightarrow u_k$. In this case, the eddies in any scale can be resolved. Thus, LES is converted to DNS.

Boussinesq Assumption

The simplest SGS model is realized by the Boussinesq assumption, which is the source of other more advanced models as well. Firstly, τ_{ij} is used to express partial stress and normal stress, where the normal stress portion is considered to be isotropic:

$$\tau_{ij} = \left(\tau_{ij} - \frac{1}{3}\tau_{kk}\delta_{ij}\right) + \frac{1}{3}\tau_{kk}\delta_{ij} \tag{1-34}$$

partial stress isotropic part

The relationship between the partial stress and the analytical deformation rate can be expressed as:

$$\frac{1}{3}\tau_{kk}\delta_{ij} = \frac{2}{3}\left(\frac{1}{2}\tau_{kk}\right)\delta_{ij} = \frac{2}{3}k_{SGS}\delta_{ij} \tag{1-35}$$

where $k_{SGS} = \frac{1}{2}\tau_{kk}$. Therefore,

$$\tau_{ij} = -2v_{SGS}\bar{S}_{ij} + \frac{2}{3}v_{SGS}\bar{S}_{ij}\delta_{ij} + \frac{2}{3}k_{SGS}\delta_{ij} \tag{1-36}$$

For incompressible flow,

$$\tau_{ij} = -2v_{SGS}\bar{S}_{ij} + \frac{2}{3}k_{SGS}\delta_{ij} \quad (1\text{-}37)$$

It can be seen that if v_{SGS} and k_{SGS} have specific value, then the unknown term in Equation 1-31 is only $\bar{u}_k$, and can be closed. The detail closure process is shown as follows.

The stress term of phase k is described as follows:

$$\tau_k = -\mu_{eff,k}\left(\nabla u_k + (\nabla u_k)^T - \frac{2}{3}I(\nabla \cdot u_k)\right) \quad (1\text{-}38)$$

where μ_{eff} represents the effective viscosity for the continuous phase, which may be assumed to be consisted of the following terms: the molecular viscosity μ_L, the turbulent viscosity μ_T and an additional term to describe bubble induced turbulence μ_{BI} (Dhotre et al., 2008). This is defined in Equation 1-39,

$$\mu_{eff,L} = \mu_{L,L} + \mu_{T,L} + \mu_{BIT,L} \quad (1\text{-}39)$$

The calculation of the effective gas viscosity is based on the effective liquid viscosity as was proposed by Jakobsen et al. (1997),

$$\mu_{eff,G} = \frac{\rho_G}{\rho_L}\mu_{eff,L} \quad (1\text{-}40)$$

The bubble induced turbulence can be modelled based on Sato's model (Sato et al., 1981), which is given by Equation 1-41

$$\mu_{\mathrm{BIT,L}} = \rho_L C_{\mu.BIT} \alpha_G d_B |u_G - u_L| \tag{1-41}$$

where $C_{\mu,\mathrm{BIT}}$ is the model constant with typical value of 0.6. It should be noted that the viscosity $\mu_{\mathrm{BIT,L}}$ characterizes turbulence behind the wake of rising bubbles, but ignores the contribution of the interactions between bubbles and the surrounding eddies with similar sizes. The additional effect of this interaction is investigated in Chapter 2.

Smagorinsky SGS Model

In Smagorinsky SGS model (Smagorinsky, 1963), v_{SGS} can be described as,

$$\mu_{SGS} = \rho(C_S\Delta)^2 \mid S \mid = \rho(C_S\Delta)^2 \sqrt{2\bar{S}_{ij}\bar{S}_{ij}} \tag{1-43}$$

where *Cs* is the Smagorinsky constant and S represents the characteristic resolved strain rate tensor. Lilly (1992) suggested a value for *Cs* of 0.17-0.21. However, in some cases this has been shown to overestimate the viscosity of large eddies at the wall due to excessive velocity gradients, so different values in the range of 0.065

to 0.12 were suggested (Milelli, 2002, Dhotre et al., 2008, Moin and Kim, 1982, Milelli et al., 2001). Different *Cs* indicate that the characteristics of the eddies are different and therefore a universal constant cannot be used to cover all cases. More advanced models are thus created.

Dynamic SGS model

Germano et al. (1991) and subsequently Lilly (1992) conceived a procedure in which the Smagorinsky model constant is dynamically computed based on the information provided by the resolved scales of motion. The dynamic procedure thus obviates the need for users to specify the model constant in advance. In the dynamic SGS model, a test cutoff length $\hat{\Delta}$ is defined in addition to the previous cutoff length. Lilly suggested the final C_{SGS} by least squares approach, and the calculated C_{SGS} varies with time and space. In some cases, however, the eddy viscosity calculated using this method becomes negative.

Finally, it should be mentioned that the main function of the SGS model is to dissipate turbulent fluctuations. The SGS model therefore needs to be given a suitable amount of dissipation. Therefore the LES needs to use a central difference format, as it does not involve additional numerical dissipation.

The flow in a 3D cylindrical bubble column is much more complex than in a 2D rectangular bubble column, and in contrast to the aperiodic flow in a rectangular bubble column, there is no significant regular low-frequency eddy structure in a cylindrical one. Since the commonly used RANS method uses time averaging, it is theoretically impossible to predict the high-frequency dynamic behaviour of the

bubble flow in RANS simulations, as the higher frequency turbulent eddy information is filtered out during the time averaging process.

The LES in gas-liquid two-phase flows has attracted the attention of many researchers in order to obtain more information on high frequencies structure. Figure 1-10 and 1-11 show the transient velocities obtained by Deen et al. (2001) using LES simulations and Liu using LES to recover the work done by Deen et al., and it is clear that the simulated dynamic results are very close to the experimental values. Due to the low gas superficial velocity, the maximum frequency of the dynamic information is not high. According to the literature, no simulations have been carried out for non-uniform flow patterns at high gas velocities, which is related to the limitations of the LES method for simulating gas-liquid two-phase flows in the Eulerian system. For the finite volume method, the successful use of simulation must ensure that the grid scale is within the inertia sub-range. Therefore, the application of LES to gas-liquid two-phase flow requires that the bubble size be smaller than the grid size, otherwise the bubble-induced grid-scale motion needs to be simulated directly, which is very difficult with respect to bubble shape and phase interface issues Milelli (2002) has suggested an optimum filter width $1.2 < \Delta/db < 1.5$ for a good performance LES grid, as shown in Figure 1-12. If the bubble size is smaller than the mesh size, the small-scale motion induced by the bubble can be modelled; however, due to the wide distribution of bubble sizes (1-50 mm) in the non-homogeneous flow regime, a very large mesh is required for LES, which causes two problems: firstly, the accuracy of the calculation cannot be met and it is difficult to

obtain mesh-independent solutions, and secondly, there is no guarantee that the inertia subregion is still present. Further discussion of the use of LES will be presented in Section 3.4.

3.3 Interphase forces

Additional interphase force models for closure are required when simulating the gas-liquid two-phase flow by using Eulerian-Eulerian two-fluid models. Interphase forces acting on bubbles include drag, lift, turbulent dispersion, virtual mass forces, wall lubrication and Basset force etc. All interphase forces arise from the inhomogeneous pressure and stress distribution on the bubble surface. When the bubbles are moving at constant velocity in a homogeneous liquid phase, they are only subject to drag forces. When the bubble is accelerated with respect to the liquid phase, it is also subject to virtual mass forces. If the bubble is moving in a non-uniform velocity field, there is also a transverse lift force. Due to the turbulent fluctuation of the liquid phase, the bubbles fluctuate and disperse under the influence of turbulent dispersion forces. When the bubble is close to the wall, the pressure in the boundary layer of the wall is higher than in the main stream due to the low velocity of the flow and the force is directed towards the main stream high speed region. The Basset force is a historical force that has a large effect on a very short time scale and can usually be ignored as the time step of the numerical simulation is much larger. The schematic of various force acting on bubbles are illustrated in Figure 1-13. The most recent study conducted by Muniz and Sommerfeld (2020) has evaluated the contributions of each force in fully developed bubble column

flows and have carefully compared the magnitude ratios of drag, lift, added mass, fluid inertia, Basset force and wall effects to the buoyancy force. Consequently, as shown in Figure 1-14, they have found that drag force can contribute approximately up to 90%, and 60%, 2-7%, 3%, 2% for added mass, Basset, transverse lift and wall lubrication force, respectively.

Drag force

The interphase momentum transfer between continuous and dispersed phases because of the drag force contributed from both viscous shear (skin drag) and the pressure gradient (form drag) is expressed by Equation (1-44),

$$\boldsymbol{F}_{D,L} = \frac{3}{4}\alpha_G \rho_L \frac{C_D}{d_B} |\boldsymbol{u}_G - \boldsymbol{u}_L|(\boldsymbol{u}_G - \boldsymbol{u}_L) \quad (1\text{-}44)$$

From Equation 1-44, the drag coefficient C_D, and bubble size $\mathrm{d_B}$ are also required to calculate the drag force. The drag force coefficient is also determined by bubble size, shape, physical conditions of the liquid phase. Thus, it is dependent on the parameters: bubble Reynolds number, Eotvos number and Morton number (Table 1-4).

Table 1- 4 Parameter related in calculating the drag coefficient

Dimensionless number	Expression	Physical Meaning	Relation
Re	$\frac{\rho_l u_b d_b}{\mu_l}$	the ratio of inertial forces to viscous forces	-
Eo	$\frac{g d_b^2 (\rho_l - \rho_g)}{\sigma}$	the ratio of gravitational forces to surface tension forces	-
We	$\frac{\rho_l u_b^2 d_b}{\sigma}$	the ratio of inertia to surface tension	$We = \frac{\mathrm{Re}^2 \, Mo^{1/2}}{Eo^{1/2}}$
Fr	$\frac{u_b}{\sqrt{g d_b}}$	the ratio of inertia to gravitational forces	-
Mo	$\frac{g \mu_l^4 (\rho_l - \rho_g)}{\rho_l^2 \sigma^3}$	combination of physical properties	$Mo = \frac{We^3}{Fr^2 \, \mathrm{Re}^4}$

In Eulerian-Eulerian two-fluid model, there are three ways of dealing with the drag coefficient: i) ignoring the bubble interactions and bubble deformation, calculate drag coefficient based on a spherical single bubble(Schiller, 1933, Moore, 1963, Morsi and Alexander, 1972, Clift, 1978); ii) considering bubble shape variation but ignoring the bubble interactions, modify the spherical drag coefficient model by introducing a shape factor(Ishii and Zuber, 1979); iii) considering bubble interactions and shape variations(Tomiyama, 1998), e.g. assume that the bubble swarm drag coefficient is a function of the gas volume fraction, the bubble swarm drag

coefficient is a factor of $(1-\alpha_G)^2$ of the single bubble drag coefficient. Generally, the common used correlations of the proposed drag force coefficients are summarized in Table 1-5.

Expressions 1-44 can also be used directly in the frame of Eulerian-Lagrangian. However, for the two-fluid model, it is necessary to establish the bubble swarm drag coefficient per unit volume. Obviously, it is more complex than the single bubble drag model. It is known that there is a strong interaction between the bubbles when in a non-homogeneous flow pattern. However, for simplicity, the ideal bubble swarm drag model is developed by ignoring the bubble interaction and then implicitly modified. The ideal bubble swarm drag coefficient is a simple superposition of the drag of individual spherical bubbles:

$$F_{D,swarm} = N_B \cdot F_{D,single} = \frac{\alpha_G}{\frac{\pi}{6}d_B^3} \cdot C_D \left(\frac{\pi}{4}d_B^2\right)\frac{\rho_L}{2} \ |\boldsymbol{u_G} - \boldsymbol{u_L}|(\boldsymbol{u_G} - \boldsymbol{u_L}) \quad (1\text{-}45)$$

Where N_B is the number of bubbles per unit volume, $N_B = \frac{\alpha_G}{\frac{\pi}{6}d_B^3}$. When the air volume fraction of a calculation cell is 1 or 0, multiplying the equation by α_L in order to ensure that the drag effect disappears, gives,

$$F_{D,swarm} = C_D \frac{3\alpha_G\alpha_L}{4}\frac{\rho_L}{d_B} \ |\boldsymbol{u_G} - \boldsymbol{u_L}|(\boldsymbol{u_G} - \boldsymbol{u_L}) \quad (1\text{-}46)$$

Table 1- 5 Popular drag force coefficient equations.

Model	Equation
Analytical	$C_D = \|24/\mathrm{Re}_b \; 0 \le \mathrm{Re}_b \le 0.2$
Schiller and Naumann (1935)	$C_D = \begin{cases} \frac{24}{Re_b}(1+0.15\mathrm{Re}_b^{0.687}) & \mathrm{Re}_b \le 1000 \\ 0.44 & \mathrm{Re}_b > 1000 \end{cases}$ $C_D = \max\{0.44, 24/Re_b(1+0.15\mathrm{Re}_b^{0.687})\}$
Moore (1963)	$C_D = \frac{48}{Re_b}\left(1 - \frac{2.2}{Re_b^{0.5}} + f(Re_b^{-5/6})\right) \; \mathrm{Re}_b \tilde{} 100$
(Morsi and Alexander, 1972)l	$C_D = a_1 + \frac{a_2}{Re_b} + \frac{a_3}{Re_b^2}$ $a_1, a_2, a_3 = \begin{cases} 0, 24, 0 & 0 < \mathrm{Re}_b < 0.1 \\ 3.690, 22.73, 0.0903 & 0.1 < \mathrm{Re}_b < 1 \\ 1.222, 29.1667, -3.8889 & 1 < \mathrm{Re}_b < 10 \\ 0.6167, 46.50, -116.67 & 10 < \mathrm{Re}_b < 10^2 \\ 0.3644, 98.33, -2778 & 10^2 < \mathrm{Re}_b < 10^3 \\ 0.357, 148.62, -47500 & 10^3 < \mathrm{Re}_b < 5\times10^3 \\ 0.46, -490.546, 578700 & 5\times10^3 < \mathrm{Re}_b < 10^4 \\ 0.5191, -1662.5, 5416700 & \mathrm{Re}_b \ge 10^4 \end{cases}$
Clift et al. (1978)	$C_D = 3/16 + 24/\mathrm{Re}_b \; \mathrm{Re}_b < 0.01$ $0 < \mathrm{Re}_b < 0.1$ $0.1 < \mathrm{Re}_b < 1$ $1 < \mathrm{Re}_b < 10$ $10 < \mathrm{Re}_b < 10^2$ $10^2 < \mathrm{Re}_b < 10^3$ $10^3 < \mathrm{Re}_b < 5\times10^3$ $5\times10^3 < \mathrm{Re}_b < 10^4$ $\mathrm{Re}_b \ge 10^4$ $C_D = 24/\mathrm{Re}_b[1+0.1315Re_b^{(0.82-0.05w)}] \; 0.01 < \mathrm{Re}_b \le 20$ $C_D = 24/\mathrm{Re}_b[1+0.1935Re_b^{0.0305}] \; 20 \le \mathrm{Re}_b \le 260$ $C_D = 24/\mathrm{Re}_b[44.005\times10^{-1.1242w+0.1558w^2}] \; 260 \le \mathrm{Re}_b \le 1500$ Where, $w = \log_{10}\mathrm{Re}_b$
Ishii and Zuber (1979)	$C_D = \max(\min(C_{D-ellipse}, C_{D-cap}), C_{D-sphdere})$ $C_{D-ellipse} = 24/\mathrm{Re}_b(1+0.15\mathrm{Re}_b^{0.75}) \; 0 \le \mathrm{Re}_b < 1000$ $C_{D-ellipse} = \frac{2}{3}Eo^{1/2} \; \mathrm{Re}_b \ge 1000$ $C_{D-cap} = \frac{8}{3}$
Mei et al. (1994)	$C_D = \frac{24}{\mathrm{Re}_b}\left\{\frac{2}{3} + \left[\frac{12}{\mathrm{Re}_b} + 0.75\left(1 + \frac{3.315}{\sqrt{\mathrm{Re}_b}}\right)\right]^{-1}\right\}$
Grevskott et al. (1996)	$C_D = \begin{cases} \frac{5.645}{\frac{1.0}{Eo} + 2.385}, & d_s \ge 2.0\mathrm{mm} \\ \frac{8}{3}(1-\alpha_g)^2, & d_s < 2.0\mathrm{mm} \end{cases}$ Where: $d_s$is solid particle diameter and $\alpha_g$is the volume fraction of gas.
Tomiyama et al. (1998)	For contaminated system $C_D = \max\left[\frac{24}{\mathrm{Re}_b}(1+0.15\mathrm{Re}_b^{0.687}), \frac{8}{3}\frac{E_O}{E_O+4}\right]$ For a slightly contaminated system $C_D = \max\left\{\min\left[\frac{24}{Re}(1+0.15Re_b^{0.687}), \frac{72}{Re}\right], \frac{8}{3}\frac{Eo}{Eo+4}\right\}$ For pure system $C_D = \max\left\{\min\left[\frac{16}{Re}(1+0.15Re_b^{0.687}), \frac{48}{Re}\right], \frac{8}{3}\frac{Eo}{Eo+4}\right\}$ $10^{-2} < Eo < 10^3, 10^{-3} < \mathrm{Re}_b < 10^6, 10^{-14} < Mo < 10^7$
Lain et al. (1999)	$C_D = \begin{cases} 24/Re_b(1.0+0.15Re_b^{0.68}), & Re_b < 500 \\ 9.5\times10^{-5}Re_b^{1.397}, & 500 < Re_b < 1500 \\ 2.61, & Re_b \ge 1500 \end{cases}$
Kurose et al. (2001)	$C_D = \begin{cases} \frac{16}{Re_b} & Re_b < 1 \\ 16/Re_b(1+0.15\mathrm{Re}_b^{0.5}) & 1 \le Re_b \end{cases}$

Model	Equation
Zhang and VanderHeyden (2002)	$0.5 \le \mathrm{Re}_b \le 200$ $C_D = 0.44 + \frac{24}{Re_b} + \frac{6}{1+\sqrt{Re_b}}$
Tomiyama (2004)	$C_D = \frac{8}{3}\frac{Eo(1-\chi^2)}{\chi^{2/3}Eo + 16\chi^{4/3}(1-\chi^2)} f(\chi)^{-2}$ Where: $f(E) = \frac{\sin^{-1}(\sqrt{1-\chi^2}) - \chi\sqrt{1-\chi^2}}{(1-\chi^2)}, \chi = \frac{1}{1+0.163Eo^{0.757}}$
Simonnet et al. (2007)	$C_D = C_{D\infty}E'$ $E' = (1-\alpha_{loc})\left[(1-\alpha_{loc})^m + \left(4.8\frac{\alpha_{loc}}{1-\alpha_{loc}}\right)^m\right]^{-2/m}$,m = 25 $C_{D\infty} = \frac{4}{3}\frac{\rho_l - \rho_g}{\rho_l} g d_b \frac{1-\alpha_{loc}}{\lvert \mathbf{U}_{\text{relative}} \rvert^2}$ $\mathbf{U}_{\text{relative}} = \mathbf{U}_g - \mathbf{U}_l$
Snyder et al. (2007)	$C_D = \begin{cases} \frac{24}{Re_b}, & Re_b < 1 \\ \left(\frac{24}{Re_b}\right)\left(1 + \frac{3.6}{Re_b^{0.313}}\left(\frac{Re_b - 1}{19}\right)^2\right), & 1 \le Re_b \le 20 \\ \left(\frac{24}{Re_b}\right)\left(1 + .15Re_b^{0.687}\right), & Re_b > 20 \end{cases}$
Loth (2008)	$C_D \approx \max(C_{D,1}, C_{D,2})$ for $Re_b > 100$ $C_{D,1} \approx 2.5\tanh(0.2We) - 1.5$ $C_{D,2} = 48/\mathrm{Re}_b G(\chi)(1 - 2.21H(\chi)/\mathrm{Re}_b)$ For $\chi > 0.5$ $G(\chi) \approx 0.1287 + 0.4256/\chi + 0.4466/\chi^2$ $H(\chi) \approx 0.8886 + 0.5693/\chi - 0.4563/\chi^2$
Roghair et al. (2011)	$C_{D,\text{swarm of bubble}} = (1-\alpha)C_{D\infty}f(\alpha)$ Where: $f(\alpha) = [(1-\alpha_{loc})^m + (4.8\alpha_{loc}/(1-\alpha_{loc}))^m]^{-2/m}$ $C_{D,\infty} = \sqrt{C_D(Eo)^2 + C_D(\mathrm{Re}_b)^2}$ $C_D(Eo) = 4Eo/(9.5 + \mathrm{E}o)$ $C_D(\mathrm{Re}_b) = \frac{16}{\mathrm{Re}_b}\left(1 + 2/\left(1 + \frac{16}{\mathrm{Re}_b} + \frac{3.315}{\sqrt{\mathrm{Re}_b}}\right)\right)$ $1 \le Eo \le 5,\ 4\times10^{-12} < Mo < 2\times10^{-9}$ For transition, $m = 25$
Rastello et al. (2011)	$C_D(\chi) = \frac{16}{\mathrm{Re}_b}\left[\frac{1 + 8/15(\chi-1) + 0.015(3G(\chi)-2)\mathrm{Re}_b}{1 + 0.015\mathrm{Re}_b} + \left[\frac{8}{\mathrm{Re}_b} + \frac{1}{2}\left(1 + \frac{3.315H(\chi)G(\chi)}{\mathrm{Re}_b}\right)\right]^{-1}\right]\left(1 + \frac{0.3}{Ro^{2.5}}\right)$ $G(\chi) = \frac{\chi^{-4/3}(\chi^{-2}-1)^{3/2}[(\chi^{-2}-1)^{1/2} - (2-\chi^{-2})\mathrm{arcsec}\,\chi^{-1}]}{3[\chi^{-2}\,\mathrm{arcsec}\,\chi^{-1} - (\chi^{-2}-1)^{1/2}]^2}$ $H(\chi) = 0.0108\chi^{-4} - 0.157\chi^{-3} + 1.5725\chi^{-2} - 2.0195\chi^{-1} - 1.617$ $\chi = 1 + 5/32We + O(We^2)$ $0.7 \le \mathrm{Re}_b \le 380,\ 0.58 \le Ro \le 26,\ 1 \le \chi \le 3$
Aoyama et al. (2016)	$C_D(\chi) = \frac{16}{\mathrm{Re}_b}\left[\frac{1 + 8/15(\chi-1) + 0.015(3G(\chi)-2)\mathrm{Re}_b}{1 + 0.015\mathrm{Re}_b} + \left[\frac{8}{\mathrm{Re}_b} + \frac{1}{2}\left(1 + \frac{3.315H(\chi)G(\chi)}{\mathrm{Re}_b}\right)\right]^{-1}\right]\left(1 + \frac{0.3}{Ro^{2.5}}\right)$ $G(\chi) = \frac{\chi^{-4/3}(\chi^{-2}-1)^{3/2}[(\chi^{-2}-1)^{1/2} - (2-\chi^{-2})\mathrm{arcsec}\,\chi^{-1}]}{3[\chi^{-2}\,\mathrm{arcsec}\,\chi^{-1} - (\chi^{-2}-1)^{1/2}]^2}$ $H(\chi) = 0.0108\chi^{-4} - 0.157\chi^{-3} + 1.5725\chi^{-2} - 2.0195\chi^{-1} - 1.617$ $\chi = \frac{1}{[1 + 0.016Eo^{1.12}\mathrm{Re}_b]^{0.388}}$ $-11 \le \log Mo \le 0.63,$ $3.2\times10^{-3} \le \mathrm{Re}_b \le 1.3\times10^{2},$ $4.2\times10^{-2} < Eo < 2.9\times10^{1}$
Buffo et al. (2016)	$C_D = C_{D,\rho}(Re_{b-\mathrm{mod}})f(\alpha_g)$ $f(\alpha_d) = \begin{cases} (1-\alpha_g)^{C_A} & \text{if } \alpha_g \le 0.8 \\ 1 & \text{if } \alpha_g > 0.8 \end{cases}$ $C_{D,\rho}(\mathrm{Re}_{b-\mathrm{mod}}) = \max\left[\frac{24}{\mathrm{Re}_{b-\mathrm{mod}}}(1 + 0.15\mathrm{Re}_{b-\mathrm{mod}}^{0.687}),\ \frac{8}{3}\frac{\mathrm{E}o}{\mathrm{E}o + 4}\right]$ $\mathrm{Re}_{b-\mathrm{mod}} = \frac{d_b\rho_g\lvert \mathbf{U}_g - \mathbf{U}_l \rvert}{\mu_{\text{eff}}}$ $\mu_{\text{eff}} = \mu_g + C_B\rho_g\frac{k^2}{\varepsilon}$ C_A, C_B are model constants.
Feng and Bolotnov (2016)	$C_D = \min[48/Re_b(1 + 3\times110^{-10}Re_b^{3.319}), 16/Re_b(1 + 0.15Re_b^{0.687})]$ Where $Re_b < 900$

Lift force

Lift is the key force driving the radial motion of bubbles and is a difficult part of gas-liquid two-phase flow simulation (Joshi, 2001). Figure 1-15 illustrates the mechanism of lift is quite complex, including Magnus lift due to bubble rotation, Saffman lift due to liquid-phase velocity gradient, and the lift due to bubble deformation (Rafique et al., 2004).

However, it is generally accepted that the main contribution of the lift force is due to liquid-phase velocity gradient, and this shear-induced lift can be derived as (Drew and Lahey Jr, 1987, Ẑun, 1980),

$$F_{L,L} = \frac{\pi}{6} C_L \rho_L d_B^3 (U_B - U_L) \times (\nabla \times U_L) \quad (1\text{-}47)$$

where C_L is the lift force coefficient. When C_L>0, the lift force points in the direction of the decrease in the velocity of the liquid phase. There are different views in the literature on the role of lift. Some numerical simulations have obtained good results without considering lift (Sanyal et al., 1999, Chen et al., 2005b, Chen et al., 2005a, Krishna et al., 2000b), while others consider that lift must be taken into account, otherwise the radial distribution of the gas holdup cannot be modelled correctly (Zhang et al., 2006, Muniz and Sommerfeld, 2020). The values of the lift coefficients in the literature vary considerably. Thomas et al. (1983) theoretically derived a lift coefficient of 0.5 for spherical particles in potential flows. Numerical simulations by Ervin and Tryggvason (1997) and experimental studies by Tomiyama (1995) have shown that the direction of lift changes when the bubble undergoes sufficient deformation. Lahey Jr (1990) suggested that the lift coefficient varies in viscous

flows down to 0.01. Furthermore, the coefficient of lift was found to be dependent on the bubble size and a model expression for the coefficient of lift was developed by Tomiyama et al. (2002):

$$C_L = \begin{cases} min[0.288\tanh(0.1221Re_B), f(E\ddot{o}_d)] & E\ddot{o}_d < 4 \\ f(E\ddot{o}_d) & 4 \le E\ddot{o}_d \le 10.7 \\ -0.28 & E\ddot{o}_d > 10.7 \end{cases} \quad (1\text{-}48)$$

where $f(E\ddot{o}_d) = 0.00105E\ddot{o}_d^3 - 0.0159E\ddot{o}_d^2 - 0.022204E\ddot{o}_d + 0.474$ and $E\ddot{o}_d$ is obtained based on $d_h = d_B\sqrt[3]{1 + 0.163E\ddot{o}^{0.757}}$ (Wellek et al., 1966). From Equation 1-48, the lift coefficient is positive for small bubbles and negative for large bubbles, the characteristic change point is at d_B=5.8 mm. It can be predicted that when the gas superficial velocity is high, there is a wide bubble size distribution range for the occurrence of bubble breakage and coalescence, in which the large bubbles tend to gather in the centre of the tower, while the small bubbles tend to disperse throughout the column, forming a parabolic radial distribution of gas hold-up.

Added mass force

When the bubble accelerating in the system, it is clear from the no-slip condition that part of the fluid in the vicinity of the bubble will be accelerated and the resulting force is called the virtual mass force or added mass force. Auton et al. (1988) proposed the expression base on the relative motion between bubbles and its surrounding liquid,

$$\boldsymbol{F}_{AM,L} = \alpha_G \rho_L C_{AM} \left(\frac{D\boldsymbol{u}_G}{Dt} - \frac{D\boldsymbol{u}_L}{Dt}\right) \quad (1\text{-}49)$$

where C_{AM} stands for the virtual mass coefficient, and a typical value of 0.5 is set for a spherical bubble in a potential flow field. Cook and Harlow (1986) suggested the value of 0.25, while Homsy et al. (1980) assumed that the virtual mass force coefficient is a function of the gas hold-up. There is a wide divergence of views in the literature on the role of virtual mass forces in the numerical simulation of bubble columns, and even the conclusions of the same authors are different (Tabib et al., 2008, Mudde and Simonin, 1999, Oey et al., 2003, Joshi, 2001).

Turbulent dispersion force

The turbulent dispersion force is another important interphase force contributing to bubble dispersion and is related to the correlation term of fluctuation velocity with gas hold-up in Equation 1-4. As seen in Figure 1-16, the turbulent eddies, which is of the same order of magnitude as the bubble size, has been shown to play a decisive role in the bubble coiling and entrainment and controls the bubble dispersion (Yang et al., 2002). The following equation for the turbulent dispersion force is proposed by Lopez de Bertodano (1992),

$$F_{TD,L} = C_{TD}\rho_L k \nabla \alpha_G \tag{1-50}$$

Where k is the turbulent kinetic energy and the value of the turbulent dispersion coefficient C_{TD} is suggested in the range of 0.1-1.

Based on the Favre-averaging on the interfacial drag, Burns et al. (2004) proposed a new turbulent dispersion force model,

$$\boldsymbol{F}_{TD,L} = C_{TD}\frac{3\alpha_G}{4}\frac{\rho_L}{d_B}(\boldsymbol{u_L} - \boldsymbol{u_G})\frac{\nu_t}{\sigma_{TD}}\left(\frac{\nabla\alpha_L}{\alpha_L} - \frac{\nabla\alpha_G}{\alpha_G}\right) \quad (1\text{-}51)$$

where C_{TD} is the turbulent dispersion coefficient and is assumed to constant 1 in this work, ν_t is the turbulent kinematic viscosity and σ_{TD} represents the turbulent Schmidt number, σ_{TD}= 0.9 is adopted here.

Wall lubrication force

Due to the surface tension, the bubbles are subjected to lateral resistance as moving towards the wall. The resistance plays a role in preventing them from a further step towards the wall, thus resulting in a lower gas gold-up in the vicinity of wall. An expression for this force is derived by Antal et al. (1991),

$$F_{W,L} = \frac{2}{d_B}\left(C_{W1} + C_{W2}\left(\frac{d_B}{2y}\right)\right)\rho_L\left|U_{slip}\right|^2 n \quad (1\text{-}52)$$

where y is the distance between bubble and wall, n is the unit vector normal to the wall, and the two factors are calculated as $C_{W1} = -0.104 - 0.06|Uslip|$ and $C_{W2} = 0.147$. However, the above model limits the condition that $y \leq 5d_B$, thus the grid resolution required by this model is relatively high. Tomiyama (1995) proposed a novel model which is depends on the pipe diameter and Eo number:

$$F_W = \frac{2}{d_B}C_{W3}\left(\frac{d_B}{2y}\right)^2\rho_L\left|U_{slip}\right|^2 n \quad (1\text{-}53)$$

where C_{W3} is a model parameter which can be determined by:

$$C_{W3} = \begin{cases} \exp(-0.933E\ddot{o} + 1.79) & 1 < E\ddot{o} < 5 \\ 0.007E\ddot{o} + 0.04 & 5 < E\ddot{o} < 33 \end{cases} \quad (1\text{-}54)$$

3.4 Bubble size distribution

The prediction of bubble sizes is essential in the numerical studies of bubble columns, as it is required by both the interphase force closure, such as drag and lift force, and the turbulence closure due to bubble's contribution. Some early stage CFD studies have used the averaged bubble size, which can only be obtained from experimental measurements or determined by repetitive trial and-error simulations. However, not only the predictive nature of CFD modelling has been lost by doing so, but more importantly, an averaged bubble size usually cannot reflect the real inhomogeneity of bubble sizes in time and space. Especially when the bubble columns are operated at the heterogeneous regime with high gas holdup and superficial velocity, the bubble sizes can be widely distributed. Different models have been developed to cope with this issue. For example, rather than explicitly using the bubble diameter, Thakre and Joshi (1999), Vitankar et al. (2002), Ekambara et al. (2005) and Dhotre et al. (2007, 2004, 2005) have used the ratio of drag coefficient and bubble diameter C_D / d_B as a lumping coefficient to close the interphase momentum exchange term. In CFD simulations of bubble columns, the average bubble size model is the most commonly used model, which requires experimental or iterative numerical simulations to determine the bubble size, and its applicability and reasonableness have been criticised. Especially at high gas velocities and high gas hold-ups, the bubble size distribution is wide and the average bubble size model is

obviously not consistent with the actual situation. For this reason, Krishna et al. (1996, 1999a) has proposed the concept of a two bubble groups model, which classified bubble sizes into large and small two groups, based on dynamic gas disengagement (DGD) experimental phenomena (Krishna and Ellenberger, 1996). At the same time, empirical formulas for calculating the size of large bubbles and the bubble drag coefficient were developed (Krishna et al., 1999b). Based on the two bubble groups model, they carried out a large number of 2D and 3D numerical simulations of a cylindrical bubble column using CFX (Krishna et al., 2000b, Van Baten and Krishna, 2003, Krishna et al., 2001, Krishna et al., 1999a, Van Baten and Krishna, 2004c, Van Baten and Krishna, 2001, Van Baten and Krishna, 2004a, Van Baten and Krishna, 2004b). It was observed that the model provides a significant improvement over the average bubble size model and significantly broadens the range of gas velocities simulated. However, the two bubble groups model was not been validated by experimental results, rather a large number of experimental studies have shown that the bubble sizes are more often in the forms of normal distribution (Desvigne et al., 2006) or logarithmic normal distribution (Wongsuchoto et al., 2003). In addition, the two bubble groups model is a static model that does not take into account the interaction between bubbles and cannot capture the dynamic changes in bubble size.

In recent years, the particle population balance (PBM) model has been applied to determine the bubble size distribution. The model is able to simulate the variation of number density and is highly valued by the academic community. Wu et al. (1998), Ishii's group (2003a, 2003b, 2004 and Sun et al., 2004), Lehr (2001, 2002),

Olmos (2001, 2003), Buwa and Ranade (2002), Wang et al. (2006), Van den Hengel et al. (2005) and Bhole et al. (2008) have done important work on this subject, proposing bubble interfacial area transport models, bubble volume transport models and bubble PBM models. All these models are the presences of different formats of the particle population balance model, with different levels of complexity, number of equations and model assumptions, but all of them are able to take bubble breakup and coalescence into account.

Wu et al. (1998) and Ishii et al. (2003a, 2003b, 2004) developed a bubble interfacial area transport model, either as a single bubble group - interfacial area concentration model (single equation) or as a double bubble group - interfacial area concentration model (two equations). When the bubble size is small and the bubbles are spherical or ellipsoidal with low gas holdup, the single bubble group - interfacial area transport model can be used. While for large and spherical bubbles with high gas holdup, double bubble group - interfacial area transport model is used. The interfacial area transport model is a simplification of the population balance model. Two assumptions are made in the derivation: firstly, the difference in sub-bubble breakup and coalescence rates within the same bubble group is not considered; secondly, the difference in velocity between sub-bubbles is ignored.

Lehr et al. (2001, 2002) developed a bubble volume transport model, which was derived in a similar way to the bubble interfacial area transport model. The model is also divided into a single bubble group model and a double bubble group model.

In addition to the bubble volume transport model, Lehr proposed a new model describing the bubble breakup and coalescence mechanism through experimental and theoretical analysis.

However, both the bubble interfacial area transport model and the bubble volume transport model are simplifications of the bubble PBM, which have the advantages of fewer equations (one or two) and lower computational effort, and are suitable for numerical simulations of large reactors. However, the effect of sub-bubble size on the rate of bubble breakup and coalescence is neglected in the derivation and the bubble size distribution cannot be predicted. With the increase in computer speed, it is possible to get as soon as possible to the original bubble PBM. Bhole et al. (2008), Van den Hengel et al. (2005), Wang et al. (2006), Buwa and Ranade (2002), Chen et al. (2005a. 2005b), Sanyal et al. (2005), and Olmos et al. (2001, 2003) have done important work on this subject; however, the bubble breakup and coalescence models used in their studies are not identical, and in particular, the number of discrete sub-bubbles varies considerably.

The core of the bubble population balance model is how to describe the bubble breakup and coalescence. The bubble coalescence in bubble column can be classified into: the coalescence due to liquid turbulent fluctuations; the coalescence due to velocity differences and bubble collision coalescence due to the shear of mean velocity gradient in the liquid phase. According to open literature, most of the bubble coalescence models are proposed based on the coalescence due to liquid turbulent fluctuations (Luo, 1993, Lehr et al., 2002, Chesters, 1991, Prince and Blanch, 1990). In terms of the bubble breakage model, the mechanism breakage consists of:

bubble breakage due to turbulent eddies collisions, bubble breakage due to liquid-phase velocity gradients that stretch the bubble, and bubble breakage due to Rayleigh-Taylor and Kelvin-Helmholtz instabilities. Of these, bubble breakage due to turbulent eddies collisions are regarded as the most important part, i.e., Luo (1993) and Lehr (2002) models. Figure 1-17 shows the comparisons of the predicted radial gas hold up profile and equivalent bubble diameter by using different bubble breakage model. Based on the most widely used Luo and Svendsen breakage model, Shi et al. derived the basic form of the BIT turbulent kinetic energy spectrum function from the wave number κ-3 characteristics of the BIT turbulent energy spectrum and the equivalent equilibrium relationship between the generation and extinction of BIT turbulent kinetic energy, and established a bubble breakage model considering the combined effect of bubble-induced turbulence and shear turbulence.

In the previous decade, significant progress has been made in LES in understanding bubbly flow in bubble column reactor. It is, however, mostly limited to the system with relative weak turbulence (low gas superficial velocities and gas hold-up). In this scenario, the LES simulation involving bubble breakage and coalescence are rarely addressed. Future research should concentrate on large-scale reactors with high gas velocity that are industrially useful. Modeling bubble coalescence and disintegration may be required in this scenario, the understanding of the nature of the bubbling behavior could become feasible soon.

4. EXPERIMENTS VALIDATION

Experimental studies of bubble columns have progressed from simple to complex, macroscopic to fine scale, steady state to unsteady state. Prior to the 1900s, the focus was on the time-averaged steady-state performance of bubble column, with the discovery of large-scale liquid-phase cycling in the reactor being the hallmark achievement. The experimental methods used during this period were relatively simple, such as bed expansion to measure the overall gas hold-up, chemical and dissolved oxygen electrodes to measure the mass transfer coefficient, conductivity probes or photoelectric probes to measure the local gas hold-up, and Pitot tube to measure the time-averaged liquid velocity. Since the 1980s, experimental fluid dynamics has developed rapidly, and a number of new test techniques have been developed, such as hot-wire anemometers, PIV (Delnoij et al., 1999, Sathe et al., 2011), LDV (Lee et al., 2001), high-speed cameras, etc., which can be used to measure local and transient liquid-phase flow fields, bubble sizes, etc. The PIV, LDV and high-speed camera are non-contact optical measuring devices that do not disturb the flow field and have a high accuracy. However, due to the strong scattering effect of bubbles on light, these optical measurement techniques can only be used for low overall gas hold-up flow fields. Since the 1990s, new test techniques such as ERT (Vijayan et al., 2007), ET (Warsito and Fan, 2001), γ-CT (Shollenberger et al., 1997, Shaikh and Al-Dahhan, 2005), X-CT (Hubers et al., 2005) and CARPT (Devanathan et al., 1990) have been utilized in experimental discoveries of bubble columns regardless of the operating conditions, which can be

used at high temperatures, high pressures and high gas volume fraction. Since then, experimental studies on bubble columns have focused on the structure and dynamic behaviours of the turbulent eddy in bubble column reactors.

4.1 Studies on averaged parameters

The average performance of a bubble column include the overall gas hold-up, mass transfer coefficient, axial diffusion coefficient and mixing time etc. There are many factors affecting the average performance parameters of a bubble column, such as temperature, pressure, gas superficial velocity, height-to-diameter ratio (H/D), column diameter, sparger's structure, density of gas and liquid phase, kinematic viscosity of the continuous phase and surface tension.

Effect of gas superficial velocity

The overall gas holdup increases as the gas superficial velocity (U_g) increases, but the rate of increase is also related to the condition of gas superficial velocity. When U_g is low, the flow in bubble column is usually homogeneous with small bubble size and relative weak interactions. In this scenario, the gas holdup increases linearly with the increasing gas superficial velocity. At higher U_g and non-homogeneous flow patterns, the bubbles interact strongly and start to coalescence, the number of large bubbles increases. The gas hold-up decreases with increasing U_g due to the higher rising velocities of large bubbles. In terms of mass transfer, Vandu et al. (Vandu and Krishna, 2003, Vandu et al., 2004b, Vandu and Krishna, 2004b) reports

that $k_l a$ increases with U_g but $k_l a/\varepsilon$ slightly decreases with the increase of U_g and keeps constant after $U_g > 0.08$ m/s. Han (2007) also reports that the mass transfer coefficients k_l and $k_l a$ increase with U_g, but k_l ceases to change at certain gas superficial velocities.

Effect of column diameter

Kumar et al. (1997) employed the CT technique to capture the radial distribution of gas holdup, and accordingly obtained the cross-sectional averaged gas hold-up. It was found that at high gas superficial velocity (U_g=0.08 m/s), the cross-sectional averaged gas holdup increased with increasing column diameter (0.1m< D <0.3m). While column diameters greater than 0.15m, the change in gas hold-up was not significant. At low gas velocities, the cross-sectional averaged gas hold-up decreases to a low point and then increases with column diameter. Luo et al. (1999) and Sommerfeld et al. (2009) reported that the column wall effect was significant for column diameters less than 0.1 m. Daly et al. (1992) found that the average gas hold-up of small diameter bubble columns was slightly higher than that of large columns under same gas superficial velocity. What can be clearly seen in the experimental studies carried out by Forret et al. (2003) showed a steady increase in gas hold-up with increasing column diameter (0.15m, 0.4m, 1m) but the difference did not exceed 5%. However, Vandu and Krishna (2004a) investigated the influence of different bubble column scales (D=0.1m, 0.15m, 0.38m) on the mass transfer coefficient in bubble columns. It was found that the average gas hold-up decreased with increasing column diameter. They attributed this phenomenon to the

fact that the large circulation velocity is enhanced due to the increasing in bubble terminal velocity when increasing column diameter. It can be seen that there are different conclusions in the literatures regarding the effect of column diameter on gas hold-up, but most agree that the effect is negligible for column diameters greater than 0.1 m. The effect of column diameter on the mass transfer coefficient has been less studied, and it is generally accepted that the mass transfer coefficient $k_l a$ is directly related to the average gas hold-up, and that a larger gas gold-up results in a larger mass transfer coefficient, making the gas hold-up an important indicator of the mass transfer coefficient. Vandu and Krishna (2004a) reported that $k_l a$ decreases slightly with increasing column diameter (0.1m, 0.15m, 0.38m), but $k_l a/\varepsilon$ is not affected by column diameter.

Effect of gas distributor

The design of gas distributors impacts the initial bubble size and the initial bubble dispersion, which in turn affects the overall gas hold-up. Luo et al. (1999) demonstrated experimentally that the effect of the distributor on gas hold-up is significant, especially at low gas superficial velocities.

Table 1- 6 Spargers design detail in the experiment conducted by Throat et al. (1998)

Name	d_o	N	Pitch, LP	%F.A
SP1	0.8	315	Triangular	
SP2	1.5	88	Triangular	
SP3	3	23	Triangular	0.13
SP4	6	6	Triangular	
SP5	10	2	–	
SP6	14	1	–	
SP7	1.5	132	Triangular	0.2
SP8	3	33	Triangular	
SP9	1.5	198	Triangular	0.3
SP10	3	50	Triangular	
SP11	1	623	Random	
SP12	1.5	269	Triangular	
SP13	3	71	Triangular	0.42
SP14	6	16	Triangular	
SP15	25	1	–	
SP16	2.5	330	Random	
SP17	4	156	Triangular	1.68
SP18	6	64	Triangular	
SP19	50	1	–	
SP20	3	823	Random	
SP21	6	210	Random	5
SP22	87	1	–	

Thorat et al. (1998) comprehensively investigated the effects of distributor type (partial/uniform aeration), opening fraction, nozzle size and H/D ratio on the average gas hold-up. The experimental set-up and the spargers used are shown in Figure 1-18 and Table 1-6. For perforated plates distributor (d_0<3mm, N_0>20), the average gas hold-up decreased with increasing liquid level (1<H/D<5), and did not change significantly with increasing liquid level (H/D>5). For the sparger (3 mm<d_0<6 mm) perforated plate distributors, the height has little effect on the gas hold-up. In contrast, the gas hold-up of very large nozzle size distributors (d_0>10

mm) increases with increasing height. It can be explained by the initial bubble diameter is large that sufficient liquid level height is required to complete the break-up of the large bubbles. The opening fraction had little effect on the gas hold-up of the small nozzle size (d_0<3 mm) perforated plate (d_0>20), consistent with the findings of Patel and Thorat (2008). In contrast, for the larger nozzle size (d_0=6 mm) distributor, the smaller the opening fraction, the greater the gas hold-up. In study of Lau et al.(2010) on a porous plate distributor (d_0=3 mm), the cross-sectional averaged gas hold-up increases and then decreases with axial height, with H/D=2 being the critical point, which is also found by available literatures(Kulkarni et al., 2001, Camarasa et al., 1999). The influence of the gas sparger on the flow regime is also studied by Besagni et al. (2018). It is found in Figure 1-19 that a concave gas volume fraction distribution was formed by the coarser sparger, which induces a "pseudo-homogeneous" flow regime. In contrast, when the mono-dispersed homogeneous flow regime was produced, by using the fine sparger, a hindrance effect is always accompanied. This effect is physically depicted as an S-shaped gas holdup curve and is thought to be linked to the Ledinegg instability, which in-turn helped stabilize the homogeneous flow regime.

In terms of mass transfer, Han and Al-Dahhan (2007) reported that the influence of the distributor on the mass transfer coefficient was significant at low gas superficial velocities (U_g<0.15m/s) and, in contrast, negligible at high gas velocities. The smaller the nozzle size of the porous plate distributor, the larger the mass transfer coefficient $k_l a$.

Another key factor influenced by gas sparger is the mixing time. Haque et al.(1986) investigated in detail the effect of distributors on mixing times in bubbling columns with low H/D ratios (D=1m, H/D=2, single nozzle, three-nozzle, single ring, double ring, cruciform etc.), the details of the spargers are shown in Figure 1-20. The mixing time of single ring sparger was found to be independent of ring diameter. The mixing time for the double-ring sparger was longer than for the single-ring, single-nozzle and three-nozzle sparger, since the double-ring distributor induced more circulation cells. The mixing time of three-nozzle sparger is slightly less than that of the single-nozzle one because the hydrostatic zone of the three-hole nozzle is obvious smaller. Abraham (1989) found that mixing times for single-nozzle distributors were less than those for multi-hole distributors. However, Ravinath et al. (2003) reported that the mixing time of the perforated plate sparger was less than that of the centrally ventilated mono sparger. It is suggested that the gas distribution was better by using the former one, and the mixing was enhanced by the better gas dispersion. It can be concluded that bubble dispersion and liquid-phase flow patterns are two different mechanisms that influence mixing time. Also, the predicted mixing time was found to be dependent on the flow patterns at the time the tracer was injected as reported by McClure et al. (2015). If multiple tracers are included, it is possible to get more accurate estimates of the mixing time in bubble columns by utilizing the average mixing time.

The mixing time increases with the growth of H/D ratio, but the rate of change is dependent on the structure of the sparger. Ravinath et al. (2003) reported that the mixing time for a multi-nozzle sparger is the H/D to the power of 0.43, for a single-

nozzle sparger is to the power of 0.5, and 0.38 for an eccentrically mounted single-nozzle sparger.

Effect of physical properties and operating conditions

The average gas hold-up increases with the growth of gas density and the volumetric mass transfer coefficient follows the same pattern (Vandu and Krishna, 2004a); the reason for this is that as the gas density increases the bubbles are more easily broken leading to more small bubbles. The gas hold-up and mass transfer coefficient increase with increasing pressure, but $k_l a/\varepsilon$ is independent of pressure (Letzel et al., 1999). Han's experimental results show that pressure increases $k_l a$ significantly, but k_l decreases slightly (Han and Al-Dahhan, 2007).

Electrolytes are another important factor affecting the average gas hold-up. Numerous experiments have shown that electrolytes inhibit the aggregation of bubbles and increase the gas hold-up (Zahradnik et al., 1995, Besagni and Inzoli, 2017a, Besagni and Inzoli, 2015, Ruthiya et al., 2006), e.g. the gas hold-up of the air-alcohol system is significantly greater than that of the air-water system. The effect of liquid viscosity on gas hold-up is also significant, with low viscosity systems having an obvious higher gas hold-up than high viscosity systems (Veera and Joshi, 2000).

In gas-liquid-solid systems, the gas hold-up reduces with the growth of solid particles loading (Zhang et al., 2021, Orvalho et al., 2018, Vandu et al., 2004b); this is due to the intensification of bubble coalescence by the presence of solid particles, together the increase in liquid viscosity, finally resulting in a significant increase in

large bubbles. Zhang et al. illustrated the potential impacts of the solid particles on the flows in bubble column, as shown in Figure 1-21. The mass transfer coefficient k_la decreases as the solid mass fraction α_S increases (Vandu and Krishna, 2003, Vandu et al., 2005). When α_S <0.1, k_la/ε is not greatly affected by the solid phase fraction; when 0.1<α_S <0.4, k_la/ε varies between 0.4-0.6 $s^{-1;}$ when α_S =0.5, k_la/ε is about 0.29 s^{-1}.

The axial diffusion coefficient of the liquid phase is the key to the development of modelling the reaction engineering. Results from the literature show that the axial diffusion coefficient is positive proportional to gas superficial velocity and pressure (Lorenz et al., 2005). Forret et al. (2003) investigated the relationship between the axial diffusion coefficient D_{ax} and the column diameter and found that Riquarts empirical formulae were in good agreement with their experimental results.

4.2 Studies on local characterisation

Gas hold-up distribution

The gas hold-up(α) distribution is the fundamental cause of the overall liquid phase circulation in bubble columns, and its distribution profile is an important criterion for determining the flow pattern. At low gas superficial velocities, the gas hold-up distribution is relatively uniform and at high gas superficial velocities, the gas hold-up distribution is parabolic with a maximum at central region. And the gradient of α becomes steeper as the gas velocity increases. The gas hold-up distribution has been measured by a number of researchers, considering the effects of

various factors. Hills (1974) was the first to use a conductivity probe to measure the radial distribution of gas hold-up in bubbling columns, the effect of the velocity functions on the gas hold-up profile is investigated, as shown in Figure 1-22.

Kumar et al. (1997) used γ-CT to measure the gas hold-up distribution in bubble columns of different column diameters (0.102, 0.14, 0.19, 0.26, 0.30 m) and found that the column diameter had a significant effect on the gas hold-up distribution. As seen in Figure 1-23, at lower gas velocities (0.02 m/s), there is no common trend in the local gas hold-up with column diameter. However, Chen et al. (2001) found that the gas hold-up distribution became more uniform with increasing column diameter (0.2, 0.4, 0.8 m), contrary to the findings of Kumar et al. one can explain is that the curves were fitted based on the limited measure-points, which brought the inaccuracy.

The structure of the distributor is one of the most important factors influencing the distribution of gas hold-up. In terms of the method of ventilation, there are uniform and non-uniform aeration. Uniformly ventilated distributors include perforate, sintered plates etc., while non-uniform distributors include single-hole nozzles, annular distributors etc. The difference in gas hold-up distribution between uniform and non-uniform distributors is significant, especially in the control area of the distributor and at low gas superficial velocities. The radial distribution profile of gas hold-up in partially ventilated bubble columns becomes flatter in the axial direction, and verse visa for uniformly ventilated distributors.

Patel and Throat (2008) used GRT (Gamma Ray Topography) to measure the radial distribution of gas hold-up in the bubbler column and investigated the effect of

clogging and orifice size of the perforated plate. As shown in Figure 1-24, the gas hold-up was found to be closely related to the bubble flow pattern at the outlet of the distributor and a criterion for the bubble flow pattern was proposed, i.e. $N_{We} = \rho_G d_0 V_0^2/\sigma_L$ When N_{We} >2, the flow pattern is bubble jetting and bubbly flow for $N_{We} < 2$. It can be seen that the critical gas velocity for the transition from the bubbly flow to jetting state decreases as the increase in clogging. The experimental results show that when the gas superficial velocity and orifice size are the same, and the bubble flow pattern at the outlet of the distributor is the same in this scenario, the gas hold-up is independent of the opening ratio. Veera and Joshi (2000) found that the effect of liquid level height on the gas hold-up of a single orifice nozzle was related to the orifice diameter (U_g=0.24 m/s). At d_0=24 mm, the liquid level height has no effect on the gas hold-up distribution at the orifice, while at d_0=87 mm, as the liquid level increases (H/D>2), the gas hold-up at the orifice decreases and the gas hold-up distribution becomes flat.

Kumar et al. (1997) investigated the variation of the gas hold-up distribution along the axial liquid level height and found that the situation in small columns (0.1 m) was significantly different from that in large columns (0.2 m). In the small diameter bubble column with high gas superficial velocity (0.1 m, 0.12 m/s) there is a clear inlet zone and a gas hold-up equilibrium zone, where the gas hold-up gradually decreases along the axial height and finally reaches equilibrium. In contrast, the equilibrium zone does not exist for large diameter bubble columns operating at low gas superficial velocities (0.26 m, 0.05 m/s), and the gas hold-up increases in the axial direction. Chen et al. (1998) used CT to measure the gas hold-up distribution

at high gas superficial velocities (0.44 m, 0.1 m/s) and found the same phenomenon. However, the results of Veera et al. (1999) (D=0.38m) show that the gas hold-up increases only in the axial direction at the centre of the column, but decreases near the walls as shown in Figure 1-25, contrary to the findings of Chen et al. and Kumar et al. This difference may be related to the different column diameters and gas velocities of the bubble columns utilized.

The effect of pressure on local gas hold-up is also substantial, but the extent of the effect is related to the apparent gas velocity. Figure 1-26 shows the gas hold-up distribution measured by Kemoun et al. (2001) using γ-CT at different pressures and gas velocities. It can be seen that the higher the gas velocity the more significant the effect of pressure. Figure 1-26(c) shows that the gas hold-up at 0.7 MPa is approximately 70% higher than the gas hold-up at atmospheric pressure. In addition, increasing the pressure also results in a more uniform gas hold-up distribution.

Velocity distribution

Forret et al. (2003) investigated the effect of column diameter on the liquid velocity distribution in bubble columns. The experimental data are in good agreement with the empirical formulae of Miyauchi (1970), Nottenkämper et al.(1983) and Zehner (1986). However, when the column diameter larger than 0.4 m, an overestimation is found by using the Riquarts formula (1981), and the error becomes more significant as the column diameter increases. While Krishna et al. (2000a) found that measurements in small columns under various gas superficial velocities were in

good agreement with the Riquarts formula. Furthermore, 2D axisymmetric numerical simulations of bubble columns in different diameters were in good agreement with the Riquarts formula as well.

Vial et al. (2001) measured the velocity distribution of the liquid phase in the fully developed region of the bubble column (H/D=8) using LDV with three distributor configurations, i.e., single-hole nozzle (d_0=5 mm), perforated plate (d_0=1 mm, N_0=50) and micro-hole plate ($d_0 \approx$15mm). The single-hole nozzle in the non-homogeneous flow region were found to produce lower time-averaged axial liquid phase velocities than the other two configurations, which were still in the homogeneous flow region; but the single-hole nozzle produced the highest root-mean-square values of fluctuation velocities, reflecting the highly chaotic nature of their flow patterns.

4.3 Studies on bubble dynamics

Bubbles are the source of energy for fluid flow in bubble columns and their properties have a substantial impact on the flow pattern, mass and heat transfer. There are many factors that influence the bubbles behaviour, including gas velocity, pressure, gas-liquid phase properties, distributor structure and column diameter etc. Mendelson Harvey (1967) specified the shape of bubbles according to the bubble diameters while classifying the terminal velocities into 4 regions. The bubbles are in spherical shape when they are smaller than 1.4 mm. When bubbles become larger, they are no longer spherical and tend to follow a zigzag or helical rising

path. According to Mendelson Harvey (1967), the bubbles begin to assume a spherical cap shape when they are larger than 6 mm. However, it has been argued that this transition size to spherical-cap bubble is not accurate. Clift et al. (1978) present that the bubbles are shown to be spherical-capped when the diameter is approximately large than 20 mm, which makes better consistence with the experimental findings by Batchelor and Batchelor (2000). The terminal velocity map of air bubbles with different sizes has been presented in Figure 1-27, based on a large amount of experimental statistics.

Tomiyama (1998) proposed a semi-empirical model for bubble shapes variations, which has given 1.36 mm and 17.3 mm as the boundaries between spherical/ellipsoidal bubbles and ellipsoidal/spherical capped bubbles respectively in a slightly contaminated air-water system. It seems that a large proportion of the bubbles in the bubble column reactors are in ellipsoidal shapes. These medium-size ellipsoidal bubbles have very significant surface oscillations and also the most complex rising trajectories. Reichardt and Sommerfeld (2008) present the oscillation and rising characteristics of single ellipsoidal air-bubble in stagnant liquid by applying particle tracking velocimetry, as shown in Figure 1-28. In the following decades, the effect of the bubble oscillation motion on liquid turbulence has been intensively studied in the experiments and E-L numerical modelling (Sommerfeld and Broder, 2009, Sommerfeld et al., 2018, Taborda et al., 2021, Taborda and Sommerfeld, 2021). The importance of the inclusion of bubble oscillation and wobbling motion will be further addressed in this LES work.

Akita and Yoshida (1974) reported that bubble size decreases with increasing U_g. However, Fukuma et al. (1987) and Saxena et al. (1990) found that the bubble size increased as the increase in U_g and that the maximum stable bubble size did not change after a certain gas velocity was reached; Li and Raymond also reported similar results. The reason might be the experimental bubble column size is limited to square cross-sectional with 30 cm in length in Akita and Yoshida's work.

Lau et al. (2010) examined in detail the effect of liquid height and gas velocity on bubble size distribution, as shown in Figure 1-29. The average bubble size increases with increasing static liquid height (H/D=0.5, 2, 4, 6) and the distribution becomes wider with the growth of column height. A smaller bubble size in the bubble column is found at H/D=2 and was thought to be affected by the bubble outlet, where surface fluctuations intensify bubbles break-up and produce more small bubbles. Therefore, in order to take advantage of the fluctuating liquid surface, they suggested that the bubble inlet and outlet side effects should cover the entire domain. At a static level of H/D<2, the bubble size in the control zone of the distributor gradually decreases in the axial direction. In the range 2< H/D <6 the bubble size distribution basically remains unchanged.

The effect of column diameter on bubble size has not been intensively studied. Koide et al. (1979) showed that the average bubble size in larger columns was slightly larger. While Daly et al. (1992) reported that the average bubble size in large columns was relative smaller when U_g was greater than 4 cm/s, as the large diameter bubble column was in a highly turbulent state. Akita and Yoshida (1974)

developed the following equation for the mean bubble size from extensive experiments,

$$\frac{\mathrm{d_{mean}}}{D} = 26\left(\frac{D^2 g\rho_L}{\sigma}\right)^{-0.5}\left(\frac{D^3 g}{\nu_L^3}\right)^{-0.12}\left(\frac{U_r}{\sqrt{gD}}\right)^{-0.12} \quad (1\text{-}55)$$

As can be seen from the above equation, $\mathrm{d_{mean}} \sim D^{-0.3}$, the mean diameter decreases as the column diameter increases, but this equation is only applicable to small diameter bubble columns. When the column diameter is D>15cm, the bubble diameter is usually considered to be independent of the column diameter.

Pressure is an important determinant of bubble size, as the growth of pressure increases the gas density, thus the inertial force of the bubble affected. Therefore, the bubble is more easily broken resulting in smaller bubble size. It has also been suggested that the increase in pressure would increase the time for bubble coalescence (Schäfer et al., 2002), resulting in a hinder effect in the coalescence rate. In addition, pressure may also reduce surface tension, since experimental studies of the relationship between pressure and surface tension are not easy to carry out, generally speaking, an increase in pressure may increase the density of the gas phase and slightly improve the surface molecular force inhomogeneity. Furthermore, if there are other substances in the gas phase, an increase in pressure may promote an increase in surface adsorption and an increase in gas solubility, which also causes the surface tension to decrease and finally helps to reduce bubble size.

The physical property of the liquid phase also has significant impact on bubble size distribution. Reducing surface tension contributes the reduction in bubble size (Schäfer et al., 2002). The higher the viscosity of the liquid, the more stable the

bubbles and the more likely to form large bubbles. In three-phase systems, as the concentration of the solid phase increases, the bubble size becomes larger and the size distribution becomes wider, because the liquid dynamic viscosity becomes larger due to the presence of solid phase particles. Additionally, since the tiny particles are attached to the surface of the bubble, making it more stable and difficult to break. Unlike the two-phase system, the bubble size in the three-phase system is larger at low gas velocities than at high gas velocities (Lau et al., 2010), as shown in the Figure 1-30.

Temperature plays a role in reducing the viscosity and surface tension of the liquid phase. Therefore, if the operating pressure is sufficiently high compared to the saturation pressure and the evaporation of the liquid phase is negligible, an increase in temperature can reduce the bubble size. However, when the evaporation of the liquid phase cannot be neglected, the rise in temperature will increase the bubble size until saturation is reached (Schäfer et al., 2002). For aqueous systems, ionic or hydrocarbon impurities can inhibit the coalescence of bubbles, which can also reduce the bubble size.

Vandu et al. (2004a) studied the size and rise velocity of large bubbles in three-phase systems and reported that the size of large bubbles is almost independent of the gas superficial velocity and solid phase concentration ($U_g > 0.1\frac{m}{s}$, $\alpha_s > 0.05$). The terminal velocity correlation is proposed for large bubbles (Lb) based on the Davis-Taylor relationship,

$$d_{Lb} = 0.069(U - U_{trans})^{0.376} \tag{1-56}$$

$$V_{Lb} = 0.71\sqrt{gd_{Lb}}(SF)(AF) \quad (1\text{-}57)$$

The SF and AF are correction coefficients for the effect of the wall and the effect of the interaction between adjacent bubbles on the bubble velocity (Krishna et al., 1999b), respectively.

4.4 Flow pattern studies

The classification of bubble column flow patterns is usually closely related to the size and shape of the bubbles. The shape of the bubble can be spherical, ellipsoidal, spherical-cap or plummeting, and the corresponding flow patterns are homogeneous flow, transitional flow, heterogeneous flow and slug flow. In general, the above flow patterns occur in sequence with increasing gas superficial velocity. However, as bubble size and shape are heavily influenced by structural factors such as the distributor, not all of these flow patterns occur, e.g. slug flow only occurs in small diameter pipes or reactors (D<10cm), while large diameter orifice distributor only generate heterogeneous flow. Only reactors with perforated plate with small orifice (d0<3 mm) or sintered plates will have homogeneous, transition and heterogeneous flow patterns in order with the growth of gas superficial velocity. Homogeneous and heterogeneous flows are the two most important types of flow. The homogeneous flow pattern is characterised by a uniform distribution of gas hold-up, small bubble size, spherical, negligible bubble interactions and no large-scale circulation. In contrast, the heterogeneous flow pattern is characterised by a radial distribution

of gas hold-up, a wide distribution of bubble sizes, strong bubble interactions, continuous bubble breakage and coalescence, large-scale circulation and a significantly enhanced turbulence intensity.

There are various methods of flow pattern identification, such as gas hold-up to gas superficial velocity mapping, drift flux, bed collapse, and dynamic signal analysis. The first two are relatively simple and are based on the rate of change of gas hold-up with gas superficial velocity to differentiate flow patterns. The model equation for the drift flux method can be expressed as,

$$\frac{U_g}{\alpha_g} = C_0\left(U_g + U_l\right) + C1 \tag{1-58}$$

The bed collapse method uses the difference in the terminal velocities of large and small bubbles to identify the flow pattern by measuring the rate of change of gas hold-up over time after the injection of gas is stopped. When in a homogeneous flow, small bubbles predominate, and the gas hold-up decreases linearly from time to time after aeration is stopped.

With the advances in on-line inspection and signal analysis, dynamic signal analysis is developing rapidly. In addition to the qualitative identification of flow patterns, dynamic signal analysis can also be used to reflect the chaotic nature of heterogeneous flow patterns, their dynamic properties and their intercellular distribution, using quantitative indicators such as energy spectrum and Kolmogorov entropy.

As shown in Figure 1-31, the turbulence in the bubble columns are different from the single-phase turbulence in pipe flows. With presence of gas and liquid two

phases in the bubble column, the two-way interactions are inevitable between the liquid phase flow and the gas bubbles with different sizes and shapes. Although the shear turbulence caused by the velocity differential of the liquid phase flow is a major contributor, interactions between gas bubbles and the carrier fluid are also likely to play an important role. Of another perspective, bubbles are the energy source of the bubble columns. After the injection of the bubbles, the eddies induced by the rising bubbles become a source of turbulence. Thus, the flow in the bubble column is consisted of the presence of both wall shear induced turbulence and bubble-induced turbulence. The turbulent eddies, in contrast to individual bubbles, are more difficult to characterize structurally and behaviourally, making it more difficult to discern how gas bubbles affect liquid-phase turbulence. When studying how bubble columns behave in turbulent environments, it is possible to utilize an analytical technique called the turbulence energy spectrum to gather statistical data.

According to the frequency or wave number of turbulence eddies, the turbulence energy spectrum can be roughly classified into energy containing and universal equilibrium ranges, which include inertial subrange and dissipation ranges, respectively. The kinetic energy of turbulence cascades sequentially from large eddies to smaller eddies. For homogeneous and isotropic turbulence in single-phase flow, the Kolmogorov -5/3 law, which can be expressed as $(\kappa) \sim \varepsilon 2/3 \kappa -5/3$, has already been widely recognized (Pope, 2001). Pseudo-turbulence caused by rising bubbles is different from single-phase turbulence, as some pioneering work has shown. Axisymmetric irrotational flow caused by a rising sphere was first described analytically

by Batchelor (1967), who concluded that the stream function behind the sphere decays with distance raised by a scaling of -3. Lance and Bataille (1991) used hot-wire and LDA to analyze the energy spectrum of bubbles as they rose through an imposed turbulence flow. The slope of the energy spectrum was gradually changed from -5/3 to -8/3 as growth of gas hold-up. Bubble wakes, where eddies were dissipated quickly before the spectral transfer, were attributed for the shift in slope. Using Karman-Howarth equation, they calculated that the exponent of power law scaling was roughly -3, which is close to -8/3, which they found empirically. The -5/3 behavior, on the other hand, has only been observed in a few experimental investigations (Mudde et al., 1997, Cui and Fan, 2004), According to these findings, the energy spectrum has the same slope as that of homogeneous and isotropic turbulence in single-phase flow. While the slope reported by Rensen et al. (2005), was slightly less steep than -5/3. Because of the presence of microbubbles, they linked this to an increase in energy at microscopic scales.

The -3 scaling for bubble-induced turbulence has been validated by Mercado et al. (2010), who employed a phase-sensitive CTA to extract bubble velocity signals from the liquid flow field.

Based on the critical gas hold-up or gas velocity, Ruzicka et al. (2001) systematically investigated the effect of column diameter and liquid static height on the flow pattern transition. It was found that increasing the column diameter and height would break the homogeneous flow pattern and lead to an early transition to heterogeneous flow. In addition, it was pointed out that the height-to-diameter ratio

could not be used as an independent parameter to replace the influence of column diameter and liquid static height.

The effect of the distributor on the flow pattern was investigated in detail by Vial et al. (2001) by analysing the radial distribution of the local gas hold-up. It was found that the single-hole nozzles only produced a heterogeneous flow pattern. The flow pattern produced by the microplates is related to the wetness of micro-orifice; if operated after wetting, the gas superficial velocity is less than 4 cm/s for a homogeneous flow pattern; 4-8 cm/s for a transition flow region; and greater than 8 cm/s for a heterogeneous flow pattern.

Thorat and Joshi (2004) investigated the effect of opening rate, orifice size and liquid height on the flow pattern of a perforated plate. The critical gas hold-up of the flow transition was found to increase with decreasing opening rate and orifice diameter and decrease with increasing liquid level.

Pressure has an important effect on bubble properties, increasing pressure reduces bubble size and therefore also affects the flow pattern. The rise of pressure increases the critical gas velocity for the flow pattern transition (Shaikh and Al-Dahhan, 2005).

The scale-up is a central concern in the study and design of bubble column reactors. As mentioned above, there has been a lot of work on bubble column scale-up, but most have been on average and time-averaged performance parameters. Clearly, this is a long way from understanding the scale-up of the dynamic flow field in bubble columns. Yano et al. (1999) have done pioneering work on the scale-up of

the dynamic properties of bubble columns; using deterministic chaos theory to analyse the instantaneous time series signals of bubbles and particles (D=0.2/0.4/0.8), they found that the correlation dimension of the gas hold-up fluctuation signal decreases with increasing column diameter and accordingly the radial distribution becomes uniform. The authors suggested that this is related to a significant change in the overall flow pattern as the diameter increases as illustrated in Figure 1-33; they also hypothesised that in 800 mm bubble columns there is a large scale individual circulation comparable to the column diameter, while in smaller columns of 200 or 400 mm the bubbles rise in "S-shape" along the centre of the bubble column, and there are a large number of small eddies in the near-wall region. However, Chen et al. (2001) found that its correlation dimension is independent to the column diameter, yet the Kolmogorov entropy decreases significantly with increasing column diameter, as shown in Figure 1-34, and the gas hold-up distribution becomes more uniform. Chen and Yano have come to the opposite conclusion regarding the column diameter effect in the correlation dimension (Figure 1-35), which may be related to the different signals they have analysed, but both agree that the flow structure has changed significantly with increasing column diameter.

5. RECAPTULATION AND CONCLUDING REMARKS ON MODELLING OF MULTIPHASE FLOWS IN BUBBLE COLUMNS

This chapter has overviewed the current status of the numerical and experimental work in gas-liquid two-phase and gas-liquid-solid three-phase flow in bubble column reactor. Various experimental techniques for measuring gas holdup, bubble behaviours and liquid phase flow fields is discussed. The research focus has been shifting from macro to micro, domain average to local characteristics. The deeper insights on the flow structure and individual bubble motion reveal the importance of the interphase interactions with the development of high-speed and high-resolution measurement devices and techniques. As Eulerian-Eulerian two-fluid modelling describes two-phase mixture motion in a macro sense, the use of this approach may be preferable for industrial applications, especially for the case of a highly dispersed void fraction system such as bubble column reactors. The use of Eulerian-Eulerian two-fluid LES modelling is more desirable because the adoption of low order turbulence models, such as the k-ε and even for the Reynolds Stress Model (RSM), may not well capture the instantaneous eddy turbulence structures which will affect the bubble entrainment, breakage and coalescence. The most critical conclusion that can be derived from the experimental and numerical research discussed in this chapter is that current understanding of gas-liquid interactions in bubble column reactors remains restricted. Specifically, the wake structure in liquid turbulence under the impact of rising bubbles have not been fully exposed experimentally, and the effects of relative motion between moving bubbles and its surrounding eddies have not been adequately explored in CFD modelling. Additionally, interphase forces closure that mostly used in the available LES work are still

based on time-average procedure, the consequence of the use of SGS spatial filtering process is not reflected in modelling, which would give rise to an inadequate prediction of the sub-grid scale motion.

In the following chapters, the studies focusing on the effect of bubble dynamic motion on the mass and momentum transfer in multiphase flows in bubble column reactor are carried out. The modified Smagorinsky SGS eddy viscosity model with the consideration of bubble-eddy interaction in sub-grid scale will be validated in Chapter 2. In Chapter 3, the novel spatial filtering process exerted on turbulent dispersion force and the consideration of bubble deformation in the proposed sub-grid scale turbulent dispersion force (SGS-TDF) will be evaluated. Furthermore, the consequence of SGS spatial filtering on added mass force leads to an additional sub-grid scale 'added mass stress' (SGS-AMS) term. This term, which can describe the contribution from the bubble oscillations due to the liquid turbulence fluctuations, will be investigated in Chapter 4. The impact of the proposed SGS-TDF and SGS-AMS models on mass transfer in bubble column reacting flow will be studied in Chapter 5. Chapter 6 will show the influence of the modified eddy viscosity model with the inclusion of bubble-eddy and particle-eddy interactions in bubble column three-phase flow. At last, the concluding remarks based on this PhD project will be summarized in Chapter 7 and some recommendations to the future work will be provided.

REFERENCES

ABRAHAM, M. 1989. Effect of sparger design on the hydrodynamics and mass transfer characteristics of a bubble column. *Ind. Chem. Eng.,* 31**,** 31-36.

AKITA, K. & YOSHIDA, F. 1974. Bubble size, interfacial area, and liquid-phase mass transfer coefficient in bubble columns. *Industrial & Engineering Chemistry Process Design and Development,* 13**,** 84-91.

AMSDEN, A. & HARLOW, F. A Simplified MAC Technique for Incompressible Fluid Calculation. *J. Comp. Phys*, 64.

ANTAL, S., LAHEY JR, R. & FLAHERTY, J. 1991. Analysis of phase distribution in fully developed laminar bubbly two-phase flow. *International journal of multiphase flow,* 17**,** 635-652.

AUTON, T., HUNT, J. & PRUD'HOMME, M. 1988. The force exerted on a body in inviscid unsteady non-uniform rotational flow. *Journal of Fluid Mechanics,* 197**,** 241-257.

AZZOPARDI, B., MUDDE, R., LO, S., MORVAN, H., YAN, Y. & ZHAO, D. 2011. Bubble Columns, Hydrodynamics of Gas-Liquid Reactors. *John Wiley Sons Ltd***,** 3-59.

BATCHELOR, C. K. & BATCHELOR, G. 2000. *An introduction to fluid dynamics*, Cambridge university press.

BESAGNI, G., & INZOLI, F. (2016). Bubble size distributions and shapes in annular gap bubble column. *Experimental Thermal and Fluid Science*, 74, 27-48.

BESAGNI, G., GALLAZZINI, L. & INZOLI, F. 2018. Effect of gas sparger design on bubble column hydrodynamics using pure and binary liquid phases. *Chemical Engineering Science,* 176**,** 116-126.

BESAGNI, G. & INZOLI, F. Influence of electrolyte concentration on holdup, flow regime transition and local flow properties in a large scale bubble column. Journal of Physics: Conference Series, 2015. IOP Publishing, 012039.

BESAGNI, G. & INZOLI, F. 2016. Comprehensive experimental investigation of counter-current bubble column hydrodynamics: Holdup, flow regime transition, bubble size distributions and local flow properties. *Chemical Engineering Science,* 146**,** 259-290.

BESAGNI, G. & INZOLI, F. 2017a. The effect of electrolyte concentration on counter-current gas–liquid bubble column fluid dynamics: Gas holdup, flow regime transition and bubble size distributions. *Chemical Engineering Research and Design,* 118**,** 170-193.

BESAGNI, G. & INZOLI, F. 2017b. The effect of liquid phase properties on bubble column fluid dynamics: Gas holdup, flow regime transition, bubble size distributions and shapes, interfacial areas and foaming phenomena. *Chemical Engineering Science,* 170**,** 270-296.

BHOLE, M., JOSHI, J. & RAMKRISHNA, D. 2008. CFD simulation of bubble columns incorporating population balance modeling. *Chemical Engineering Science,* 63**,** 2267-2282.

BIRD, R. B., STEWART, W. E. & LIGHTFOOT, E. N. 2006. *Transport phenomena*, John Wiley & Sons.

BOUFFANAIS, R. 2010. Advances and challenges of applied large-eddy simulation. *Computers & Fluids,* 39**,** 735-738.

BRAUER, H. 1981. Particle/fluid transport processes. *Prog. Chem. Eng.,* 19**,** 61-99.

BURNS, A. D., FRANK, T., HAMILL, I. & SHI, J.-M. The Favre averaged drag model for turbulent dispersion in Eulerian multi-phase flows. 5th International Conference on Multiphase Flow, ICMF, 2004. ICMF, 1-17.

BUWA, V. V., DEO, D. S. & RANADE, V. V. 2006. Eulerian–Lagrangian simulations of unsteady gas–liquid flows in bubble columns. *International Journal of Multiphase Flow,* 32**,** 864-885.

BUWA, V. V. & RANADE, V. V. 2002. Dynamics of gas–liquid flow in a rectangular bubble column: experiments and single/multi-group CFD simulations. *Chemical Engineering Science,* 57**,** 4715-4736.

CAMARASA, E., VIAL, C., PONCIN, S., WILD, G., MIDOUX, N. & BOUILLARD, J. 1999. Influence of coalescence behaviour of the liquid and of gas sparging on hydrodynamics and bubble characteristics in a bubble column. *Chemical Engineering and Processing: Process Intensification,* 38**,** 329-344.

CHEN, J., GUPTA, P., DEGALEESAN, S., AL-DAHHAN, M. H., DUDUKOVIĆ, M. P. & TOSELAND, B. A. 1998. Gas holdup distributions in large-diameter bubble columns measured by computed tomography. *Flow Measurement and instrumentation,* 9**,** 91-101.

CHEN, P.-C., SHI, W., DU, R. & CHEN, V. 2008. Scrubbing of CO2 greenhouse gases, accompanied by precipitation in a continuous bubble-column scrubber. *Industrial & Engineering Chemistry Research,* 47**,** 6336-6343.

CHEN, P., DUDUKOVIĆ, M. & SANYAL, J. 2005a. Three-dimensional simulation of bubble column flows with bubble coalescence and breakup. *AIChE Journal,* 51**,** 696-712.

CHEN, P., SANYAL, J. & DUDUKOVIĆ, M. 2005b. Numerical simulation of bubble columns flows: effect of different breakup and coalescence closures. *Chemical Engineering Science,* 60**,** 1085-1101.

CHEN, R., REESE, J. & FAN, L. S. 1994. Flow structure in a three-dimensional bubble column and three-phase fluidized bed. *AIChE Journal,* 40**,** 1093-1104.

CHEN, W., HASEGAWA, T., TSUTSUMI, A. & OTAWARA, K. 2001. Scale-up effects on the time-averaged and dynamic behavior in bubble column reactors. *Chemical Engineering Science,* 56**,** 6149-6155.

CHESTERS, A. K. 1991. Modelling of coalescence processes in fluid-liquid dispersions: a review of current understanding. *Chemical Engineering Research and Design,* 69**,** 259-270.

CLIFT, R. 1978. Bubbles. *Drops and Particles,* 117.

CLIFT, R., GRACE, J. R. & WEBER, M. E. 2005. *Bubbles, drops, and particles*.

COOK, T. L. & HARLOW, F. H. 1986. Vortices in bubbly two-phase flow. *International Journal of Multiphase Flow,* 12**,** 35-61.

CUI, Z. & FAN, L. 2004. Turbulence energy distributions in bubbling gas–liquid and gas–liquid–solid flow systems. *Chemical Engineering Science,* 59**,** 1755-1766.

DALY, J., PATEL, S. & BUKUR, D. 1992. Measurement of gas holdups and sauter mean bubble diameters in bubble column reactors by dynamics gas disengagement method. *Chemical Engineering Science,* 47**,** 3647-3654.

DANCKWERTS, P. 1951. Significance of liquid-film coefficients in gas absorption. *Industrial & Engineering Chemistry,* 43**,** 1460-1467.

DARMANA, D., DEEN, N. & KUIPERS, J. 2005. Detailed modeling of hydrodynamics, mass transfer and chemical reactions in a bubble column using a discrete bubble model. *Chemical engineering science,* 60**,** 3383-3404.

DARMANA, D., HENKET, R., DEEN, N. & KUIPERS, J. 2007. Detailed modelling of hydrodynamics, mass transfer and chemical reactions in a bubble column using a discrete bubble model: Chemisorption of CO2 into NaOH solution, numerical and experimental study. *Chemical engineering science,* 62**,** 2556-2575.

DE BERTODANO, M. A. L. 1992. *Turbulent bubbly two-phase flow in a triangular duct.* Rensselaer Polytechnic Institute.

DEEN, N. G., SOLBERG, T., & HJERTAGER, B. H. 2001. Large eddy simulation of the gas–liquid flow in a square cross-sectioned bubble column. *Chemical Engineering Science*, **56**(21-22), 6341-6349.

DEEN, N. G., VAN SINT ANNALAND, M. & KUIPERS, J. 2004. Multi-scale modeling of dispersed gas–liquid two-phase flow. *Chemical Engineering Science,* 59**,** 1853-1861.

DEGALEESAN, S., DUDUKOVIC, M. & PAN, Y. 2001. Experimental study of gas-induced liquid-flow structures in bubble columns. *AIChE Journal,* 47**,** 1913-1931.

DEGALEESAN, S., ROY, S., KUMAR, S. & DUDUKOVIĆ, M. 1996. Liquid mixing based on convection and turbulent dispersion in bubble columns. *Chemical Engineering Science,* 51**,** 1967-1976.

DELNOIJ, E., KUIPERS, J., VAN SWAAIJ, W. P. M. & WESTERWEEL, J. 2000. Measurement of gas–liquid two-phase flow in bubble columns using ensemble correlation PIV. *Chemical Engineering Science,* 55**,** 3385-3395.

DELNOIJ, E., WESTERWEEL, J., DEEN, N. G., KUIPERS, J. & VAN SWAAIJ, W. P. M. 1999. Ensemble correlation PIV applied to bubble plumes rising in a bubble column. *Chemical Engineering Science,* 54**,** 5159-5171.

DESVIGNE, D., DONNAT, L. & SCHWEICH, D. 2006. Simulating the effects of liquid circulation in bubble columns with internals. *Chemical Engineering Science,* 61**,** 4195-4206.

DEVANATHAN, N., MOSLEMIAN, D. & DUDUKOVIC, M. 1990. Flow mapping in bubble columns using CARPT. *Chemical Engineering Science,* 45**,** 2285-2291.

DHOTRE, M., EKAMBARA, K. & JOSHI, J. 2004. CFD simulation of sparger design and height to diameter ratio on gas hold-up profiles in bubble column reactors. *Experimental Thermal and Fluid Science,* 28**,** 407-421.

DHOTRE, M., NICENO, B. & SMITH, B. 2008. Large eddy simulation of a bubble column using dynamic sub-grid scale model. *Chemical Engineering Journal,* 136**,** 337-348.

DHOTRE, M., SMITH, B. & NICENO, B. 2007. CFD simulation of bubbly flows: Random dispersion model. *Chemical Engineering Science,* 62**,** 7140-7150.

DHOTRE, M. T., VITANKAR, V. S. & JOSHI, J. B. 2005. CFD simulation of steady state heat transfer in bubble columns. *Chemical Engineering Journal,* 108**,** 117-125.

DREW, D. & LAHEY JR, R. 1987. The virtual mass and lift force on a sphere in rotating and straining inviscid flow. *International Journal of Multiphase Flow,* 13**,** 113-121.

DSOUZA, G. C. 2020. *CFD Simulations of Bubble Column Equipped with Bundles of Concentric Tubes.* Master of Engineering Science, The University of Western Ontario.

EKAMBARA, K., DHOTRE, M. T. & JOSHI, J. B. 2005. CFD simulations of bubble column reactors: 1D, 2D and 3D approach. *Chemical Engineering Science,* 60**,** 6733-6746.

ERVIN, E. A. & TRYGGVASON, G. 1997. The Rise of Bubbles in a Vertical Shear Flow. *Journal of Fluids Engineering,* 119**,** 443-449.

FORRET, A., SCHWEITZER, J., GAUTHIER, T., KRISHNA, R. & SCHWEICH, D. 2003. Influence of scale on the hydrodynamics of bubble column reactors: an experimental study in columns of 0.1, 0.4 and 1m diameters. *Chemical Engineering Science,* 58**,** 719-724.

FU, X. & ISHII, M. 2003a. Two-group interfacial area transport in vertical air–water flow-II. Model evaluation. *Nuclear Engineering and Design,* 219**,** 169-190.

FU, X. & ISHII, M. 2003b. Two-group interfacial area transport in vertical air–water flow: I. Mechanistic model. *Nuclear Engineering and Design,* 219**,** 143-168.

FUKUMA, M., MUROYAMA, K. & YASUNISHI, A. 1987. Properties of bubble swarm in a slurry bubble column. *Journal of Chemical Engineering of Japan,* 20**,** 28-33.

GERMANO, M., PIOMELLI, U., MOIN, P. & CABOT, W. H. 1991. A dynamic subgrid-scale eddy viscosity model. *Physics of Fluids A: Fluid Dynamics,* 3**,** 1760-1765.

GRACE, J. 1976. Shapes and velocities of single drops and bubbles moving freely through immiscible liquids. *Transactions of the Institution of Chemical Engineers,* 54**,** 167-174.

GROEN, J. 2004. *Scales and structures in bubbly flows.*

GUPTA, A. & ROY, S. 2013. Euler–Euler simulation of bubbly flow in a rectangular bubble column: Experimental validation with Radioactive Particle Tracking. *Chemical Engineering Journal,* 225**,** 818-836.

HAN, L. & AL-DAHHAN, M. H. 2007. Gas–liquid mass transfer in a high pressure bubble column reactor with different sparger designs. *Chemical Engineering Science,* 62**,** 131-139.

HAQUE, M., NIGAM, K. & JOSHI, J. 1986. Optimum gas sparger design for bubble columns with a low height-to-diameter ratio. *Chemical Engineering Journal,* 33**,** 63-69.

HARLOW, F. H. 1988. PIC and its progeny. *Computer Physics Communications,* 48**,** 1-10.

HARLOW, F. H. & WELCH, J. E. 1965. Numerical calculation of time-dependent viscous incompressible flow of fluid with free surface. *The Physics of Fluids,* 8**,** 2182-2189.

HIGBIE, R. 1935. The rate of absorption of a pure gas into a still liquid during short periods of exposure. *Trans. AIChE,* 31**,** 365-389.

HILLS, J. H. 1974. Radial Non-Uniformity of Velocity and Voidage in a Bubble Column. *Transactions of the Institution of Chemical Engineers*.

HIRT, C. & NICHOLS, B. 1981a. A computational method for free surface hydrodynamics. *ASME. J. Pressure Vessel Technol.*

HIRT, C. W. & NICHOLS, B. D. 1981b. Volume of fluid (VOF) method for the dynamics of free boundaries. *Journal of Computational Physics,* 39**,** 201-225.

HLAWITSCHKA, M., KOVÁTS, P., ZÄHRINGER, K. & BART, H.-J. 2017. Simulation and experimental validation of reactive bubble column reactors. *Chemical Engineering Science,* 170**,** 306-319.

HOMSY, G., EL-KAISSY, M. & DIDWINIA, A. 1980. Instability waves and the origin of bubbles in fluidized beds—II Comparison with theory. *International Journal of Multiphase Flow,* 6**,** 305-318.

HUBERS, J. L., STRIEGEL, A. C., HEINDEL, T. J., GRAY, J. N. & JENSEN, T. C. 2005. X-ray computed tomography in large bubble columns. *Chemical Engineering Science,* 60**,** 6124-6133.

ISHII, M., PARANJAPE, S., KIM, S. & SUN, X. 2004. Interfacial structures and interfacial area transport in downward two-phase bubbly flow. *International Journal of Multiphase Flow,* 30**,** 779-801.

ISHII, M. & ZUBER, N. 1979. Drag coefficient and relative velocity in bubbly, droplet or particulate flows. *AIChE Journal,* 25**,** 843-855.

JAIN, D., KUIPERS, J. & DEEN, N. G. 2015. Numerical modeling of carbon dioxide chemisorption in sodium hydroxide solution in a micro-structured bubble column. *Chemical Engineering Science,* 137**,** 685-696.

JOSHI, J. 2001. Computational flow modelling and design of bubble column reactors. *Chemical Engineering Science,* 56**,** 5893-5933.

JOSHI, J., PARASU, U., PRASAD, C., PHANIKUMAR, D., DESHPANDE, N. & THORAT, B. 1998. Gas hold-up structures in bubble column reactors. *Proceedings of the Indian National Science Academy,* 64**,** 441-567.

KANTARCI, N., BORAK, F. & ULGEN, K. O. 2005. Bubble column reactors. *Process Biochemistry,* 40**,** 2263-2283.

KEMOUN, A., ONG, B. C., GUPTA, P., AL-DAHHAN, M. H. & DUDUKOVIC, M. P. 2001. Gas holdup in bubble columns at elevated pressure via

computed tomography. *International Journal of Multiphase Flow,* 27**,** 929-946.

KENDOUSH, A. A., GAINES, K. W. & WHITE, C. W. 2016. Theory and Indirect Measurements of the Drag Force Acting On a Rising Ellipsoidal Bubble. *Journal of Fluid Flow, Heat and Mass Transfer* 3**,** 92-98.

KHAN, I., WANG, M., ZHANG, Y., TIAN, W., SU, G., & QIU, S. 2020. Two-phase bubbly flow simulation using CFD method: A review of models for interfacial forces. Progress in Nuclear Energy, 125, 103360.

KOIDE, K., MOROOKA, S., UEYAMA, K., MATSUURA, A., YAMASHITA, F., IWAMOTO, S., KATO, Y., INOUE, H., SHIGETA, M. & SUZUKI, S. 1979. Behavior of bubbles in large scale bubble column. *Journal of Chemical Engineering of Japan,* 12**,** 98-104.

KOLMOGOROV, A. N. 1991. The local structure of turbulence in incompressible viscous fluid for very large Reynolds numbers. *Proceedings of the Royal Society of London. Series A: Mathematical and Physical Sciences,* 434**,** 9-13.

KRISHNA, R. & ELLENBERGER, J. 1996. Gas holdup in bubble column reactors operating in the churn-turbulent flow regime. *AIChE Journal,* 42**,** 2627-2634.

KRISHNA, R., URSEANU, M., VAN BATEN, J. & ELLENBERGER, J. 1999a. Influence of scale on the hydrodynamics of bubble columns operating in the churn-turbulent regime: experiments vs. Eulerian simulations. *Chemical Engineering Science,* 54**,** 4903-4911.

KRISHNA, R., URSEANU, M., VAN BATEN, J. & ELLENBERGER, J. 1999b. Rise velocity of a swarm of large gas bubbles in liquids. *Chemical Engineering Science,* 54**,** 171-183.

KRISHNA, R., URSEANU, M., VAN BATEN, J. & ELLENBERGER, J. 2000a. Liquid phase dispersion in bubble columns operating in the churn-turbulent flow regime. *Chemical Engineering Journal,* 78**,** 43-51.

KRISHNA, R., VAN BATEN, J., ELLENBERGER, J., HIGLER, A. & TAYLOR, R. 1999c. CFD simulations of sieve tray hydrodynamics. *Chemical Engineering Research and Design,* 77**,** 639-646.

KRISHNA, R., VAN BATEN, J. & URSEANU, M. 2000b. Three-phase Eulerian simulations of bubble column reactors operating in the churn-turbulent regime: a scale up strategy. *Chemical Engineering Science,* 55**,** 3275-3286.

KRISHNA, R., VAN BATEN, J., URSEANU, M. & ELLENBERGER, J. 2001. A scale up strategy for bubble column slurry reactors. *Catalysis Today,* 66**,** 199-207.

KRISHNA, R., WILKINSON, P. & VAN DIERENDONCK, L. 1991. A model for gas holdup in bubble columns incorporating the influence of gas density on flow regime transitions. *Chemical Engineering Science,* 46**,** 2491-2496.

KULKARNI, A. A., JOSHI, J. B., KUMAR, V. R. & KULKARNI, B. D. 2001. Application of multiresolution analysis for simultaneous measurement of gas and liquid velocities and fractional gas hold-up in bubble column using LDA. *Chemical Engineering Science,* 56**,** 5037-5048.

KUMAR, S. B., MOSLEMIAN, D. & DUDUKOVIĆ, M. P. 1997. Gas-holdup measurements in bubble columns using computed tomography. *AIChE Journal,* 43**,** 1414-1425.

LAHEY JR, R. 1990. The analysis of phase separation and phase distribution phenomena using two-fluid models. *Nuclear Engineering and Design,* 122**,** 17-40.

LAIN, S. & SOMMERFELD, M. 2003. Turbulence modulation in dispersed two-phase flow laden with solids from a Lagrangian perspective. *International Journal of Heat and Fluid Flow,* 24**,** 616-625.

LANCE, M. & BATAILLE, J. 1991. Turbulence in the liquid phase of a uniform bubbly air–water flow. *Journal of fluid mechanics,* 222**,** 95-118.

LAU, R., MO, R. & SIM, W. S. B. 2010. Bubble characteristics in shallow bubble column reactors. *Chemical Engineering Research and Design,* 88**,** 197-203.

LEE, D., MCLAIN, B., CUI, Z. & FAN, L.-S. 2001. Pressure effect on the flow fields and the Reynolds stresses in a bubble column. *Industrial & Engineering Chemistry Research,* 40**,** 1442-1447.

LEHR, F. & MEWES, D. 2001. A transport equation for the interfacial area density applied to bubble columns. *Chemical Engineering Science,* 56**,** 1159-1166.

LEHR, F., MILLIES, M. & MEWES, D. 2002. Bubble-size distributions and flow fields in bubble columns. *AIChE Journal,* 48**,** 2426-2443.

LEONARD, A. 1975. Energy cascade in large-eddy simulations of turbulent fluid flows. *Advances in Geophysics.* Elsevier.

LETZEL, H., SCHOUTEN, J., KRISHNA, R. & VAN DEN BLEEK, C. 1999. Gas holdup and mass transfer in bubble column reactors operated at elevated pressure. *Chemical Engineering Science,* 54**,** 2237-2246.

LEWIS, W. K. & WHITMAN, W. G. 1924. Principles of gas absorption. *Industrial & Engineering Chemistry,* 16**,** 1215-1220.

LI, W.-L., ZHONG, W.-Q., JIN, B.-S., XIAO, R. & HE, T.-T. 2013. Flow regime identification in a three-phase bubble column based on statistical, Hurst, Hilbert–Huang transform and Shannon entropy analysis. *Chemical Engineering Science,* 102**,** 474-485.

LIER, S., RIESE, J., CVETANOSKA, G., LESNIAK, A. K., MÜLLER, S., PAUL, S., SENGEN, L. & GRÜNEWALD, M. 2018. Innovative scaling strategies for a fast development of apparatuses by modular process engineering. *Chemical Engineering and Processing-Process Intensification,* 123**,** 111-125.

LILLY, D. K. 1992. A proposed modification of the Germano subgrid-scale closure method. *Physics of Fluids A: Fluid Dynamics,* 4**,** 633-635.

LIU, Z., WU, Y., & LI, B. 2020. An assessment on the performance of sub-grid scale models of large eddy simulation in modeling bubbly flows. *Powder Technology*, 374, 470-481.

LORENZ, O., SCHUMPE, A., EKAMBARA, K. & JOSHI, J. 2005. Liquid phase axial mixing in bubble columns operated at high pressures. *Chemical Engineering Science,* 60**,** 3573-3586.

LUCAS, D. & ZIEGENHEIN, T. 2019. Influence of the bubble size distribution on the bubble column flow regime. *International Journal of Multiphase Flow,* 120**,** 103092.

LUCAS, M. S., PERES, J. A. & PUMA, G. L. 2010. Treatment of winery wastewater by ozone-based advanced oxidation processes (O3, O3/UV and O3/UV/H2O2) in a pilot-scale bubble column reactor and process economics. *Separation and Purification Technology,* 72**,** 235-241.

LUO, H. 1993. *Coalescence, breakup and liquid circulation in bubble column reactors.* University of Trondheim.

LUO, X., LEE, D., LAU, R., YANG, G. & FAN, L. S. 1999. Maximum stable bubble size and gas holdup in high-pressure slurry bubble columns. *AIChE Journal,* 45**,** 665-680.

MANJREKAR, O. N., SUN, Y. J., HE, L., TANG, Y. J. & DUDUKOVIC, M. P. 2017. Hydrodynamics and mass transfer coefficients in a bubble column photo-bioreactor. *Chemical Engineering Science,* 168, 55-66.

MANJREKAR, O. N. & DUDUKOVIC, M. P. 2019. Identification of flow regime in a bubble column reactor with a combination of optical probe data and machine learning technique. *Chemical Engineering Science: X,* 2**,** 100023.

MCCLURE, D. D., ABOUDHA, N., KAVANAGH, J. M., FLETCHER, D. F. & BARTON, G. W. 2015. Mixing in bubble column reactors: experimental study and CFD modeling. *Chemical Engineering Journal,* 264**,** 291-301.

MEDJIADE, W. T., ALVARO, A. R. & SCHUMPE, A. 2017. Flow regime transitions in a bubble column. *Chemical Engineering Science,* 170**,** 263-269.

MENDELSON, H. D. 1967. The prediction of bubble terminal velocities from wave theory. *AIChE Journal,* 13**,** 250-253.

MERCADO, J. M., GOMEZ, D. C., VAN GILS, D., SUN, C. & LOHSE, D. 2010. On bubble clustering and energy spectra in pseudo-turbulence. *Journal of Fluid Mechanics,* 650**,** 287-306.

MÉTRAILLER, D., REBOUX, S. & LAKEHAL, D. 2017. Near-wall turbulence-bubbles interactions in a channel flow at Reτ= 400: A DNS investigation. *Nuclear Engineering and Design,* 321**,** 180-189.

MILELLI, M. 2002. *A numerical analysis of confined turbulent bubble plumes.* ETH Zurich.

MILELLI, M., SMITH, B. & LAKEHAL, D. 2001. Large-eddy simulation of turbulent shear flows laden with bubbles. *Direct and Large-Eddy Simulation IV.* Springer.

MIYAUCHI, T. 1970. Flow of fluid in gas-bubble columns. *Chemical Engineering,* 34**,** 958-964.

MOIN, P. & KIM, J. 1982. Numerical investigation of turbulent channel flow. *Journal of Fluid Mechanics,* 118**,** 341-377.

MOORE, D. 1963. The boundary layer on a spherical gas bubble. *Journal of Fluid Mechanics,* 16**,** 161-176.

MORSI, S. & ALEXANDER, A. 1972. An investigation of particle trajectories in two-phase flow systems. *Journal of Fluid mechanics,* 55**,** 193-208.

MUDDE, R., GROEN, J. & VAN DEN AKKER, H. 1997. Liquid velocity field in a bubble column: LDA experiments. *Chemical Engineering Science,* 52**,** 4217-4224.

MUDDE, R. F. 2005. Gravity-driven bubbly flows. *Annual Reviews of Fluid Mechanics,* 37**,** 393-423.

MUDDE, R. F. & SIMONIN, O. 1999. Two-and three-dimensional simulations of a bubble plume using a two-fluid model. *Chemical Engineering Science,* 54**,** 5061-5069.

MUNIZ, M. & SOMMERFELD, M. 2020. On the force competition in bubble columns: A numerical study. *International Journal of Multiphase Flow,* 128**,** 103256.

NOTTENKÄMPER, R., STEIFF, A. & WEINSPACH, P. 1983. Experimental investigation of hydrodynamics of bubble columns. *Ger. Chem. Eng.(Engl. Transl.),* 6.

OEY, R., MUDDE, R. & VAN DEN AKKER, H. 2003. Sensitivity study on interfacial closure laws in two-fluid bubbly flow simulations. *AIChE Journal,* 49**,** 1621-1636.

OLMOS, E., GENTRIC, C. & MIDOUX, N. 2003. Numerical description of flow regime transitions in bubble column reactors by a multiple gas phase model. *Chemical Engineering Science,* 58**,** 2113-2121.

OLMOS, E., GENTRIC, C., VIAL, C., WILD, G. & MIDOUX, N. 2001. Numerical simulation of multiphase flow in bubble column reactors. Influence of bubble coalescence and break-up. *Chemical Engineering Science,* 56**,** 6359-6365.

ONG, B. 2003. *Experimental investigation of bubble column hydrodynamics: effect of elevated pressure and superficial gas velocity*, Washington University in St. Louis.

ORVALHO, S., HASHIDA, M., ZEDNIKOVA, M., STANOVSKY, P., RUZICKA, M. C., SASAKI, S. & TOMIYAMA, A. 2018. Flow regimes in slurry bubble column: Effect of column height and particle concentration. *Chemical Engineering Journal,* 351**,** 799-815.

OSHER, S., FEDKIW, R. & PIECHOR, K. 2004. Level set methods and dynamic implicit surfaces. *Applied Mechanics Reviews,* 57**,** B15-B15.

PATEL, A. K. & THORAT, B. N. 2008. Gamma ray tomography—An experimental analysis of fractional gas hold-up in bubble columns. *Chemical Engineering Journal,* 137**,** 376-385.

POPE, S. B. 2001. Turbulent flows. IOP Publishing.

PRINCE, M. J. & BLANCH, H. W. 1990. Bubble coalescence and break-up in air-sparged bubble columns. *AIChE Journal,* 36**,** 1485-1499.

QIAN, D., MCLAUGHLIN, J., SANKARANARAYANAN, K., SUNDARESAN, S. & KONTOMARIS, K. 2006. Simulation of bubble breakup dynamics in homogeneous turbulence. *Chemical Engineering Communications,* 193**,** 1038-1063.

RAFIQUE, M., CHEN, P. & DUDUKOVIĆ, M. 2004. Computational modeling of gas-liquid flow in bubble columns. *Reviews in Chemical Engineering,* 20**,** 225-375.

RAVINATH, M., KASAT, G. R. & PANDIT, A. B. 2003. Mixing time in a short bubble column. *The Canadian Journal of Chemical Engineering,* 81**,** 185-195.

RENSEN, J., LUTHER, S. & LOHSE, D. 2005. The effect of bubbles on developed turbulence. *Journal of Fluid Mechanics,* 538**,** 153-187.

RIQUARTS, H. 1981. A physical model for axial mixing of the liquid phase for heterogeneous flow regime in bubble columns. *Germ. Chem. Eng.,* 4**,** 18-23.

ROGHAIR, I., BALTUSSEN, M., ANNALAND, M. V. S. & KUIPERS, J. 2013. Direct numerical simulations of the drag force of bi-disperse bubble swarms. *Chemical Engineering Science,* 95**,** 48-53.

ROLLBUSCH, P., BOTHE, M., BECKER, M., LUDWIG, M., GRÜNEWALD, M., SCHLÜTER, M. & FRANKE, R. 2015. Bubble columns operated under industrially relevant conditions–current understanding of design parameters. *Chemical Engineering Science,* 126**,** 660-678.

RUTHIYA, K. C., VAN DER SCHAAF, J., KUSTER, B. F. & SCHOUTEN, J. C. 2006. Influence of particles and electrolyte on gas hold-up and mass transfer in a slurry bubble column. *International Journal of Chemical Reactor Engineering,* 4.

RUZICKA, M., DRAHOŠ, J., FIALOVA, M. & THOMAS, N. 2001. Effect of bubble column dimensions on flow regime transition. *Chemical Engineering Science,* 56**,** 6117-6124.

RUZICKA, M., DRAHOŠ, J., MENA, P. & TEIXEIRA, J. 2003. Effect of viscosity on homogeneous–heterogeneous flow regime transition in bubble columns. *Chemical Engineering Journal,* 96**,** 15-22.

SANYAL, J., MARCHISIO, D. L., FOX, R. O. & DHANASEKHARAN, K. 2005. On the comparison between population balance models for CFD simulation of bubble columns. *Industrial & Engineering Chemistry Research,* 44**,** 5063-5072.

SANYAL, J., VÁSQUEZ, S., ROY, S. & DUDUKOVIC, M. 1999. Numerical simulation of gas–liquid dynamics in cylindrical bubble column reactors. *Chemical Engineering Science,* 54**,** 5071-5083.

SATHE, M. J., MATHPATI, C. S., DESHPANDE, S. S., KHAN, Z., EKAMBARA, K. & JOSHI, J. B. 2011. Investigation of flow structures and transport phenomena in bubble columns using particle image velocimetry and miniature pressure sensors. *Chemical Engineering Science,* 66**,** 3087-3107.

SAXENA, S., RAO, N. & SAXENA, A. 1990. Heat-transfer and gas-holdup studies in a bubble column: air-water-glass bead system. *Chemical Engineering Communications,* 96**,** 31-55.

SCHÄFER, R., MERTEN, C. & EIGENBERGER, G. 2002. Bubble size distributions in a bubble column reactor under industrial conditions. *Experimental Thermal and Fluid Science,* 26**,** 595-604.

SCHILLER, L. 1933. A drag coefficient correlation. *Zeit. Ver. Deutsch. Ing.,* 77**,** 318-320.

SCHMIDT, D. & VELTEN, K. 2016. Numerical simulation of bubble flow homogenization in industrial scale wine fermentations. *Food and Bioproducts Processing,* 100, 102-117.

SHAH, Y., KELKAR, B. G., GODBOLE, S. & DECKWER, W. D. 1982. Design parameters estimations for bubble column reactors. *AICHE Journal,* 28**,** 353-379.

SHAIKH, A. & AL-DAHHAN, M. 2005. Characterization of the hydrodynamic flow regime in bubble columns via computed tomography. *Flow Measurement and Instrumentation,* 16**,** 91-98.

SHAIKH, A. & AL-DAHHAN, M. H. 2007. A review on flow regime transition in bubble columns. *International Journal of Chemical Reactor Engineering,* 5.

SHI, W., YANG, X., SOMMERFELD, M., YANG, J., CAI, X., LI, G., & ZONG, Y. 2019. Modelling of mass transfer for gas-liquid two-phase flow in bubble column reactor with a bubble breakage model considering bubble-induced turbulence. *Chemical Engineering Journal,* 371, 470-485.

SHIEA, M., MOSTOUFI, N. & SOTUDEH-GHAREBAGH, R. 2013. Comprehensive study of regime transitions throughout a bubble column using resistivity probe. *Chemical Engineering Science,* 100**,** 15-22.

SHOLLENBERGER, K., TORCZYNSKI, J., ADKINS, D., O'HERN, T. & JACKSON, N. 1997. Gamma-densitometry tomography of gas holdup

spatial distribution in industrial-scale bubble columns. *Chemical Engineering Science,* 52**,** 2037-2048.

SHU, S., VIDAL, D., BERTRAND, F. & CHAOUKI, J. 2019. Multiscale multiphase phenomena in bubble column reactors: A review. *Renewable Energy,* 141**,** 613-631.

SMAGORINSKY, J. 1963. General circulation experiments with the primitive equations: I. The basic experiment. *Monthly weather review,* 91**,** 99-164.

SMITH, J. S., VALSARAJ, K. T. & THIBODEAUX, L. J. 1996. Bubble column reactors for wastewater treatment. 1. Theory and modeling of continuous countercurrent solvent sublation. *Industrial & Engineering Chemistry Research,* 35**,** 1688-1699.

SODJA, J. 2007. Turbulence models in CFD. University of Ljubljana, 1-18.

SOKOLICHIN, A., EIGENBERGER, G., LAPIN, A. & LÜBERT, A. 1997. Dynamic numerical simulation of gas-liquid two-phase flows Euler/Euler versus Euler/Lagrange. *Chemical Engineering Science,* 52**,** 611-626.

SOMMERFELD, M. & BRODER, D. 2009. Analysis of hydrodynamics and microstructure in a bubble column by planar shadow image velocimetry. *Industrial & Engineering Chemistry Research,* 48**,** 330-340.

SOMMERFELD, M., MUNIZ, M. & REICHARDT, T. 2018. On the importance of modelling bubble dynamics for point-mass numerical calculations of bubble columns. *Journal of Chemical Engineering of Japan,* 51**,** 301-317.

SUN, X., KIM, S., ISHII, M. & BEUS, S. G. 2004. Modeling of bubble coalescence and disintegration in confined upward two-phase flow. *Nuclear Engineering and Design,* 230**,** 3-26.

TABIB, M. V., ROY, S. A. & JOSHI, J. B. 2008. CFD simulation of bubble column—an analysis of interphase forces and turbulence models. *Chemical Engineering Journal,* 139**,** 589-614.

TABORDA, M. A., KIPPING, R., HAMPEL, U. & SOMMERFELD, M. 2021. Advanced analysis of bubble columns: Comparison of Euler/Lagrange simulations and experiments under CO2 chemisorption conditions. *Chemical Engineering Research and Design,* 170**,** 389-405.

TABORDA, M. A. & SOMMERFELD, M. 2021. Reactive LES-Euler/Lagrange modelling of bubble columns considering effects of bubble dynamics. *Chemical Engineering Journal,* 407**,** 127222.

THAKRE, S. & JOSHI, J. 1999. CFD simulation of bubble column reactors: importance of drag force formulation. *Chemical Engineering Science,* 54**,** 5055-5060.

THOMAS, N., AUTON, T., SENE, K. & HUNT, J. Entrapment and transport of bubbles by transient large eddies in multiphase turbulent shear flows. International Conference on the Physical Modelling of Multi-Phase Flow, 1983. 169-184.

THORAT, B. & JOSHI, J. 2004. Regime transition in bubble columns: experimental and predictions. *Experimental Thermal and Fluid Science,* 28**,** 423-430.

THORAT, B., SHEVADE, A., BHILEGAONKAR, K., AGLAWE, R., VEERA, U. P., THAKRE, S., PANDIT, A., SAWANT, S. & JOSHI, J. 1998. Effect of sparger design and height to diameter ratio on fractional gas hold-up in bubble columns. *Chemical Engineering Research and Design,* 76**,** 823-834.

TOMIYAMA, A. Effects of Eotvos number and dimensionless liquid volumetric flux on lateral motion of a bubble in a laminar duct flow. 2nd Int. Conf. an Multiphase Flow, 1995.

TOMIYAMA, A. 1998. Struggle with computational bubble dynamics. *Multiphase Science and Technology,* 10**,** 369-405.

TOMIYAMA, A., TAMAI, H., ZUN, I. & HOSOKAWA, S. 2002. Transverse migration of single bubbles in simple shear flows. *Chemical Engineering Science,* 57**,** 1849-1858.

TRYGGVASON, G., BUNNER, B., ESMAEELI, A., JURIC, D., AL-RAWAHI, N., TAUBER, W., HAN, J., NAS, S. & JAN, Y.-J. 2001. A front-tracking method for the computations of multiphase flow. *Journal of Computational Physics,* 169**,** 708-759.

VAN BATEN, J. & KRISHNA, R. 2001. Eulerian simulations for determination of the axial dispersion of liquid and gas phases in bubble columns operating in the churn-turbulent regime. *Chemical Engineering Science,* 56**,** 503-512.

VAN BATEN, J. & KRISHNA, R. 2003. Comparison of hydrodynamics and mass transfer in airlift and bubble column reactors using CFD. *Chemical Engineering & Technology: Industrial Chemistry-Plant Equipment-Process Engineering-Biotechnology,* 26**,** 1074-1079.

VAN BATEN, J. & KRISHNA, R. 2004a. CFD Modeling of a Bubble Column Reactor carrying out a consecutive A→ B→ C Reaction. *Chemical Engineering & Technology: Industrial Chemistry-Plant Equipment-Process Engineering-Biotechnology,* 27**,** 398-406.

VAN BATEN, J. & KRISHNA, R. 2004b. CFD modeling of bubble column reactor including the influence of gas contraction. *Chemical Engineering & Technology: Industrial Chemistry-Plant Equipment-Process Engineering-Biotechnology*, 27**,** 1302-1308.

VAN BATEN, J. & KRISHNA, R. 2004c. Scale effects on the hydrodynamics of bubble columns operating in the heterogeneous flow regime. *Chemical Engineering Research and Design,* 82**,** 1043-1053.

VAN DEN HENGEL, E., DEEN, N. & KUIPERS, J. 2005. Application of coalescence and breakup models in a discrete bubble model for bubble columns. *Industrial & Engineering Chemistry Research,* 44**,** 5233-5245.

VANDU, C., KOOP, K. & KRISHNA, R. 2004a. Large bubble sizes and rise velocities in a bubble column slurry reactor. *Chemical Engineering & Technology: Industrial Chemistry-Plant Equipment-Process Engineering-Biotechnology,* 27**,** 1195-1199.

VANDU, C., KOOP, K. & KRISHNA, R. 2004b. Volumetric mass transfer coefficient in a slurry bubble column operating in the heterogeneous flow regime. *Chemical Engineering Science,* 59**,** 5417-5423.

VANDU, C. & KRISHNA, R. 2003. Gas holdup and volumetric mass transfer coefficient in a slurry bubble column. *Chemical Engineering & Technology:*

Industrial Chemistry-Plant Equipment-Process Engineering-Biotechnology, 26**,** 779-782.

VANDU, C. & KRISHNA, R. 2004a. Influence of scale on the volumetric mass transfer coefficients in bubble columns. *Chemical Engineering and Processing: Process Intensification*, 43**,** 575-579.

VANDU, C. & KRISHNA, R. 2004b. Volumetric mass transfer coefficients in slurry bubble columns operating in the churn-turbulent flow regime. *Chemical Engineering and Processing: Process Intensification*, 43**,** 987-995.

VANDU, C. O., VAN DEN BERG, B. & KRISHNA, R. 2005. Gas-Liquid Mass Transfer in a Slurry Bubble Column at High Slurry Concentrations and High Gas Velocities. *Chemical Engineering & Technology: Industrial Chemistry-Plant Equipment-Process Engineering-Biotechnology*, 28**,** 998-1002.

VEERA, U. P. & JOSHI, J. 1999. Measurement of gas hold-up profiles by gamma ray tomography: effect of sparger design and height of dispersion in bubble columns. *Chemical Engineering Research and Design*, 77**,** 303-317.

VEERA, U. P. & JOSHI, J. 2000. Measurement of gas hold-up profiles in bubble column by gamma ray tomography: effect of liquid phase properties. *Chemical engineering research and design*, 78**,** 425-434.

VIAL, C., LAINE, R., PONCIN, S., MIDOUX, N. & WILD, G. 2001. Influence of gas distribution and regime transitions on liquid velocity and turbulence in a 3-D bubble column. *Chemical Engineering Science*, 56**,** 1085-1093.

VIJAYAN, M., SCHLABERG, H. & WANG, M. 2007. Effects of sparger geometry on the mechanism of flow pattern transition in a bubble column. *Chemical Engineering Journal,* 130**,** 171-178.

VITANKAR, V., DHOTRE, M. & JOSHI, J. 2002. A low Reynolds number k–ε model for the prediction of flow pattern and pressure drop in bubble column reactors. *Chemical Engineering Science,* 57**,** 3235-3250.

WANG, T., WANG, J. & JIN, Y. 2006. A CFD–PBM coupled model for gas–liquid flows. *AIChE Journal,* 52**,** 125-140.

WARSITO, W. & FAN, L.-S. 2001. Measurement of real-time flow structures in gas–liquid and gas–liquid–solid flow systems using electrical capacitance tomography (ECT). *Chemical Engineering Science,* 56**,** 6455-6462.

WELLEK, R., AGRAWAL, A. & SKELLAND, A. 1966. Shape of liquid drops moving in liquid media. *AIChE Journal,* 12**,** 854-862.

WONGSUCHOTO, P., CHARINPANITKUL, T. & PAVASANT, P. 2003. Bubble size distribution and gas–liquid mass transfer in airlift contactors. *Chemical Engineering Journal,* 92**,** 81-90.

WU, Q., KIM, S., ISHII, M. & BEUS, S. 1998. One-group interfacial area transport in vertical bubbly flow. *International Journal of Heat and Mass Transfer,* 41**,** 1103-1112.

YANG, X., THOMAS, N., GUO, L. & HOU, Y. 2002. Two-way coupled bubble laden mixing layer. *Chemical Engineering Science,* 57**,** 555-564.

YANO, T., KURAMOTO, K., TSUTSUMI, A., OTAWARA, K. & SHIGAKI, Y. 1999. Scale-up effects in nonlinear dynamics of three-phase reactors. *Chemical Engineering Science,* 54**,** 5259-5263.

ZAHRADNIK, J., FIALOVA, M., KASTANEK, F., GREEN, K. & THOMAS, N. 1995. The effect of electrolytes on bubble coalescence and gas holdup in bubble-column reactors. *Chemical Engineering Research & Design,* 73**,** 341-346.

ZEHNER, P. 1986. Momentum, mass and heat transfer in bubble columns. Part 1. Flow model of the bubble column and liquid velocities. *International Journal of Chemical Engineering,* 26**,** 22.

ZHANG, D., DEEN, N. & KUIPERS, J. 2006. Numerical simulation of the dynamic flow behavior in a bubble column: a study of closures for turbulence and interface forces. *Chemical Engineering Science,* 61**,** 7593-7608.

ZHANG, D., DEEN, N. G. & KUIPERS, J. 2009. Euler− Euler modeling of flow, mass transfer, and chemical reaction in a bubble column. *Industrial & Engineering Chemistry Research,* 48**,** 47-57.

ZHANG, H., GUO, Z., WANG, Y., SHEN, X. & WANG, T. 2021. Effect of particles on hydrodynamics and mass transfer in a slurry bubble column: Correlation of experimental data. *Authorea Preprints*.

ZIEGENHEIN, T. & LUCAS, D. 2017. Observations on bubble shapes in bubble columns under different flow conditions. *Experimental Thermal and Fluid Science,* 85**,** 248-256.

ẐUN, I. 1980. The transverse migration of bubbles influenced by walls in vertical bubbly flow. *International Journal of Multiphase Flow,* 6**,** 583-588.

FIGURES

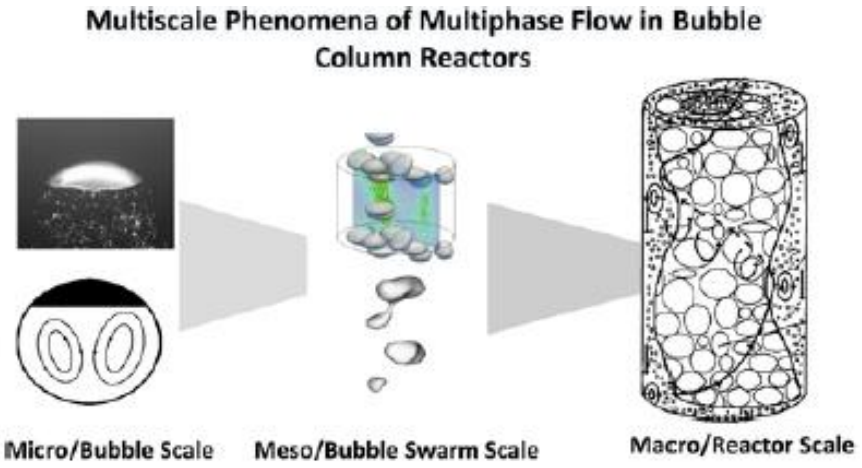

Figure 1- 1 Multiscale phenomena of bubbly flow in bubble column (Chen et al., 1994, Kendoush et al., 2016, Qian et al., 2006, Roghair et al., 2013, Shu et al., 2019)

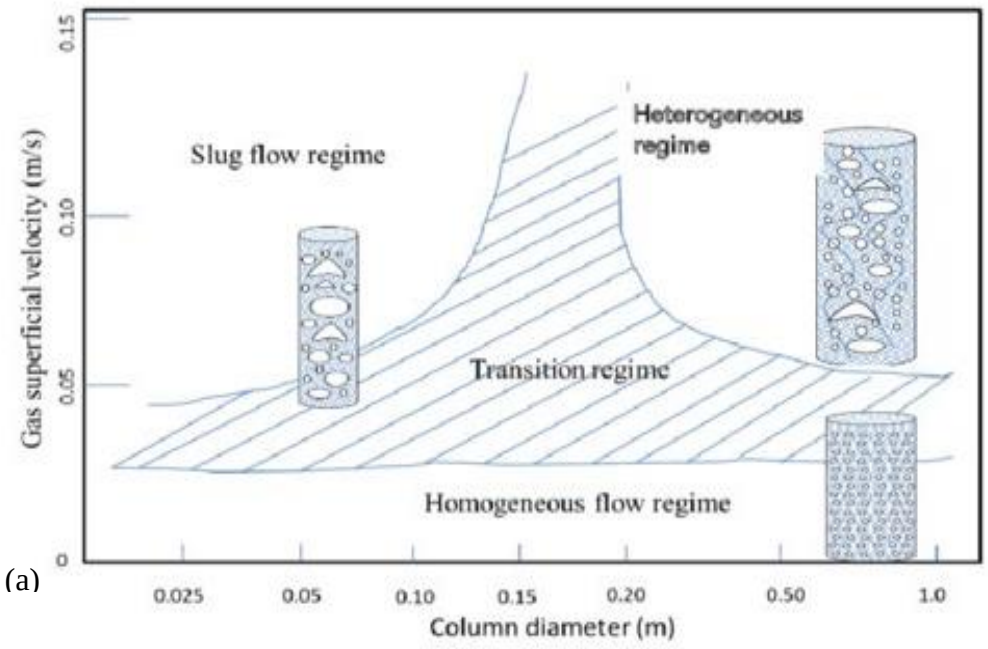

(a)

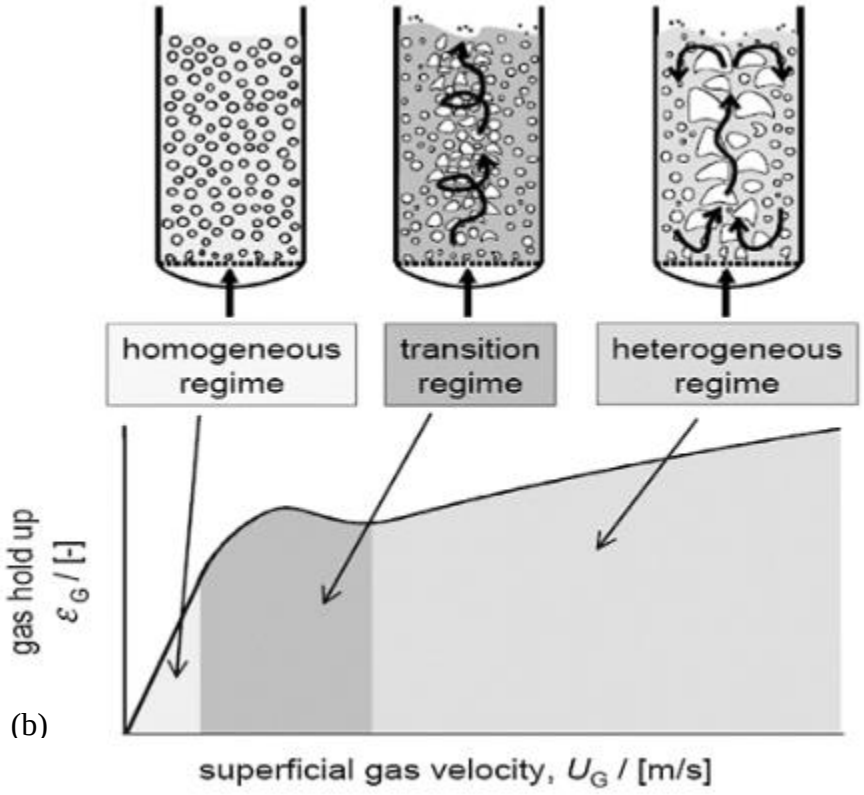

Figure 1- 2 Schematic of correlation of flow regime with gas superficial velocity and column diameter. (DSouza, 2020, Manjrekar and Dudukovic, 2019)

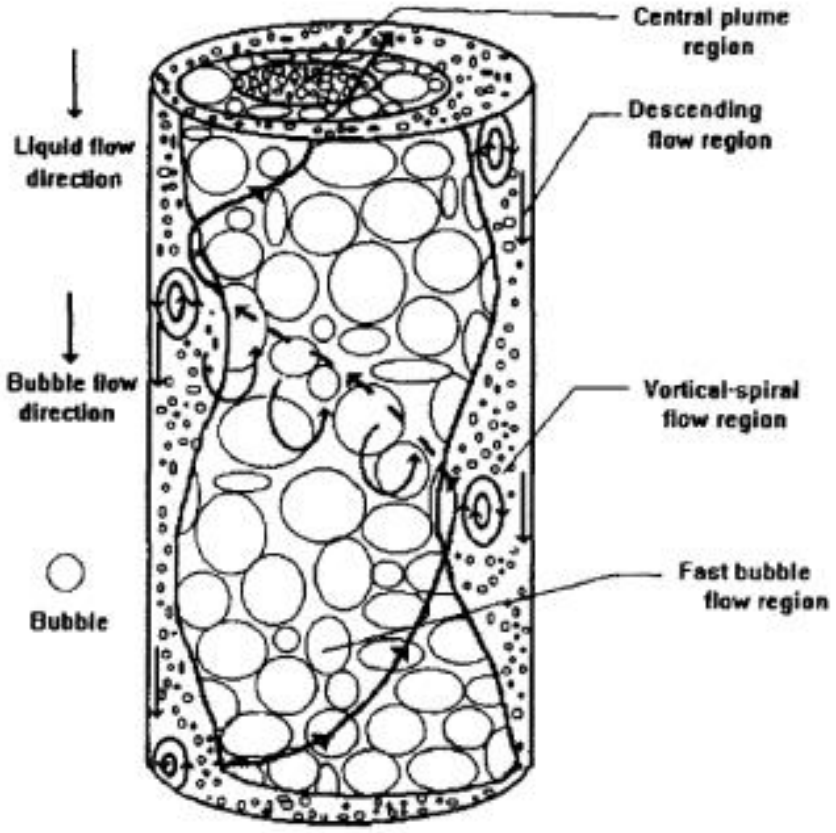

Figure 1- 3 Detailed flow structure in the vortical-spiral flow regime in bubbly flow bubble column (Chen et al., 1994)

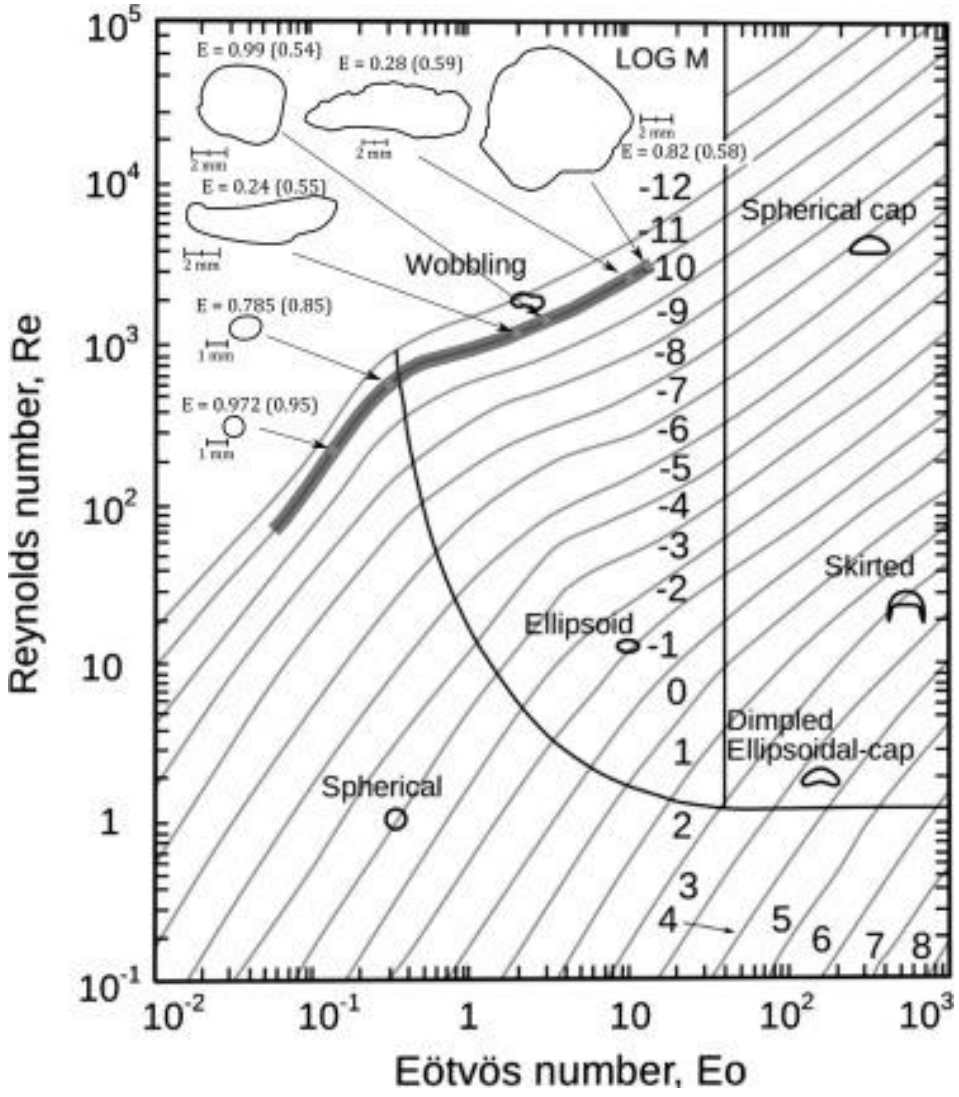

Figure 1- 4 Grace diagram, selected bubble shapes are shown with the bubble aspect ratio. (Grace, 1976, Clift et al., 2005, Ziegenhein and Lucas, 2017)

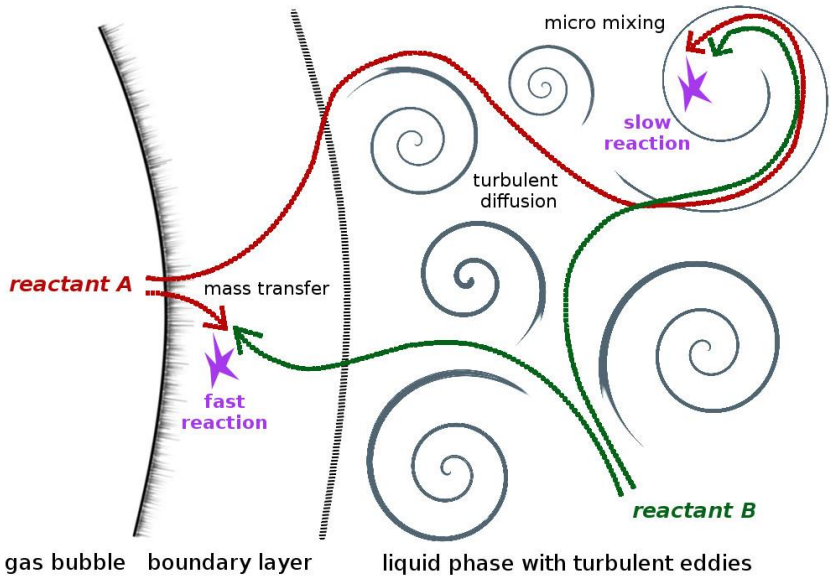

Figure 1- 5 Mass transfer mechanism in reactive flow

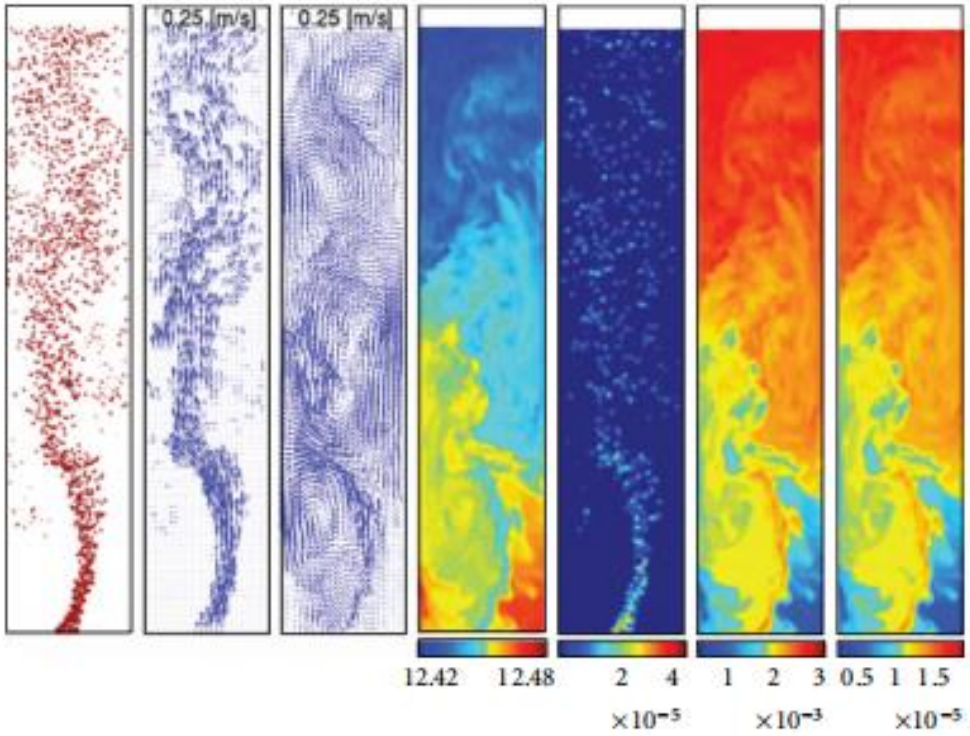

Figure 1- 6 Instantaneous captures in the absorption of carbon dioxide in bubble columns at t=60s. Figures from left to right: bubble position, gas velocity vectors,

liquid velocity vectors, pH value, concentration of $\mathbf{CO_2}, \boldsymbol{HCO_3^{-1}}, \boldsymbol{CO_3^{2-}}$. (Darmana et al., 2007)

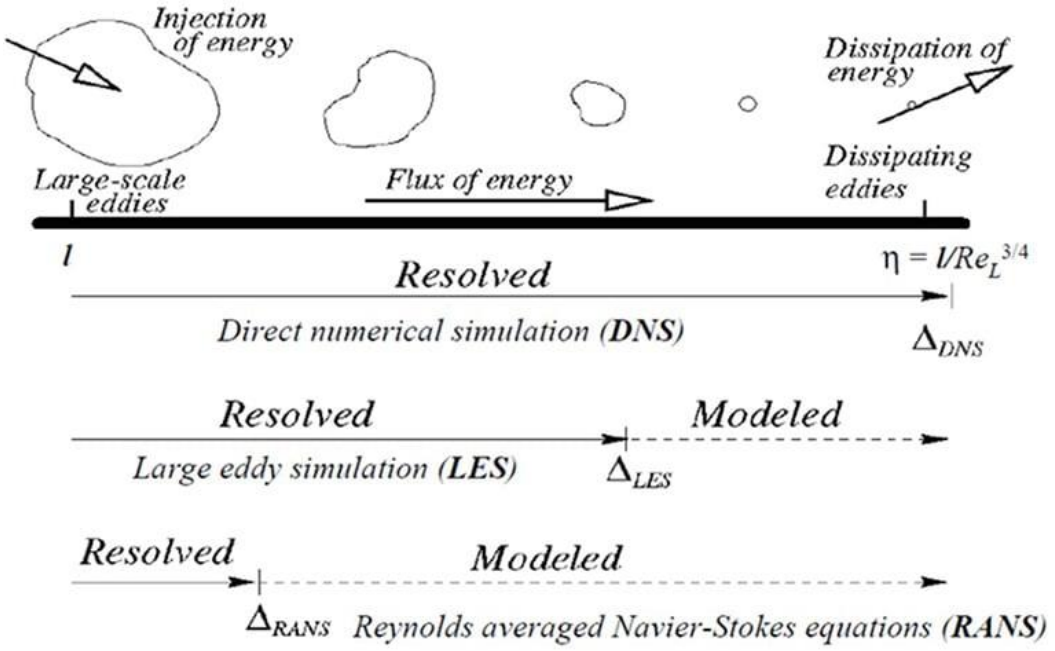

Figure 1- 7 Turbulent models according to solve different scales of eddies (Sodja, 2007).

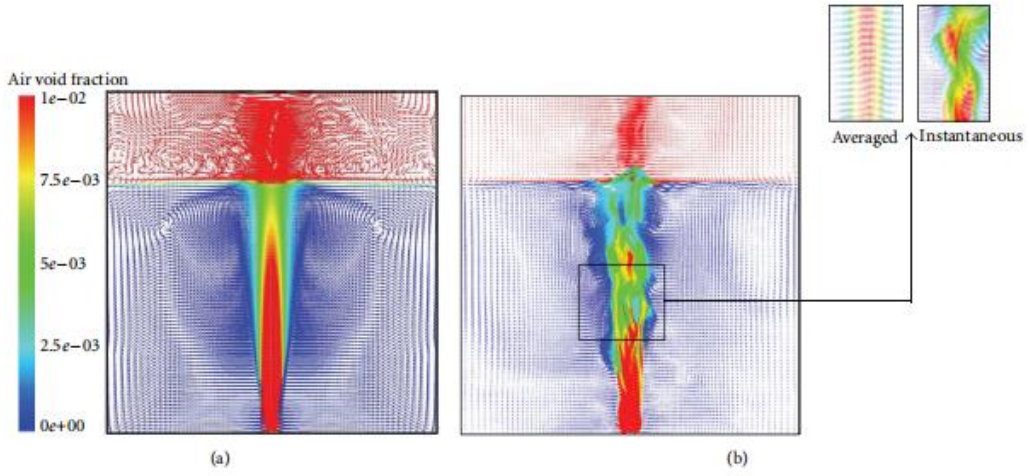

Figure 1- 8 Comparison between the contour of axial velocity vectors highlighted by air volume fraction using (a) k-e model and (b) EELES model (Dhotre et al., 2008)

(a)

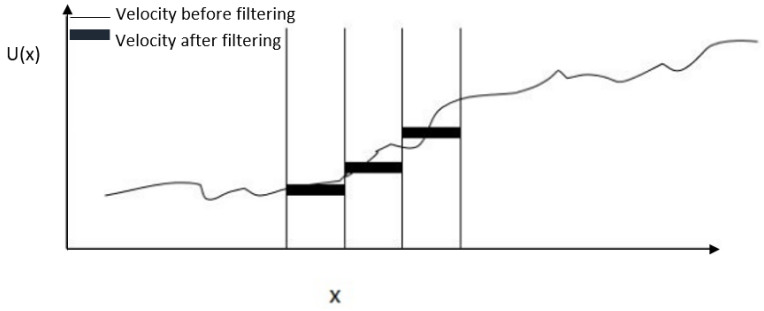

(b)

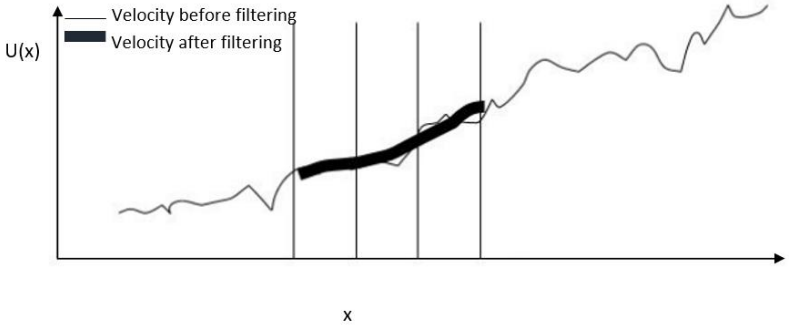

Figure 1- 9 Schematic diagram of the axial velocity against axial distance after (a) box filtering (b) Gaussian filtering

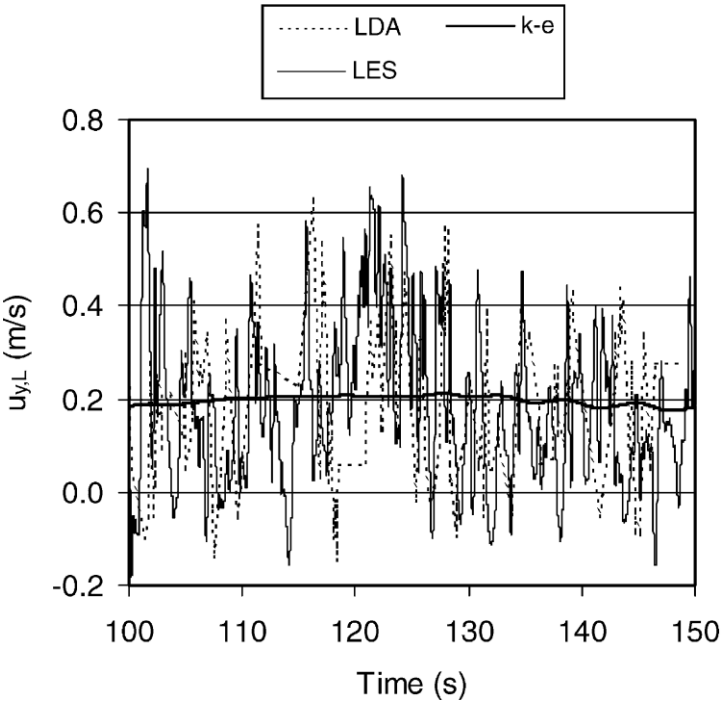

Figure 1- 10 Predicted time history of the stream-wise liquid velocity. (Deen et al., 2001)

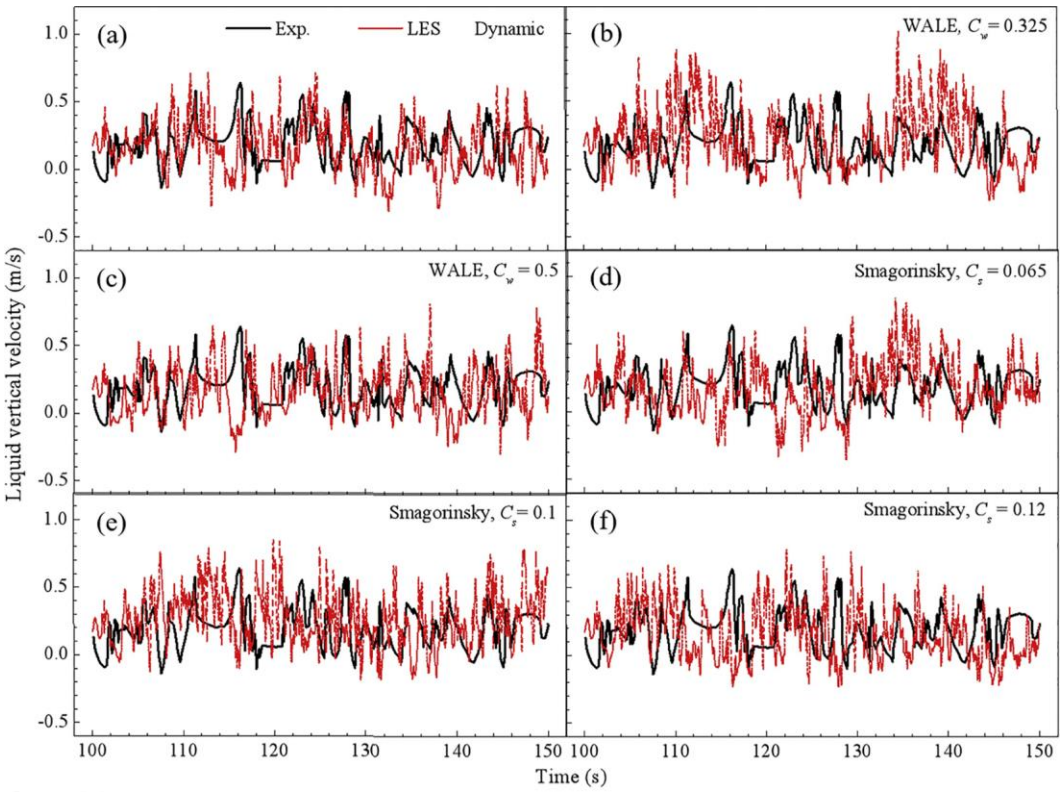

Figure 1- 11 Time history of the stream-wise liquid velocity based on the experiment carried out by Deen et al. (2001). (Liu et al., 2020)

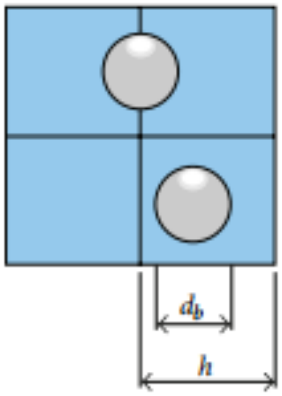

Figure 1- 12 Schematic of an optimum filter width. (Milelli, 2002)

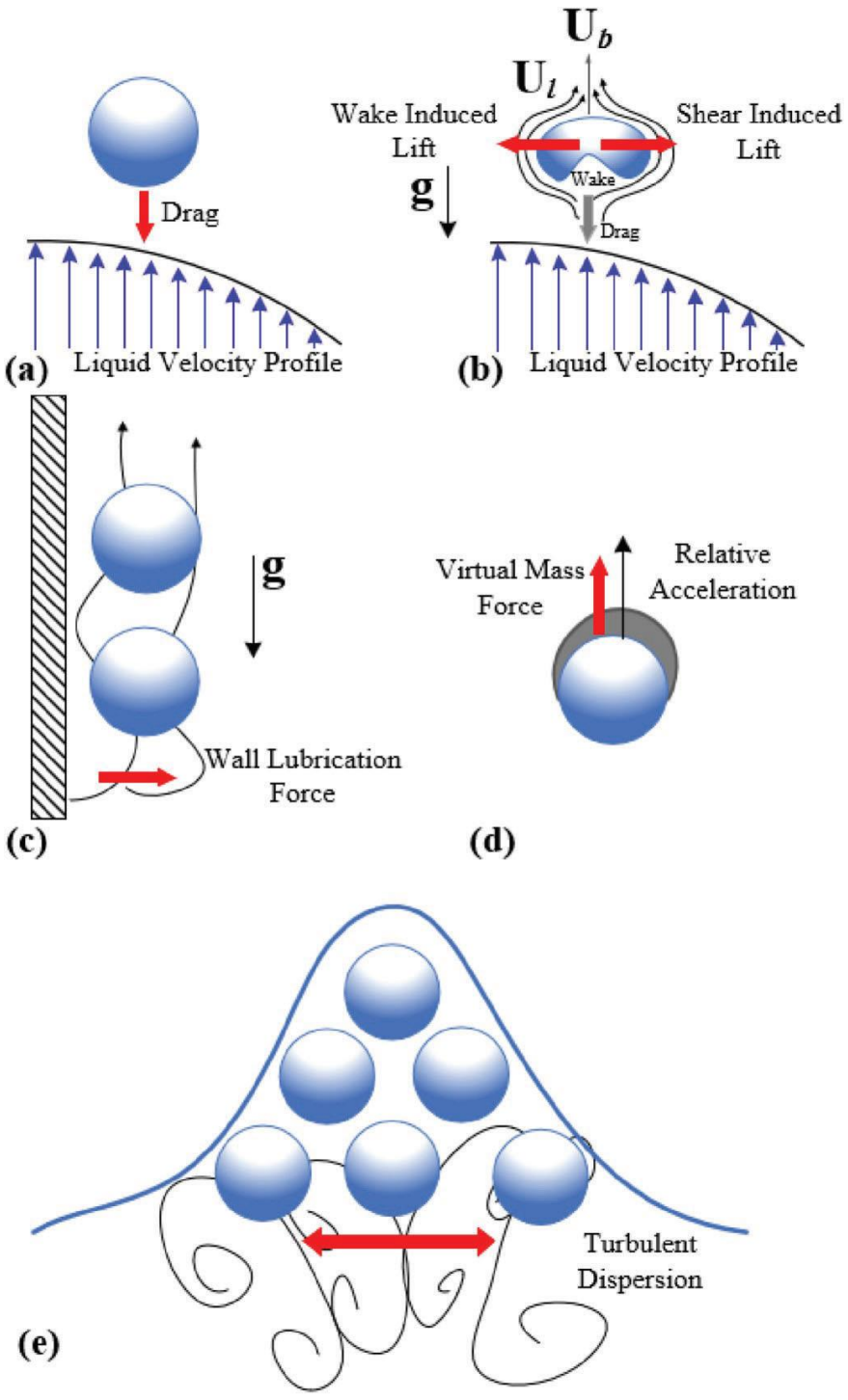

Figure 1- 13 The schematic of various force acting on bubbles in bubble column bubbly flow: (a) drag force; (b) lift force; (c) wall lubrication force; (d) virtual mass force; (d) turbulent dispersion force. (Khan et al., 2020)

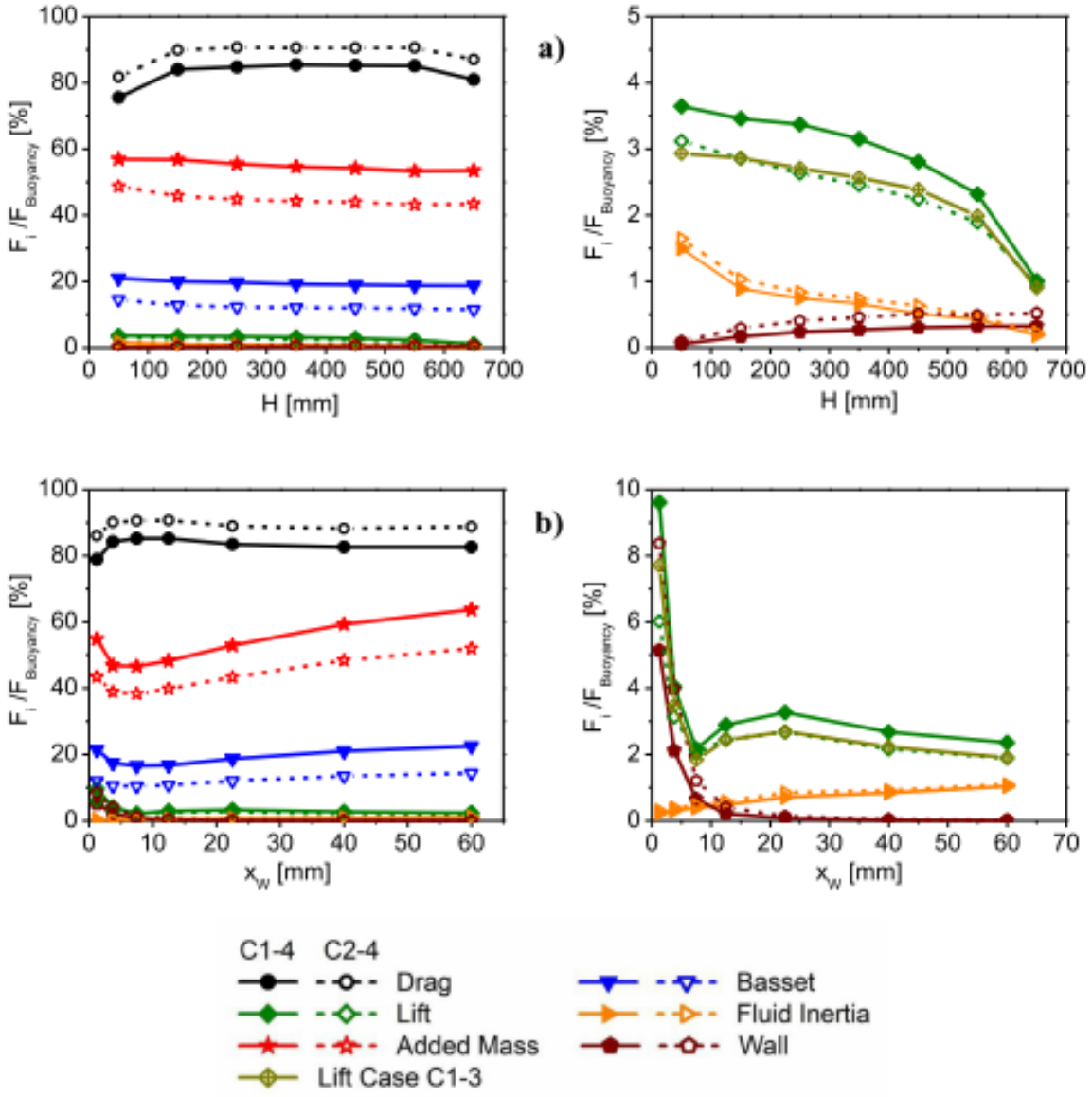

Figure 1- 14 Time-averaged local face ratios for C1-4 ($\alpha_B = 1.26\%, d_B = 2.55$ mm) and C2-4 ($\alpha_B = 1.40\%, d_B = 3.31$ mm) against a) the height of bubble column; b) wall distance. (Muniz and Sommerfeld, 2020)

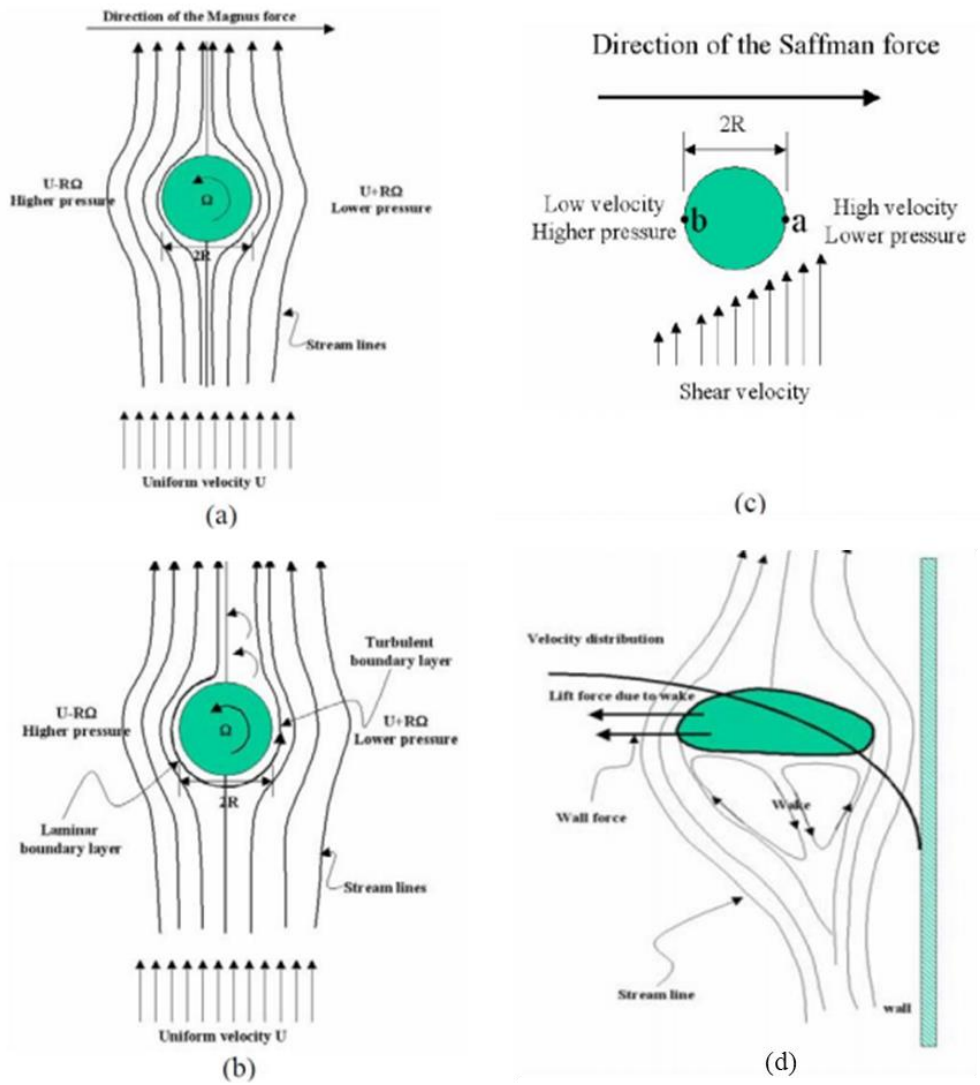

Figure 1- 15 Schematic diagram of lift force (taken from Chen (2004)): (a) Magnus lift force in uniform flow field; (b) Magnus lift force with laminar boundary layer on one side and turbulent boundary layer on the other side of the bubble; (c) Saffman lift force; (d) lift force due to bubble deformation.

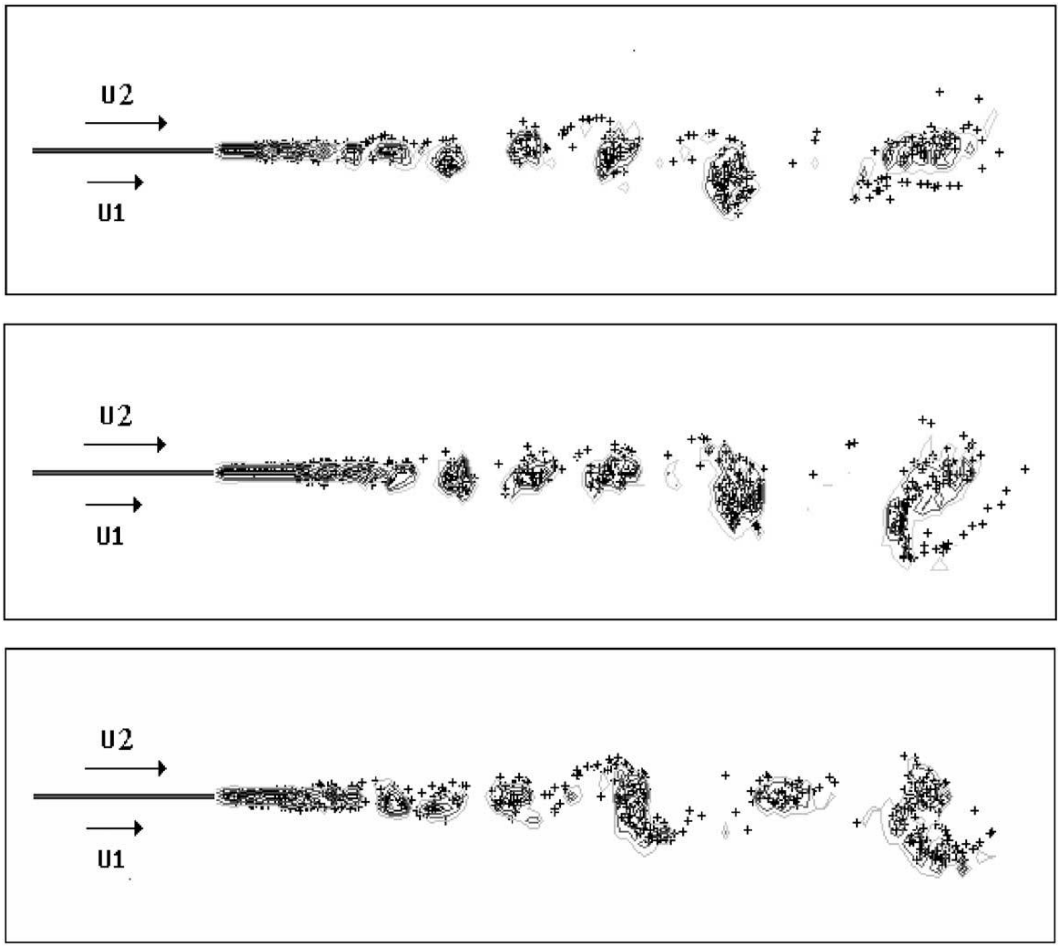

Figure 1- 16 Instantaneous contours of bubble dispersion and vorticity at St = 1:1 and Fr = 2:887. "+" denotes the bubble position. From top to bottom: Bubble concentration = 0:08, 0.08 and 0.4 respectively. (Yang et al. 2002)

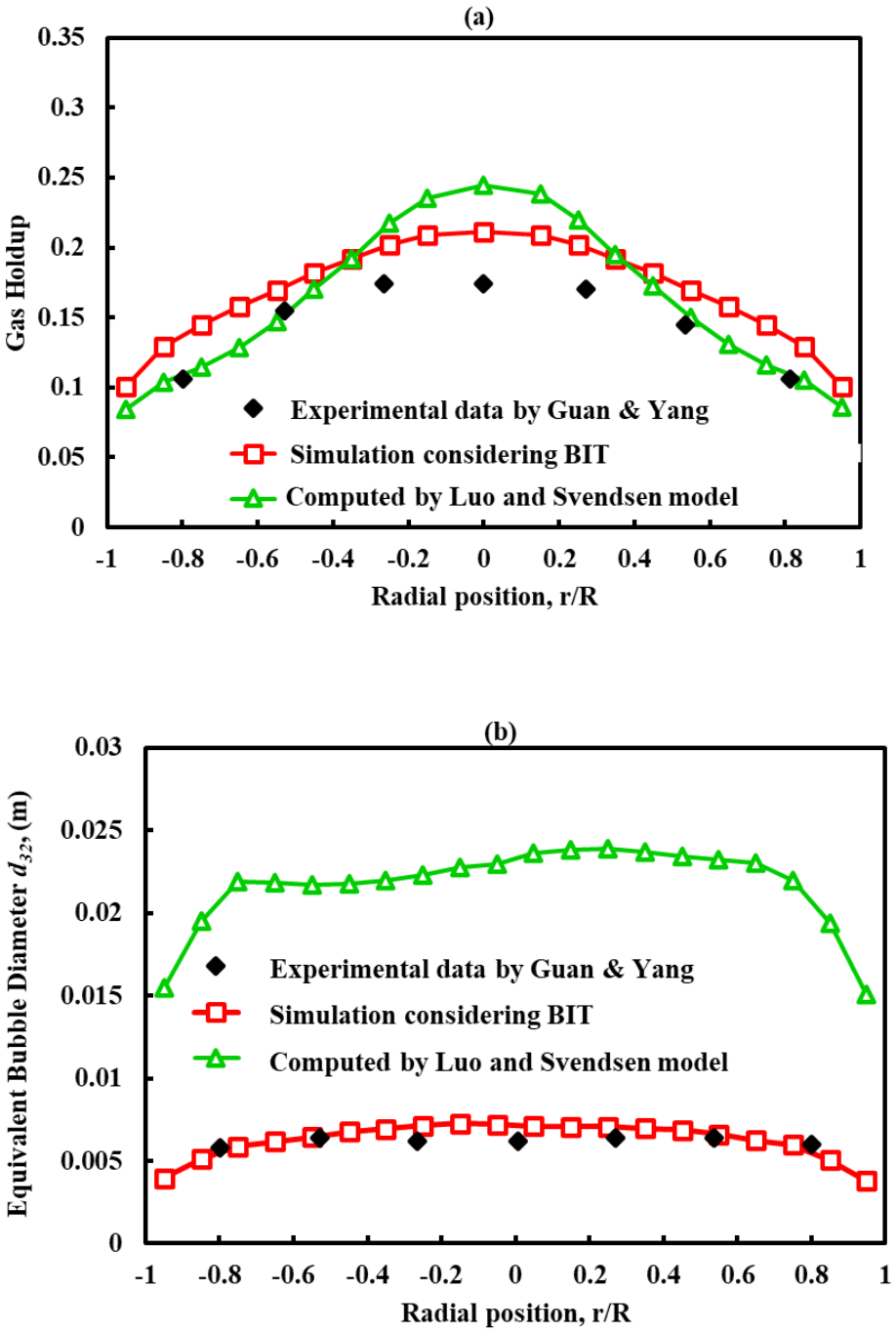

Figure 1- 17 Comparison of the predicted (a) gas hold up and (b) equivalent bubble size by different breakage models. (Shi et al., 2019)

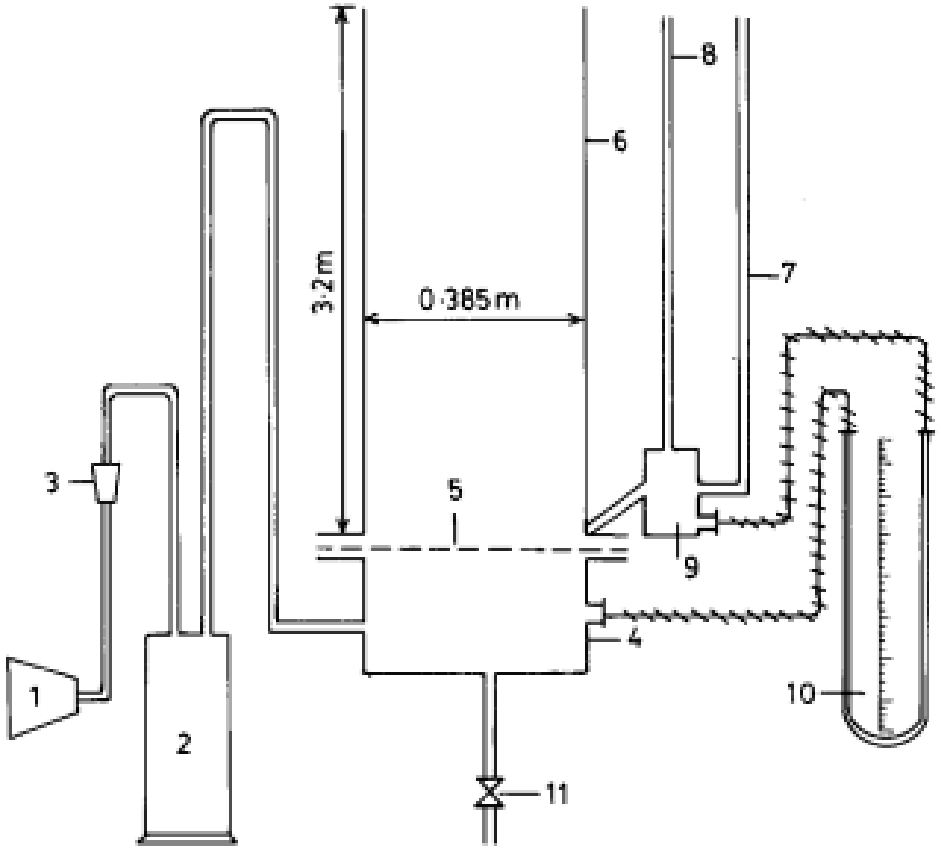

Figure 1- 18 Experimental set-up in the experiment conducted by Throat et al. (1998)

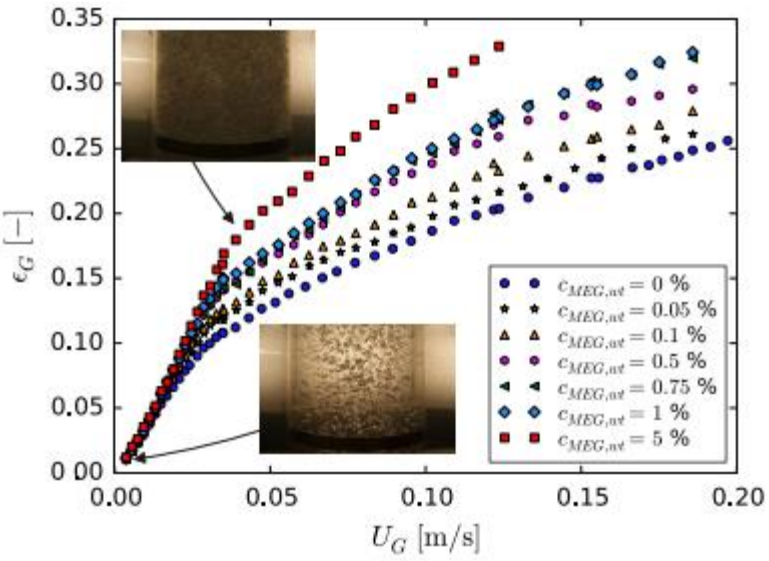

(a)

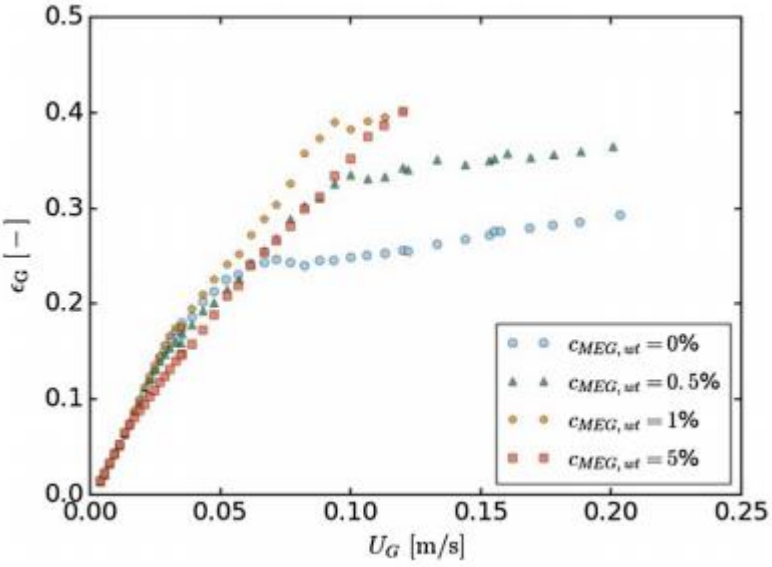

(b)

Figure 1- 19 Gas hold-up profile predicted by using (a) coarse sparger (b) fine sparger. (Besagni et al., 2018)

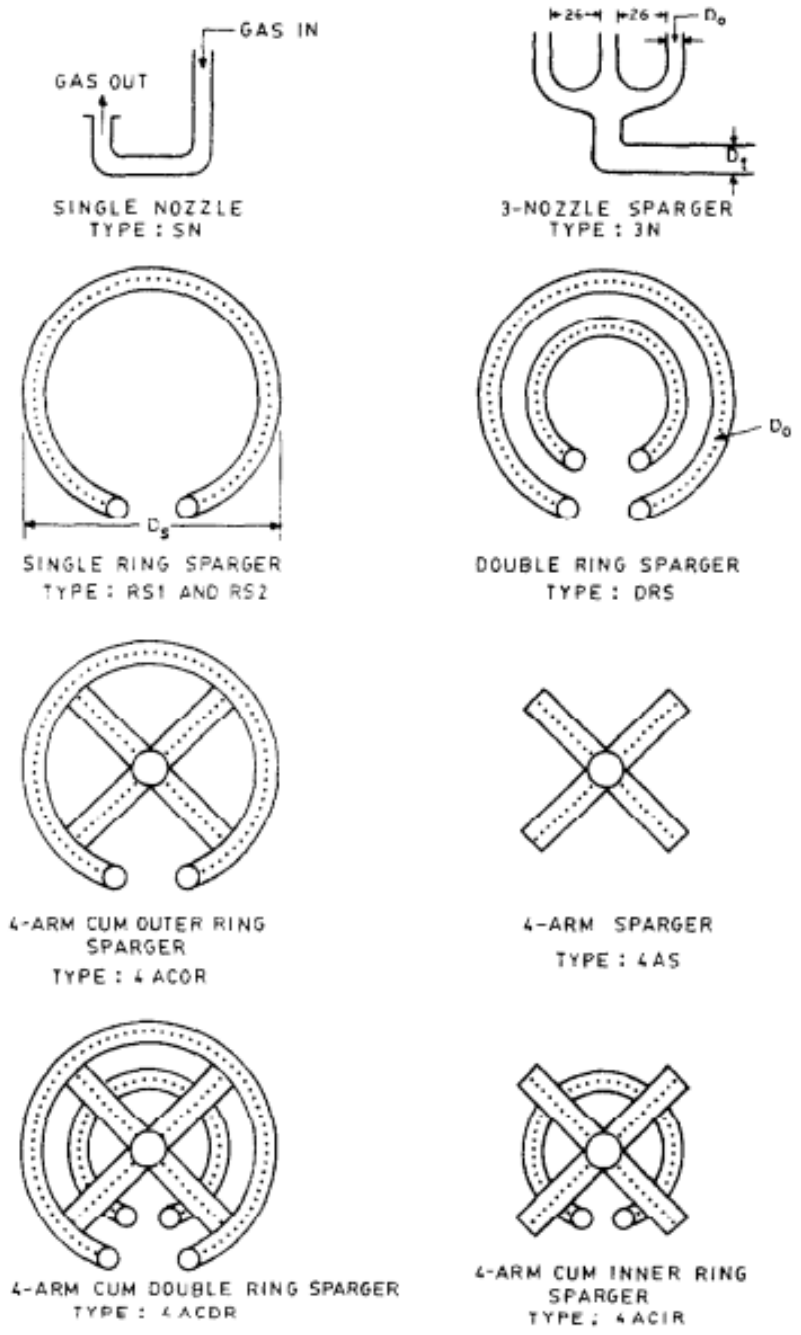

Figure 1- 20 Different sparger designs. (Haque et al., 1986)

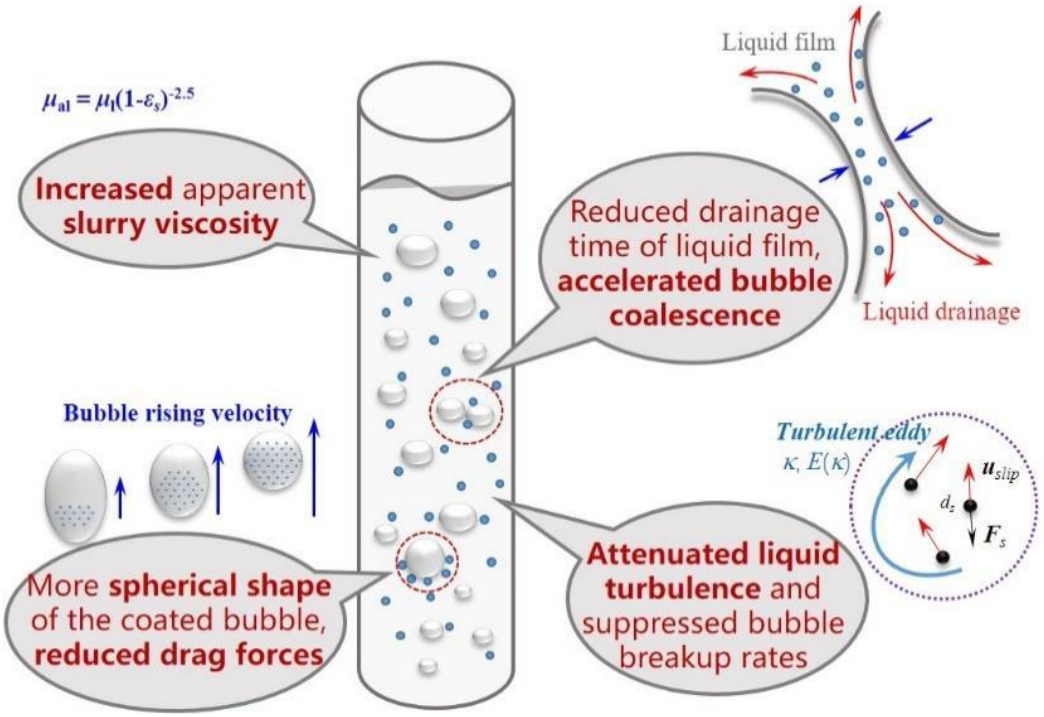

Figure 1- 21 Schematic diagram of the influence from the solid particles on gas-liquid-solid three-phase flow in bubble column reactor. (Zhang et al., 2021)

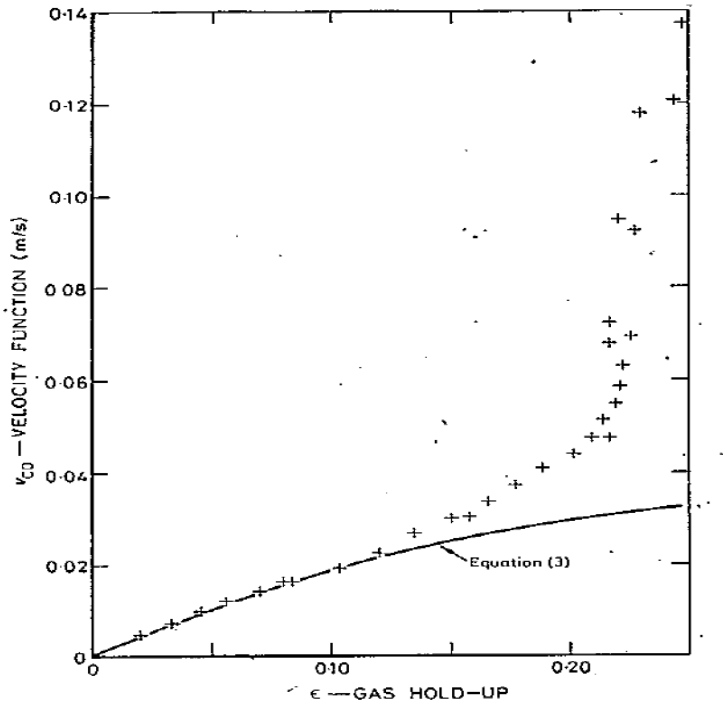

Figure 1- 22 Relationship of gas superficial velocity and overall gas holdup (Hills, 1974)

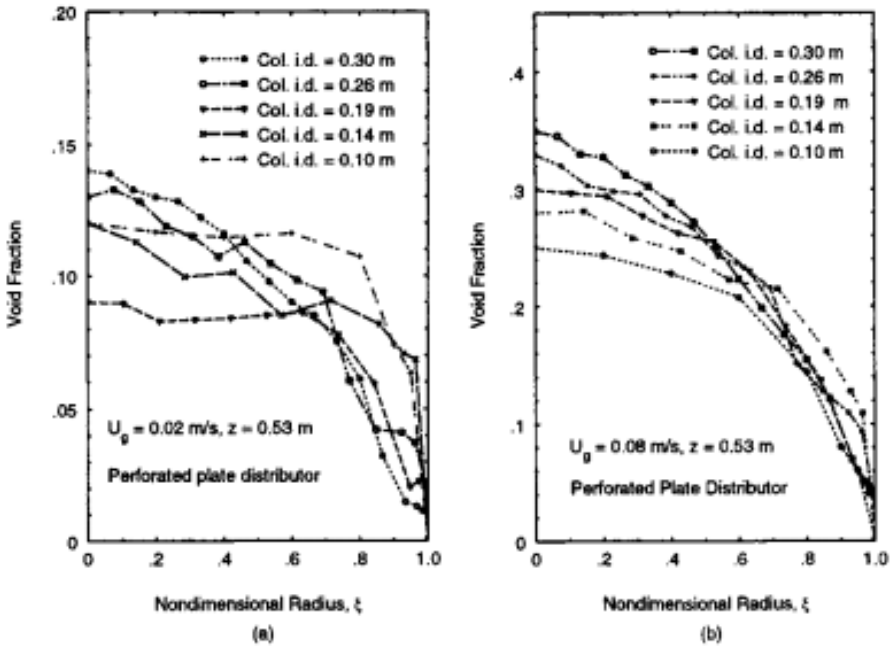

Figure 1- 23 Effect of column inner diameter on gas void fraction profile (a) $\mathbf{U_g} = \mathbf{0.02}\ \boldsymbol{m/s}$ (b) $\mathbf{U_g} = \mathbf{0.08}\ \boldsymbol{m/s}$ (Kumar et al., 1997)

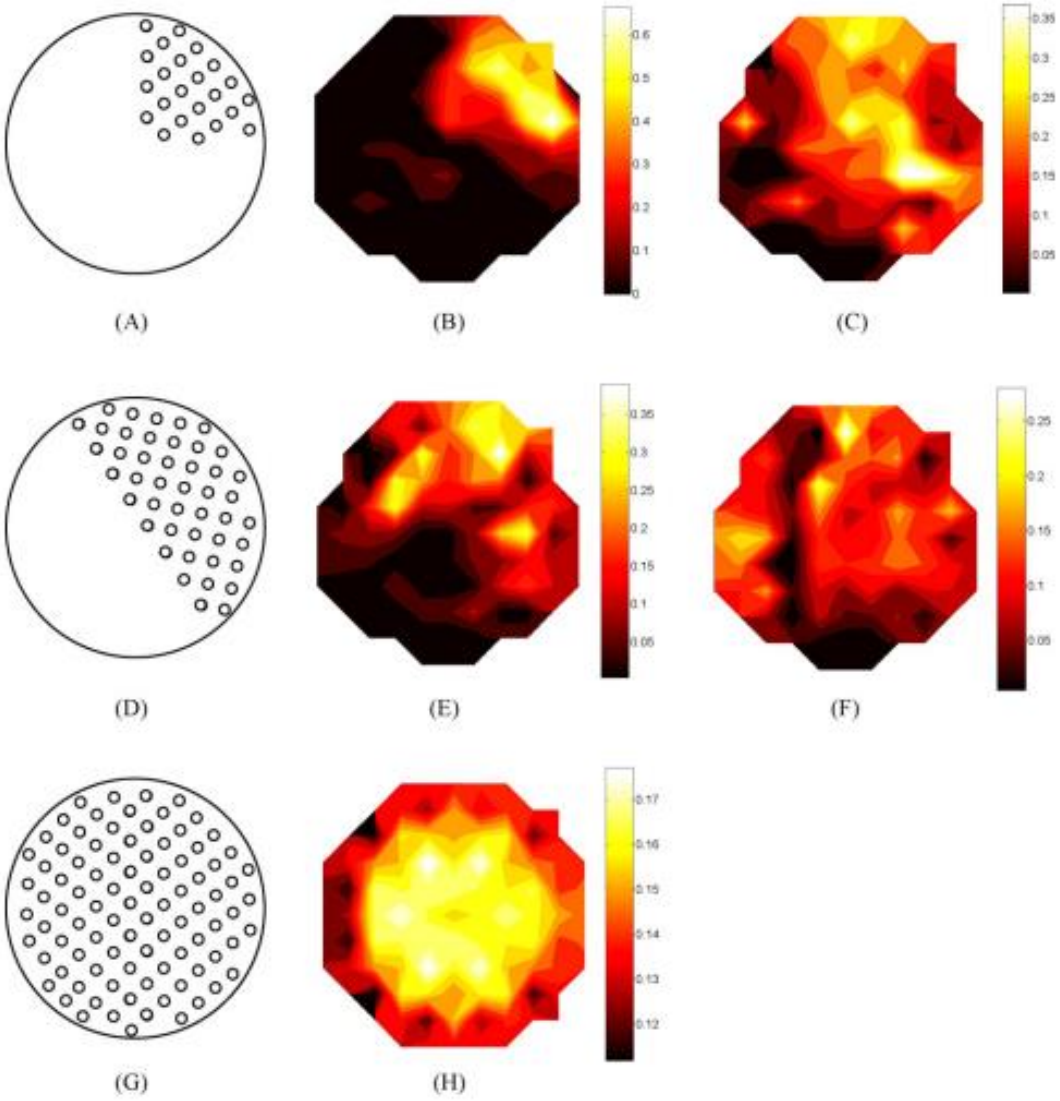

Figure 1- 24 Gas hold-up profile with sparger clogging as a parameter. i) For 75% clogging: (A) distributor plate; (B) at *H*/*D* = 0.785; (C) at *H*/*D* = 2.75. ii) For 0% clogging: (D) distributor plate; (E) at *H*/*D* = 0.785; (F) at *H*/*D* = 2.75. iii) For full open: (G) distributor plate; (H) at *H*/*D* = 0.785; (I) at *H*/*D* = 2.75. (Patel and Throat, 2008)

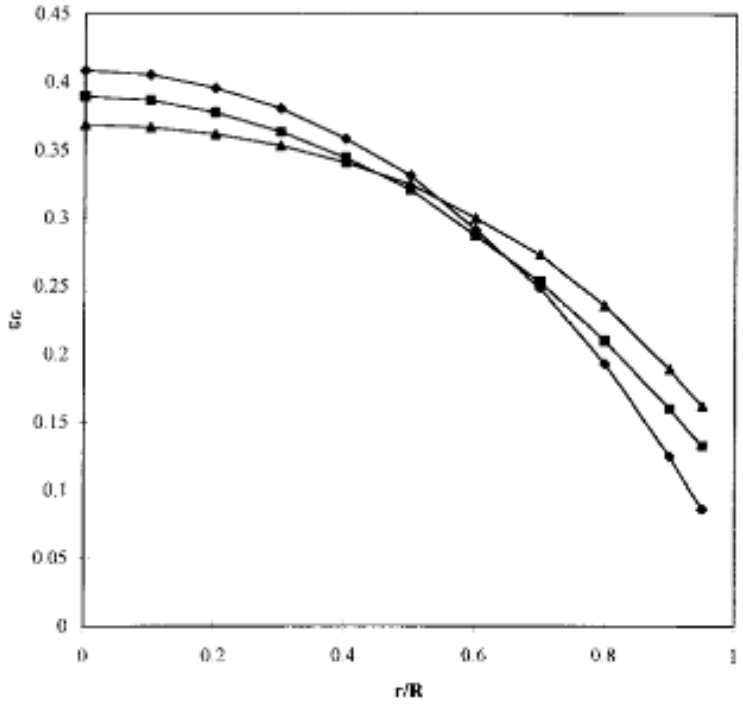

Figure 1- 25 Investigation of the relationship between radial gas holdup profile and different H/D ratio ▲H/D=0.259,■H/D=3,◆H/D=5. (Veera et al., 1999)

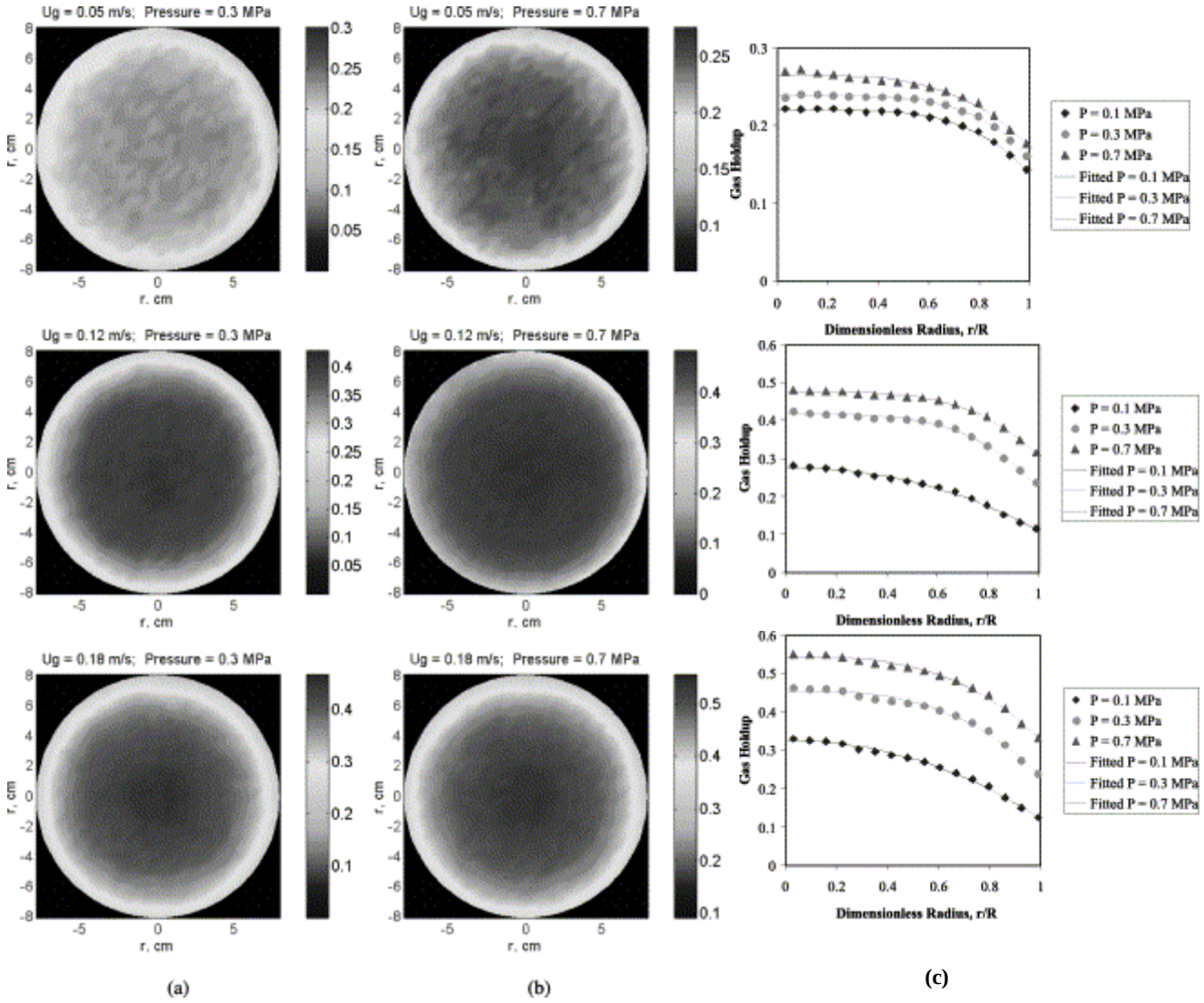

Figure 1- 26 Cross-sectional gas hold-up distribution under different superficial velocities at (a) P=0.3 MPa (b) P=0.7 MPa and (c)radial gas hold-up distribution under different pressure at $\boldsymbol{U_g = 0.05, 0.12}$ and 0.18 m/s from top to bottom. (Ke-moun et al., 2001)

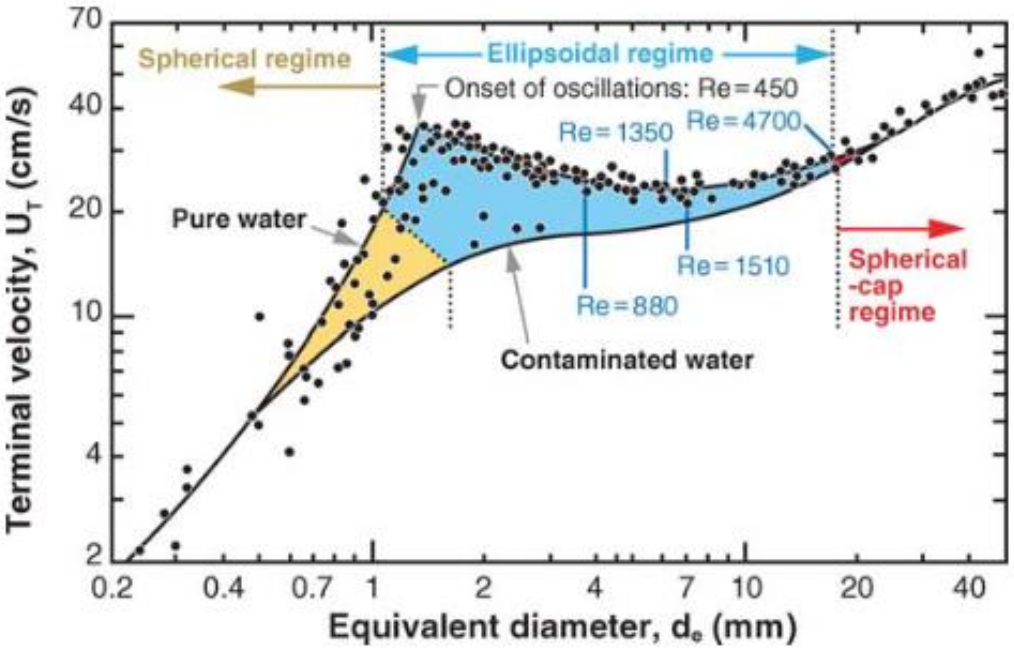

Figure 1- 27 Diagram of the relationship between terminal velocity of single bubble and equivalent diameter (Clift, 1978).

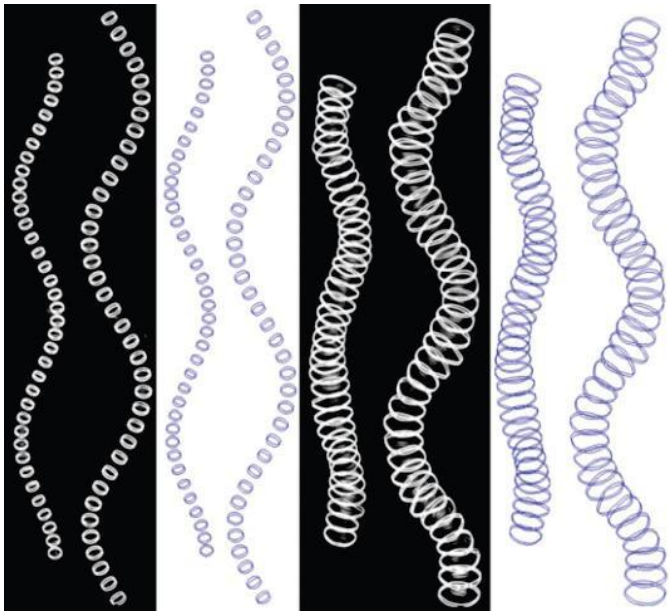

Figure 1- 28 Stereo imaging of bubble rise in stagnant liquid about 700 mm above the injection location for two bubble sizes given with their volume equivalent diameter, two images left) 2.3 mm, two images right) 5.2 mm (taken from Reichardt and Sommerfeld (2008)).

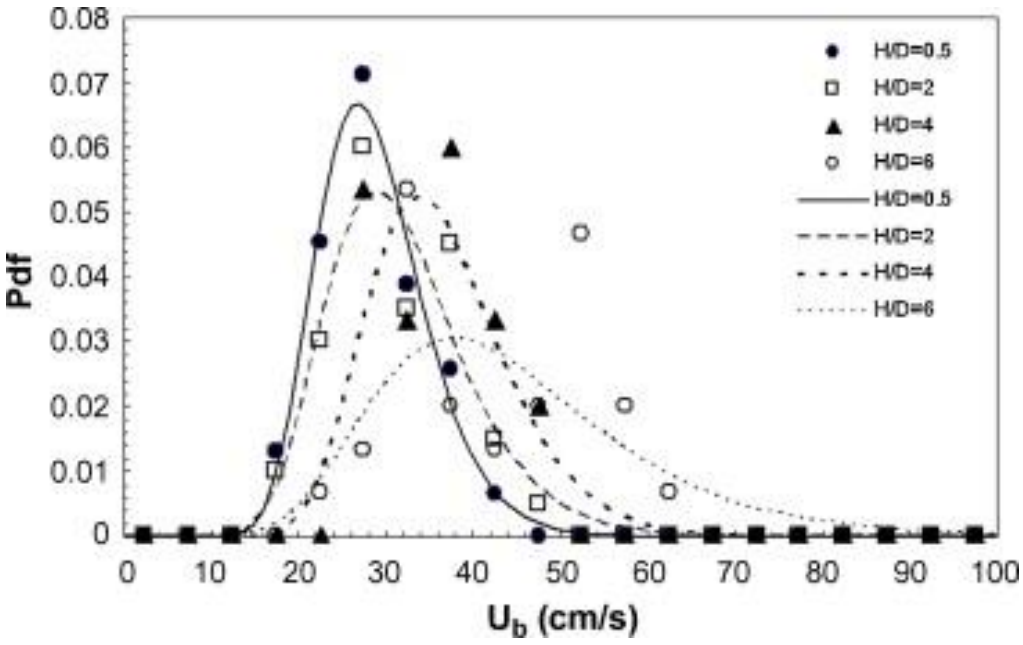

Figure 1- 29 Effect of liquid height on bubble size distribution at different axial heights (Lau et al., 2010).

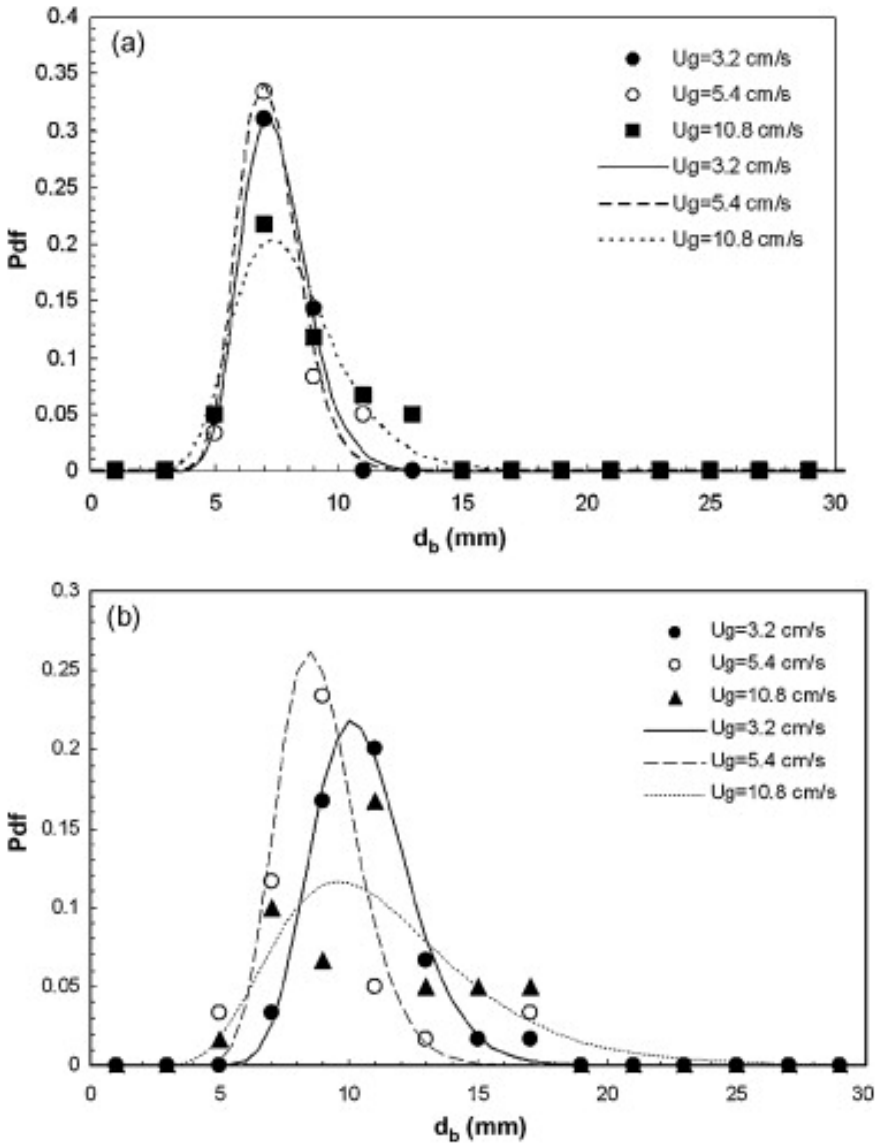

Figure 1- 30 Effect of solid particles on bubble size distribution in shallow bubble column (H/D=4) (a) $\boldsymbol{\alpha_S = 0}$%;(b) $\boldsymbol{\alpha_S = 5}$%. (Lau et al., 2010)

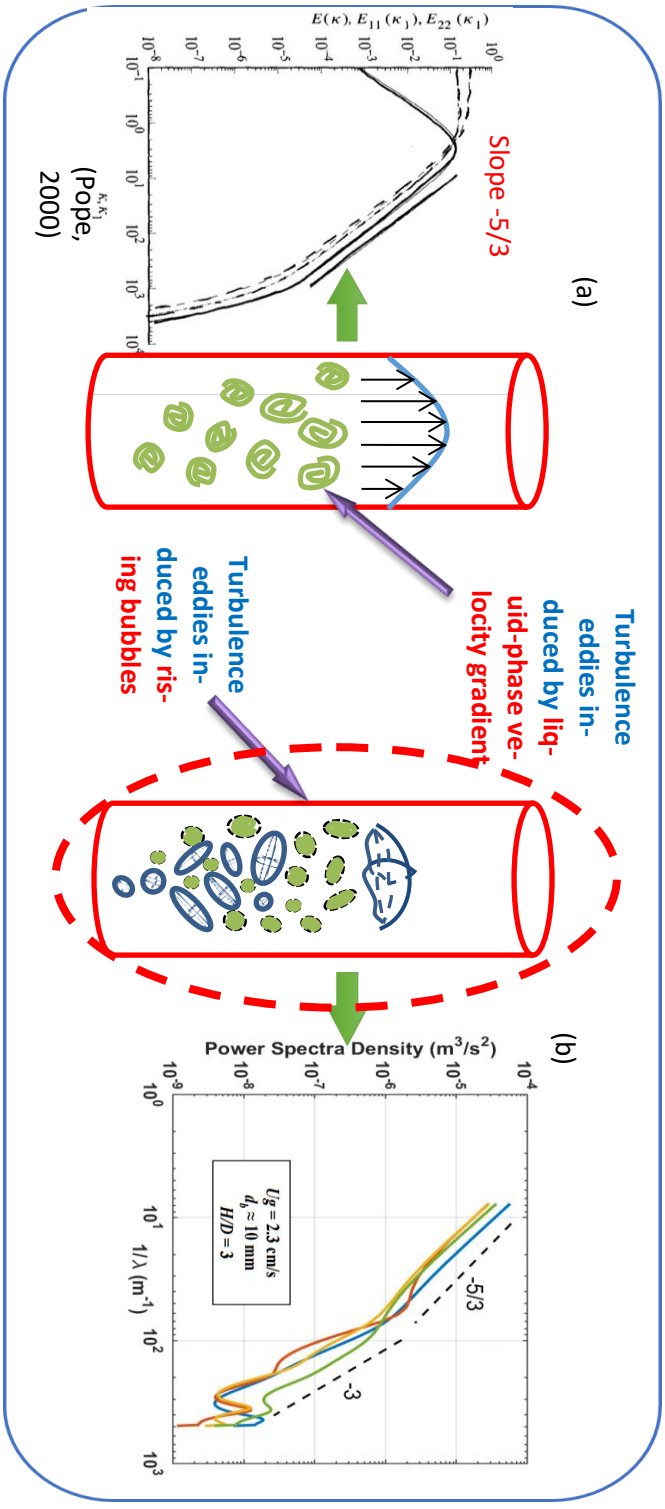

Figure 1- 31 Turbulence Mechanisms in bubble columns: (a) shear turbulence; (b) bubble-induced turbulence

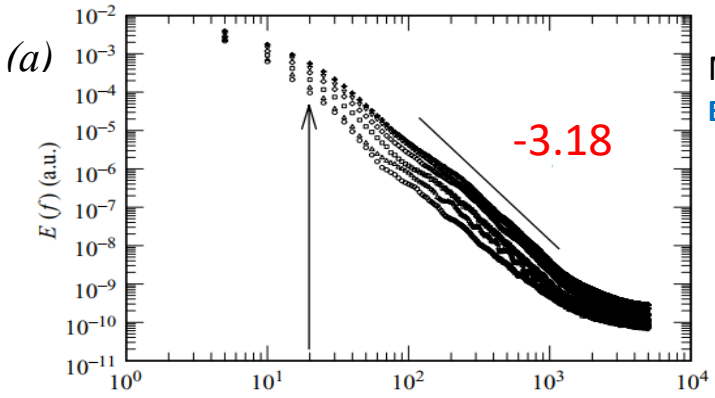

Mercado *et al.* (2010)

Experimental Techniques:

Optical fiber + Hot-film (CTA probe)

+

PTV

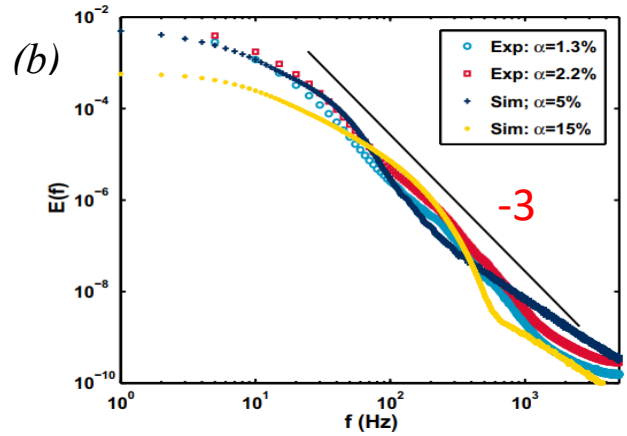

Roghair *et al.* (2011)

Experimental Techniques:

DNS

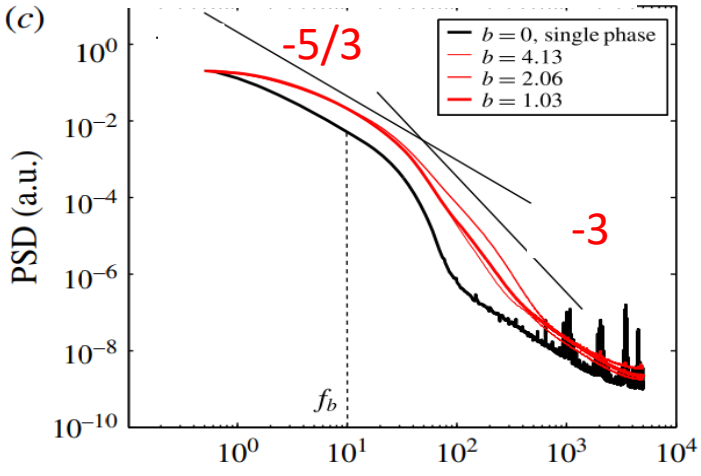

Prakash *et al.* (2016)

Experimental Techniques:

CTA probe

+

LDA

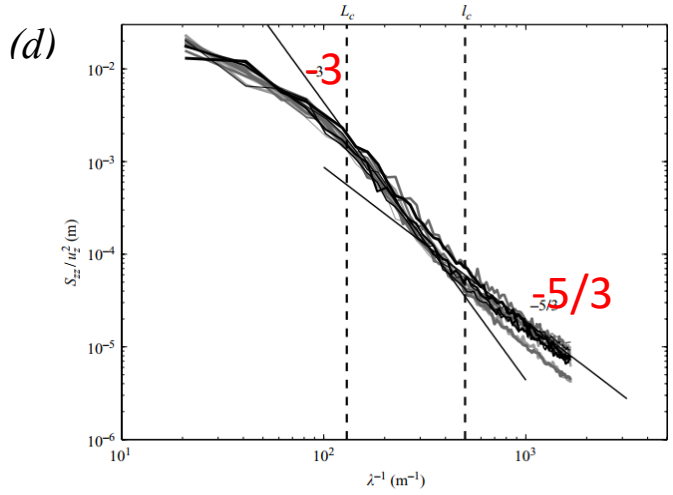

Riboux *et al.* (2010)

Experimental Techniques:

PIV

Figure 1- 32 Experimental findings of κ^{-3} power law scaling for inertia subrange on turbulence energy spectrum.

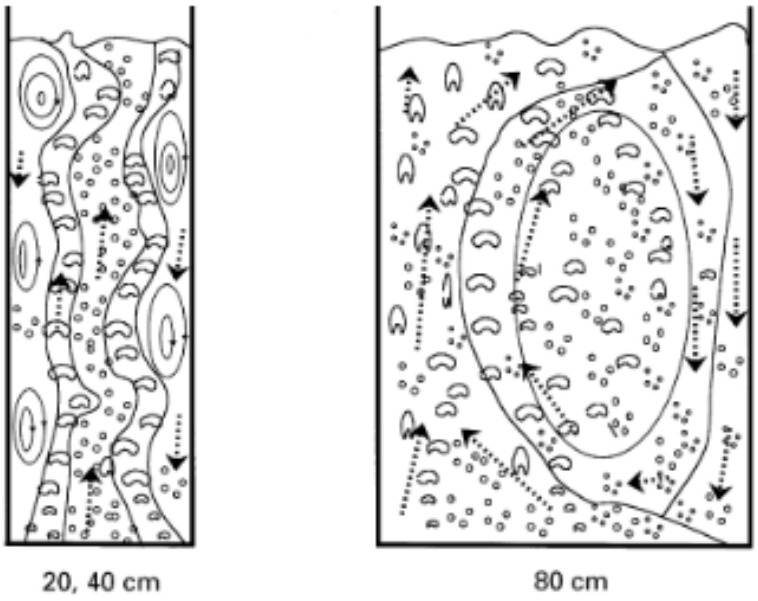

Figure 1- 33 Schematic diagram of flow structures in bubble column with different diameter (Yano et al., 1999).

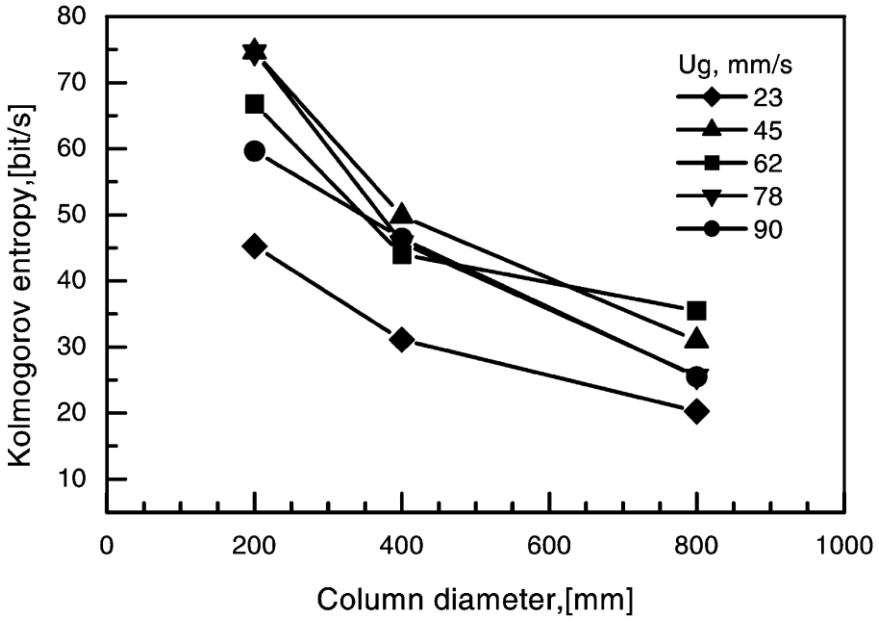

Figure 1- 34 Effect of column diameter on the Kolmogorov entropy (Chen et al., 2001).

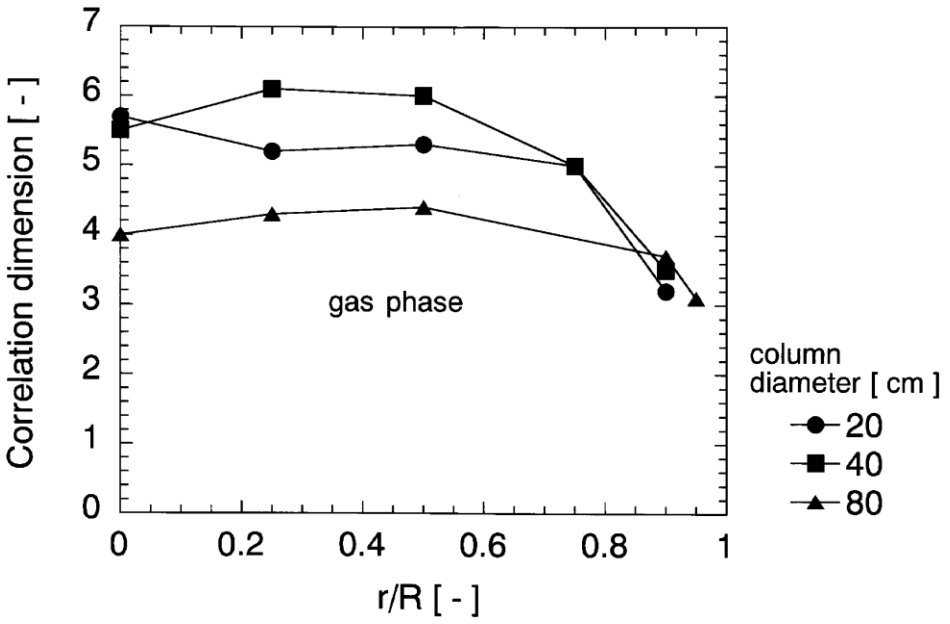

Figure 1- 35 Effect of column diameter on the radial correlation dimension distribution (Yano et al., 1999).

CHAPTER 2: LARGE-EDDY SIMULATION OF GAS-LIQUID TWO-PHASE FLOW IN A BUBBLE COLUMN REACTOR USING A MODIFIED SUB-GRID SCALE MODEL WITH THE CONSIDERATION OF BUBBLE-EDDY INTERACTION

SUMMARY

In Chapter 1, the current status and the methodology adopted for large eddy simulation (LES) of two-phase bubbly flows together with the concerned modelling issues have been reviewed. However, when considering the turbulent eddy viscosity in LES, apart from the well-accepted contributions from shear turbulence and bubble induced turbulence (BIT), the effect of the interaction between entrained bubbles and eddies with a similar turbulence length scale to the sub-grid scale (SGS) cannot be neglected. This chapter will discuss this effect on LES modelling. With the consideration of the bubble response to the eddies on the induced sub-grid stresses, a modified SGS model, which incorporates the Stokes number, St, was proposed. The Eulerian–Eulerian Large-eddy simulations (LES) of gas–liquid two-phase flow in a cylindrical bubble column reactor have been conducted. The results of LES clearly indicate that the use of the modified SGS model can effectively capture the transient bubbly flow in the cylindrical bubble column. The power turbulent kinetic energy spectrum obtained in LES indicates that a slope similar to

Kolmogorov -5/3 scaling law and the -3 scaling law can still be identified for a critical frequency f=10.70 Hz.

1. INTRODUCTION

Large eddy simulation (LES) of bubbly flow in bubble column reactors adopts two approaches, which are Eulerian-Eulerian (E-E) and Eulerian-Lagrangian (E-L). The E-L approach adopts the way that the liquid phase momentum equations are solved under the Eulerian frame while the equations for dispersed phase are solved in a Lagrangian framework. The transportation of bubbles is tracked by integrating the bubble motion equation accounting for the forces acted by the liquid phase on the bubbles. A closure model in the liquid and gas momentum equations must be provided to account for liquid-bubble interactions. The bubble size distribution can be calculated as part of the solution at each time step and models are also required to account for break-up and coalescence of the bubbles. However, this kind of approach is quite computationally intensive, thus, it is still inhibitive for studying two-phase bubbly flows in large-scale bubble column reactors or at high void fraction system. As Eulerian-Eulerian two-fluid modelling describes two-phase mixture motion in a macro sense, the use of this approach may be preferable for industrial applications, especially for the case of a highly dispersed void fraction system such as bubble column reactors. The use of Eulerian-Eulerian two-fluid LES modelling is more desirable because the adoption of low order turbulence models, such as the k-ε and even for the Reynolds Stress Model (RSM), may not well capture the instantaneous eddy turbulence structures which will affect the bubble entrainment,

breakage and coalescence. Deen *et al.* (2001) did pioneering study on LES modelling for gas-liquid flow in a square cross-sectional bubble column. The simulation results were compared with employing the k-ε model. It was concluded that the turbulent viscosity was overestimated by using the k-ε model and only the low frequency unsteady flows could be validated. This is very likely attributable to the transient bubble-eddy interactions being ignored. It has been well accepted that LES can reproduce high frequency experimental data and predict the transient motion of the bubble plume, as experimentally observed. Lakehal *et al.* (2002) pointed out that because Reynolds Averaging Navier-Stokes (RANS) models depend on time averaging, they appear to screen out the local fluctuations related to the turbulence as well as the fluctuations related to the interaction between the bubbles and surrounding eddies. However, these local fluctuations are at least partially remained in LES modelling, instead of time averaging, the spatial filtering is employed. It resolves turbulent eddies with the size larger than computational grid directly, while in sub-grid scale (SGS), the behaviour of eddies as well as the interaction between bubbles and the carrier phase are modelled (Milelli et al., 2001). Furthermore, RANS models are derived by assuming the turbulences are isotropic in different scale, though the bubbly flows are capable of high anisotropy in velocity fluctuations, especially in the direction of gravity (Dhotre et al., 2008). Conversely, LES modelling only assume isotropy for unresolved scales instead of applying it to resolved scales at the same time.

Less studies have been done on the LES modelling of gas-liquid two-phase flow, which is more challenging, than RANS models. Bombardelli *et al.* (2006) conducted simulations of wandering motion in bubble plumes by using both k-ε model and LES. The results show that the wandering effect can be reasonably reproduced by employing Smagorinsky SGS model and bubble-slip model, however, the k-ε model can only capture the wandering effect at the beginning of the simulation. They also compared both modelling results and indicated that time-averaged axial velocities at different heights above the diffuser for the plane located at mid-thickness by LES still have some discrepancies between the modelling and experimental data. The LES Smagorinsky SGS model has been widely used in recent years, and it has been general practice that the turbulence dissipation introduced by the model is proportional to the Smagorinsky constant, C_S. Deen *et al.* (2001) used constant value 0.1 for Smagorinsky constant in the SGS model to simulate the bubbly flow in a bubble column (Smagorinsky, 1963), but the sensitivity of the simulation results regarding to C_S is not investigated. It has been accepted that Smagorinsky's eddy viscosity model $\mathrm{v_T} = (C_s\Delta)^2|\bar{S}|$, where the model constant $\mathrm{C_s}$ can be set to 0.1 is working in the most of single-phase shear flows. However, in subsequent fluid dynamics investigations, researchers have employed this formula directly into two-phase and three-phase flow by changing the model constant from 0.1 to 0.18 empirically, neglecting the multiphase fluid mechanisms behind them. The motivation behind this doing is very likely to consider the change in typical mixing length due to the hybrid effect of the presence of bubbles in the flow. Furthermore, the use

of this type of Bossinesq's viscosity model to describe the turbulence energy dissipation in bubbly flow is inappropriate as the bubble wakes also feed the so-called bubble induced turbulence into the flow. Smith and Milelli (1998) considered the contribution of bubble induced turbulence into the LES work on liquid phase in bubble plumes, and simulated the dispersed phase by using random dispersion model (RDM). The bubbly flow in a bubble column at low Reynolds number was also simulated by using LES accounting for the effect of bubble induced turbulence by Ma *et al.* (2016). A similar LES modelling for a cylindrical bubble column was conducted by Milelli *et al.* (2001) using a relatively coarse cylindrical coordinate grid. They compared both constant and dynamic Smagorinsky SGS model in vertical shear layers laden with bubbles at very low overall gas hold-up, revealing that the dynamic Smagorinsky SGS model proposed by Germano *et al.* (1991) did not have better performance than the constant Smagorinsky model. They also modified the SGS model by taking bubble induced dissipation into account and found that the new SGS model did not remarkably improve the simulation results. It has been revealed by the above researchers that the bubble-induced turbulence model introduced by Sato *et al.* (1975) did not have much influence on the turbulent velocity fluctuations in a rectangular bubble column. However, these studies have indicated that the use of the Smagorinsky SGS model with and without considering BIT overpredicted the averaged axial velocity and gas hold up profile. The kinetic energy in sub-grid scale was obtained in a LES work of bubbly flows conducted by Ničeno *et al.* (2008). They derived the turbulent dispersion force as well as the contribution from bubble induced turbulence yielding the transported SGS kinetic energy. They

also compared it with the simulation result employing dynamic Smagorinsky SGS model, an improvement was found, but there were still discrepancies with the experimental data. Liu and Li (2018) used dynamic Smagorinsky SGS model to simulate the bubbly flow in a bubble column. Different ratios of filter width to bubble diameter were tested to check the mesh independency and the results were compared with the published data. The authors analysed the obtained power spectral density from LES and reported that there exist two zones with slopes of -5/3 and -25/3, respectively. They claimed that the steep falling off of the slope in the power energy spectrum is due to the BIT as the result of injection of bubbles. Thus, it can be expected that a LES SGS model considering the contribution from BIT in bubbly flow may lead to the simulation results becoming better consistent with the experimental data but depending on how to appropriately consider the BIT. It should be pointed out that the turbulent viscosity model accounting for the BIT in two-phase flow as proposed by Sato and Sekoguchi (1975) was derived by assuming the flow about a fixed bubble as the flow about a cylinder. In reality, the bubbles will response to the turbulent eddies that entrain the bubbles. This response should exist at the sub-grid scale where the bubbles may not follow the turbulent eddy motion faithfully. When assessing this type of bubbles' dynamic response to eddies, one can consider the slip velocity between the bubbles and eddies to be influenced by the response of the bubbles to eddies. The bubbles appear to escape from the turbulent eddies where they are entrapped because of the buoyancy effect. Therefore, the instantaneous fluctuation of bubbles would always differ from it of the surrounding turbulent eddies in sub-grid scales, especially for the eddies having the

similar size with the bubble diameter (Kruis and Kusters, 1997). Secondly, in bubbly flow, the interfacial forces acting on the bubbles are strongly influenced by the interactions between the bubbles and the near eddies, and these forces have to be properly implemented in LES SGS modelling. In addition, the bubbles that rise in the bubble column will encounter those turbulent eddies generated by the shear turbulence and the preceding bubble wakes in their paths. The relative size difference between bubbles and eddies lead to different relaxation times. Therefore, the instantaneous filtered velocity of a bubble is strongly correlated to the turbulent eddy fluctuation velocity.

It should be mentioned here that bubble size distribution has a pivotal role in predicting gas-liquid interfacial area, which will further influence the prediction of the mass and heat transfer between phases. To obtain the bubble size distribution when using the E-E approach, additional equations accounting for bubble breakup and coalescence, together with bubble growth or shrinkage because of mass transfer are required. Studies on the bubble size distribution in various bubbly flows can be found in the literature. Different models derived from population balance equation were developed, such as the multiple size group model (MUSIG) (Lo, 1996), the interfacial area transport models (Wu et al., 1998; Ishii et al., 2002; Fu and Ishii, 2003; Yao and Morel, 2004; Ishii et al., 2005). When using the E-E modelling approach for practical applications (Liao et al., 2018), the dispersed bubbles are treated as a quasi-continuum with each computational grid in whole domain con-

taining corresponding fractions of the carrier and dispersed phases. Separate momentum and continuity equations are solved together on the same grid for each phase. For LES, by applying the filtering at a filter scale (Δ), the filter scale should fall into the inertial sub-range region in turbulent kinetic energy spectrum as a key criteria for a successful E-E LES as indicated by Niceno *et al.* (2008), and thereby the scale of motion greater than Δ can be resolved. However, it is noticeable that the bubble-induced large scale turbulent eddies with the size larger than Δ cannot be resolved properly in LES, due to the missing information of interphase details above filter scale. In addition, bubble-induced turbulence not only affects the carrier phase liquid flow for the length scale smaller than bubbles but also has the impact on the large scale flow as reflected in the predicted turbulent kinetic energy spectrum obtained from the LES modelling. This may deteriorate the accuracy of predicting the resolved scale motion of the large eddies in LES. Thus the grid requirements may sometimes be in confliction when modelling with the E-E LES. Milelli (2002) has proposed the requirement of gird size in the E-E LES and carried out a parametric investigation on different mesh resolutions and bubble diameters. It was suggested that $1.2 < \Delta/d_B < 1.5$ ($0.67 < d_B/\Delta < 0.83$) would be an optimum filter width. The comparative study was conducted by Dhotre et al. (2013) for Δ/d_B = 1.2 and 2.5, and they found that good agreement with the experimental data can be still obtained for both grids. Niceno et al. (2008) has trialed a grid refinement study on Δ/d_B =1.25 and 2.5 but demonstrated similar quantitative vertical gas and liquid velocity to be shown by applying both grids. Liu and Li (2018) also employed the E-E LES model with 5 different Δ/d_B in their study on bubble column bubbly

flows and have revealed that the adoption of the ratio of grid to bubble size Δ/d_B =1.25 and 1.5 can yield the results agreed with the experimental results. Generally speaking, the application of Δ/d_B >1.0 for the E-E LES modelling is required based on the previous studies mentioned above. It should be noted that the E-E LES modelling of bubbly flows accounting for the bubble size distribution coupled with ~~for~~ bubble coalescence and breakage is still rarely reported, to the best knowledge of the authors.

This work aims to implement a modified Smagorinksy SGS model which accounts for the bubble response to the surrounding turbulent eddies through introducing a Stokes number into the LES simulation of a cylindrical bubble column. The mathematical modelling and numerical methods are presented in Section 2. The simulation results and related discussion will be then followed in Section 3, focusing on the effect of bubble response to the turbulent eddies in SGS scale and the BIT influence on the simulated turbulent kinetic energy power spectrum together with the correlations between the turbulent eddy structures and bubble distribution in the bubble column. Finally, this chapter will end with a conclusive summary of key findings.

2. MATHEMATICAL MODELLING AND NUMERICAL METHODS

2.1 Governing equation

The LES model is obtained by spatially filtering the equations of momentum. The current study employs a Eulerian-Eulerian two-fluid model with each phase being described by separate equations. For phase *k*, the filtered equations of mass and momentum can be expressed by Equations (2-1) and (2-2),

$$\frac{\partial}{\partial t}(\rho_k \alpha_k) + \nabla \cdot (\alpha_k \rho_k \boldsymbol{u}_k) = 0 \tag{2-1}$$

$$\frac{\partial}{\partial t}(\alpha_k \rho_k \boldsymbol{u}_k) + \nabla \cdot (\alpha_k \rho_k \boldsymbol{u}_k \boldsymbol{u}_k) = -\nabla \cdot (\alpha_k \tau_k) - \alpha_k \nabla p + \alpha_k \rho_k \boldsymbol{g} + \boldsymbol{M}_{F,k} \tag{2-2}$$

where $k = G$ and $k = L$ represents for gas and liquid respectively. The terms on the right-hand side of Equation (2-2) stand for the contributions due to the stress, the pressure gradient, gravity and momentum exchange between each phase that arise from the actions from interfacial forces individually. The stress term can be defined by Equation (2-3),

$$\tau_k = -\mu_{eff}\left(\nabla \boldsymbol{u}_k + (\nabla \mathbf{u}_\mathrm{k})^T - \frac{2}{3} I (\nabla \cdot \boldsymbol{u}_k)\right) \tag{2-3}$$

where μ_{eff} represents the effective viscosity for the continuous phase, which may be assumed to be consisted of the following terms: the molecular viscosity μ_L, the turbulent viscosity μ_T and an additional term to describe bubble induced turbulence μ_{BI} (Dhotre et al., 2008). This is defined in Equation (2-4).

$$\mu_{eff} = \mu_{L,L} + \mu_{T,L} + \mu_{BI,L}. \tag{2-4}$$

The bubble induced turbulence can be modelled based on Sato's model (Sato et al., 1981), which is given by Equation (2-5).

$$\mu_{BI,L} = \rho_L C_{\mu,BI} \alpha_G d_B |\boldsymbol{u}_G - \boldsymbol{u}_L|. \tag{2-5}$$

2.2 Interphase forces

The momentum exchange term that introduces the interface forces is defined by Equation (2-6),

$$\boldsymbol{M}_{F,L} = -\boldsymbol{M}_{F,G} = \boldsymbol{M}_{D,L} + \boldsymbol{M}_{L,L} + \boldsymbol{M}_{TD,L} + \boldsymbol{M}_{AM,L} \tag{2-6}$$

where the terms including, from left to right, the interface drag force, lift force, turbulence dispersion force and virtual mass force, respectively.

Drag force

The interphase momentum transfer between continuous and dispersed phases because of the drag force contributed from both viscous shear (skin drag) and the pressure gradient (form drag) is expressed by Equation (2-7),

$$\boldsymbol{M}_{D,L} = \frac{3}{4}\alpha_G \rho_L \frac{C_D}{d_B}|\boldsymbol{u}_G - \boldsymbol{u}_L|(\boldsymbol{u}_G - \boldsymbol{u}_L) \tag{2-7}$$

where the drag coefficient, C_D, can be expressed by using Equation (2-8) with regard to distorted bubbles (Ishii and Zuber, 1979),

$$C_D = \frac{2}{3}E_O^{\frac{1}{2}} \tag{2-8}$$

where the Eötvos number $E_0 = \frac{g\Delta\rho d_B^2}{\sigma}$ stands for the ratio of the buoyancy to the surface tension forces.

Lift force

Due to the radial velocity gradient in the bubble column, the lift force acts on the rising bubbles perpendicularly to the relative motion of gas and liquid phases. The correlation between slip velocity and the curl of liquid velocity is associated with the lateral lift force (Zun, 1980; Auton, 1987), which is given by

$$\boldsymbol{M}_{L,L} = \rho_L C_L(\boldsymbol{u}_B - \boldsymbol{u}_L) \times (\nabla \times \boldsymbol{u}_L) \tag{2-9}$$

where C_L is the lift force coefficient and is based on the estimation according to Tomiyama *et al.* (2002) by

$$C_L = \begin{cases} min[0.288tanh(0.121Re_B), f(E_O')\,] & E_O' \le 4 \\ f(E_O') & 4 < E_O' < 10 \\ -0.29 & E_O' > 10 \end{cases} \quad (2\text{-}10)$$

where Re_B is the bubble Reynolds number and $E_O' = \frac{g(\rho_l - \rho_g)d_h^2}{\sigma}, d_h = d(1 + 0.163E_O'^{0.757})^{1/3}$.

Added mass force

The relative acceleration of the bubble and surrounding liquid is considered by the added mass force (Jakobsen et al., 1997), which can be estimated by

$$\boldsymbol{M}_{AM,L} = \alpha_G \rho_L C_{AM} \left(\frac{D\boldsymbol{u_G}}{Dt} - \frac{D\boldsymbol{u_L}}{Dt}\right) \quad (2\text{-}11)$$

where C_{AM} stands for the virtual mass coefficient and a constant 0.5 is used through this paper.

Turbulent dispersion force

Considering the effect of the random fluctuations of turbulent eddies, the turbulent dispersion force is considered in the current simulation. The formulation proposed by Burns *et al.* (2004) to estimate the force is adopted, given by

$$\boldsymbol{M}_{TD,L} = C_{TD}\frac{3\alpha_G}{4}\frac{\rho_L}{d_B}(\boldsymbol{u_L} - \boldsymbol{u_G})\frac{\nu_t}{\sigma_{TD}}\left(\frac{\nabla\alpha_L}{\alpha_L} - \frac{\nabla\alpha_G}{\alpha_G}\right) \quad (2\text{-}12)$$

where C_{TD} is the turbulent dispersion coefficient and is assumed to constant 1 in this work, ν_t is the turbulent kinematic viscosity and σ_{TD} represents the turbulent Schmidt number, σ_{TD}= 0.9 is adopted here.

2.3 Eddy viscosity model

In LES, the velocity in Equations (2-1) and (2-2) are described by Equation (2-13),

$$\boldsymbol{u}_k = \widetilde{\boldsymbol{u}}_k - \boldsymbol{u}'_k \quad (2\text{-}13)$$

where $\boldsymbol{u}_k$ is the velocity that needs to be resolved in filtering, while $\widetilde{\boldsymbol{u}}_k$ represents the instantaneous velocity and $\boldsymbol{u}'_k$ stands for the unresolved part that requires the closure from the use of the SGS model in the LES simulations. It needs to be noted that the equations of mass and momentum are derived by time-averaging in RANS models. In LES modelling, these equations are solved by spatial filtering, hence, $\widetilde{\boldsymbol{u}}_k$ and $\boldsymbol{u}'_k$ are referred to grid scale and sub-grid scale velocity, respectively.

Following Garcia's work (Garcia, 2001) but considering the contribution from the added mass on bubble translation, the relative velocity between the carrier fluid and the bubble can be obtained from Equation (2-14),

$$\boldsymbol{u_\lambda} \sim \frac{(\varepsilon\lambda)^{\frac{1}{3}}}{\left(1+\frac{1}{2(\rho_B+C_{AM}\rho_L)V}C_D\rho_L S\lambda\right)^{\frac{1}{2}}} \quad (2\text{-}14)$$

where λ represents the different turbulent length scales in the range between the integral and Kolmogorov scales ($L>\lambda>\eta$) and C_{AM} is the added mass coefficient. When the derivative of u_λ equals zero at a certainλ, u_λ will have a maximum, as defined by Equation (2-15).

$$\lambda^* \sim \frac{4(\rho_B + C_{AM}\rho_L)V}{C_D \rho_L S} \tag{2-15}$$

Substituting λ^*into Equation (2-14) yields

$$\boldsymbol{u}_{\boldsymbol{\lambda}}^* \sim (\varepsilon d)^{\frac{1}{3}} \left(\frac{1}{C_D}\right)^{\frac{1}{3}} \left(\frac{\rho_B + C_{AM}\rho_L}{\rho_L}\right)^{\frac{1}{3}} \tag{2-16}$$

In this turbulent length scale range, $(d\varepsilon)^{1/3}$ can be regarded as the fluctuating velocity of the bubble. Thus, $\boldsymbol{u}_{\boldsymbol{\lambda}}^*$ can be expressed as,

$$\boldsymbol{u}_{\boldsymbol{\lambda}}^* \sim \boldsymbol{u}_G' \left(\frac{1}{C_D}\right)^{\frac{1}{3}} \left(\frac{\rho_B + C_{AM}\rho_L}{\rho_L}\right)^{\frac{1}{3}} \tag{2-17}$$

The size of the bubbles and their surrounding turbulence eddies are different, hence, bubbles will not response immediately to the flow motion of the eddies. Taking their slip velocity into account, the bubbles appear to get rid of the controlling from

the eddies where they are entrapped (Bhole et al., 2008). As demonstrated in Equation (2-18), the instantaneous fluctuation of bubbles would always smaller from the surrounding turbulent eddies' fluctuation in sub-grid scales, especially for the eddies having the similar size with the bubble diameter. Considering the modified bubble equation of motion with the Stokes number and the interaction between bubbles and eddies, the Smagorinksy model of sub-grid eddy viscosity can be modified for the case where the drag force can be regarded as the dominant acting force. According to Kruis and Kusters (1997), the correlation between the fluctuating velocity of bubble and liquid in terms of the turbulent eddies with length scales in the inertia subrange can be expressed by Equation (2-18).

$$\frac{\boldsymbol{u}_G^{'2}}{\boldsymbol{u}_L^{'2}} = \frac{1}{1+St} \tag{2-18}$$

When Equation (2-18) is implemented into the sub-grid scale, the relationship can be defined as $\frac{\boldsymbol{u}_G'^2}{\boldsymbol{u}_{L,SGS}'^2} = \frac{1}{1+St_{SGS}}$, where St_{SGS} is the non-dimensional Stokes number given by $\mathrm{St} = \frac{\tau_{\mathrm{bubble}}}{\tau_{L,SGS}}$. Here, the bubble response time scale is proposed by Sommerfeld *et al.* (2018), $\tau_{\mathrm{bubble}} = \frac{4(\rho_G+0.5\rho_L)d_B^2}{3\mu_L C_D Re_B}$. Bubble Reynolds number $Re_{B,max} = \frac{\rho_L d_B u_{slip}}{\mu_L} \approx 1121$ in this chapter. In terms of liquid response time in SGS, $\tau_{L,SGS} = \Delta/\boldsymbol{u}'_{\mathrm{L,SGS}}$, where $\Delta = \left(\Delta_i\Delta_j\Delta_k\right)^{1/3}$ is the filter width and $\mathrm{u_{L,SGS}}$ stands for the liquid velocity in local grid.

As $u_L'^2 \sim (\lambda\varepsilon)^{2/3}$, one can obtain Equation (2-19) which is given by

$$\boldsymbol{u}_{\boldsymbol{\lambda}}^{*}\sim\left(\frac{1}{1+St_{SGS}}\right)^{\frac{1}{2}}(\lambda\varepsilon)^{\frac{1}{3}}\left(\frac{1}{C_D}\right)^{\frac{1}{3}}\left(\frac{\rho_B+C_{AM}\rho_L}{\rho_L}\right)^{\frac{1}{3}} \tag{2-19}$$

The turbulence dissipation due to the bubbles corresponds to the inertial subrange can be assumed that mainly occurs when λ approach to λ^*, and the dissipation can be estimated by Equation (2-20).

$$-\tau_{ij}\overline{S_{ij}}|_G\sim\rho_L C_D\left(\frac{\rho_L}{\rho_B}\right)\frac{\boldsymbol{u}_{\boldsymbol{\lambda}}^{\boldsymbol{3}}}{d_B}\overline{\alpha_G}=\mathrm{C_b}\rho_L\varepsilon\overline{\alpha_G}\frac{\lambda}{d_B}\left(\frac{1}{1+St_{SGS}}\right)^{\frac{3}{2}} \tag{2-20}$$

Different values of the constants C_b have been trialled, but a value of 0.7 is employed which demonstrates good agreement with Camarasa's results. $\overline{\alpha_G}$ stands for the local gas hold-up after filtering. The total dissipation is given by Equation (2-21).

$$-\tau_{ij}S_{ij}\sim\rho_L\varepsilon(1+\mathrm{C_b}\overline{\alpha_G}\frac{\lambda}{d_B}\left(\frac{1}{1+St_{SGS}}\right)^{\frac{3}{2}}) \tag{2-21}$$

Employing the eddy viscosity model, the liquid-phase turbulence modified SGS viscosity can be modified as represented by Equation (2-22),

$$\mu_{T,L}\;=\;\rho_L\,(\,C_s\,\Delta)^2\,|\,S\,|\left[\,1\;+\;C_b\,\overline{\alpha}_G\;\frac{\Delta}{d_B}\left(\frac{1}{1\,+\,St_{SGS}}\right)^{3/2}\right] \tag{2-22}$$

where *Cs* is the Smagorinsky constant and *S* represents the characteristic resolved strain rate tensor. λ has been assumed as the filter length scale Δ in the range of the inertia subrange.

2.4 Numerical Modelling

In order to demonstrate the reliability of the proposed modified LES SGS model, the simulation of bubbly flow in the bubble column reactor, based on the work of Camarasa *et al*. (1999) and Kulkarni *et al*. (2001), have been carried out. The experimental settings are summarized in Table 2-1. Based on Camarasa's experimental work, a distributor containing 62 holes that are 1 mm in diameter was evenly placed at the bottom of the bubble column. Based on Kulkarni's work, air was sparged through a $20\mu m$ perforated plate using an oil-free diaphragm compressor.

Table 2- 1 Details of experimental set-up.

Experiment	Diameter (m)	Height (m)	Superficial Gas Velocity (m/s)	Static Liquid Height (m)	Observation Height (m)
Camarasa *et al.* [34]	0.1	2	0.0372	0.9	0.6
Kulkarni *et al.* [35]	0.15	1.5	0.0382	0.65	0.3

The solver of ANSYS CFX 18.0 was employed in the LES simulation. The physical

properties for two phases are: $\rho_g = 1.185 \frac{kg}{m^3}$, $\mu_g = 1.83e-5 \frac{kg}{m\,s}$, $\rho_L = 997\ \frac{kg}{m^3}$, $\mu_L = 8.89e-4 \frac{kg}{m\,s}$. At inlet, a mass flow rate condition normal to inlet was used. In the current work, the inlet mass flow rate is given by $\dot{m} = \rho_g A_D v_g$, and the volume fraction for liquid and gas phases are specified as $\alpha_L = 0$ and $\alpha_G = 1$. The bubble diameter of 4 mm is adopted in this work, which is the typical value of gas-liquid bubble columns under the same pressure, superficial velocities and air-inlet distributor conditions (Camarasa et al., 1999; Kulkarni et al., 2001).

At the top surface of the bubble column, a pressure-constant boundary (relative pressure of 0) is applied. No slip condition is employed for the wall. It should be noted that the bubble size will increase along the height of bubble columns and this change in bubble size is usually very small, thus leading to the negligence of such change in the numerical simulation, certainly in the currently available reported studies using Eulerian-Eulerian LES (Deen et al., 2001; Milelli et al., 2002; Dhotre et al., 2008; Ničeno et al., 2008; Liu and Li, 2018; Mohammadi et al., 2019). According to Zhao's *et al.* (2016) study on evolution of bubble size distribution from gas blowout in shallow water, the compressibility factor can be used for characterisation of bubble size changes with liquid depth. By approximating of the cases of bubble column bubbly flows, the variation of the compressibility factor *z* for bubble size along a stationary liquid level height of 0.9m in the bubble column is very marginal. Also, the bubble rise-up in a stationary water tank is considered as an example. Assuming that the water level height is 0.9 m and the ambient pressure to be 1 bar, one can roughly use the equation of status to estimate the bubble diameter for the bubble to just reach the surface of the water if a bubble is released from the

bottom of the tank with an initial diameter of 4 mm, which only yields 4.11 mm. It can be seen clearly that the percentage of the diameter increment for the bubble released from the sparger of the bubble column is approximately 3%. Accordingly, the bubble size change with the local pressure along the bubble column height can be disregarded if no bubble breakup or coalescence takes place and bubbly flow is dilute.

A central differencing scheme is implemented for the discretisation of the advection term, while a second-order backward Euler scheme is used for the time discretisation in the simulations. Employing a Eulerian-Eulerian approach and the LES model, the bubble column was discretised with uniform $\Delta x^+ = 100$ and $\Delta r^+ = 5$ with a growth rate of 1.5 in the region near the wall. Three grids were used in the central region of the bubble column in the current work: $d_B/\Delta = 0.57, 0.75, 0.9$ with globally 1,778,700 mesh elements in the finest grid and 5,344,600 in the coarsest one. The corresponding grid resolution study regarding the modified SGS model is presented in next section.

3. RESULTS AND DISCUSSION

The gas-liquid flow in the bubble columns have been simulated using a constant time step size of 0.001 s for resolving the temporal variations of the flow field. Since the bubbly flow in the bubble column is transient, the simulation was run for 100 s and the data was collected over the last 50 s until the turbulent flow field becomes statistically stationary. The results and findings based on the simulations are discussed as follows.

3.1 Grid independency study

In this section, the results obtained on various d_B/Δ values from 0.57 to 0.9 were compared with the published experimental data by Camarasa *et al*. (1999). Figure 2-2 (a) and (b) shows the comparisons of time-averaged gas velocity and gas hold-up at H/D=6. The velocity and gas hold-up were calculated by collecting the instantaneous velocity at different positions along the radius of bubble column between 50 s and 100 s using the ensemble averaging (equivalent to time averaging) method. The time-averaged velocities are obtained by using the following relation:

$$\bar{u}_B(r) = \frac{1}{N\Delta t}\sum_{i=1}^{N} \boldsymbol{u_{Bi}}(r,t)\Delta t \tag{2-23}$$

where $\bar{u}_B$ is the average bubble velocity, *N* is the sampling number for collection of the instantaneous bubble velocity at the given radial position and Δt is the time step for the simulation.

It can be seen from the figure that the LES results using three grids generally follow up the trend of the experimental axial gas velocity. One can observe that there is not significant difference in the predicted axial velocity profiles for the grids of $d_B/\Delta = 0.75$ and slightly refined mesh d_B/Δ =0.9. The results of both the two grids are in good agreement with the experimental data compared with the result obtained by using the coarse mesh d_B/Δ=0.57. In Figure 2-2(b), the time-averaged gas hold-up is obtained by using the following expression:

$$\alpha_{Gcross}(H) = \frac{1}{\pi R^2}\int_0^R \left(\frac{1}{T_1 - T_0}\int_{T_0}^{T_1} \alpha_G(r, H, t)dt\right) 2\pi r dr \qquad (2\text{-}24)$$

where T_0 and T_1 are the beginning and end time for sampling. As can be seen the figure that the predicted gas-holdup profiles using all three different grids have higher values in the range of large r/R but there is only tiny difference in the predicted gas holdup profiles using the meshes of d_B/Δ=0.75 and 0.9. Further detailed discussion and comparisons on the simulations using the standard Smagorinsky SGS and the proposed modified SGS model will be presented in Section 3.2. It can be seen from the comparisons that compared with the results obtained using the coarse mesh d_B/Δ=0.57, the simulations using d_B/Δ=0.75 and 0.9 do give better prediction on the axial gas velocity and air void fraction, consistent with the experimental ones. With caution, $d_B/\Delta = 0.75$ has been adopted in the present E-E LES modelling (around 1,200,000 mesh elements in total were adopted, especially in the center region of the bubble column. It should be noted here that this grid resolution is consistent with the condition used in Milelli's work (2002) and it is expected that the turbulence with the scale being larger than the bubble diameter can be well resolved.

3.2 Predicted flow patterns, gas holdup and velocity distributions

Chen *et al*. (1994) have indicated that the bubbly flow in bubble columns consists of four flow regions including descending flow region, vortical-spiral flow region, fast bubble region and the central plume region. It is shown in Figure 2-3 that the

LES simulation implemented the modified SGS model has well captured the features of vortical-spiral upward bubbly flow in the bubble column. As illustrated in Figure 2-3, the flow patterns for the flow time of 3.78, 50.0, 75.0 and 90.0 s, displayed with instantaneous velocity vectors based on instantaneous gas hold-up, clearly exhibits bubbles spirally rising-up. The descending flow can be observed to take place near the wall in the form of the downward velocity vectors pointing downwards, while the higher gas hold-up at the central region of the bubble column indicates that the bubbles are clustered and entrained by large eddies that rise up in the centre of the bubble column. At t = 3.78s, the vortical-spiral flow is not yet fully established while at t = 50.0, 75.0 and 90.0 s, it can be found from Figure 2-3 that a large amount of large vortices are oscillating throughout the bubble column, accompanied by the numbers and distributions of large eddies that fluctuate with time and position.

In Figure 2-4, the averaged bubble and liquid velocity profiles at H/D = 6 obtained by applying both the modified SGS and standard Smagorinsky SGS models are presented. By applying the same method as evaluated using Equation (2-23), a quantitative comparison is made with the published experimental data obtained by Camarasa *et al.* (1999). It can be shown from Figure 2-4 that the averaged bubble axial velocities obtained from the LES with the modified SGS model are in good agreement with the experimental results, remarkably improved in comparison to the use of standard SGS Smagorinsky model. However, such consistency becomes

poor close to the column wall. A likely reason is that the interaction between bubbles and turbulent eddies may be not well reflected in the modified SGS model as the bubble size is greater than the grid size. In terms of the grid set-up employed in the present simulation, Milelli's condition is only held in the central part of the bubble column, while d_B/Δ close to the wall region is much larger than 0.75 (Mielli, 2002). This causes a relatively poor performance of the modified SGS model in the estimation of the eddy viscosity in the region near the wall. However, as LES imposes the requirement of $5 < r^+ < 10$, the use of Milelli's condition will violate this constraint. This remains for further investigation.

Figure 2-5 shows the cross-sectional averaged gas hold-up variation along the bubble column height after time-averaging, which can be obtained by using Equation (24). As can be seen from Figure 2-5 that the averaged gas hold-up is decreasing with the increasing of the axial height for the region where the bubble rise-up is close to the gas distributor at the inlet. The released bubbles from the distributor have not achieved the sub-steady spiral rise-up status. The bubbles are strongly affected by the recirculation large vortices near the inlet, which result in a significant fluctuation in the simulated bubble volume fraction. After the flow reaches a certain height, the bubble entrainment becomes relatively steady, yielding a result of the bubble volume fraction being almost unchanged along the height. It appears that the bubbly flow in the bubble column for present study condition can be divided into two regions where the characteristics of bubble volume fraction can either

change significantly or less significantly. The two regions are separated at approximately H/D = 2.5.

The time-averaged gas holdup distribution at H/D = 6 in the radial direction is presented in Figure 2-6. It can be obtained that the simulation is quantitatively consistent with the experimental data as reported in Camarasa's *et al.* work (1999). It should be noted, however, that the profile of the averaged gas hold-up by LES is over-predicted for the location between the column wall and core region. One explanation is that the inhomogeneity which causes bubble induced turbulence during the ascending recirculation flow near the bubble column wall is not well reflected by the proposed modified SGS model in the present LES. This requires further investigation.

In order to further demonstrate the reliability of our modified SGS model, the quantitative comparison between the LES results and the experimental results from Kulkarni *et al.* (2001) is also made. In their experimental work, Kulkarni *et al.* settled the measurement points radially at the height of 0.3 m, corresponding to H/D = 2. It is expected that the flow field may still be not fully developed and would be influenced by the gas inlet condition. In fact, the air was introduced by a sintered plate in their experiments, which may cause uniform gas inlet distribution. The normalised axial liquid velocity and the gas hold-up against the radial position at H/D = 2 obtained from our LES with the modified SGS model are shown in Figures 2-7 and 2-8. It can be seen from the figures that generally good agreements with the

experimental data were still achieved, clearly indicating the suitability of the modified SGS model.

3.3 Turbulent kinetic energy contributed by shear turbulence and bubble induced turbulence characterized by LES with the modified SGS model

The liquid axial velocity-time series between 50 s and 100 s at the centre of H/D = 6, obtained by the modified SGS LES is shown in Figure 2-9. For comparison purpose, the experimental time-dependent liquid axial velocity sampled corresponding to the same location but acquired by Kulkarni et al. (2001) is also plotted in the figure. It needs to be noted here that the experimental data obtained by Kulkarni *et al.* (2001) covering a period of 50 s has 8192 sample points while the results of the modified SGS LES have adopted 10,000 sample points. The LES simulation has reasonably recapture the transient fluctuations as exhibited by the experiment, even the amplitudes of the fluctuations predicted by the modified SGS LES are also consistent with the experimental ones. The observed differences are likely caused by the different sampling rates and the unavoidable noise from the bubble detection in the experiment. As discussed in Kulkarni's work, since it is not guaranteed that all the bubbles pass entirely and centrally through the measurement volume, the chordal passage will cause refraction on bubbles that eventually lead to the relative higher amplitude liquid velocity (Kulkarni et al., 2001). Thus, the probability density function (PDF) and turbulent kinetic energy spectral analysis relating to the time-dependent liquid velocities would be able to provide the physical insight into

bubble induced turbulence in the bubble column.

Figure 2-10 presents the standardised PDFs for the axial liquid velocity calculated from the simulations for single phase flow, bubbly flow employed modified eddy viscosity model and standard Smagorinsky SGS model. The PDFs of the standardised velocity $(\tilde{u}_i - \overline{\tilde{u}_l})/\tilde{u}_{l,rms}$ are presented. The PDF of liquid velocity based on a single-phase turbulent flow at a superficial liquid velocity of 0.03162 m/s is presented as the reference, which is nearly distributed as Gaussian statistics. It is observed from Figure 2-10, the liquid velocity PDFs for the gas-liquid two-phase flow in the bubble column are asymmetric and show deviation from the single-phase flow's Gaussian behavior with a tail. The occurrence of positive tails has been shown to be caused by the wake behind the rising bubbles and, hence, a larger probability of upward fluctuations (Risso and Ellingsen, 2002; Alméras et al., 2017; Risso, 2018; Lai et al., 2018). Compared with the Smagorinsky SGS model without modification, the relative longer as well as higher positive tails of liquid velocity obtained from the modified SGS model clearly may indicate that the transient behaviour of the bubbles' response to eddies has been captured. It is noted here that the fluctuation caused by the bubbles' response to the turbulent eddies of the similar size with the bubble diameter has been taken into account in the modified SGS model.

Regarding to the turbulent kinetic energy of the liquid phase, the LES-filtered power energy spectrum $E(\kappa)$ of the axial turbulent velocity fluctuation obtained at

the middle point in the line across the bubble column at H/D = 6 are presented in Figure 2-11(a) and 2-11(b). The power spectrum is obtained by taking the Fast Fourier Transform (FFT) of the time correlation of axial turbulent velocity fluctuations using the Welch method (Welch, 1967). Figure 2-11(a) also presents the one-dimensional spectrum of single-phase flow in accordance with Pope's model [42]. The model is described as

$$\mathrm{E}_{11}(\kappa) = \mathrm{C}_0 \varepsilon^{\frac{2}{3}} \kappa^{-\frac{5}{3}} \left(\frac{\kappa L}{\sqrt{(\kappa L)^2 + C_L}} \right)^{\frac{5}{3}+p_0} \exp\left(-\beta \left(\left[(\kappa_1 \eta)^4 + C_\eta^4 \right]^{\frac{1}{4}} - C_\eta \right) \right) \tag{2-25}$$

where L and η stand for integral and Kolmogorov length scale, respectively, and the model constants are $\mathrm{C}_0 = 0.49, p_0 = 0$ for a -5/3 spectral slope by default, $\mathrm{C}_\mathrm{L} = 6.78, C_\eta = 0.4$, and $\beta = 5.2$ (Lai et al., 2019). As shown in Figure 2-11(a), the turbulent kinetic energy spectrum predicted by the modified SGS model follows Pope's model well and the modified SGS LES model captures -5/3 scaling in the inertial subrange and recovers -3 scaling laws for the wave number greater than the typical wave number characterized by the bubble size, i.e. $\kappa_B = 2\pi/d_B$. It is interesting to note here that the representative bubble frequencies, estimated by $f_B = |\boldsymbol{u}_G - \boldsymbol{u}_L|/2\pi d_B$, is 12 Hz when the bubble diameter is 4 mm (Prakash et al., 2016). In general wave equations, $\kappa = \frac{2\pi}{\lambda} = \frac{2\pi\nu}{u}$, where ν is the frequency of the wave, λ is the wavelength and u is the mean liquid velocity (Risso and Ellingsen, 2002). Thus f_B can be converted to $\kappa_{\mathrm{B1}} = 302.80 \mathrm{m}^{-1}$. It can be observed from Figure 10(a) that the transition of the $\mathrm{E}_{11}(\kappa)$ takes place at $\kappa_{\mathrm{B2}} \approx 270\ \mathrm{m}^{-1}$($f$≈10.70 Hz) where the left of $\kappa_{\mathrm{B2}} = 270\ \mathrm{m}^{-1}$demonstrates the -5/3 slope, while the right demonstrates the

-3 scaling. This indicates that the turbulent kinetic energy is fed into the liquid with the bubbles' contribution at frequencies around f = 10.70 Hz, which is close to the representative bubble frequency. Lance and Bataille (1991) have indicated that the eddies induced by bubble wake are very quickly dissipated by viscosity before turbulence spectral transfer can take place. Pope also stated that the directional information of the large scales is missing with the energy passing down the cascade. In the energy cascade ($l < l_{EI}$), the dominant process is composed of the energy transfer to successively smaller scales and viscous dissipation. Here, l_{EI} is the turbulence length scale between the anisotropic large eddies and the isotropic small eddies, which is hypothesised by Kolmogorov (Kolmogorov, 1991). Thus, the input energy of bubbles will not take part in large length scales, which correspond to low wave numbers, but contribute towards higher wave numbers. The production of eddies with the size of the bubbles will contribute towards the dissipation in the higher frequency range as indicated by Lance and Bataille (1991). Since the bubble induced turbulence dissipation can be estimated by $\nu E(\kappa)\kappa^3$, the drag force acting on the gas phase in the turbulent bubbly flow in the bubble column is roughly balanced by the bubble buoyancy on average and one can have the following estimation, given by

$$\nu E(\kappa)\kappa^3 \sim C_B \alpha_G \left[\frac{3}{4}\frac{C_D}{d_B}(u_B - u_L)^2\right]|\boldsymbol{u}_G - \boldsymbol{u}_L| \tag{2-26}$$

This leads to $E(\kappa)\sim\kappa^{-3}$, which is also demonstrated by the existing experimental work as well as DNSs and consistent with our LES results as shown in Figure 2-11

(Bouche et al., 2014; Mendez-Diaz et al., 2013; Mercado et al., 2010; Murai et al., 2000; Riboux et al., 2010; Bunner and Tryggvason, 2003; Riboux et al., 2013; Roghair et al., 2011; Sugiyama et al., 2001). Based on the modelling discussion, it can be assumed that the total turbulent dissipation rate ε_L is consisted of the turbulent dissipation rate due to shear turbulence and the dissipation due to the bubble-eddy interaction as described by Equation (2-27), viz.

$$\varepsilon_L = \varepsilon + \varepsilon_B = \varepsilon\left(1 + \mathrm{C_b}\overline{\alpha_G}\frac{\lambda}{\mathrm{d}}\left(\frac{1}{1+St_{SGS}}\right)^{\frac{3}{2}}\right) = 2\nu\int_0^{\infty}\kappa^2\,E(\kappa)d\kappa \qquad (2\text{-}27)$$

The difference in the power spectrum for different SGS models is noted in Figure 2-11(b). The higher magnitude of $\mathrm{E}_{11}(\kappa)$ in $\kappa > \kappa_B$ predicted by the modified SGS model may be caused by the eddy viscosity estimation that considers the bubbles response to eddies. The modified eddy viscosity model takes the competitive fluctuation velocity in the sub-grid scale between bubbles and eddies into account, which is absolutely neglected by the standard LES SGS model. Thus, the energy fed in the system by bubbles are more comprehensively described, leading to a steeper slope when $\kappa > \kappa_B$ in direct cascade, and the slope is much closer to the -3 scaling law compared with the standard model.

3.4 Correlation between large eddy structures and local gas holdup

The present study has adopted the vorticity to characterise the large eddy behaviour

in the bubble column, defined as the curl of the flow velocity field by $\boldsymbol{\omega} = \boldsymbol{\nabla} \times \boldsymbol{u_L}$.

It is expected that the large eddy structure development in the bubble column would be significantly affected by the entrained bubbles while this interaction between bubbles and turbulent eddies has been accounted for in the modified SGS model. Thus, a correlation to reflect this coupling can be presented. Figure 2-12 shows the isosurface of $\alpha_G = 0.23$ highlighted by the vorticity and $|\omega_L| = 58\, s^{-1}$ highlighted by air volume fraction at t = 90 s. It can be observed that the bubble volume fraction is strongly coupled with the vorticity. The following spatial correlation between local gas hold-up and vorticity magnitude to characterize the variation of such correlation along the axial height of the bubble column is proposed and can be defined as

$$R(\Delta h) = \frac{\overline{|\boldsymbol{\omega}'(h_0)|\alpha_G'(h_0+\Delta h)}}{\sqrt{|\boldsymbol{\omega}'^2(h_0)|}\sqrt{\alpha_G'^2(h_0)}} \tag{2-28}$$

Figure 2-13 presents the spatial correlation coefficient $R(\Delta h)$ along the centerline at different axial height from 0 to 0.35m. As shown in Figure 2-13, three large peaks are clearly shown in the correlation against the different axial height of the bubble column in the ranges of 0.025-0.05, 0.14-0.2 and 0.32-0.34 m, indicating a strong bubble clustering with the large eddies. It is also noted that the peak of the correlation coefficient of the third one is relatively lower than the first two. This may be explained by the change in the axial height along the column where the large eddies are oscillating. In the range of 0.32-0.34 m, the weaker fluctuation indicates that

the typical fluctuated large eddy size may be smaller, entrapping fewer numbers of bubbles. Thus, the value of correlation for the third peak becomes smaller, supported by the predicted $\sqrt{\alpha_G'^2(h_0)}$ being always positive along the axial height. A positive value of the spatial correlation coefficient indicates that the vorticity carried by the large eddies strongly affect the bubble motion and thus, the gas hold-up. Figure 2-14 displays the cross-section averaged gas hold-up superimposed by the correlation coefficient distribution. As the combination shown in Figure 2-14, the occurrence of high gas hold-up is accompanied by the presence of a high spatial correlation coefficient.

3.5 Interfacial mass transfer across bubbles using the modified SGS model

The volumetric mass transfer coefficient $k_L a$ is an important parameter to evaluate the efficiency of interfacial mass transfer. Besides, when employing the species transport equation to find the species concentration, the contribution from the interfacial mass transfer across the bubbles of the source terms can be calculated with the presence of $k_L a$ (Shi et al., 2018). As the spherical bubble assumption was made in the present work, the interfacial area concentration *a* for the bubbles in the bubble column can be estimated by

$$a = \frac{6\bar{\alpha}_B}{d_B} = \frac{6}{d_B V}\int_V \alpha_g dV \tag{2-29}$$

where $\bar{\alpha}_B$ is the bubble column volumetric averaged gas holdup. Thus, the coefficient of mass transfer k_L and the interfacial area concentration can be obtained individually from various models of mass transfer. Since the modified SGS model that taking the turbulence kinetic energy contribution from BIT and bubble interaction with the turbulence eddies into account, the relative velocity between gas and liquid and energy dissipation rate play significant roles in estimating the value of interfacial mass transfer coefficient k_L. The eddy cell model was reported by Lamont and Scott (1970) and indicated that the very small scale of the turbulent eddies plays significant roles in mass transfer and these motions lead to a sophisticate viscosity, once these small-scale behaviors can be controlled and the surface renewal rate as well as the mass transfer mechanism can be then defined analytically and shown as,

$$k_L \propto D_L^{1/2} \left(\frac{\varepsilon_L}{\nu}\right)^{1/4} \tag{30}$$

where D_L is liquid mass diffusivity of liquid phase, ε_L is the turbulence dissipation rate. It can be figured out that k_L can be estimated based on the eddy cell model through a key parameter, turbulence dissipation rate ε_L. The influences of the eddies induced by the bubble wakes and bubbles' dynamic responses to the surrounding liquid on the liquid turbulent kinetic energy spectrum were illustrated in Figure 2-11. Therefore, apart from the consideration of the simply shear turbulent dissipation, the effect of the interactions between bubbles and eddies is also needed to be

addressed. After substituting Equation (2-27) into Equation (2-30) yields the estimation for k_L based on the eddy cell model can be expressed as,

$$k_L \propto D_L^{1/2}\left(\frac{\varepsilon\left(1+C_b\overline{\alpha_G}\frac{\lambda}{d}\left(\frac{1}{1+St_{SGS}}\right)^{\frac{3}{2}}\right)}{\nu}\right)^{1/4} \propto D_L^{1/2}\left(\frac{2\nu\int_0^{\infty}\kappa^2 E(\kappa)d\kappa}{\nu}\right)^{1/4} \quad (31)$$

Equation (2-31) shows that k_L is related to the kinetic energy integrated from the energy spectrum obtained in Section 3.3. In addition, the assumption can be reasonably made that the mass transfer between the bubbles and the eddies of the similar size or marginally larger is dominant in whole process.

As shown in Figure 2-15(b), a higher volumetric mass transfer coefficient seems to be more likely in the vicinity of the column wall when implementing the SGS model without considering bubble response to turbulent eddies. However, when the eddy size is slightly larger than the bubble and in the inertial subrange, the bubbles will be strongly entrained by eddies. This phenomenon is well demonstrated by Figure 2-15(a), where the volumetric mass transfer coefficient is more uniformly distributed compared to the SGS model without modification. Therefore, by employing the modified SGS model, the distribution behavior of mass transfer characterized by $k_L a$ inside the bubble column can be better analyzed.

4. CONCLUSIONS

LES Simulation of gas-liquid flow in a bubble column reactor has been carried out using the modified SGS model, which has taken the bubble-eddy interaction into account. The results of LES simulations clearly indicate that by employing the modified SGS model with consideration of Stokes number, the bubble entrainment transient behaviour in the cylindrical bubble column that was observed in experimental work can be reasonably captured. The effect of the modified SGS model on the velocity profile and gas hold-up is also demonstrated by the simulation. The main conclusions reached as a result of the present study can be summarised as follows:

(1) It can be observed from the simulation resulting from the modified SGS model that the gas hold-up and velocity profiles demonstrate a better agreement overall with the experimental results (Camarasa et al., 1999; Kulkarni et al., 2001) compared with the standard Smagorinsky SGS model, but both gas hold-up and the streamwise gas velocity are slightly over-predicted in the vicinity of the bubble column wall.

(2) The use of the modified SGS turbulence model is able to capture the detailed flow behaviour of bubbly flow in the bubble column.

(3) The power turbulent kinetic energy spectrum of the axial liquid velocity indicates that the slope of classical -5/3 law can still be observed for the frequency range of f < 10.70 Hz, followed approximately by a -3 scaling law when the frequency f > 10.70 Hz, the representative bubble frequency calculated according to $f_B = |\boldsymbol{u}_G - \boldsymbol{u}_L|/2\pi d_B$ is 12Hz. This is consistent with the recent findings on the

bubble induced turbulence as reported by Prakash *et al*. (2016), Bouche *et al*. (2014), Mendex-diaz *et al*. (2013), Mercado *et al*. (2010), Murai *et al*.(2000), Riboux *et al*. (2010, 2013), Bunner and Tryggvason(2003), Roghair *et al*. (2011) as well as Sugiyama *et al*. (2001), indicating that the slope of -3 law has been also recovered by using the modified SGS LES for the bubble column.

(4) The spatial correlation between the cross-sectional averaged gas hold-up and local vorticity clearly indicates that the bubbles rising-up is strongly entrained by large spirally turbulent eddies with the trend of bubbles to cluster in the central region of the bubble column.

(5) Based on the eddy cell theory, the volumetric mass transfer coefficient estimated by using the modified SGS model can have better accuracy of estimation of the interfacial mass transfer between bubbles and liquid than that using the standard SGS model.

REFERENCES

Alméras, E., Mathai, V., Lohse, D., & Sun, C. (2017). Experimental investigation of the turbulence induced by a bubble swarm rising within incident turbulence. *Journal of Fluid Mechanics*, **825**, 1091-1112.

Auton, T. R. (1987). The lift force on a spherical body in a rotational flow. *Journal of fluid Mechanics*, **183**, 199-218.

Bhole, M. R., Joshi, J. B., & Ramkrishna, D. (2008). CFD simulation of bubble columns incorporating population balance modeling. *Chemical Engineering Science*, **63**(8), 2267-2282.

Bombardelli, F.A., Buscaglia, G.C., García, M., Dari, E.A. (2006). Simulation of bubble plume wandering phenomena in a bubble plume using a k-e model and a large eddy simulation (LES) approach. *Mecanica Computat*. **23**, 1969–1994.

Bouche, E., Roig, V., Risso, F., & Billet, A. M. (2014). Homogeneous swarm of high-Reynolds-number bubbles rising within a thin gap. Part 2. Liquid dynamics. *Journal of Fluid Mechanics*, **758**, 508-521.

Bunner, B., & Tryggvason, G. (2003). Effect of bubble deformation on the properties of bubbly flows. *Journal of Fluid Mechanics*, **495**, 77-118.

Burns, A.D., Frank, T., Hamill, I., Shi, J. The favre averaged drag model for turbulent dispersion in Eulerian multi-phase flows, in: Proceeding of the Fifth International Conference on Multiphase Flow, Yokohama, Japan, 2004.

Camarasa, E., Vial, C., Poncin, S., Wild, G., Midoux, N., & Bouillard, J. (1999). Influence of coalescence behaviour of the liquid and of gas sparging on hydrodynamics and bubble characteristics in a bubble column. *Chemical Engineering and Processing: Process Intensification*, **38**(4-6), 329-344.

Chen, R. C., Reese, J., & Fan, L. S. (1994). Flow structure in a three-dimensional bubble column and three-phase fluidized bed. *AIChE Journal*, **40**(7), 1093-1104.

Deen, N. G., Solberg, T., & Hjertager, B. H. (2001). Large eddy simulation of the gas–liquid flow in a square cross-sectioned bubble column. *Chemical Engineering Science*, **56**(21-22), 6341-6349.

Dhotre, M. T., Deen, N. G., Niceno, B., Khan, Z., & Joshi, J. B. (2013). Large eddy simulation for dispersed bubbly flows: a review. *International Journal of Chemical Engineering*, 2013.

Dhotre, M. T., Niceno, B., & Smith, B. L. (2008). Large eddy simulation of a bubble column using dynamic sub-grid scale model. *Chemical Engineering Journal*, **136**(2-3), 337-348.

Fu, X. Y., & Ishii, M. (2003). Two-group interfacial area transport in vertical air–water flow-II. Model evaluation. *Nuclear Engineering and Design*, **219**(2), 169-190.

Garcia, J. (2001). Study of the turbulence modulation in particle-laden flows using LES. *Annual Research Briefs*-2001, 177.

Germano, M., Piomelli, U., Moin, P., & Cabot, W. H. (1991). A dynamic subgrid-scale eddy viscosity model. *Physics of Fluids A: Fluid Dynamics*, **3**(7), 1760-1765.

H.A. Jakobsen, B.H. Sannes, S. Grevskott, H.F. Svendsen, Modeling of vertical bubble-driven flows, *Industrial and Engineering Chemistry Research.* **36** (1997) 4052–4074.

Ishii, M., & Zuber, N. (1979). Drag coefficient and relative velocity in bubbly, droplet or particulate flows. *AIChE Journal*, **25**(5), 843-855.

Ishii, M., Kim, S., & Kelly, J. (2005). DEVELOPMENT OF INTERFACIAL AREA TRANSPORTEQUATION. *Nuclear Engineering and Technology*, **37**(6), 525-536.

Ishii, M., Kim, S., & Uhle, J. (2002). Interfacial area transport equation: Model development and benchmark experiments. *International Journal of Heat and Mass Transfer*, **45**(15), 3111-3123.

Kolmogorov, A. N. (1991). The local structure of turbulence in incompressible viscous fluid for very large Reynolds numbers. *Proceedings of the Royal Society of London. Series A: Mathematical and Physical Sciences*, **434**(1890), 9-13.

Kruis, F. E., & Kusters, K. A. (1997). The collision rate of particles in turbulent flow. *Chemical Engineering Communications*, **158**(1), 201-230.

Kulkarni, A. A., Joshi, J. B., Kumar, V. R., & Kulkarni, B. D. (2001). Application of multiresolution analysis for simultaneous measurement of gas and liquid velocities and fractional gas hold-up in bubble column using LDA. *Chemical Engineering Science*, **56**(17), 5037-5048.

Lai, C. C. K., Fraga, B., Dodd, M., & Chan, R. (2018). Energy cascade in a homogeneous swarm of bubbles rising in a vertical channel. Centre for Turbulence Research, Proceedings of the Summer Program 2018, 55-64.

Lai, C. C., & Socolofsky, S. A. (2019). The turbulent kinetic energy budget in a bubble plume. *Journal of Fluid Mechanics*, **865**, 993-1041.

Lakehal, D., Smith, B. L., & Milelli, M. (2002). Large-eddy simulation of bubbly turbulent shear flows. *Journal of Turbulence*, **3**(25), 1-21.

Lamont, J. C., & Scott, D. S. (1970). An eddy cell model of mass transfer into the surface of a turbulent liquid. *AIChE Journal*, **16**(4), 513-519.

Lance, M., & Bataille, J. (1991). Turbulence in the liquid phase of a uniform bubbly air–water flow. *Journal of Fluid Mechanics*, **222**, 95-118.

Liao, Y., Ma, T., Liu, L., Ziegenhein, T., Krepper, E., & Lucas, D. (2018). Eulerian modelling of turbulent bubbly flow based on a baseline closure concept. *Nuclear Engineering and Design*, **337**, 450-459.

Liu, Z., & Li, B. (2018). Scale-adaptive analysis of Euler-Euler large eddy simulation for laboratory scale dispersed bubbly flows. *Chemical Engineering Journal*, **338**, 465-477.

Lo, S. (1996). Application of Population Balance to CFD Modelling of Bubbly Flow via the MUSIG model, *AEA Technology*, AEAT-1096.

Ma, T., Ziegenhein, T., Lucas, D., & Fröhlich, J. (2016). Large eddy simulations of the gas–liquid flow in a rectangular bubble column. *Nuclear Engineering and Design*, **299**, 146-153.

Mendez-Diaz, S., Serrano-Garcia, J. C., Zenit, R., & Hernandez-Cordero, J. A. (2013). Power spectral distributions of pseudo-turbulent bubbly flows. *Physics of Fluids*, **25**(4), 043303.

Mercado, J. M., Gomez, D. C., Van Gils, D., Sun, C., & Lohse, D. (2010). On bubble clustering and energy spectra in pseudo-turbulence. *Journal of Fluid Mechanics*, **650**, 287-306.

Milelli, M. (2002). A numerical analysis of confined turbulent bubble plumes (Doctoral dissertation, ETH Zurich).

Milelli, M., Smith, B. L., & Lakehal, D. (2001). Large-eddy simulation of turbulent shear flows laden with bubbles. In Direct and Large-Eddy Simulation IV (pp. 461-470). Springer, Dordrecht.

Milelli, M., Smith, B. L., & Lakehal, D. (2001). Subgrid-scale dynamic modelling in les of turbulent bubbly flows. In TSFP DIGITAL LIBRARY ONLINE. Begel House Inc..

Mohammadi, M. H., Sotiropoulos, F., & Brinkerhoff, J. R. (2019). Eulerian-Eulerian large eddy simulation of two-phase dilute bubbly flows. *Chemical Engineering Science*, 208, 115156.

Murai, Y., Kitagawa, A., Song, X. Q., Ohta, J., & Yamamoto, F. (2000). Inverse Energy Cascade Structure of Turbulence in a Bubble Flow: Numerical Analysis Using Eulerian-Lagrangian Model Equations. *JSME International Journal Series B Fluids and Thermal Engineering*, **43**(2), 197-205.

Ničeno, B., Dhotre, M. T., & Deen, N. G. (2008). One-equation sub-grid scale (SGS) modelling for Euler–Euler large eddy simulation (EELES) of dispersed bubbly flow. *Chemical Engineering Science*, **63**(15), 3923-3931.

Pope, S. B. (2001). Turbulent flows. Cambridge University Press.

Prakash, V. N., Mercado, J. M., van Wijngaarden, L., Mancilla, E., Tagawa, Y., Lohse, D., & Sun, C. (2016). Energy spectra in turbulent bubbly flows. *Journal of Fluid Mechanics*, **791**, 174-190.

Riboux, G., Legendre, D., & Risso, F. (2013). A model of bubble-induced turbulence based on large-scale wake interactions. *Journal of Fluid Mechanics*, **719**, 362-387.

Riboux, G., Risso, F., & Legendre, D. (2010). Experimental characterization of the agitation generated by bubbles rising at high Reynolds number. *Journal of Fluid Mechanics*, **643**, 509-539.

Risso, F. (2018). Agitation, mixing, and transfers induced by bubbles. *Annual Review of Fluid Mechanics*, **50**, 25-48.

Risso, F., & Ellingsen, K. (2002). Velocity fluctuations in a homogeneous dilute dispersion of high-Reynolds-number rising bubbles. *Journal of Fluid Mechanics*, **453**, 395-410.

Roghair, I., Mercado, J. M., Annaland, M. V. S., Kuipers, H., Sun, C., & Lohse, D. (2011). Energy spectra and bubble velocity distributions in pseudo-turbulence: Numerical simulations vs. experiments. *International Journal of Multiphase Flow*, **37**(9), 1093-1098.

Sato, Y., & Sekoguchi, K. (1975). Liquid velocity distribution in two-phase bubble flow. *International Journal of Multiphase Flow*, **2**(1), 79-95.

Sato, Y., Sadatomi, M., & Sekoguchi, K. (1981). Momentum and heat transfer in two-phase bubble flow—I. Theory. *International Journal of Multiphase Flow*, **7**(2), 167-177.

Shi, W., Yang, J., Li, G., Zong, Y., & Yang, X. (2018). Modelling of Bubbly Flow in Bubble Column Reactors with an Improved Breakup Kernel Accounting for Bubble Shape Variations. Heat and Mass Transfer: Advances in Modelling and Experimental Study for Industrial Applications, 65. InTechOpen.

Smagorinsky, J. (1963). General circulation experiments with the primitive equations. *Monthly Weather Review*, **91**, 99–165.

Smith, B. L., & Milelli, M. (1998). An investigation of confined bubble plumes. In: Proceedings of the Third International Conference on Multiphase Flow, 8–12.

Sommerfeld, M., Muniz, M., & Reichardt, T. (2018). On the Importance of Modelling Bubble Dynamics for Point-mass Numerical Calculations of Bubble Columns. *Journal of Chemical Engineering of Japan*, **51**(4), 301-317.

Sugiyama, K., Takagi, S., & Matsumoto, Y. (2001). Multi-scale analysis of bubbly flows. *Computer methods in applied Mechanics and Engineering*, **191**(6-7), 689-704.

Tomiyma, A., Tamai, H., Zun, I. S. Hosokawa, Transverse migration of single bubbles in simple shear flows, *Chemical Engineering Science.* **57** (2002) 1949–1958.

Welch, P. (1967). The use of fast Fourier transform for the estimation of power spectra: a method based on time averaging over short, modified periodograms. *IEEE Transactions on audio and electroacoustics*, **15**(2), 70-73.

Wu, Q., Kim, S., Ishii, M. and Beus, S. G. (1998). One-group interfacial area transport in vertical bubbly flow. *International Journal of Heat and Mass Transfer*, **41**(8-9), 1103-1112.

Yao, W., & Morel, C. (2004). Volumetric interfacial area prediction in upward bubbly two-phase flow. *International Journal of Heat and Mass Transfer*, **47**(2), 307-328.

Zhao, L., Boufadel, M. C., Lee, K., King, T., Loney, N., & Geng, X. (2016). Evolution of bubble size distribution from gas blowout in shallow water. *Journal of Geophysical Research: Oceans*, **121**(3), 1573-1599.

Ẑun, I. (1980). The transverse migration of bubbles influenced by walls in vertical bubbly flow. *International Journal of Multiphase Flow*, **6**(6), 583-588.

FIGURES

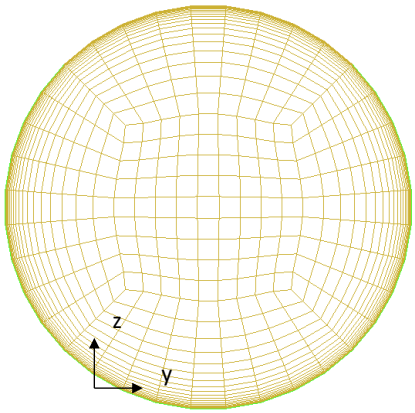

Figure 2- 1 Cross section of the mesh set-up ($\mathbf{d_B/\Delta = 0.75}$) in the bubble column.

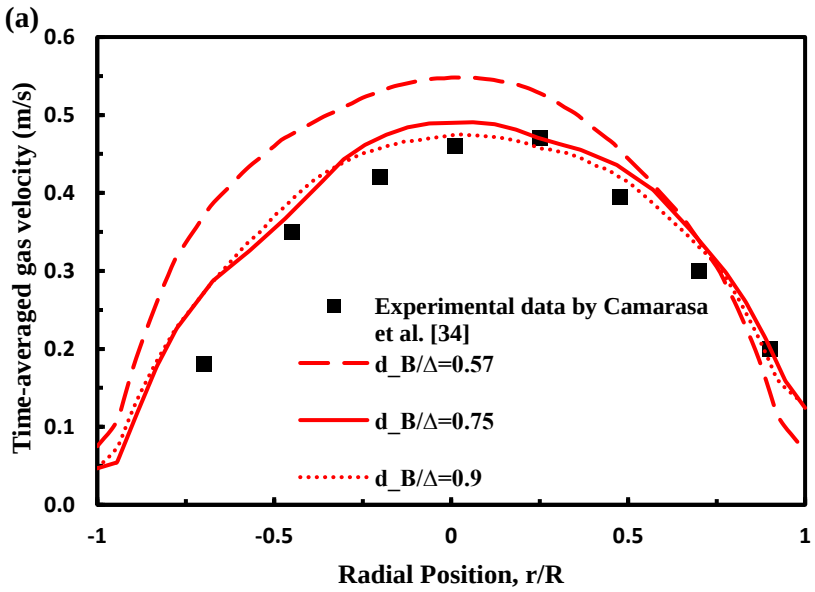

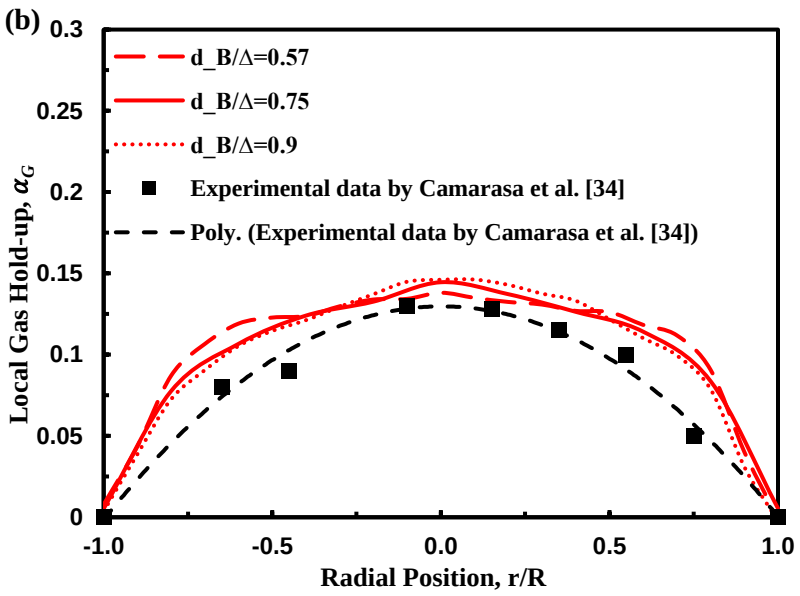

Figure 2- 2 Time-averaged (a) axial gas velocity and (b) radial distribution of gas hold-up at H/D=6 obtained on three grids, and experiments (Camarasa et al., 1999).

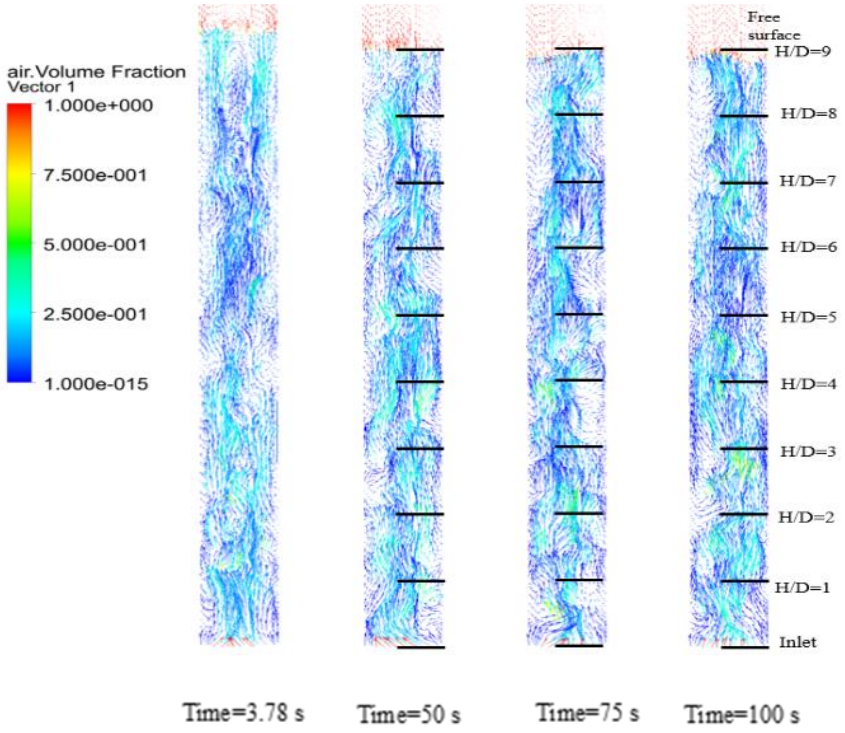

Figure 2- 3 Snapshots of LES simulated instantaneous velocity vectors highlighted by gas hold-up distribution.

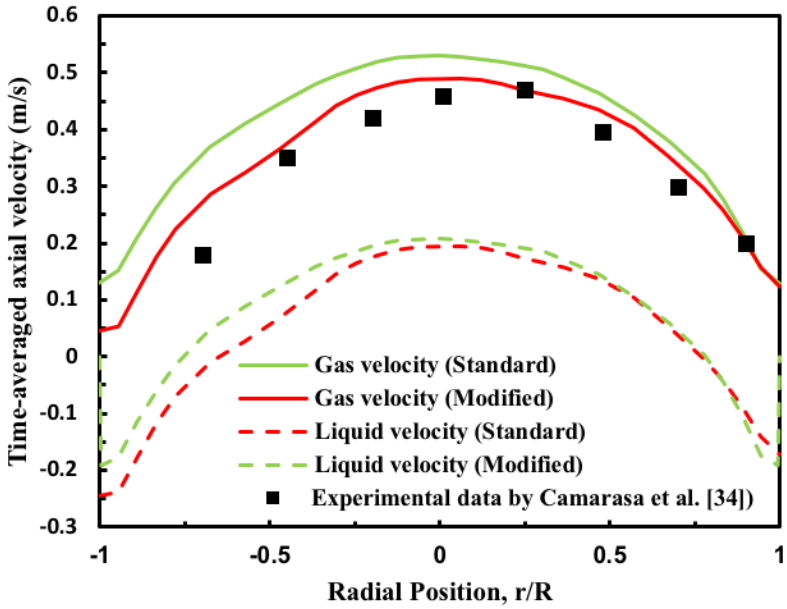

Figure 2- 4 Time-averaged axial gas and liquid velocity at H/D=6 (Green line: standard Smagorinsky SGS model; Red line: Modified Smagorinsky SGS model; Solid line: Gas; Dashed line: Liquid).

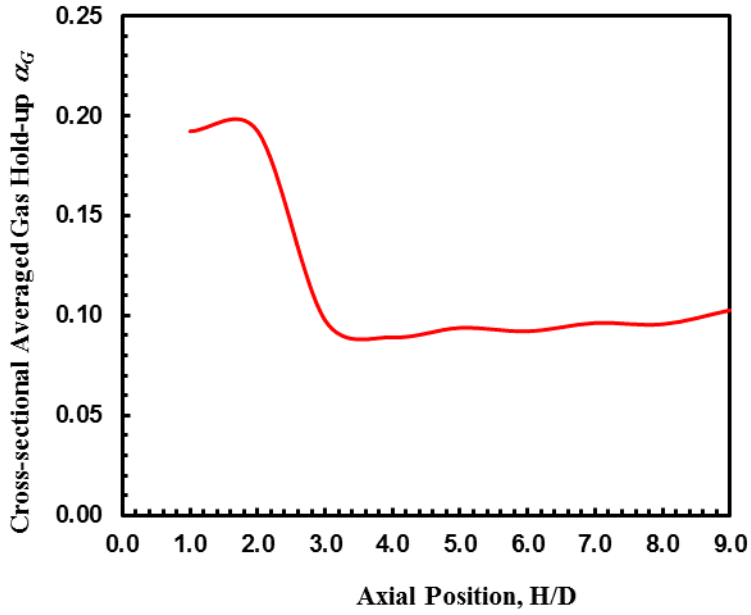

Figure 2- 5 Time-averaged axial distribution of gas hold-up at centreline.

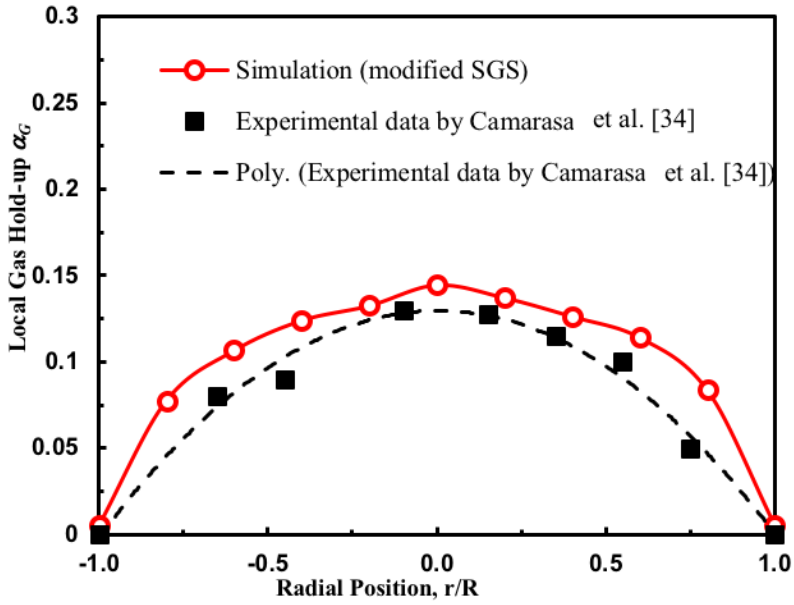

Figure 2- 6 Time-averaged radial distribution of gas hold-up at H/D=6.

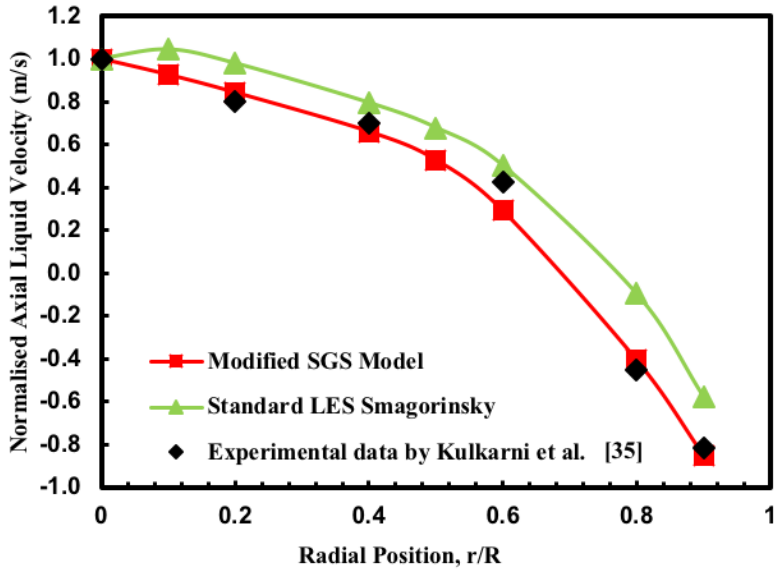

Figure 2- 7 Time-averaged axial liquid velocity at H/D=2.

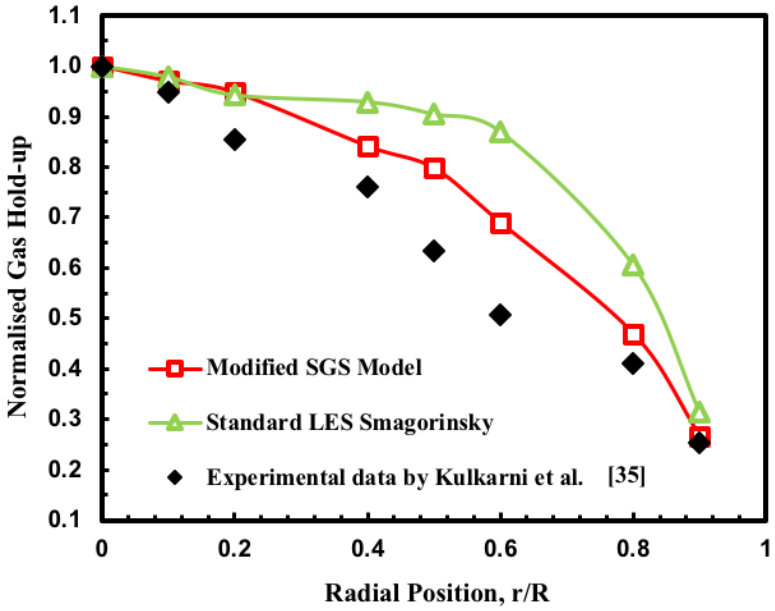

Figure 2- 8 Time-averaged radial distribution of gas hold-up at H/D=2.

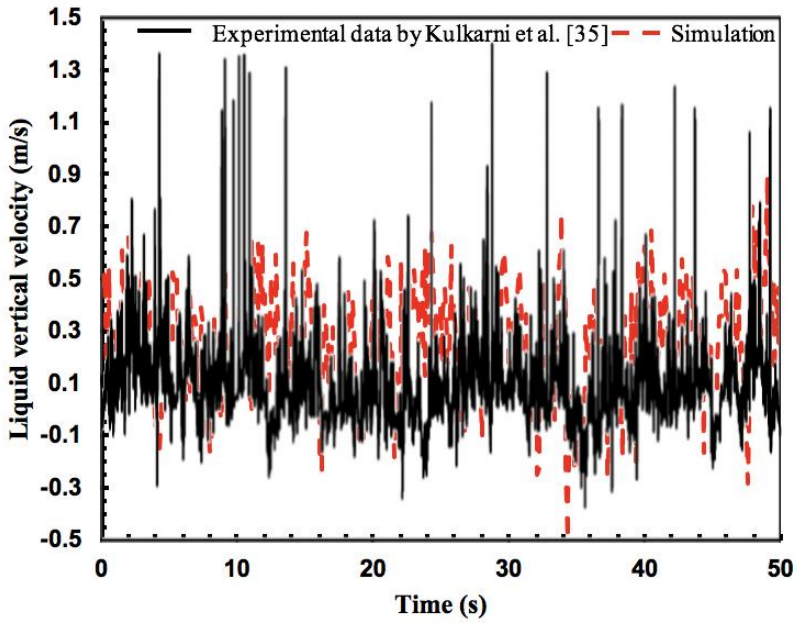

Figure 2- 9 Instantaneous axial velocity-time series.

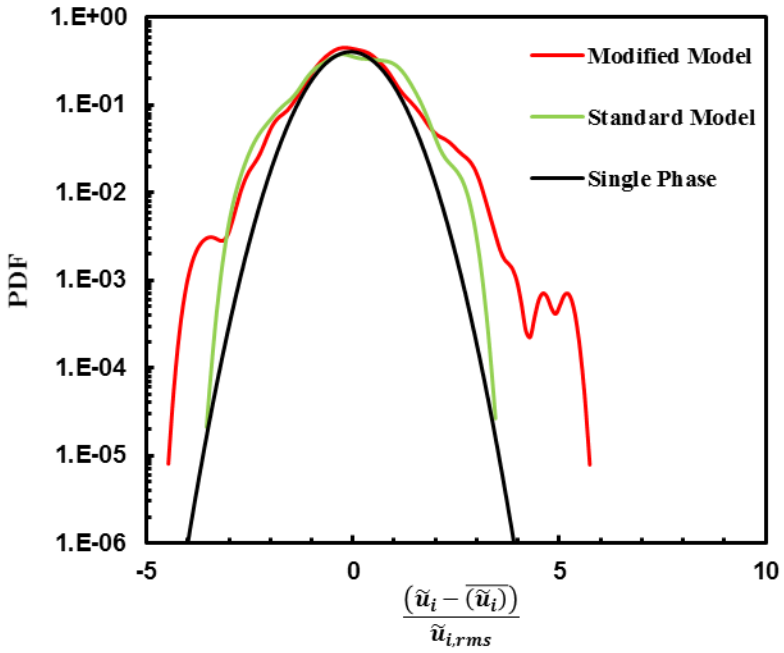

Figure 2- 10 PDFs of the liquid velocity normalized by the RMS velocity.

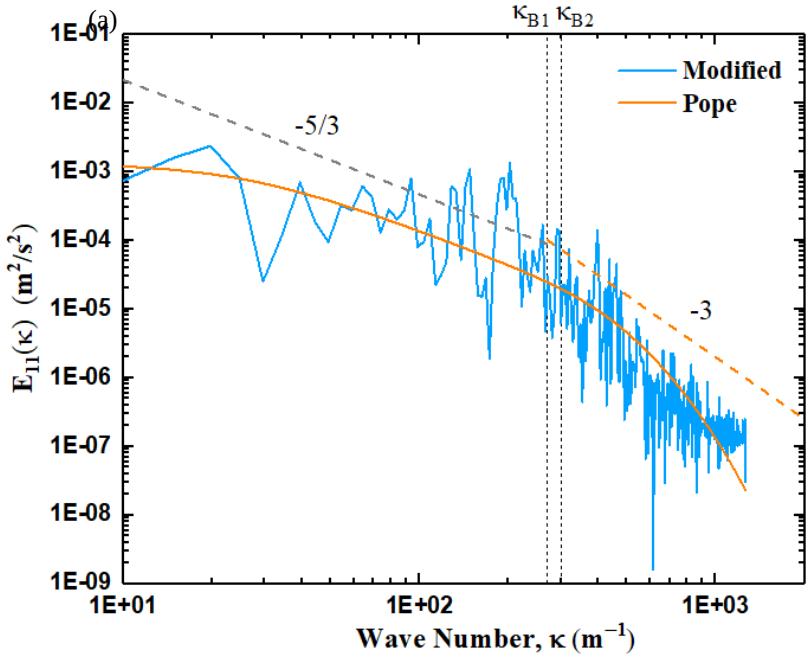

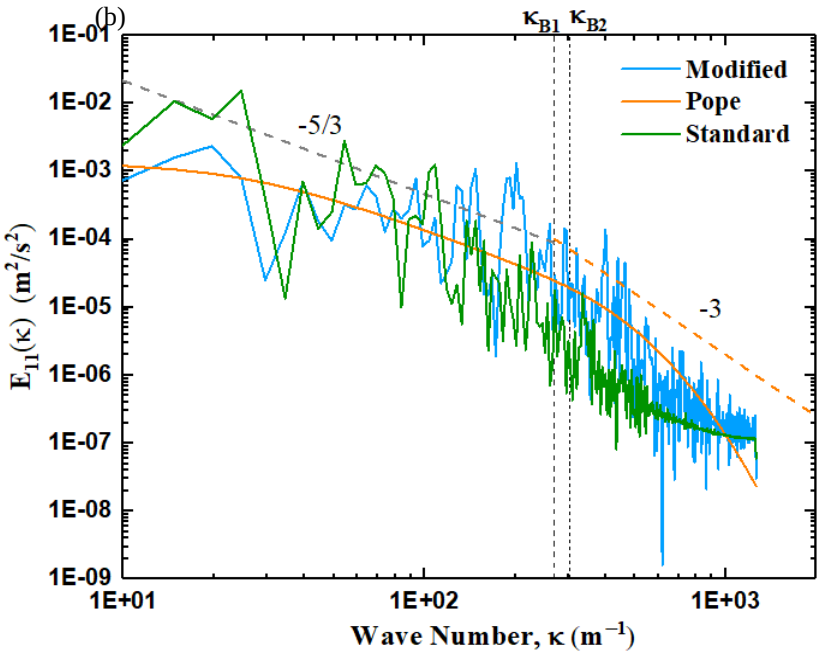

Figure 2- 11 Turbulent kinetic energy spectrum of liquid axial velocity fluctuation, calculated along the centreline at H/D=6. (a)Modified Model; (b) Comparison between Modified and Standard Smagorinsky SGS model.

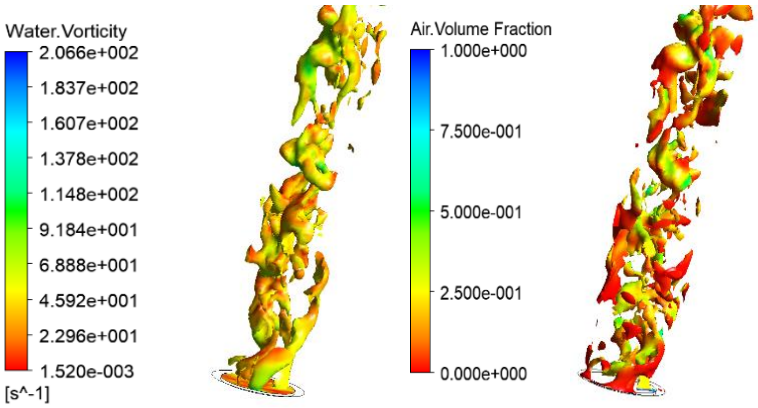

Figure 2- 12 Iso-surface of (a) $\boldsymbol{\alpha_G = 0.23}$ highlighted by water vorticity (b) $\boldsymbol{|\omega_L| = 58\ s^{-1}}$ highlighted by air volume fraction at t=90s.

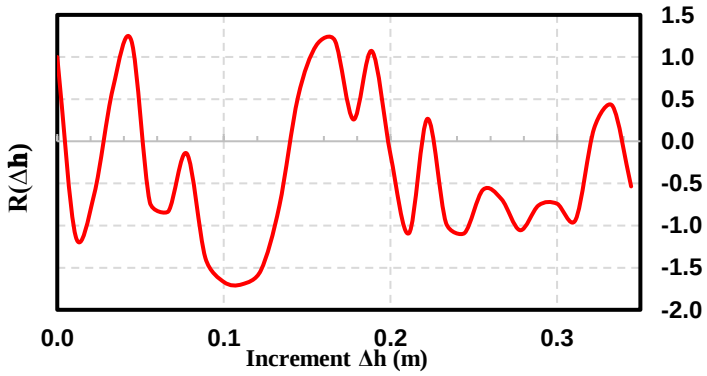

Figure 2- 13 Spatial correlation coefficient $\boldsymbol{R}(\Delta \boldsymbol{h})$ at t=90s.

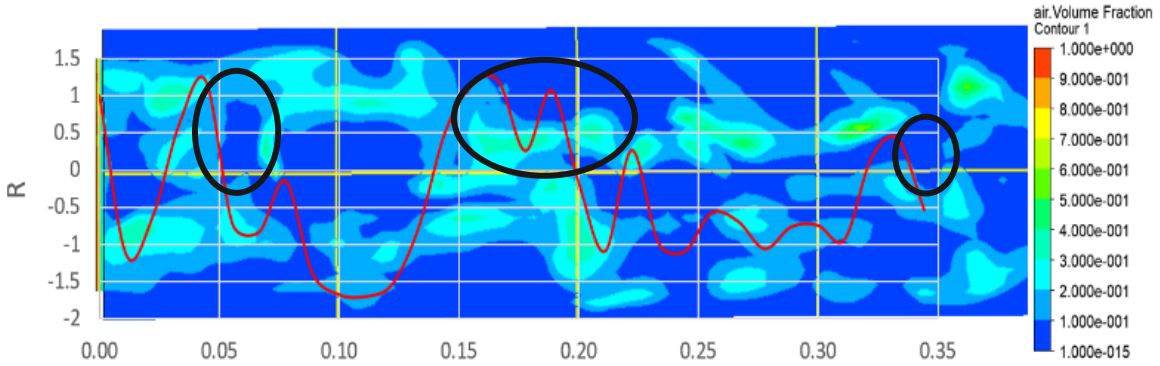

Figure 2- 14 Combination of instantaneous gas hold-up and spatial correlation coefficient at t = 90s.

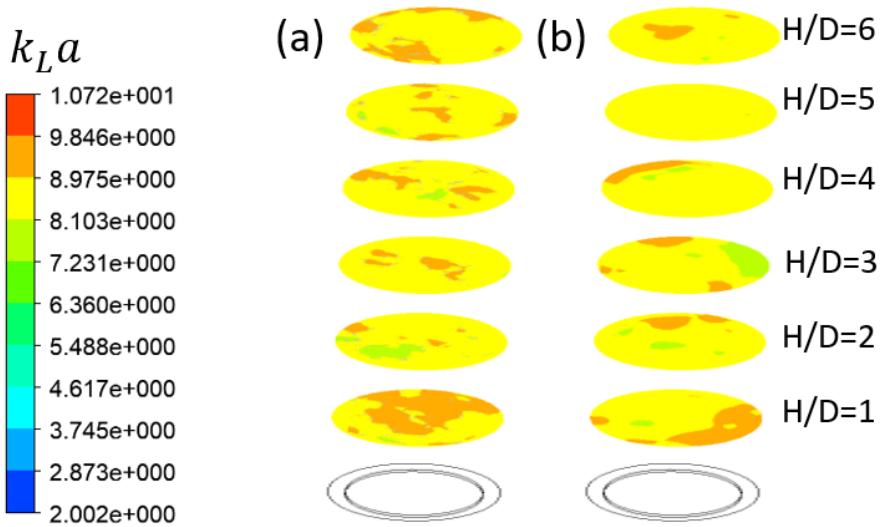

Figure 2- 15 Estimated volumetric mass transfer coefficient at different axial height for (a) modified SGS model (b) SGS model without modification.

CHAPTER 3: LARGE EDDY SIMULATION OF BUBBLE COLUMN BUBBLY FLOWS BY CONSIDERING SUB-GRID SCALE TURBULENT DISPERSION EFFECT ON MODULATING BUBBLE TRANSPORT

SUMMARY

In Chapter 2, the modified eddy viscosity model which takes the bubble dynamic response to the eddies into account in the LES modelling has been proposed while such modification has improved the prediction of the momentum and estimation of the mass transfer rates. However, for a better prediction in the momentum and mass transfer in bubble column bubbly flows, it is crucial for the momentum exchange terms in the momentum equations employed in the LES modelling to be described appropriately through the interfacial force closures. These interfacial force closures are strongly associated with the averaging on the applied momentum equations (time averaging for RANS modelling and filtering for large eddy simulation (LES) modelling). As a result of the averaging process, there will exist the correlations that are related to the turbulent fluctuations, for example, the term so referred to as turbulent dispersion force. Yet the impact of the turbulent dispersion on bubble transport in two-fluid Euler/Euler LES modelling in sub-grid scale are rarely addressed. It has now been recognised that the turbulent dispersion force plays an

important role in interphase momentum transfer. As the turbulent eddies in the surrounding areas of bubbles interact strongly with the bubbles in bubbly flow, such interactions induce the continuous deformation of the bubble surface, leading to the fluctuation of bubble trajectories and bubble oscillation accordingly. When using large eddy simulation for modelling bubbly flow, the SGS filtered velocity fluctuations of liquid phase can be interpreted as the eddy action on the surface of bubbles, consequently giving rise to bubble shape variations and the dispersion of bubbles. This Chapter presents a few cases through Euler/Euler large-eddy simulations (LES) modelling to demonstrate that the turbulent dispersion of bubbles can be used to effectively indicate the effect of turbulent eddies on bubble dynamics, in particular the bubble cluster oscillations, which leads to remarkable improvements in the prediction of bubble lateral dispersion behaviour. The use of spatially filtered-averaging to model the $\overline{(\alpha_k' u_k')}$ term related to turbulent bubble dispersion is proposed with a modification on SGS eddy viscosity to reflect turbulent dispersion due to bubble induced turbulence. It was found that by using the proposed model, the time-averaged LES modelled bubble velocities and bubble volume fraction profiles are in good agreement with the experimental data while the turbulent kinetic energy spectrum obtained at the location on the centreline of the bubble column still exhibits the conventional -5/3 scaling for shear induced turbulence and -3 scaling in slope for bubble induced turbulence.

1. INTRODUCTION

When employing the Euler-Euler large eddy simulation (LES) approach in the prediction of bubble column bubbly flows, modelling of the interfacial interactions between the bubbles and carrier fluid plays a key role in evaluation of the hydrodynamics, in particular shear turbulence and bubble induced turbulence characteristics, and heat and mass transfer. Recent progress on understanding the interphase forces involved in bubble column bubbly flows has led to several versions of modified models for interfacial force closure, in particular for the drag force experienced by the bubbles. However, there is still no consensus formed so far for contributions from each individual interfacial force considered in modelling bubble column bubbly flows. Representative cases are: i) neglecting the contribution from transverse lift forces (Pfleger *et al.*, 1999, Mudde and Simonin, 1999, Chen *et al.*, 2005, Kerdouss *et al.*, 2006, Shi *et al.*, 2017); ii) ignoring the effect of virtual mass force (Tabib *et al.*, 2008, Thakre and Joshi, 1999, Hunt *et al.*, 1987, Deen *et al.*, 2001, Sokolichin *et al.*, 2004); iii) negligible contribution from wall lubrication force comparing with other interfacial forces (Rzehak *et al.*, 2012) and considering wall lubrication force with three typical models (Antal *et al.*, 1991, Tomiyama, 1995, Hosokawa *et al.*, 2002). However, the results using these different models have revealed the effect on the prediction was not notable; iv) disregarding the turbulent dispersion force, especially in RANS modelling (Muniz and Sommerfeld, 2020, Darmana *et al.*, 2007, Drew, 2003, Laviéville *et al.*, 2017, Gosman *et al.*, 1992, Burns *et al.*, 2004, Laín and Grillo, 2007). Of particular concern in this work is the importance of turbulent dispersion in modulating the bubble transportation in bubble column bubbly

flows. It has become a heat debating problem on how to formulate the contribution of turbulent dispersion force since the derivation of the two-phase flow governing equations may employ different averaging approach. The turbulent dispersion force is used to describe the turbulent dispersion of the gas phase caused by the turbulent liquid eddies that act on the bubbles. Using the turbulent dispersion force for describing the eddy diffusion effect, the void fraction gradient is entailed to calculate the gas-phase flux in the mass conservation equation. However, the shortcoming of this modelled force lies in that it may still give out the result of existing the flux of the dispersed phase even when the dispersed phase velocity is zero. As a result, dispersion effect disappears from the continuity equation when using Favre averaging for formulation while such effect is reflected as a source term in momentum equation (Tabib and Schwarz, 2011). Generally speaking, the turbulent dispersion can be modelled in the following relationships: (i) being proportional to the volume fraction gradient (Lahey Jr *et al.*, 1993, Carrica *et al.*, 1999, Drew, 2001); (ii) being proportional to the product of the gradient of bubble volume fraction and the liquid turbulent kinetic energy (de Bertodano, 1992, Lahey Jr *et al.*, 1993); (iii) being proportional to the Reynolds stress tensor (Drew, 2001, De Bertodano, 1998); (iv) a proposed random dispersion model without any tuneable coefficients (Dhotre *et al.*, 2007) and (v) a Favre-Averaged Drag (FAD) model by conducting the double-time averaging of drag term in the Reynolds time-averaged momentum transport equation for multiphase flows in the Eulerian frame (Burns *et al.*, 2004). Burns' *et al.* model has been mathematically analysed and validated for modelling turbulent dispersion. In addition, even if the suitable value of CTD is not chosen, their FAD

turbulent dispersion model can still work well in many CFD simulations for bubbly flows. As pointed out by Lavieville *et al.* (2017), such turbulent dispersion may result in the bubbles to disperse from the high concentration region to the low concentration region, and consequently make the local bubble volume fraction peak smoothly in the bubbly flows. The turbulent dispersion force has been discussed and the formulation has been proposed by Lubchenko *et al.* (2018), again assuming the hypothesis of the dispersion associated with the gradient of local bubble volume fraction. Bertodano (1992) proposed one of the first empirical models for description of turbulent dispersion force (TDF) as the product of proportionality coefficient and the gradient of dispersed phase (bubbles) volume fraction. However, the use of such models fully depends on the actual bubbly flow situations. For example, the proportionality coefficient CTD can change from a value of 0.1 to 0.5 for bubbles with the diameter of 1-5 mm. Lahey *et al.* (1993) conducted both experiments and numerical simulations to analyse the gas-liquid two-phase flow's lateral phase distribution. In their CFD modelling, the turbulent dispersion force proposed by Bertodano was employed but the proportionality coefficient CTD was set 0.1. Drew (2001) proposed a relationship for describing turbulent dispersion, which is suitable for bubbly flows to account for the ratio of turbulent eddy time scale to bubble relaxation time scale, the reciprocal of the Stokes number. Lucas *et al.* (2001) have indicated that the extra turbulence dispersion force caused by bubble deformation induced turbulence is necessary for prediction the radial bubble volume fraction

distribution in the pipe bubbly flows. They have indicated that the bubble deformation induced turbulence may play a role in smoothing the radial bubble volume fraction profiles in gas-liquid two-phase bubbly flow in the pipe.

As turbulent eddies interact with the bubbles in bubbly flows, the prediction of turbulence dispersion needs the suitable turbulence model and reasonable near-wall treatment while such models are usually associated with the turbulent eddy viscosity and turbulent intensity. For those turbulent eddies which scales are falling into the range of inertial sub-range (where Taylor integral length scale usually is located in this range) and larger than the imposed grid size, the use of large eddy simulation (LES) modelling can be better resolve the turbulent dispersion effect at larger scales as the turbulent eddy fluctuations that cannot be well caught up in the RANS can be differentiated in LES spatial filtering process. The impact from the SGS eddy fluctuation on bubble dispersion can be modelled. In addition, the shear turbulence generated in the liquid phase significantly affects the entrainment and migration of bubbles because bubbles may be entrapped by larger eddies while they may be also bombarded by those turbulent eddies with the size smaller than bubbles (Bhole *et al.*, 2008). The turbulent dispersion force model proposed by Bertodano (1994) has indicated the influences of liquid phase turbulent kinetic energy with the local turbulent intensity on the discrete phase (bubbles) dispersion in the bubbly flow. The model proposed by Burns *et al.* (2004) considered the effects of turbulent eddy viscosity and turbulent Prandtl number on evaluation of the dispersion of dispersed phase. Lavieville's *et al.* (2017) have proposed a generalised turbulent dispersion

(GTD) model which is also based on the assumption of including the influence of liquid turbulence on the drag force. They have also taken the statistical average of drag coefficient CD and added mass coefficient CVM into consideration for their GTD force model. Tabib and Schwarz (2011) also proposed a sub-grid-scale turbulent dispersion force model for large eddy simulation (LES) by introducing the SGS turbulent kinetic energy into Bertodano's model.

Due to the liquid phase turbulent eddies strong interaction with the bubbles, the bubbles are continuously subjected to the eddy hitting on their surface, consequently giving rise to the deformation of the bubble shapes if there are no bubble breakage or coalescence taking place and the variation of oscillation of the mass centre of the bubbles. Phenomenally, one can observe the bubbles to tumble in the bubble column. Sommerfeld *et al.* (2018) adopted LES-Eulerian-Lagrangian modelling to study bubble dynamics in particular the bubble oscillations and tumbling motion in the bubble column using the equation of motion for bubble motion by accounting for drag, transverse lift, added mass, wall forces and to implement the sub-grid-scale-turbulence modulation due to bubbles in the LES simulation. They also revealed that the Basset force actually has an important impact on bubble wriggling in its trajectory (Muniz and Sommerfeld, 2020). As the turbulence dispersion force plays a role in redistributing the bubble volume fraction in the bubble column while their contribution has been overlooked by some previous studies related to the bubble dynamics, it becomes necessary to highlight the impact of turbulent dispersion force on bubble fluctuations in the coupled SGS Eulerian-Eulerian LES

modelling. In other words, the effort of the modification of turbulent dispersion force on bubble dynamics can be viewed in the frame of the sub-grid scale. As it has been widely recognised that the use of Eulerian-Eulerian two-fluid model approach can efficiently describe both carrier and dispersed phase dynamics with lower computational demand, especially for large scale systems, the aim of the present work will be further elucidating the effect of considering turbulent dispersion force on the bubble dynamics in the bubble column.

When employing the Eulerian-Eulerian modelling approach to model bubbly flow, the averaging procedure will normally give rise to the term of so-called turbulent dispersion force in the interphase momentum exchange source terms. The turbulent dispersion force can be regarded as a hydrodynamic interaction that the carrier phase turbulent eddies entrain the bubbles, consequently contributing to the change in the radial spreading of bubble volume fraction profile (Moraga *et al.*, 2003). To consider mimicking the bubble dynamics such as bubble cluster fluctuation using the frame of Eulerian-Eulerian modelling approach, one may interpret the bubble tumbling and deformation as the consequence of the interactions between bubbles and the surrounding turbulent eddies, where the turbulent fluctuations can be envisaged as the different size of small eddies continuously acting on the surfaces of the bubbles. In reality, the reason for this tumbling motion can be described by the observation of clustered bubble oscillation. The turbulent fluctuations caused by turbulent eddies due to LES filtering process can be interpreted as a number of adjacent and anisotropic small eddies acting on the bubbles as illustrated in Figure

3-1. The surficial shapes of the bubbles dynamically deform as the consequence of the continuous hitting by these surrounding eddies, which will either stretch or squeeze the large bubble simultaneously. As a result, this action may lead to the fluctuation of the bubble mass-centre as schematically illustrated in Figure 3-2. The bubbles may be also entrapped in a relatively larger eddy and deformed by the eddy induced shear, the change of the surface curvature eventually leads to the oscillation of the bubble mass centre as can be schematically indicated in Figure 3-2. Thus, the interphase forces exerting on the dispersed phase are strongly affected by interactions between the bubbles and the shear caused by nearby turbulent eddies. These interfacial momentum transfer exchanges have to be properly implemented in the sub-grid scale LES modelling for bubble column bubbly flows.

In the present study, the effect of adoption of the spatial filtering to the interfacial momentum exchange term on the turbulent dispersion of bubbles in bubble column bubbly flows is examined, in particular to the drag force acting on the bubbles that is proportional to the slip velocity between the phases and interfacial area density. By taking both phase velocity fluctuations and area interfacial area density fluctuations into account, the spatial filtering of the drag force term will give rise to the extra term proportional to the area density slip velocity correlation i.e., turbulent dispersion. After employing the SGS eddy diffusivity hypothesis, the spatial-filtered drag force term is used to mimic the turbulent dispersion effect in the frame of Eulerian-Eulerian two-fluid model approach, implicitly revealing the dynamic behaviour of bubble tumbling in the bubble column. In our modified SGS Smagorinsky model, the modified SGS eddy viscosity ν_T that has considered the bubble

dynamic response to the eddy induced shear has been implemented into the filtered turbulent dispersion term (Long *et al.*, 2020).

The remainder of this chapter is organised as follows. The essential mathematical modelling and the numerical method to bubble column bubbly flow are described in Section 2. In Section 3, the numerical results is summarized when considering the effect of turbulent dispersion on bubble entrainment by turbulent eddies and discuss the results of various statistics involving the fluctuating velocity field, turbulent kinetic energy spectra with a special emphasis on the large-scale structure of bubble transport in the bubble column and the implication for turbulent dispersion that may partially play a role in giving rise to bubble cluster oscillation and wobbling in the bubble column. The main conclusions are given in section 4.

2. MATHEMATICAL MODELLING AND NUMERICAL METHODS

2.1 Governing equation

The two-fluid model is employed based on the LES spatial filtering of mass and momentum conservation equations. In the current work, both the continuous liquid phase and dispersed bubble phase are modelled as two interpenetrating continuums. It can be assumed that the filtered equations of the large-scale length turbulent eddies in bubble column bubbly flow can be solved by using the filtered equations. While the sub-grid-scale models are used for closure regarding to the unresolved

turbulent scales. Regardless of the mass transfer between the carrier and dispersed phase, the flow is assumed to be adiabatic. When employing this Eulerian-Eulerian two-fluid model, each phase requires separate filtered equations. Apply the filtering operation to the phase-weighted microscopic conservation equation, the filtering form of the governing equations are given by

$$\frac{\partial}{\partial t}(\rho_k \alpha_k) + \nabla \cdot (\alpha_k \rho_k \boldsymbol{u}_k) = 0 \tag{3-1}$$

$$\frac{\partial}{\partial t}(\alpha_k \rho_k \boldsymbol{u}_k) + \nabla \cdot (\alpha_k \rho_k \boldsymbol{u}_k \boldsymbol{u}_k) = -\nabla \cdot (\alpha_k \tau_k) - \alpha_k \nabla p + \alpha_k \rho_k g + \boldsymbol{M}_{F,k} \,. \tag{3-2}$$

In Equations (3-1) and (3-2), α_k is the filtered void fraction of phase *k*, defined by averaging the phase-indicator function (Drew and Passman, 2006). *k* signifies the component, liquid or bubbles with k=G for gas phase and k=L for liquid. Velocities in Equations (3-1) and (3-2), $\boldsymbol{u}_k$ is the filtered velocity vector for phase *k* in grid scale, given as $\widetilde{\boldsymbol{u}}_k = \boldsymbol{u}_k + u'_k$. Here $\widetilde{\boldsymbol{u}}_k$ is the instantaneous velocity and $\boldsymbol{u}'_k$ stands for the sub-grid scale (SGS) velocity, which needs to be modelled. The terms on the right-hand side of Equation (3-2) respectively represent the stress, the pressure gradient, gravity and the filtered interphase momentum exchange, which arises from the actions of the interface forces. The stress term is expressed as Equation (3-3), given by

$$\tau_k = -\mu_{eff}\left(\nabla \boldsymbol{u}_k + (\nabla \mathbf{u}_\mathrm{k})^T - \frac{2}{3} I (\nabla \cdot \boldsymbol{u}_k)\right) \tag{3-3}$$

where μ_{eff} is the effective viscosity of the liquid phase, which may be assumed to be composed of three contributions; the molecular viscosity, the turbulent eddy viscosity and an extra term to model bubble induced turbulence as shown by Equation (3-4),

$$\mu_{eff} = \mu_{L,L} + \mu_{T,L} + \mu_{BI,L} . \tag{3-4}$$

The extra viscosity caused by the bubble induced turbulence is now usually modelled based on Sato's model, which is given by

$$\mu_{BI,L} = \rho_L C_{\mu,BI} \alpha_G d_B |\boldsymbol{u}_G - \boldsymbol{u}_L| . \tag{3-5}$$

However, as will be discussed later in the present work, this viscosity due to the bubble induced turbulence may also be contributed by the relative fluctuation differences between the bubbles and those turbulent eddies that have equivalent or slightly larger length scale and entrapped the bubbles (Long *et al.*, 2020). The filtered momentum exchange term can be classified as different contributions from the interface forces, which are defined by

$$\boldsymbol{M}_{F,L} = -\boldsymbol{M}_{F,G} = \boldsymbol{M}_{D,L} + M_{L,L} + \boldsymbol{M}_{VM,L} + \boldsymbol{M}_{TD,L} \tag{3-6}$$

where the terms on the right-hand side are interphase forces acting on the bubbles that caused by the drag, lift, added mass and turbulence dispersion individually. The adopted forces expressions are summarised in Table 3-1.

Table 3- 1 Interphase force closure.

Forces	Expressions
Drag	$\boldsymbol{M}_{D,L} = \frac{3}{4}\alpha_G \rho_L \frac{C_D}{d_B}\lvert\boldsymbol{u}_G - \boldsymbol{u_L}\rvert(\boldsymbol{u}_G - \boldsymbol{u_L}),$ $C_D = \frac{2}{3}E_O^{\frac{1}{2}}, E_0 = \frac{g\Delta\rho d_B^2}{\sigma}$
Lift	$\boldsymbol{M}_{L,L} = \rho_L C_L(\boldsymbol{u}_B - \boldsymbol{u}_L) \times (\nabla \times \boldsymbol{u}_L),$ $C_L = \begin{cases} min[0.288tanh(0.121Re_B), f(E_O')] & E_O' \le 4 \\ f(E_O') & 4 < E_O' < 10 \\ -0.29 & E_O' > 10 \end{cases}$ $E_O' = \frac{g(\rho_l - \rho_g)d_h^2}{\sigma}, d_h = d(1 + 0.163E_O'^{0.757})^{1/3}$
Added mass	$\boldsymbol{M}_{AM,L} = \alpha_G \rho_L C_{AM}\left(\frac{D\boldsymbol{u}_G}{Dt} - \frac{D\boldsymbol{u}_L}{Dt}\right)$

With regards to the turbulent dispersion term $\boldsymbol{M}_{TD,L}$, it can be obtained by spatial filtering the phase-averaged interface drag force term. The mechanism responsible for bubble acceleration due to liquid phase velocity fluctuations is associated with the interphase momentum transfer. Thus, it would be reasonable to assume that turbulent dispersion may be modelled using the spatial filtering the fluctuating part

of the interphase momentum force, especially the drag force. The attention is restricted here to the interphase drag force. The interphase drag force can then be specified to be proportional to slip velocity and area density,

$$\widetilde{\boldsymbol{M}}_D = \frac{1}{8}\tilde{C}_D \tilde{A}_{GL} \rho_G |\widetilde{\boldsymbol{u}}_G - \widetilde{\boldsymbol{u}}_L| (\widetilde{\boldsymbol{u}}_G - \widetilde{\boldsymbol{u}}_L) \tag{3-7}$$

where the bubble area density is given by

$$\tilde{A}_{GL} = \frac{6\widetilde{\alpha}_G}{d_B}. \tag{3-8}$$

Taking the spatial filtering Equation (3-7) by accounting for velocity fluctuations and area density fluctuations, Equation (3-9) is obtained,

$$\boldsymbol{M}_D = \boldsymbol{M}_{D,L} + \boldsymbol{M}_{TD,L} = \frac{1}{8} C_D A_{GL} \rho_G |\boldsymbol{u}_G - \boldsymbol{u}_L| (\boldsymbol{u}_G - \boldsymbol{u}_L) + \frac{1}{8} C_D \rho_G |\boldsymbol{u}_G - \boldsymbol{u}_L| \overline{A'_{GL}(\boldsymbol{u}'_G - \boldsymbol{u}'_L)} \tag{3-9}$$

where the drag coefficient and bubble diameter have been assumed to remain unchanged in the spatial filtering process. It can be seen from Equation (3-9) that the filtering the interfacial drag force gives rise to the filtered drag term, written in terms of spatial-filtered variables, plus an extra term proportional to the area density-slip-velocity correlation $\frac{1}{8} C_D \rho_G |\boldsymbol{u}_G - \boldsymbol{u}_L| \overline{A'_{GL}(\boldsymbol{u}'_G - \boldsymbol{u}'_L)}$. If this correlation is modelled by using the SGS eddy diffusivity hypothesis, this is given by

$$\frac{1}{8}C_D\rho_G|\boldsymbol{u}_G-\boldsymbol{u}_L|\overline{A'_{GL}(\boldsymbol{u}'_G-\boldsymbol{u}'_L)}=\frac{1}{8}C_D\rho_G|\boldsymbol{u}_G-\boldsymbol{u}_L|\left(\frac{\nu_{SGS,G}}{\sigma_{SGS,G}}-\frac{\nu_{SGS,L}}{\sigma_{SGS,L}}\right)\frac{\nabla\overline{A_{GL}}}{\overline{A_{GL}}} \tag{3-10}$$

where $\overline{A'_{\mathrm{k}}\boldsymbol{u}'_{\mathrm{k}}}$ is related to turbulent dispersion as it reflects the effect of turbulent eddies interaction with bubbles on the change of bubble interface area, caused by turbulent eddy fluctuations characterised by the fluctuating velocities. By analogy with the eddy diffusivity hypothesis, the relationship between the SGS area density fluctuation and SGS relative velocities can be specified in the format of relationship between volume fraction and fluctuation velocity and modelled with aid of Equation (8), which is given by

$$\frac{\overline{A'_{GL}(\boldsymbol{u}'_G-\boldsymbol{u}'_L)}}{\overline{A_{GL}}}=\frac{\overline{\alpha'_G(\boldsymbol{u}'_G-\boldsymbol{u}'_L)}}{\overline{\alpha_G}} \tag{3-11}$$

where $\nu_{SGS,k}$ is the SGS turbulent kinematic viscosity and $\sigma_{SGS,L}$ denotes the SGS turbulent Schmidt number in terms of the interfacial area density. $\sigma_{SGS,L}$ = 0.9 has been used in the present study. Thus, the turbulent dispersion term can be expressed and simplified as

$$\boldsymbol{M}_{TD,L}=-\frac{3}{4}\rho_G\frac{C_D}{d_G}|\boldsymbol{u}_G-\boldsymbol{u}_L|\left(\frac{\overline{\alpha'_G u'_G}}{\alpha_G}-\frac{\overline{\alpha'_L u'_L}}{\alpha_L}\right)=-\frac{3}{4}\rho_G\frac{C_D}{d_G}|\boldsymbol{u}_G-\boldsymbol{u}_L|\frac{\nu_{SGS}}{\sigma_{SGS}}\left(\frac{\nabla\alpha_G}{\alpha_G}-\frac{\nabla\alpha_L}{\alpha_L}\right). \tag{3-12}$$

Since $\alpha_L+\alpha_G=1$ in this two-phase flow system and $\nabla\alpha_L+\nabla\alpha_G=0$, this would yield Equation (3-13):

$$\boldsymbol{M}_{TD,L} = -\frac{3}{4}\rho_G \frac{C_D}{d_G}|\boldsymbol{u}_G - \boldsymbol{u}_L|\frac{\nu_{SGS}}{\sigma_{SGS}}\left(\frac{1}{\alpha_L}+\frac{1}{\alpha_G}\right)\nabla\alpha_G \,. \tag{3-13}$$

As mentioned in section 1, one can think of the deformation of bubbles as a result of the interactions between bubbles and the surrounding turbulent eddies in the frame of Eulerian-Eulerian modelling, which gives rise to the bubble cluster fluctuation. Following the previous work of Long *et al.*(2020) by considering bubble dynamic response to the shear caused by turbulent eddies acting on the bubbles, the liquid-phase turbulence eddy viscosity can be modified as the sum from the filtered turbulent shear and dynamic SGS eddy viscosities, which is written as,

$$\mu_{T,L} = \rho_L(C_s\Delta)^2|S|(1 + \mathrm{C_b}\alpha_G \frac{\lambda}{d_B}\left(\frac{1}{1+St_{SGS}}\right)^{\frac{3}{2}}) \tag{3-14}$$

where λ represents the different turbulent length scales in the range between the integral and Kolmogorov scales ($L>\lambda>\eta$), *Cs* is a model constant, *S* is the characteristic filtered rate of strain tensor and St_{SGS} is the non-dimensional Stokes number expressed as $St_{SGS} = \frac{\tau_{\mathrm{bubble}}}{\tau_{L,SGS}}$. Here, the bubble response time scale is proposed by Sommerfeld *et al.* (2018), $\tau_{\mathrm{bubble}} = \frac{4(\rho_G+0.5\rho_L)d_B^2}{3\mu_L C_D Re_B}$. Bubble Reynolds number $Re_{B,max} = \frac{\rho_L d_B u_{slip}}{\mu_L} \approx 714.95$ in this chapter. The turbulent eddy turn-over time in sub-grid scale can be estimated by $\tau_{L,SGS} = \Delta/\boldsymbol{u}'_{\mathrm{L,SGS}}$, where $\Delta = \left(\Delta_i\Delta_j\Delta_k\right)^{1/3}$ is the filter width and $\mathrm{u}'_{\mathrm{L,SGS}}$ stands for the liquid fluctuation velocity in local grid. That $\lambda\sim\Delta$ is assumed since the filter length scale is usually to fall into the range of

inertia subrange wave length of turbulent kinetic energy spectrum. Thus, the turbulent dispersion considering turbulent eddies interaction with bubbles, which may give rise to bubble deformation or oscillation in bubble column bubbly flow can be evaluated by

$$\boldsymbol{M}_{TD,L} = C_{TD}\frac{3}{4}\rho_G\alpha_G\frac{C_D}{d_G}|\boldsymbol{u}_G - \boldsymbol{u}_L|\frac{(C_s\Delta)^2|S|\left(1+C_b\alpha_G\frac{\Delta}{d_B}\left(\frac{1}{1+St_{SGS}}\right)^{\frac{3}{2}}\right)}{\sigma_A}\left(\frac{1}{\alpha_L}+\frac{1}{\alpha_G}\right)\nabla\alpha_L \,. \tag{3-15}$$

It can be seen that the effect of sub-grid scale bubble induced turbulence on SGS turbulent dispersion and viscosity has been incorporated into Equation (3-15). Equation (3-15) will be implemented into the present LES simulations and it is referred to as the modified sub-grid turbulent dispersion force model (SGS-TDF).

2.2 Numerical Modelling

The reliability of the proposed SGS turbulent dispersion model was validated by comparing the simulation results with the detailed experimental data as reported by Sommerfeld *et al.* (2018) and the author's experiment using the PIV. Both the modelled circular bubble column and the actual bubble column used in the experiments have an internal diameter of 140 mm, which was filled with liquid at a static height of 0.65m. The experimental bubble column has a gas sparger that contains 50 evenly distributed capillaries at 0.4 mm in diameter, injecting the gas from the annular region within 100 mm in diameter. The detailed operation parameters for the selected case are listed in Table 3-2.

Table 3- 2 Operation parameter.

Gas Flow Rate (L/h)	Global Gas Hold-up (%)	Number-averaged Bubble Diame-ter(mm)	Static Liquid Height (m)	Observa-tion Height (m)
160	1.26	2.55	0.65	0.325

The same measured number weighted bubble size distribution (BSD) among the entire bulk phase obtained in the experiment was adopted. A good prediction of the BSD is crucial for estimating the interfacial area, which directly has an impact on calculating the thermal and mass transfer rate in the bubble column reactor. In the previous studies on bubble column bubbly flow, a Gaussian distribution of the BSD at the bubble column inlet area was assumed for various configuration of bubble distributors or spargers and applied for different superficial velocity conditions (Polli *et al.*, 2002). As an example, Polli *et al.* (2002)suggested an empirical correlation for approximately estimating the bubble size distribution at the gas distributor,

$$\mathrm{f_i} = q \cdot \exp\left(-\frac{(d_i-\bar{d})^2}{\left(\gamma^p d_{i,min}^3\right)^{2/3}}\right) \tag{3-16}$$

where, *i* denotes the *i*-th class of bubbles at the sparger region, *f* represents the void

fraction of the *i*-th class of bubbles and *d* stands for the bubble diameter. $\bar{d}$ denotes the bubble mean diameter, *p* and *q* are the coefficients which satisfy the requirement of $\sum_{i=1}^{n} f_i = 1$. γ stands for the volume increment ratio. In general, the original BSD must be related to the quantity and the diameter of the sparger capillaries, properties of the carrier phase and superficial velocities. In terms of trial simulations, the correlation between f_i and $\bar{\mathrm{d}}$ together with γ may be much more efficient. After considering the condition of the gas aerator used in the experimental set-up and the correlations suggested for the inlet superficial velocity and the averaged BSD in the studies (Kulkarni *et al.*, 2004, Bhole *et al.*, 2008, Yang and Xiao, 2017), the BSD adopted at the inlet and the experimental set-up of bubble column as shown in Figure 3-3 was used to specified for the mean diameter of the bubbles in the present LES simulation. It should be noted here that during the bubble rising up to the liquid top surface in the bubble column, they may coalescence with other bubbles or break up. Consequently, these interactions within the reactor can produce bubbles of different diameters, shapes and velocities. Yet, when talking about the homogeneous regime in bubble column reactor i.e., $\alpha_G < 0.04$, the diameters of the bubbles and the slip velocities are nearly the same for bubbles transported in the column. Apart from these, bubbles move with small collision, breakup and coalescence rates (Pourtousi *et al.*, 2015). If no coalescence and breakup occurrence is assumed, the bubble number density equation can be expressed by

$$\frac{\partial n}{\partial t} + \nabla \cdot (\boldsymbol{u}_G \mathrm{n}) = 0. \tag{3-17}$$

In order to simulate the dispersed phase, a mean diameter of the dispersed particles, droplets or bubbles needs to be specified. In terms of spherical particles, the mean diameter is the actual diameter. While for non-spherical particles and bubbles or droplets, a Sauter mean diameter (the diameter of a sphere with the same volume as the particles) is required and can then be obtained by

$$d_{G32} = \left(\frac{6\alpha_G}{\pi n}\right)^{1/3}. \tag{3-18}$$

It can be assumed that the local bubble equivalent diameter's variation is the same order of the level of grid scales, therefore, the bubble size can be characterised with the 0-th moment of the bubble size distribution i.e., only taking the local mean bubble diameter. Thus, one mean bubble diameter rather than a range of bubble sizes can be specified. This approach requires much less computational effort and offers a surprisingly good agreement with available experimental data in comparison with other ways for evaluating bubble sizes such as the adoption of population balance model (PBM) (Huang *et al.*, 2018).

ANSYS CFX 18.0 with complied CCL is employed for Euler/Euler LES modelling in the present study. The physical properties for two phases are: $\rho_g = 1.185\frac{kg}{m^3}$, $\mu_g = 1.83e-5\frac{kg}{m\,s}$, $\rho_L = 997\ \frac{kg}{m^3}$, $\mu_g = 8.89e-4\frac{kg}{m\,s}$. The boundary conditions are set as follows. At inlet, a mass flow rate perpendicular to the inlet is adopted, which is corresponding to the experimental conditions as reported in Sommerfeld

et al. (2018), and the volume fraction for each phase is specified as: $\alpha_L = 0, \alpha_G = 1$. At the top surface of the reactor, a pressure-constant boundary i.e., relative pressure being specified to be 0, is used. A non-slip condition is used for the inner wall of the bubble column. A central-differencing discretisation scheme is used for the momentum equations, while a second-order backward Euler scheme is employed regarding to the discretization algorithm for the transient term in all of the simulations. The mesh set-up for the current LES modelling is illustrated in Figure 3-4.

The bubble column was discretized with the cell size of Δx^+=100 and Δr^+=5 with growth rate of 1.2. In order to validate the proposed SGS-TDF model, the mesh independency was check with $d_{mean}/\Delta = 0.51$, 0.6375 and 0.85 in the cross section at z=325mm of the bubble column as shown in Figure 4. The time-averaged bubble velocities at middle point at z=325mm obtained from three mesh set-up cases are compared with the experimental results obtained from the present study and carried out by Sommerfeld *et al.* (2018). The time averaged velocity is calculated by using the relationship given by

$$\overline{u_B} = \frac{1}{N\Delta t}\sum_{i=1}^{N} \boldsymbol{u_{Bi}}(r,t)\Delta t \tag{3-19}$$

where $\overline{u_B}$ represents the time-averaged bubble velocity, *N* stands for the number of the collected samples, Δt is the sampling time period. Close inspection of the Figure 5 shows that the predicted results employing three grids follow the trend of the experimental axial bubble velocity. No notable variations are found between the

mesh of $d_{mean}/\Delta = 0.6375$ and the finer one. Both grids produce results that are in good accord with the experiments when comparing to the coarser grid $d_{mean}/\Delta = 0.51$. Details on simulation results utilizing the modified model will be discussed in the following section. Regarding to the more accurate predictions of the axial bubble velocity, which are compatible with the experimental values. With caution and the perspective of the computational cost, $d_{mean}/\Delta = 0.6375$ in the core-region was used in the current Eulerian-Eulerian LES modelling. The grid resolution adopted in the simulation is considered reasonably close to Milelli's limit (Milelli, 2002). By using this mesh set-up, the control volume cell size is and large enough to contain the interface details and fine enough to resolve large scale turbulence. The mesh set-up with 95,400 cells was thus adopted throughout our LES simulations.

3. RESULTS AND DISCUSSION

Two cases with and without considering turbulent dispersion force model have been investigated and four simulations have been carried out using the Euler/Euler LES approach, by adopting the uniform bubble diameter $d_b = 2.55mm$ and the MUSIG model but with the BSD that has been experimentally obtained for the bubble column sparger inlet, respectively. The time step is set in terms of CFL criterion, $\min(\frac{|\boldsymbol{u}_L|\delta t_E}{\Delta}, \frac{|\boldsymbol{u}_G - \boldsymbol{u}_L|\delta t_E}{\Delta}) < 1.0$, varying from 0.0005 s to 0.001s for capturing the transient behaviour of turbulent shear eddy evolution in the bubble column. The simulations were run to last for 100 seconds while the instantaneous velocities at given

positions were monitored and recorded during the calculation process. In order to obtain the turbulence statistical characteristics, the time average was taken over a period of 50 seconds after the bubbly flow fluctuation patterns have been well established, i.e. about 4 periods have been achieved.

3.1 Effects of accounting for the turbulent dispersion in LES on bubble transport

Figure 3-6 shows the normalised time-averaged liquid axial liquid and instantaneous velocity field in the cutting plane of the bubble column. As the unsteady turbulence prediction from LES can better resolve the most of large-scale turbulence in space and time, the time-averaged results of LES for liquid velocity and residence time can be used to estimate the large turbulent eddy length and time scales, which is approximately the Taylor integral scale for the bubble column reactor. For bubble column bubbly flow, it has been observed the existence of a wide range of length and time scales to affect the transport processes in the bubble column, which can be regarded as the combination of four flow patterns, including the descending flow, large eddy spiraling, fast bubble rising up and central pluming. As can be seen from Figure 3-7, the LES simulation using the modified SGS-TDF model has well captured the characteristics of the ascending gas-liquid two-phase flow in the bubble column. The instantaneous velocity vector field at t=3.0, 50.0, 75.0, and 90.0s, highlighted by the instantaneous bubble volume fraction, clearly shows the bubble spirally rising-up induced flow. It can be seen from the figure that the descending flow takes place near the wall, characterised by the downward velocity vectors

while higher bubble void fraction occurring in the centre of the column points out that the bubbles are collected and entrained by the central large turbulent eddies. At t = 3.0 s, the large eddy flow may not be fully developed, but at t = 50.0, 75.0, and 90.0 s, it can be seen clearly that there are a number of large eddy fluctuating in the entire liquid zone, accompanied by time-dependent fluctuations of the bubble volume fraction contours.

To highlight the importance of the turbulent dispersion in affecting the bubble transport in Eulerian-Eulerian LES modelling, the results obtained by using our modified SGS-TDF model are also compared with those using Euler/Lagrange LES simulation (Sommerfeld *et al.*, 2018) as shown in Figures 3-8 and 3-9. In Figure 3-8, the time-averaged liquid and bubble axial velocity profiles predicted by using the modified and standard turbulent dispersion force models at height z=0.325m are illustrated. The experimental results reported and the Eulerian-Lagrangian simulation results carried out by Sommerfeld *et al.* (2018) are also presented for comparison. According to their Euler/Lagrange simulation, the interfacial forces such as drag, wall lubrication, lift, buoyancy, added mass forces are accounted. Our Euler/Euler LES simulation has employed the forces that include the time averaged drag, lift, buoyancy, added mass forces together with the use of the modified SGS-TDF bubble turbulent dispersion and took the bubble induced turbulence into account (Cases 2 and 4). Since the standard turbulent dispersion force is modified with the consideration of bubble response to eddies, the result obtained for Case 4 can be therefore compared with Case A of Sommerfeld *et al.* (2018). In addition,

an additional factor with bubble shape change, i.e. the ratio of the long axis to short axis of the bubble, for bubble oscillation was considered in their simulation (Case B). It can be seen from Figure 3-8 that the use of adjusted BSD at inlet for our Euler/Euler LES by implementing either the modified or standard SGS-TDF force model (Cases 3 and 4) performs better than the simple use of one bubble diameter (Cases 1 and 2) for prediction of both liquid and bubble velocity profiles. It is worth noting that the transient behaviour of different sizes of bubbles is actually different from the one described by specifying an equivalent mean bubble size. Here, the findings imply the significance of adopting a multi group sizes of bubble diameter model.

When restricting the attention to the results using the MUSIG approach (Cases 3 and 4), the predicted bubble axial velocity profile is in good agreement with the experimental data as reported by Sommerfeld *et al.* (2018). It can be seen from Figure 3-8 that the liquid axial flow is distinctly upward in the central region, while a descending flow can be observed in the vicinity of the wall, consistent with the trend based on the experimental observation. The position of flow reversal is clearly seen to take place at a radial location of around r/R=0.6–0.8. The bubble velocity profile predicted by neglecting the SGS-TDF contribution shows a greater difference from the experimental result. This clearly demonstrates that the inclusion of the modified SGS-TDF in LES simulation has a remarkable influence on the bubble radial migration. It should be noted that the consistency of Euler/Euler LES modelling results on predicted liquid phase axial velocity and volume fraction profiles

compared with the experimental data are slightly poor in the central region of the bubble column but becomes good in the near-wall region. This may be attributed to the fact that bubbles are more likely to coalescence in the central region where the equivalent bubble diameter d_B may change quite a lot. While a roughly 4 mm bubble size was allocated in this region, which corresponds to $\frac{d_B}{\Delta} \in (0.875, 1.025)$ and has violated the criterion of Milelli *et al.* (2002), the use of BSD may overestimate the bubble fluctuation in the main flow direction so that the induced liquid velocity may be slightly overestimated. On the other hand, relatively small bubbles are likely to accumulate near the wall region, which are very sensitive to the surrounding turbulent eddies. This further indicates that the use of the modified SGS-TDF model has a function that modulates the bubble dispersion behaviour, consequently giving rise to a better estimation of the void fraction gradient and a better prediction of the bubble lateral dispersion. Based on the comparison with Euler/Lagrange LES results (Case B) of Sommerfeld *et al.* (2018), it has been shown that our Euler/Euler LES coupled with the modified SGS-TDF model can still deliver consistent results for bubble dynamics when comparing with the experimental data.

Figure 3-9 shows the time-averaged radial bubble volume fraction distribution obtained by using the standard SGS-TDF and modified SGS-TDF models that are marked as cases 3 and 4, compared with the Euler/Lagrange LES simulation results reported by Muniz and Sommerfeld (2020). It is worth mentioning that the adoption of the bubble dynamic model has significantly improved the simulation results that were well matched the experimental data in their work. Two dash lines represents

the predicted bubble volume fraction with (blue) and without (orange) bubble dynamics model. The prediction of bubble void fraction profiles can be used as an indicator to assess whether the proposed TDF model is working properly. It can be observed that the predicted profile by using the modified SGS-TDF model is comparable to the blue dashed line, also consistent with the bubble velocity profiles (Figure 3-8). Compared to the one without using the modified SGS-TDF model, a noticeable improvement was found especially in the near wall region though the magnitude of contribution from the turbulent dispersion force predicted using the modified SGS-TDF is small as compared to the other forces. The fact that the results obtained by considering the fluctuating $\overline{\alpha_k' \boldsymbol{u}_k'}$ with dynamic response to surrounding eddies are improved and are better consistent with the experimental results highlights the need for inclusion of the SGS-TDF for properly modelling bubble dispersion especially bubble radial migration in the bubble column bubbly flow. It can be cautiously claimed that the bubble lateral dispersion effect may be highly associated with the bubble oscillations as the filtered turbulent eddy fluctuations bring out the bubble surface deformation if there is no coalescence occurring (see Figures 3-1 and 3-2).

3.2 Quantification of SGS-turbulent dispersion force contribution and effect on bubble oscillation

In the preceding section, $\overline{A_k' \boldsymbol{u}_k'}$ has been identified to be related to filtered eddy fluctuation induced turbulent dispersion and it has a potential impact on turbulent eddies interaction with bubbles, which may result in the change of bubble interface

area. With the eddy diffusivity hypothesis, the relationship between the SGS area density fluctuation and SGS relative velocities can be specified in the format of relationship between volume fraction and fluctuation velocity as expressed by Equation (3-19)

$$\frac{\overline{A'_{GL}(\boldsymbol{u}'_G-\boldsymbol{u}'_L)}}{\overline{A_{GL}}}=\frac{\overline{\alpha'_G(\boldsymbol{u}'_G-\boldsymbol{u}'_L)}}{\overline{\alpha_G}}. \tag{3-19}$$

For the derivation of Equation (3-19), it has been assumed that the bubble diameter is unchanged by using equation (3-8). If this constraint is released, equation (3-19) can be approximated:

$$\frac{\overline{\alpha'_G(\boldsymbol{u}'_G-\boldsymbol{u}'_L)}}{\overline{\alpha_G}}\approx\frac{\overline{(A_{GL}d_B)'(\boldsymbol{u}'_G-\boldsymbol{u}'_L)}}{\overline{(A_{GL}d_B)}} \tag{3-20}$$

In fact, the bubbles would change their shapes in the duration of the rise-up in the bubble column, which would be characterised by the interfacial area and equivalent diameter variations. Thus, one can envisage Equation (3-20) to implicitly indicate the behaviour of instantaneous bubble shaper variations in the bubble column. In order to characterise the contribution from turbulent dispersion, the ratios of turbulent dispersion force and dominant drag force at different cross-sections along the height of the bubble column have been shown in Figure 3-10.

The radial turbulent dispersion force component at a given height has been obtained by the following averaging method,

$$\boldsymbol{M}_{TD,L}(\mathrm{r},\mathrm{z}) = \frac{1}{2\pi r}\int_0^{2\pi}\left[C_{TD}\,\frac{3}{4}\rho_G\alpha_G\,\frac{C_D}{d_G}\,|\boldsymbol{u}_G-\boldsymbol{u}_L|\,\frac{(C_s\Delta)^2|S|\left(1+C_b\alpha_G\frac{\lambda}{d}\left(\frac{1}{1+St_{SGS}}\right)^{\frac{3}{2}}\right)}{\sigma_A}\left(\frac{1}{\alpha_L}+\frac{1}{\alpha_G}\right)\nabla\alpha_L\right]rd\theta. \quad (3\text{-}21)$$

The turbulent dispersion resulted from sub-grid eddies cannot be experimentally measured or validated at the current stage. Figure 3-10 shows the quantification of the sub-grid turbulent dispersion force (instantaneous and filtering-averaged). By comparing the magnitude and the directional dominance in relation to drag force, the relative influence of filtering-averaged SGS-TDF within the particular flow system is able to be scaled. Figure 3-10(a) shows the ratio of instantaneous SGS-turbulent dispersion force to drag force along centreline and the cross-sectional averaged ratio at different cross-sections along the bubble column height at 100s. It can be seen from the figure that along the centreline, the absolute ratio of SGS-TDF to drag can reach 20%. Furthermore, a cross-sectional averaged ratio of 10% is reached at z=0.075m and the force ratio around 5% is remained along the height of the column. The decrease in the ratio of instantaneous SGS-turbulent dispersion force to drag force along the column height reveals that the bubble lateral dispersion is highly associated with the bubble cluster oscillations. Since the smaller distance from the gas distributor, the higher flow turbulence which is always accompanied

by higher frequency of bubble oscillations. Figures 3-10(b) shows the radial distribution of the ratio of time-averaged SGS-TDF to drag at z=0.2, 0.325 and 0.575 m, respectively. It becomes clear that the ratio is usually greater in the vicinity of the wall at each axial position, which further demonstrates the effect of the modified SGS-TDF term on bubble lateral dispersion. In terms of the ratio profile at z=0.2m, compared with the averaged drag force, the SGS-TDF magnitude can be even 1.7 times greater than the averaged drag force in the lower part of the bubble column. Apparently, high correlation of the bubble oscillation with the bubble dispersion does exist while the effects of SGS-turbulent dispersion force may retard the bubble cluster oscillation close to the wall, as evidenced by a larger ratio of SGS-TDF/Drag occurring with increase of the radial position. According to most of previously reported studies, the drag force can take around 60%-80% of all the considered interfacial forces (Muniz and Sommerfeld, 2020). Thus, the present study has highlighted the importance of the contribution of SGS-TDF.

Figure 3-11 displays instantaneous bubble volume fraction gradient at different height at different times together with the instantaneous SGS turbulent dispersion force distribution. A closer observation on the contours of the SGS-TDF force and bubble volume fractions indicates that the SGS-TDF is correlated with the variation of the instantaneous dispersed phase void fraction gradient and has a significant impact on bubble transport in radial direction than in the axial direction, i.e. the main flow direction for the bubble column.

3.3 Effects of turbulent dispersion on turbulent shear structures and turbulent kinetic energy spectra

In order to assess the impact of turbulent dispersion on the turbulent kinetic energy of the liquid phase, the one-dimensional LES-filtered turbulent kinetic energy power spectral density (PSD) E(κ) are presented in Figure 3-12 with the data extracted for Case 3 and 4. The axial turbulent velocity are monitored at the centre of the cross section at z = 0.325 m. The turbulent energy spectrum is obtained by taking the Fast Fourier Transform (FFT) of the time correlation of axial turbulent velocity fluctuations based on the Welch method (Welch, 1967). The one-dimensional model energy spectrum for single-phase flow as proposed by Pope is also shown in Figure 3-12 (Pope, 2001).

As can be seen from Figure 3-12, the PSD predicted by the modified SGS-TDF model can be still approximated and described by Pope's model spectrum, which is valid in the wide energy spectrum of turbulence, defined by

$$E(\kappa) = C\varepsilon^{2/3}\kappa^{=5/3}\left[\frac{\kappa L}{\sqrt{(\kappa L)^2+C_L}}\right]^{\frac{5}{3}+p_0} exp\left[-\beta\left\{\left[(\kappa\eta)^4+C_\eta^4\right]^{1/4}-C_\eta\right\}\right] \qquad (3\text{-}22)$$

in which η is the Kolmogorov micro-scale and L is the integral scale, characterising the large eddy size. This model spectrum can well indicate the shape of $E(\kappa)$ including the energy-containing and dissipation subranges of turbulence. The Kolmogorov constant C is normally set equal to 1.5 (Pope, 2001) but the value for C

was found to be around 1.65 in the present work. The parameter values C_L and C_η are calculated from the below integral constraints based on the spectrum obtained by the LES, which satisfy:

$$k = \int_0^\infty E(\kappa)d\kappa \tag{3-23}$$

and

$$\varepsilon = \int_0^\infty 2\nu\kappa^2 E(\kappa)d\kappa \tag{3-24}$$

The parameters β and p_0 are found to be equal to 5.2 and 2.0, respectively. The modified SGS-TDF model gives a -5/3 scaling in lower frequency zone while presents a -3 scaling law measured based on the wave number κ larger than the typical wave number characterized by the bubble size, i.e. $\kappa_B = \frac{2\mathrm{p}}{d_B} = 1049.73\ m^{-1}$. Here the representative bubble frequency is estimated by $f_b = |\boldsymbol{u}_G - \boldsymbol{u}_L|/2\pi d_B$= 12.48 Hz using the bubble mean diameter of 2.55 mm (Prakash *et al.*, 2016). It can be seen from Figure 3-12 that the transition for different scaling laws in $E_{11}(\kappa)$ takes place at about $f_1 \approx$ 14.80 Hz, where the left of the transition location shows the -5/3 slope while the right side of the transition give rise to the -3 scaling, clearly indicating the feature of feeding of bubble induced turbulence to the turbulent kinetic energy. For the present case, this may indicate that the turbulence due to the bubble wake induced turbulence is fed into the liquid shear turbulence at frequencies around $f_1 \approx$14.80 Hz, close to the representative bubble frequency. The kinetic energy power spectral density of the axial liquid velocities, predicted at the middle

point at z= 0.2m and z=0.4m are also shown in Figure 3-12(c) and 3-12(d). Similarly, the clear trends of -3 scaling after the -5/3 scaling law are observed for the spectrums obtained from the case of using the modified SGS-TDF model in LES simulation.

In order to describe the effect of accounting the SGS TDF on turbulent eddy structural behaviour in the bubble column, the vorticity based on Q-criterion was assessed. As Q represents the local balance between the shear strain rate and vorticity magnitude, defining vortices as the zone where the vorticity magnitude is greater than the magnitude of rate-of-strain, it can be expected that such evaluation would give a qualitative description of the eddy structures existing in the bubble column. The velocity gradient tensor $\overline{D}$ is defined by $\boldsymbol{D}_{ij} = \frac{\partial \boldsymbol{u}_{Li}}{\partial x_j}$ and can be decomposed into a symmetric and askew-symmetric part: $\boldsymbol{D}_{ij} = \boldsymbol{S}_{ij} + \boldsymbol{\Omega}_{ij}$, where the shear strain rate $\boldsymbol{S}_{ij} = \frac{1}{2}\left(\frac{\partial \boldsymbol{u}_{Li}}{\partial x_j} + \frac{\partial \boldsymbol{u}_{Lj}}{\partial x_i}\right)$, the vorticity $\boldsymbol{\Omega}_{ij} = \frac{1}{2}\left(\frac{\partial \boldsymbol{u}_{Li}}{\partial x_j} - \frac{\partial \boldsymbol{u}_{Lj}}{\partial x_i}\right)$. The expression for Q, which characterises the eddy structure evolution, is thus defined by $Q = \frac{1}{2}\left|\left|\overline{\boldsymbol{\Omega}}\right|\right|^2 - \left|\left|\overline{\boldsymbol{S}}\right|\right|^2$. It is expected that turbulent large eddy structure development in the bubble column would be significantly affected by the entrained bubbles while this interaction between the bubbles and turbulent eddies has been accounted for in the modified SGS model. Thus, a correlation to reflect this coupling can be presented. Figure 3-13 shows the vorticity indicator Q (Q = 32.0176 s^{-2}) in the bubble column at t=90 s, highlighted by the local bubble volume fraction value. It can be

observed that the bubble volume fraction is strongly coupled with the vorticity indicator *Q*, in particular for the central high bubble volume fraction region. The following spatial correlation between the local bubble volume fraction and *Q* magnitude to characterise the interaction of large turbulent eddies with the entrained bubbles along the axial height of the bubble column is proposed and can be defined by

$$R(\Delta h) = \frac{\overline{\alpha_G'(h_0)|\boldsymbol{Q}'(h_0+\Delta h)|}}{\sqrt{\alpha_G'^2(h_0)}\sqrt{|\boldsymbol{Q}'^2(h_0)|}} \tag{3-25}$$

where equation (3-25), α_G' and Q' are defined by

$$\alpha_G' = \alpha_G - \frac{1}{h}\int_0^h \alpha_G dz\,, \tag{3-26}$$

$$Q' = Q - \frac{1}{h}\int_0^h Q dz\,. \tag{3-27}$$

Figure 3-14 presents the spatial correlation coefficient $R(\Delta h)$ along the centreline at different axial height from $\Delta h = 0$ to $\Delta h = 0.325$m with background superposed by the snapshots of the instantaneous *Q* distribution in the cutting plane of the bubble column. It can be seen from the figure that along the centreline, higher values of *Q*, coloured in red, are always accompanied by larger variations in the correlation coefficient $R(\Delta h)$ along the height. This can be interpreted as the consequence of energy containing turbulent large eddy development, which give rise to the local vorticity fluctuation around the spatially averaged shear induced vorticity along the height of the bubble column. Such turbulence induced vorticity changes strongly affect the entrainment of the bubbles, characterised by the local bubble volume

fraction fluctuations as can be seen from Figure 3-15. This phenomenon is also supported by the lower amplitude of the spatial correlation coefficient appearing in the region when h > 200mm, where the magnitude of the turbulent large eddy induced vorticity is gradually reduced.

4. CONCLUSIONS

Euler/Euler Large Eddy Simulations of the bubble column bubbly flow with the consideration of bubble induced turbulence SGS turbulent dispersion have been conducted. The transient turbulent bubbly flow velocities, transient local volume fraction and bubble fluctuations are captured. The time-averaged velocity profiles of both liquid and gas phases obtained from the LES are compared with the experimental data and the simulations using the SGS model without modification, and the liquid phase turbulent kinetic energy spectrum at the location in the centreline of the bubble column was presented. The main concluding remarks are summarised as follows:

1) The consistency of the axial bubble velocity profile by using the adjusted BSD at the inlet shows that bubble transportation cannot be well captured by using a mono size bubble diameter. Bubble dynamics in the bubble column can be captures by using the adequate SGS-TDF model in Eulerian-Eulerian LES modelling, when mimicking the bubble dynamic motion in sub-grid scale. It has been demonstrated clearly that by using Euler/Euler large-eddy simulations (LES) modelling with considering the effect of bubble-eddy interaction on SGS turbulent dispersion model,

the improvement on the prediction of bubble dynamics was achieved based on the bubble axial velocity and bubble void fraction profiles. This can imply that the modified SGS turbulent dispersion model plays an equivalent role in revealing the bubble fluctuating motion predicted by using Euler/Lagrange LES modelling approach but with the stochastic dispersion model (Sommerfeld *et al.*, 2018).

2) The cross-sectional averaged absolute ratio of SGS-TDF force to the time averaged drag force along the height of the bubble column is around 5%-10% with the higher percentage taking place in the lower part of the column. This indicates that the bubble dispersion, especially bubble lateral dispersion is highly associated with the SGS turbulence. SGS-TDF plays an important role in radial re-distribution of bubble volume fraction profiles while the time averaged drag force to great extent determines the bubble dispersion in the main flow direction.

3) The turbulent kinetic energy spectrum obtained from the Euler/Euler LES modelling for the axial liquid velocity at the given locations by using the modified SGS-TDF model has shown that the turbulent kinetic energy spectrum is still consistent with the trend predicted using the model spectrum as proposed by Pope (2001), likely being attributed to the lower bubble volume fraction bubbly flow in the bubble column. For the wavenumber of the turbulent eddies smaller than the characteristic wavenumber based on the bubble size, a -5/3 scaling law is observed, while a -3 scaling law can be observed for the wavenumber being larger than the characteristic wavenumber. This clearly demonstrates the effect of turbulent eddies with the

equivalent length scale to the bubbles or smaller ones on the bubble induced turbulence as shown by the turbulent kinetic energy spectrum. The transition location for the slope in the turbulent kinetic spectrum obtained using the modified SGS turbulent dispersion model for the cases in the present study occurs at f = 14.80 Hz, which is close to the characteristic frequency of bubble rising-up f_B =12.48 Hz.

4) A correlation between vorticity indicator Q and the local bubble volume fraction is proposed, revealing how the bubble dispersion is affected by the surrounding turbulent eddies.

REFERENCES

ANTAL, S., LAHEY JR, R. & FLAHERTY, J. 1991. Analysis of phase distribution in fully developed laminar bubbly two-phase flow. *International Journal of Multiphase Flow*, **17**, 635-652.

BHOLE, M., JOSHI, J. & RAMKRISHNA, D. 2008. CFD simulation of bubble columns incorporating population balance modeling. *Chemical Engineering Science*, **63**, 2267-2282.

BURNS, A. D., FRANK, T., HAMILL, I. & SHI, J.-M. The Favre averaged drag model for turbulent dispersion in Eulerian multi-phase flows. *5th International Conference on Multiphase Flow (ICMF2004).* ICMF, 1-17.

CARRICA, P., DREW, D., BONETTO, F. & LAHEY JR, R. 1999. A polydisperse model for bubbly two-phase flow around a surface ship. *International Journal of Multiphase Flow*, **25**, 257-305.

CHEN, P., DUDUKOVIĆ, M. & SANYAL, J. 2005. Three dimensional simulation of bubble column flows with bubble coalescence and breakup. *AIChE journal*, **51**, 696-712.

DARMANA, D., HENKET, R., DEEN, N. & KUIPERS, J. 2007. Detailed modelling of hydrodynamics, mass transfer and chemical reactions in a bubble column using a discrete bubble model: Chemisorption of CO2 into NaOH solution, numerical and experimental study. *Chemical Engineering Science*, **62**, 2556-2575.

DE BERTODANO, M. A. L. 1992. Turbulent bubbly two-phase flow in a triangular duct. PhD Dissertation, Rensselaer Polytechnic Institute.

DE BERTODANO, M. A. L. 1998. Two fluid model for two-phase turbulent jets. *Nuclear Engineering and Design*, **179**, 65-74.

DE BERTODANO, M. L., LAHEY JR, R. & JONES, O. 1994. Turbulent bubbly two-phase flow data in a triangular duct. *Nuclear Engineering and Design*, **146**, 43-52.

DEEN, N. G., SOLBERG, T. & HJERTAGER, B. H. 2001. Large eddy simulation of the gas–liquid flow in a square cross-sectioned bubble column. *Chemical Engineering Science*, **56**, 6341-6349.

DHOTRE, M., SMITH, B. & NICENO, B. 2007. CFD simulation of bubbly flows: Random dispersion model. Chemical Engineering Science, **62**, 7140-7150.

DREW, D. A. 2001. A turbulent dispersion model for particles or bubbles. *Journal of Engineering Mathematics*, **41**, 259-274.

Drew, D.A., 2003. A Turbulent Dispersion Model for Particles or Bubbles. In Analysis and Simulation of Multifield Problems (pp. 3-12). Springer, Berlin, Heidelberg.

Drew, D.A. and Passman, S.L., 2006. Theory of multicomponent fluids (Vol. **135**). Springer Science & Business Media.

GOSMAN, A., LEKAKOU, C., POLITIS, S., ISSA, R. & LOONEY, M. 1992. Multidimensional modeling of turbulent two-phase flows in stirred vessels. *AIChE Journal*, **38**, 1946-1956.

HOSOKAWA, S., TOMIYAMA, A., MISAKI, S. & HAMADA, T. Lateral migration of single bubbles due to the presence of wall. *Fluids Engineering Division Summer Meeting*, 2002. 855-860.

HUANG, Z., MCCLURE, D. D., BARTON, G. W., FLETCHER, D. F. & KAVANAGH, J. M. 2018. Assessment of the impact of bubble size modelling in CFD simulations of alternative bubble column configurations operating in the heterogeneous regime. *Chemical Engineering Science*, **186**, 88-101.

HUNT, J., AUTON, T., SENE, K., THOMAS, N. & KOWE, R. ICHMT International seminar on transient phenomena in multiphase flow. Dubrovnik, Yugoslavia, 1987. 103-125.

KERDOUSS, F., BANNARI, A. & PROULX, P. 2006. CFD modeling of gas dispersion and bubble size in a double turbine stirred tank. *Chemical Engineering Science*, **61**, 3313-3322.

KULKARNI, A. A., JOSHI, J. B. & RAMKRISHNA, D. 2004. Determination of bubble size distributions in bubble columns using LDA. *AIChE journal*, **50**, 3068-3084.

LAHEY JR, R., DE BERTODANO, M. L. & JONES JR, O. 1993. Phase distribution in complex geometry conduits. *Nuclear Engineering and Design*, **141**, 177-201.

LAÍN, S. & GRILLO, C. 2007. Comparison of turbulent particle dispersion models in turbulent shear flows. *Brazilian Journal of Chemical Engineering*, **24**, 351-363.

LAVIÉVILLE, J., MÉRIGOUX, N., GUINGO, M., BAUDRY, C. & MIMOUNI, S. 2017. A generalized turbulent dispersion model for bubbly flow numerical simulation in NEPTUNE_CFD. *Nuclear Engineering and Design*, **312**, 284-293.

LONG, S., YANG, J., HUANG, X., LI, G., SHI, W., SOMMERFELD, M. & YANG, X. 2020. Large-eddy simulation of gas–liquid two-phase flow in a bubble column reactor using a modified sub-grid scale model with the consideration of bubble-eddy interaction. *International Journal of Heat and Mass Transfer*, **161**, 120240.

LUBCHENKO, N., MAGOLAN, B., SUGRUE, R. & BAGLIETTO, E. 2018. A more fundamental wall lubrication force from turbulent dispersion regularization for multiphase CFD applications. *International Journal of Multiphase Flow*, **98**, 36-44.

LUCAS, D., KREPPER, E. & PRASSER, H.-M. 2001. Prediction of radial gas profiles in vertical pipe flow on the basis of bubble size distribution. *International Journal of Thermal Sciences*, **40**, 217-225.

MILELLI, M. 2002. A numerical analysis of confined turbulent bubble plumes. PhD Dissertation, ETH Zurich.

MORAGA, F., LARRETEGUY, A., DREW, D. & LAHEY JR, R. 2003. Assessment of turbulent dispersion models for bubbly flows in the low Stokes number limit. *International Journal of Multiphase Flow*, **29**, 655-673.

MUDDE, R. F. & SIMONIN, O. 1999. Two-and three-dimensional simulations of a bubble plume using a two-fluid model. *Chemical Engineering Science*, **54**, 5061-5069.

MUNIZ, M. & SOMMERFELD, M. 2020. On the force competition in bubble columns: A numerical study. *International Journal of Multiphase Flow*, **128**, 103256.

PFLEGER, D., GOMES, S., GILBERT, N. & WAGNER, H.-G. 1999. Hydrodynamic simulations of laboratory scale bubble columns fundamental studies of the Eulerian–Eulerian modelling approach. *Chemical Engineering Science*, **54**, 5091-5099.

POLLI, M., DI STANISLAO, M., BAGATIN, R., BAKR, E. A. & MASI, M. 2002. Bubble size distribution in the sparger region of bubble columns. *Chemical Engineering Scienc*e, **57**, 197-205.

POPE, S. B. 2001. Turbulent flows. Cambridge University Press, IOP Publishing.

POURTOUSI, M., GANESAN, P. & SAHU, J. 2015. Effect of bubble diameter size on prediction of flow pattern in Euler–Euler simulation of homogeneous bubble column regime. *Measurement*, **76**, 255-270.

PRAKASH, V. N., MERCADO, J. M., VAN WIJNGAARDEN, L., MANCILLA, E., TAGAWA, Y., LOHSE, D. & SUN, C. 2016. Energy spectra in turbulent bubbly flows. *Journal of Fluid Mechanics*, **791**, 174-190.

RZEHAK, R., KREPPER, E. & LIFANTE, C. 2012. Comparative study of wall-force models for the simulation of bubbly flows. *Nuclear Engineering and Design*, **253**, 41-49.

SHI, W., YANG, N. & YANG, X. 2017. A kinetic inlet model for CFD simulation of large-scale bubble columns. *Chemical Engineering Science*, **158**, 108-116.

SOKOLICHIN, A., EIGENBERGER, G. & LAPIN, A. 2004. Simulation of buoyancy driven bubbly flow: established simplifications and open questions. *AIChE Journal*, **50**, 24-45.

SOMMERFELD, M., MUNIZ, M. & REICHARDT, T. 2018. On the importance of modelling bubble dynamics for point-mass numerical calculations of bubble columns. *Journal of Chemical Engineering of Japan*, **51**, 301-317.

TABIB, M. V., ROY, S. A. & JOSHI, J. B. 2008. CFD simulation of bubble column—an analysis of interphase forces and turbulence models. *Chemical Engineering Journal*, **139**, 589-614.

TABIB, M. V. & SCHWARZ, P. 2011. Quantifying sub-grid scale (SGS) turbulent dispersion force and its effect using one-equation SGS large eddy simulation

(LES) model in a gas–liquid and a liquid–liquid system. *Chemical Engineering Science*, **66**, 3071-3086.

THAKRE, S. & JOSHI, J. 1999. CFD simulation of bubble column reactors: importance of drag force formulation. *Chemical Engineering Science*, **54**, 5055-5060.

TOMIYAMA, A. Effects of Eotvos number and dimensionless liquid volumetric flux on lateral motion of a bubble in a laminar duct flow. *2nd Int. Conf. an Multiphase Flow*, 1995.

WELCH, P. 1967. The use of fast Fourier transform for the estimation of power spectra: a method based on time averaging over short, modified periodograms. *IEEE Transactions on Audio and Electroacoustics*, **15**, 70-73.

YANG, N. & XIAO, Q. 2017. A mesoscale approach for population balance modeling of bubble size distribution in bubble column reactors. *Chemical Engineering Science*, **170**, 241-250.

FIGURES

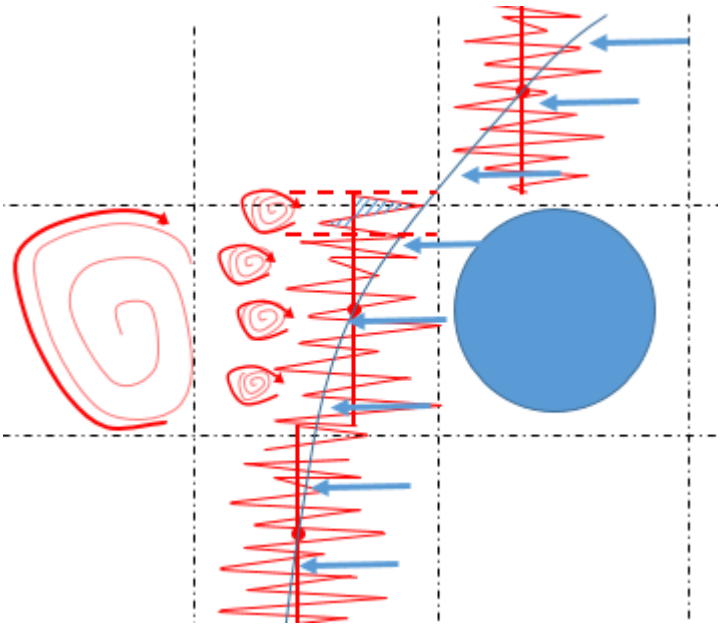

Figure 3- 1 Schematic of turbulent eddy fluctuations around the bubbles using the LES spatial filtering in bubble column bubbly flows.

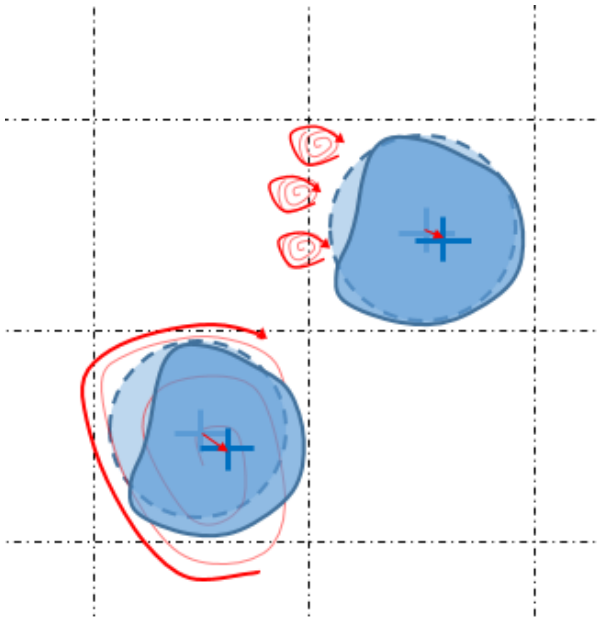

Figure 3- 2 Bubble shape variation caused by smaller turbulent eddies acting on the surface of the bubbles and larger turbulent eddies applying the shear on the bubbles.

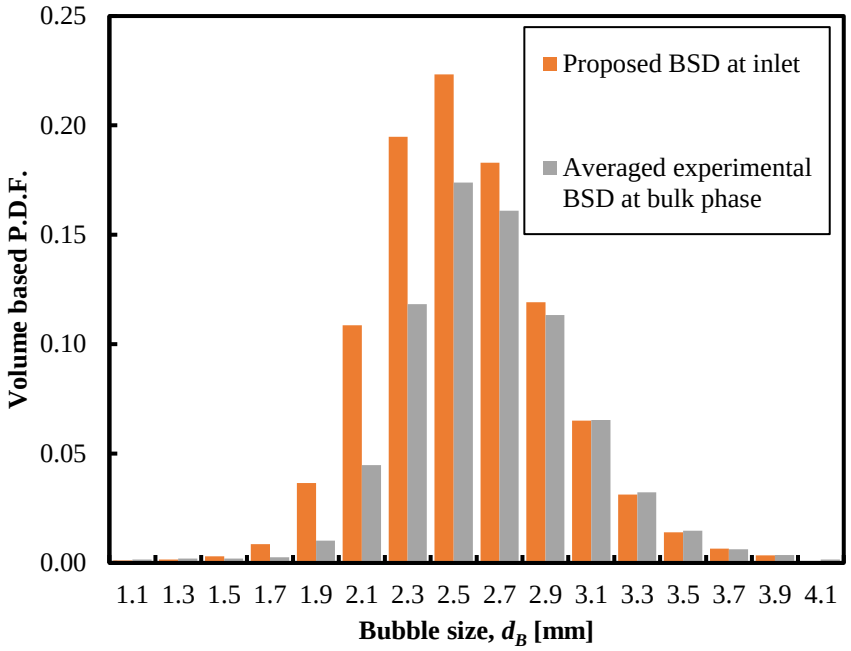

Figure 3- 3 Comparison of domain-averaged BSD and the adjusted BSD employed in the present LES simulation.

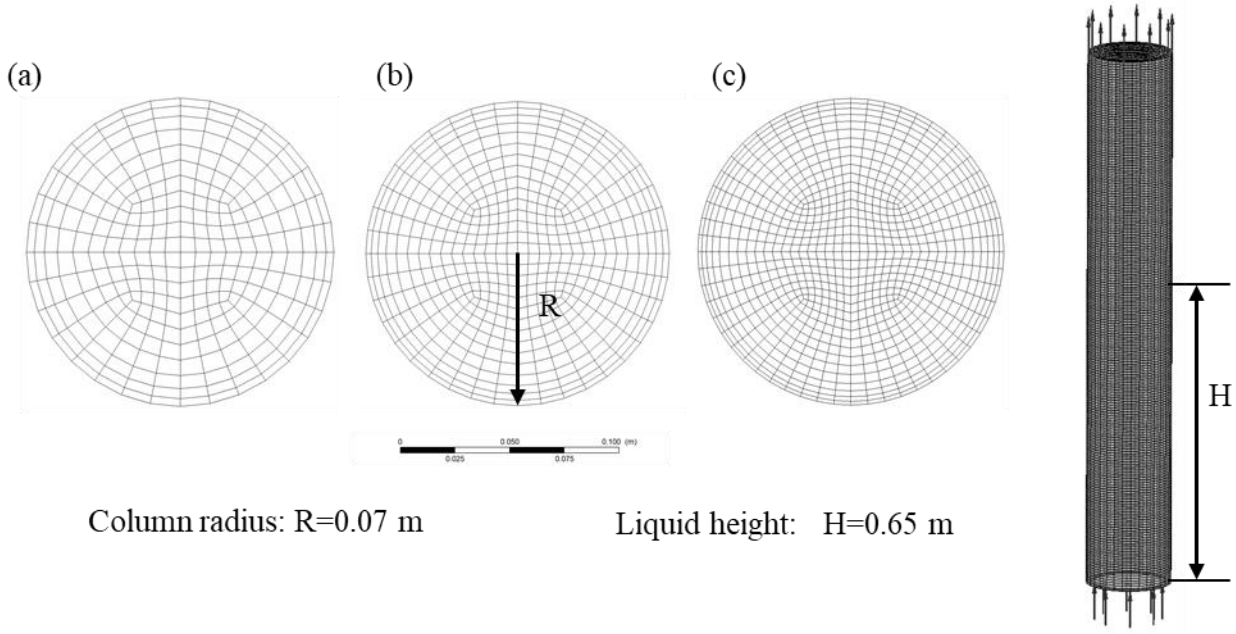

Figure 3- 4 Schematic of the mesh set-up (a) $\boldsymbol{d_{mean}/\Delta = 0.51}$ (b) $\boldsymbol{d_{mean}/\Delta = 0.6375}$ (c) $\boldsymbol{d_{mean}/\Delta = 0.85}$ and the bubble column configuration used in the simulations of the resent study.

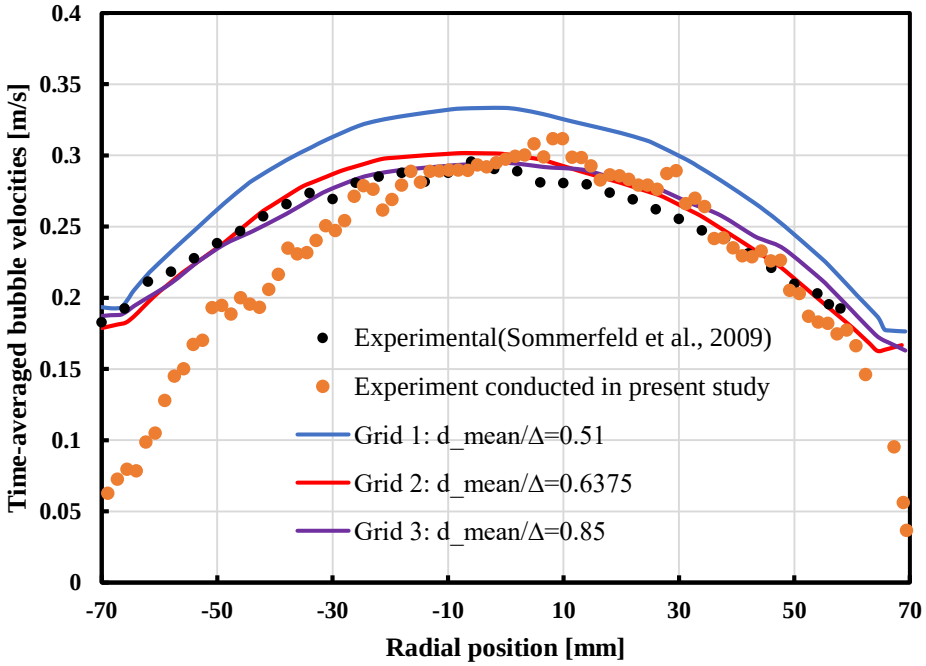

Figure 3- 5 Grid independence analysis by employing modified SGS-TDF with adjusted BSD at inlet at z=325mm. (Blue: Figure 3-4(a); Red: Figure 3-4(b); Purple: Figure 3-4(c)).

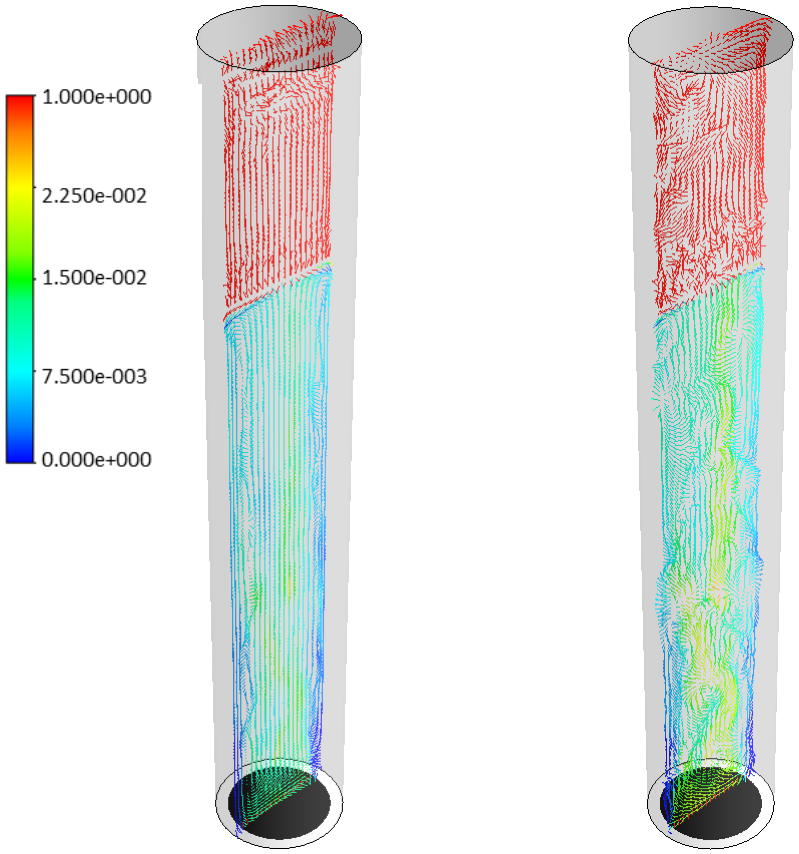

(a) (b)

Figure 3- 6 Liquid axial liquid velocity field in the bubble volume highlighted by local bubble volume fraction. (a) Time-averaged velocity field; (b) Instantaneous velocity field at 100s.

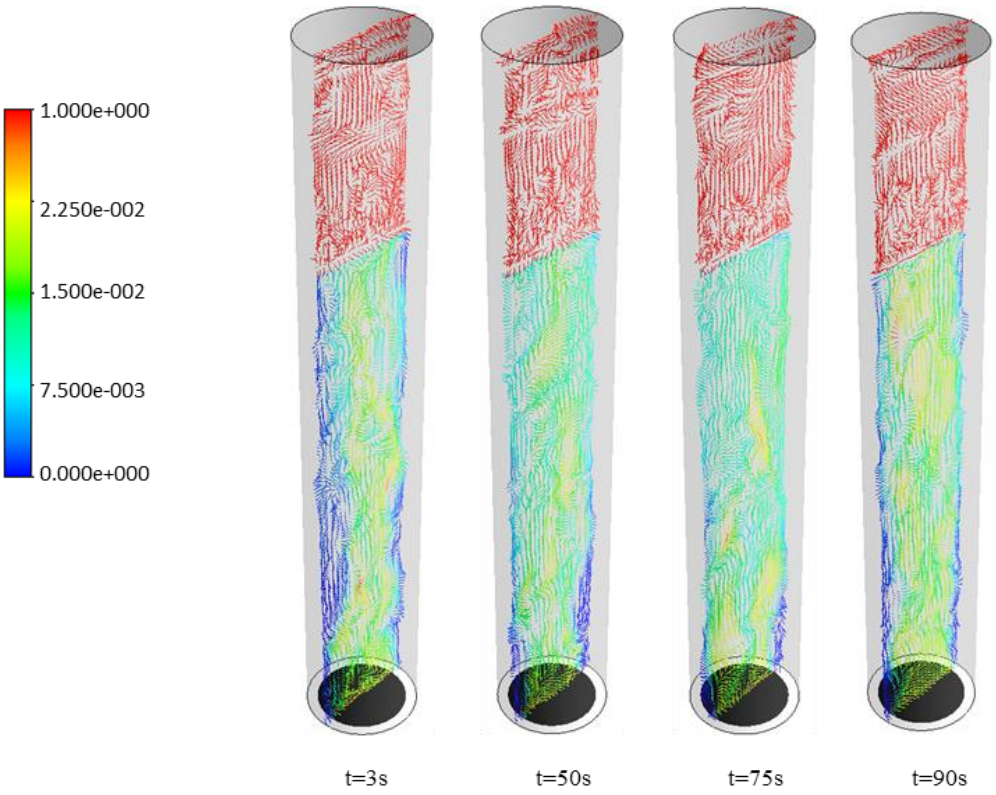

Figure 3- 7 Instantaneous liquid phase velocity distribution at different times, obtained in the cutting plane of the bubble column, highlighted by the local bubble volume fraction.

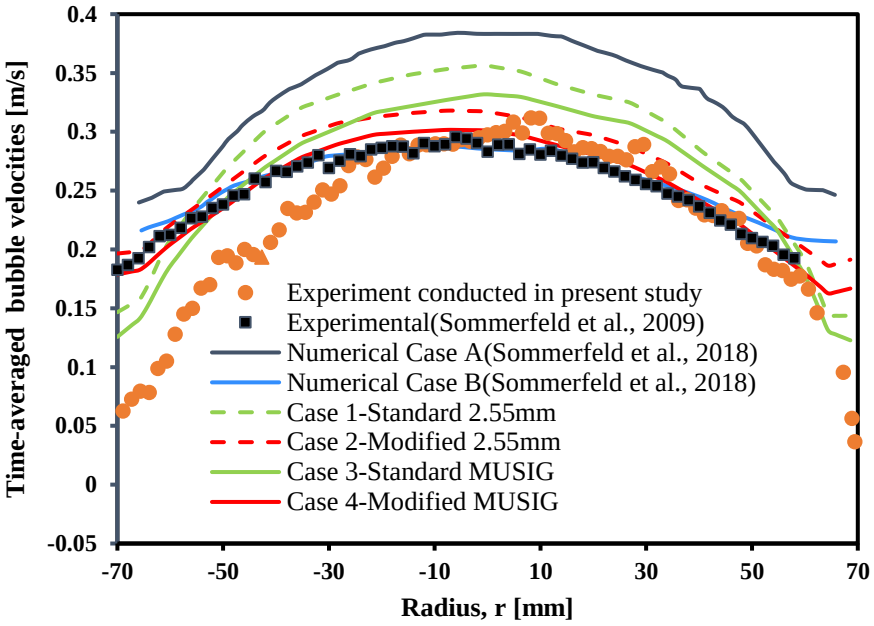
Time-averaged bubble velocities [m/s]
0.4
0.35
0.3
0.25
0.2
0.15
0.1
0.05
0
-0.05
-70
-50
-30
-10
10
30
50
70
Radius, r [mm]
Experiment conducted in present study
Experimental(Sommerfeld et al., 2009)
Numerical Case A(Sommerfeld et al., 2018)
Numerical Case B(Sommerfeld et al., 2018)
Case 1-Standard 2.55mm
Case 2-Modified 2.55mm
Case 3-Standard MUSIG
Case 4-Modified MUSIG

(a)

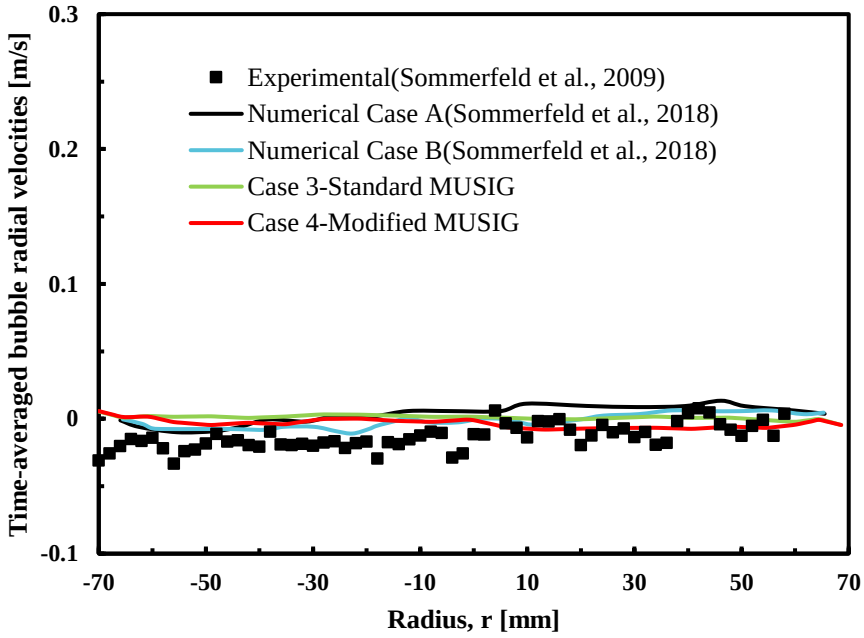
Time-averaged bubble radial velocities [m/s]
0.3
0.2
0.1
0
-0.1
-70
-50
-30
-10
10
30
50
70
Radius, r [mm]
Experimental(Sommerfeld et al., 2009)
Numerical Case A(Sommerfeld et al., 2018)
Numerical Case B(Sommerfeld et al., 2018)
Case 3-Standard MUSIG
Case 4-Modified MUSIG

(b)

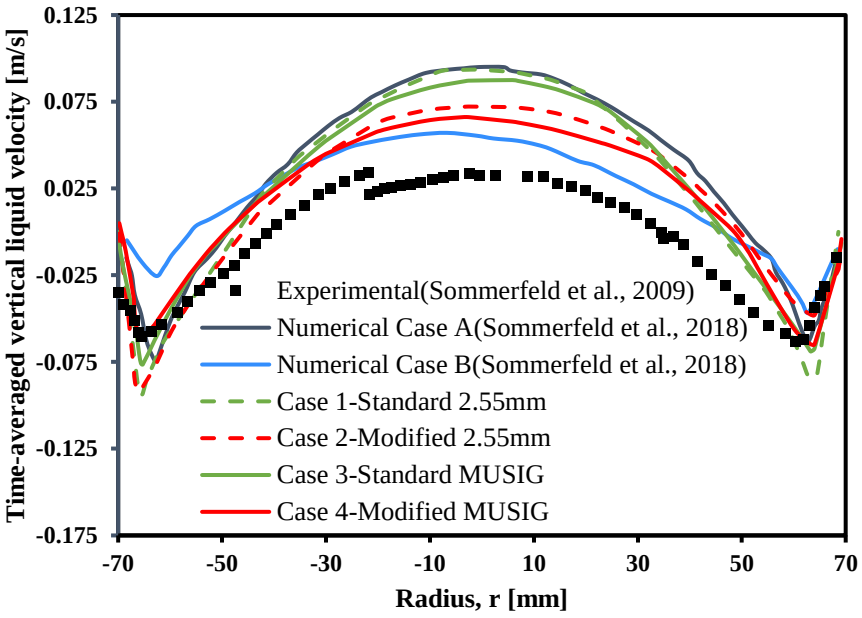

(c)

Figure 3- 8 Comparison of LES predicted time-averaged liquid and bubble velocity profiles at the cross-section z=325 mm. (a) Bubble axial velocity distribution; (b) Bubble radial velocity distribution; (c)Liquid axial velocity distribution.

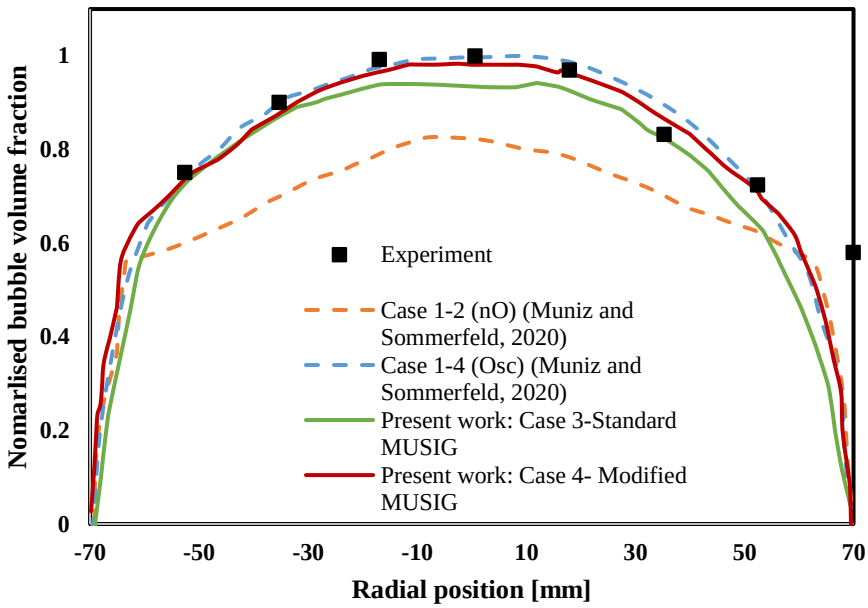

Figure 3- 9 Comparison of Euler/Euler LES (present study) with Euler/Lagrange LES (Muniz and Sommerfeld (Muniz and Sommerfeld, 2020)) for the predicted time-averaged bubble volume fraction profiles at z=325mm. Labels: nO: no bubble dynamics model; Osc: with bubble dynamics model.

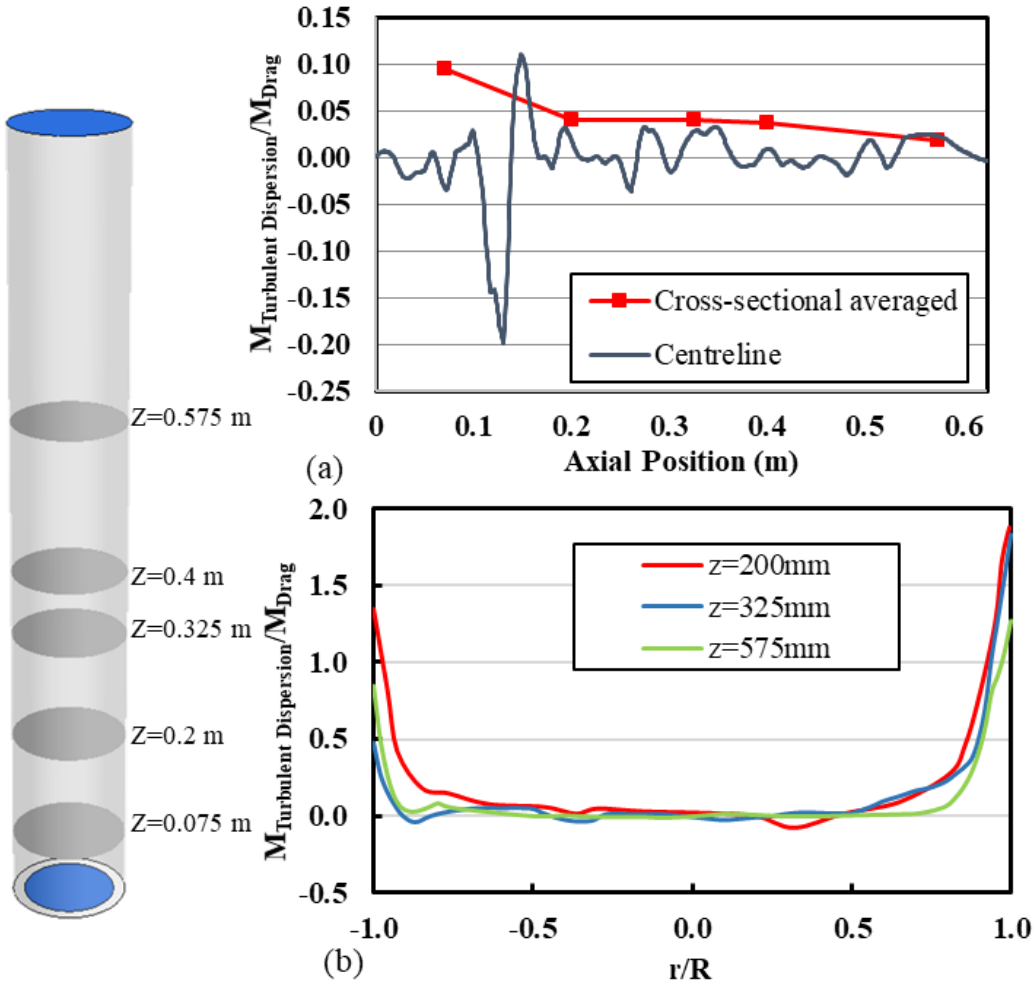

Figure 3- 10 Quantification of SGS turbulent dispersion force (TDF) contribution: (a) instantaneous SGS-TDF/Drag force along centreline and cross-sectional averaged ratio at different cross-sections along the bubble column height at 100s. (b) Time-averaged SGS-TDF/Drag force ratio in radial direction at different cross-sections along the bubble column height.

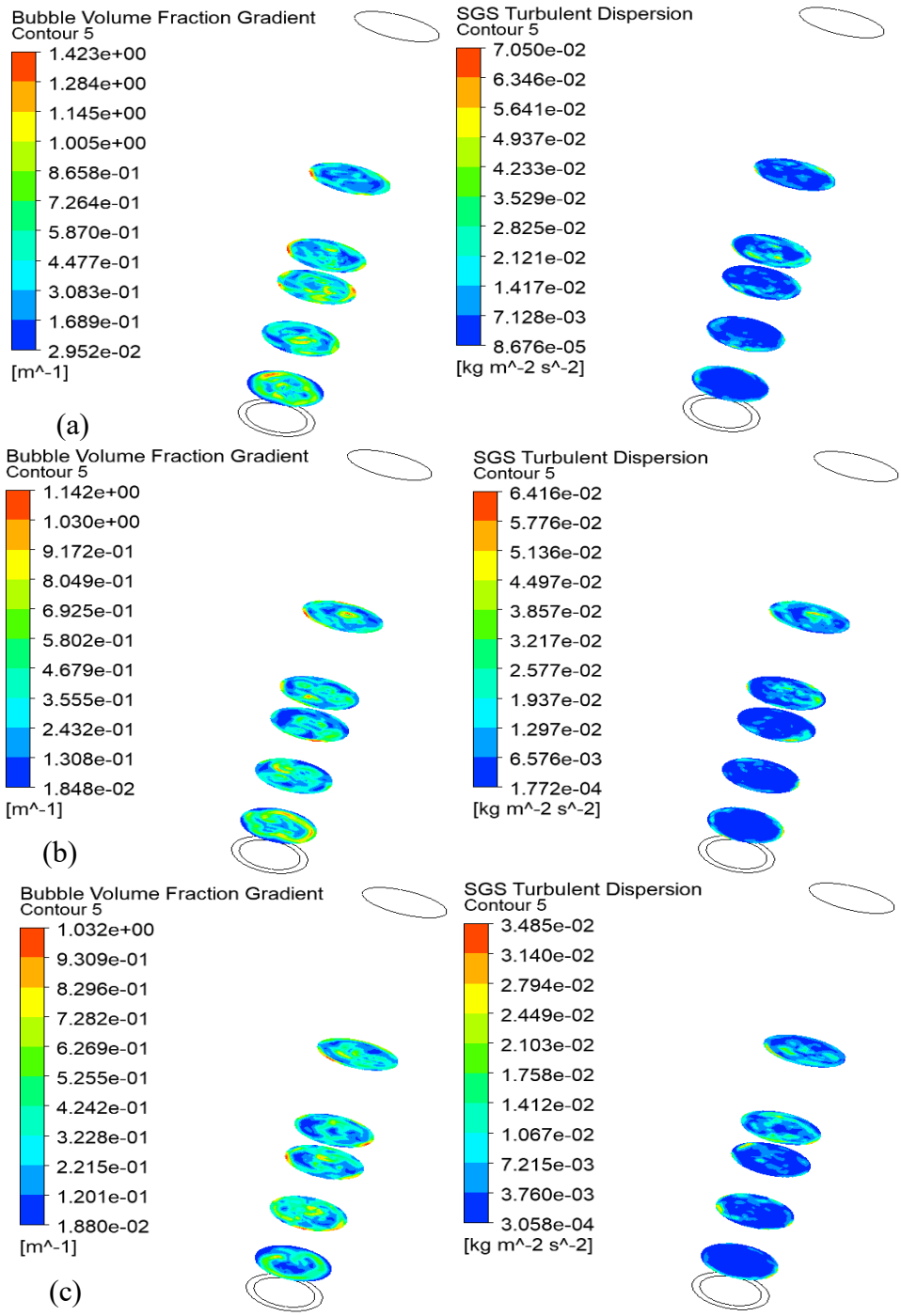

Figure 3- 11 Instantaneous contour plots of bubble volume fraction gradient and instantaneous SGS turbulent dispersion force per unit volume at different cross-sections along the bubble column height at different time. (a) t=80 s; (b) t=90 s; (c) t=100 s.

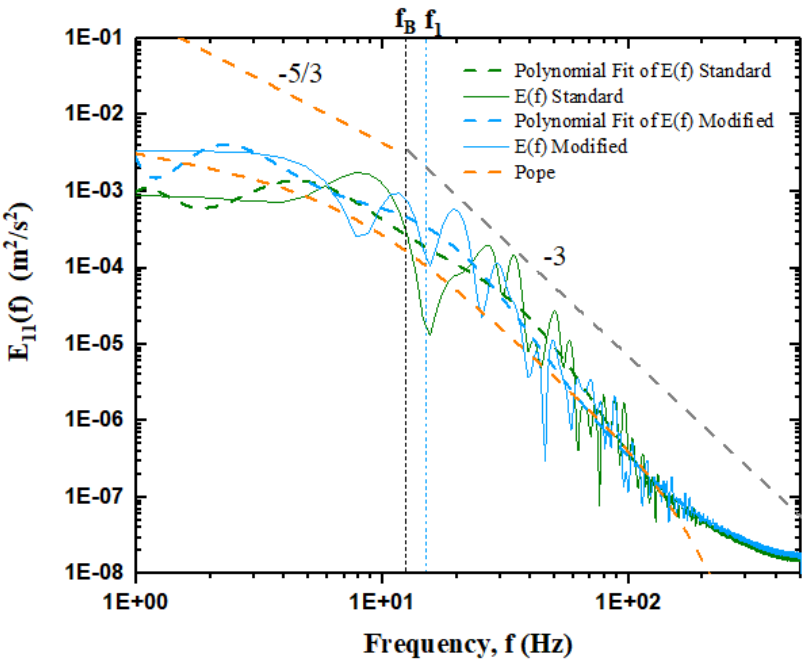
f_B f_1
-5/3
-3
Polynomial Fit of E(f) Standard
E(f) Standard
Polynomial Fit of E(f) Modified
E(f) Modified
Pope
$E_{11}(f)$ (m^2/s^2)
Frequency, f (Hz)
1E-01
1E-02
1E-03
1E-04
1E-05
1E-06
1E-07
1E-08
1E+00
1E+01
1E+02

(a)

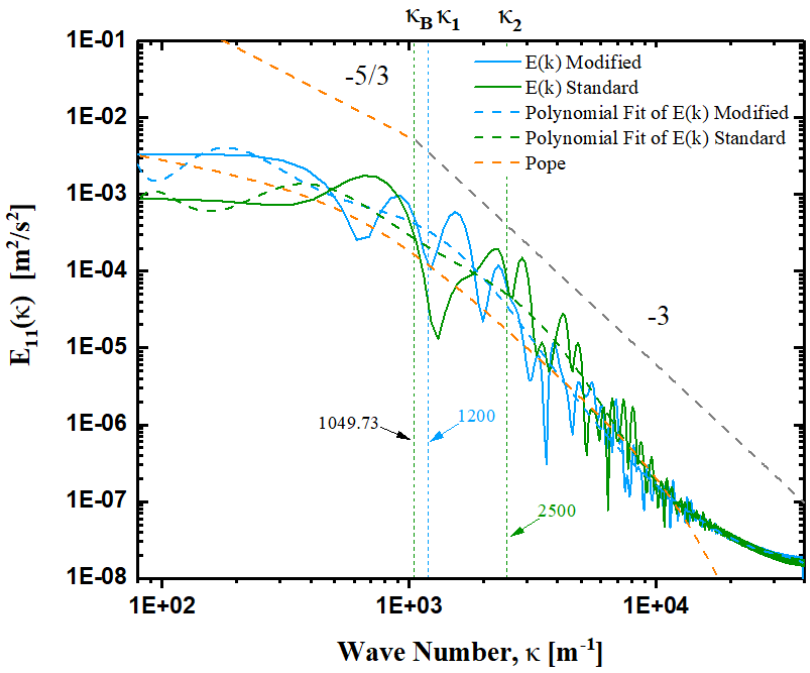
κ_B κ_1 κ_2
-5/3
-3
E(k) Modified
E(k) Standard
Polynomial Fit of E(k) Modified
Polynomial Fit of E(k) Standard
Pope
1049.73
1200
2500
$E_{11}(\kappa)$ [m^2/s^2]
Wave Number, κ [m^{-1}]
1E-01
1E-02
1E-03
1E-04
1E-05
1E-06
1E-07
1E-08
1E+02
1E+03
1E+04

(b)

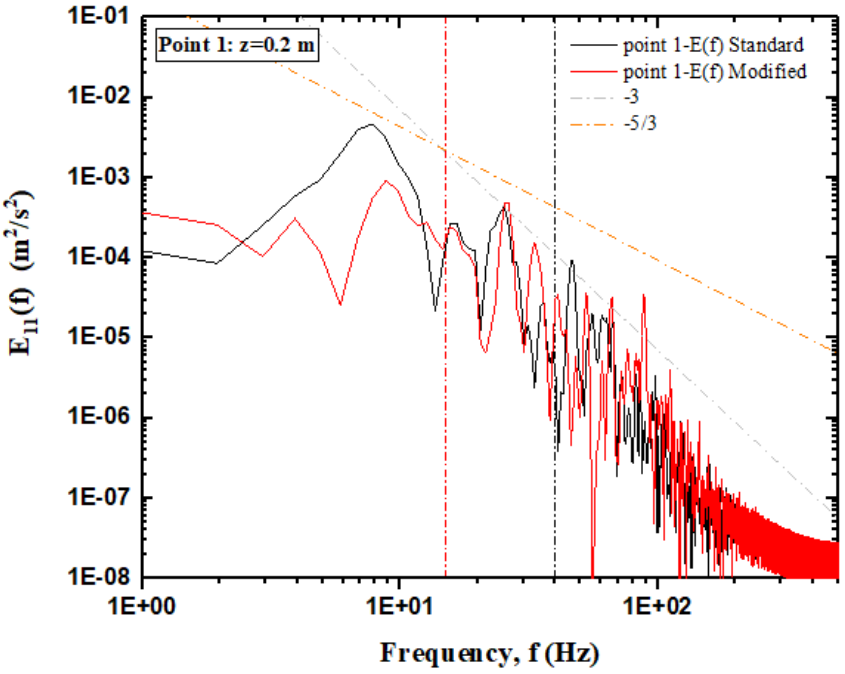

(c)

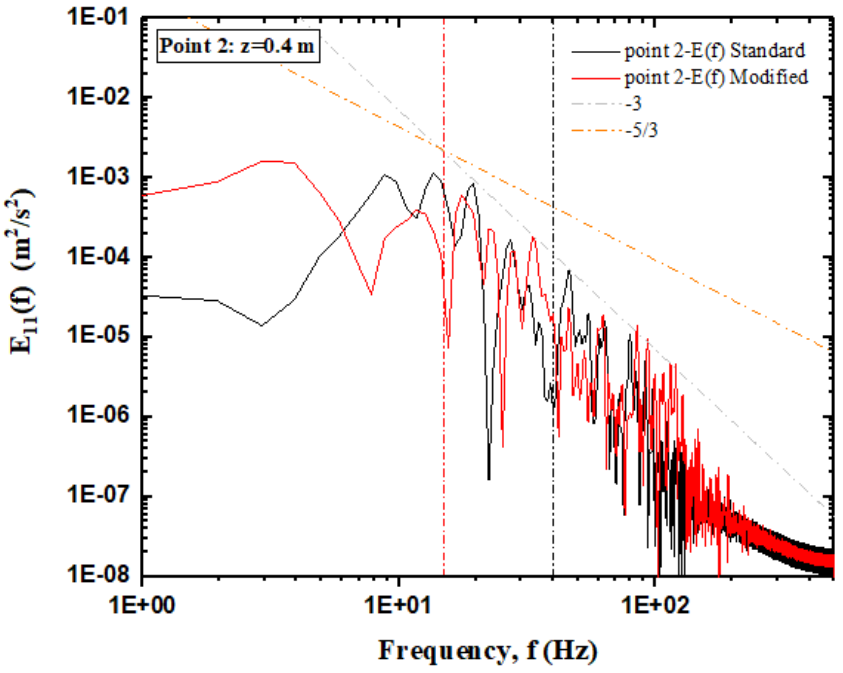

(d)

Figure 3- 12 Power spectrum density: (a) Liquid axial fluctuation velocity; (b) One with 9th-order polynomial fitting approximation (Polynomial: Dashed Lines),

extracted from the location in the centreline at z=325mm. (c) at z=200mm; (d) at z=400m.

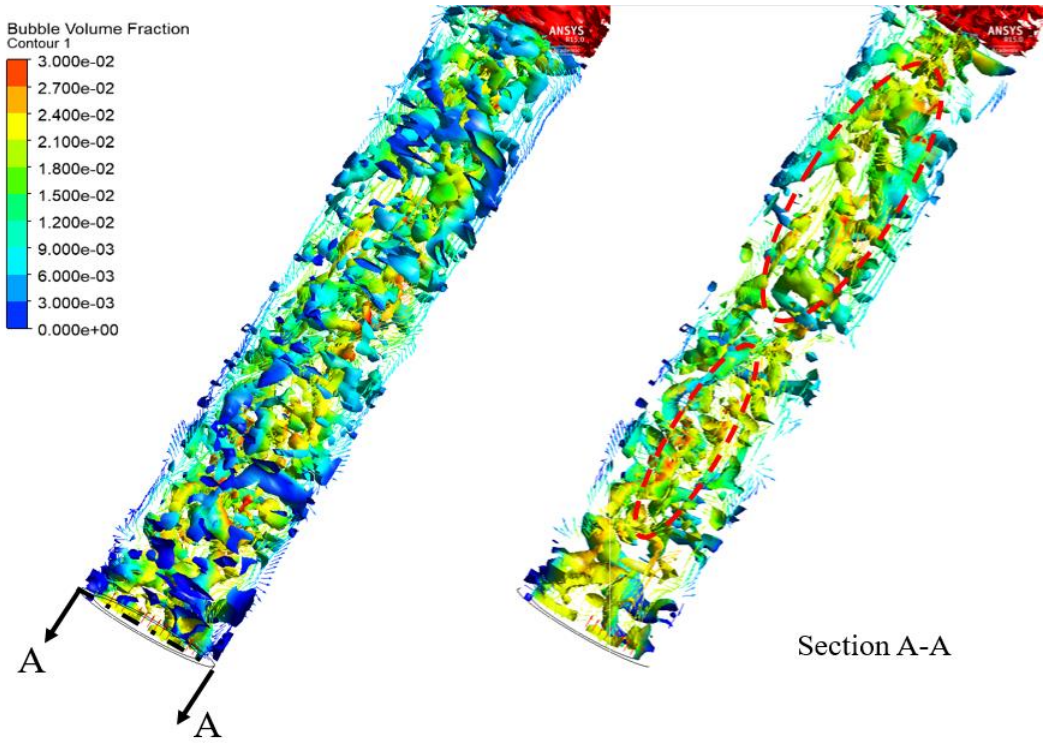

(a) (b)

Figure 3- 13 (a) Iso-surface of liquid phase invariant Q, highlighted by bubble volume fraction; (b) Central cutting plane view.

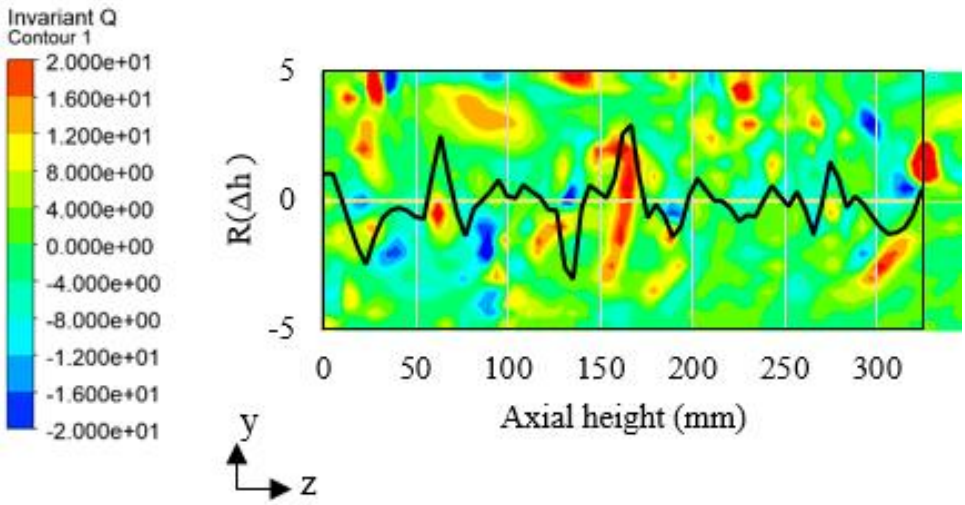

Figure 3- 14 Spatial correlation coefficient R(Δh) along the height of the bubble column from z=0 to z=325mm. The background was superimposed with the contours of liquid phase invariant Q.

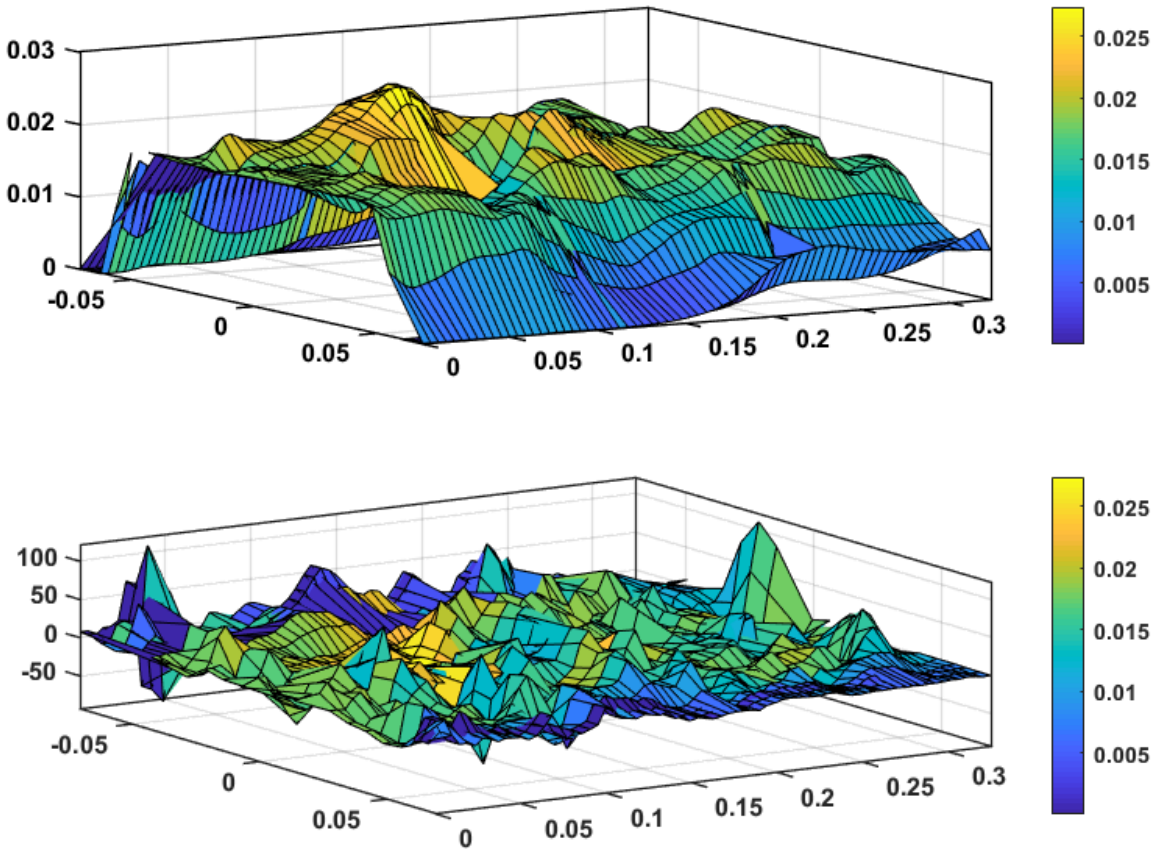

Figure 3- 15 (a) 3D Contours of bubble volume fraction distribution in YZ plane at X=0, coloured by the proposed spatial correlation coefficient R; (b) Spatial correlation R distribution in YZ plane at X=0, highlighted by bubble volume fraction.

CHAPTER 4: LARGE EDDY SIMULATION OF BUBBLE FLOW IN BUBBLE COLUMN REACTOR BY CONSIDERING SUB-GRID SCALE TURBULENT DIFFUSION EFFECT AND BUBBLE OSCILLATION

SUMMARY

In Chapter 3, the effect of implementation of the modified sub-grid scale (SGS) turbulent dispersion force (TDF) model in large eddy simulation (LES) on modulation of bubble transport in bubble column bubbly flows has been evaluated. Bubble deformation and the mimicked bubble oscillation which can be interpreted as the result of bubble-eddy interaction in the SGS have been demonstrated in the LES simulation with the modified SGS-TDF model. Clearly, the bubble lateral dispersion is better predicted when using the modified SGS-TDF model than using the standard time-averaged TDF model. However, the consequence of SGS spatial filtering process usually involves the filtering of added mass force, which would give rise to an extra force, the added mass stress force (SGS-AMS). The present chapter will particularly assess the impact of inclusion of the SGS-AMS term in the LES modelling on bubble dispersion in the bubble column bubbly flows. It can be postulated that the turbulent eddies in the fronts of the rising bubbles in the bubble column would generate local fluctuations while such fluctuations would significantly affect the bubble transport and dispersion, leading to the bubble continuous

deformation and bubble oscillation accordingly. When applying the large eddy simulation (LES) for modelling bubbly flows, most of the existing studies usually just consider the interfacial momentum exchange terms contributed from the drag and non-drag forces that are modelled as the lift force, added mass force and turbulent dispersion force. These forces are expressed in terms of the resolved quantities of the flow (mean or filtered variables) but this treatment approach may underestimate the effect of unresolved SGS fluctuations on the bubble dispersion. This chapter will demonstrate that bubble dynamics in the bubble column bubbly flows can be captured by using the adequate SGS-TDF and SGS-AMS models in Eulerian-Eulerian LES modelling when mimicking the bubble transport in the bubble column. By using Euler/Euler large-eddy simulations (LES) modelling with considering the effect of bubble-eddy interactions on the SGS turbulent dispersion and added mass stress models, the improvement on the prediction of bubble dynamics was apparent based on the bubble axial velocity and bubble volume fraction profiles. This may indicate that the modified SGS-TDF and SGS-AMS models may play an equivalent role in indicating the bubble fluctuating motion predicted by using Euler/Lagrange LES modelling approach but with the stochastic dispersion model (Sommerfeld et al., 2018).

1. INTRODUCTION

As Euler/Euler two-fluid model large eddy simulation (LES) modelling involves many interphase momentum exchange terms, appropriate modelling of these terms has a pivotal role in predicting those important parameters in the bubble column bubbly flows such as bubble volume fraction distribution, bubble and liquid phase velocity distribution, turbulent kinetic energy and turbulence dissipation, also the interfacial mass transfer. However, for the contributions from each individual interphase force considered in bubbly flow in bubble column reactors, there is still actually no consensus formed so far, especially for the momentum exchange terms as the results of averaging process (spatial filtering for LES modelling). Typical examples are the turbulent dispersion and added mass stress forces (as will be the focus of this paper). In terms of turbulent dispersion force, Burns *et al.* (2004) proposed the most commonly used turbulent dispersion force model, which was extracted by employing the ensemble averaging to the instantaneous drag force experienced by dispersed phase (bubbles) and therefore is able to assess the turbulent dispersion behaviour of dispersed phase. Lavieville *et al.* (2017) also employed the Lagrangian description into Euler/Euler two-fluid one-pressure model and proposed a generalized turbulent dispersion model. The Euler/Euler LES turbulence model has shown significant promise in unearthing flow details in bubble column bubbly flow (Deen et al., 2001, Dhotre et al., 2007, Tabib et al., 2008, Zhang et al., 2009, Ničeno et al., 2008a, Fard et al., 2020, Ma et al., 2015). Though there exists a disadvantage when applying the Euler/Euler LES, which requires the largest in-

terface details should be smaller than the grid size in order to maintain the assumption of interpenetrating continua to be held. This means that the cell size must be larger than the particle size. Consequently, the grid adopted might not be fine enough to capture all turbulent fluctuation details in Euler/Euler LES modelling of bubble column bubbly flows. Fairly speaking, lots of the turbulent details move to sub-grid scale (SGS) level in the bubble column, and they need to be captured or modelled appropriately. So far various LES SGS models such as constant Smagorinsky model, dynamic Smagorinsky model and one-equation SGS-turbulent kinetic energy LES model has been tested in modelling of the bubble column bubbly flows (Darmana, 2006, Ničeno et al., 2008b, Dhotre et al., 2008). Niceno *et al.* (2008b) were the first to apply the One-equation SGS-TKE LES model to Euler/Euler multiphase gas–liquid flow. Their simulation results have revealed that the one-equation SGS model gives much improved results than those using the Dynamic model, giving information on the modelled SGS turbulent kinetic energy at the same time. They also suggested that the sub-grid scale (SGS) information may be used to access the sub-grid scale interfacial forces, in particular the so-called sub-grid scale turbulent dispersion force (SGS-TDF). However, the effect of sub-grid scale turbulent dispersion force has to be modelled properly for the case of bubble column bubbly flows as the bubble size is almost equivalent to the mesh-grid size and a proper extension of research ahead would be to quantify the effect of sub-grid scale turbulent dispersion in Euler/Euler LES framework.

When applying two-fluid model Euler/Euler large eddy simulation, the filtering process involves the use of phasic 'function of presence' approach to the momentum equation by accounting for co-sharing of a control volume by different phases. As a result, this leads to the terms denoting interfacial momentum forces, contributed by the dot product of total stress term and gradient of 'function of presence' term, and indicates the forces induced by the local flow perturbations at the interface of second phase (bubbles). The subsequent averaging (ensemble averaging for RANS turbulence or spatial filtering for LES model) to the momentum equation and the interfacial momentum terms leads to the additional terms that can be attributed to the drag and other parts that can be modelled as non-drag forces such as lift force, added mas force and turbulent dispersion force (SGS-TDF) together with the added mass stress (SGS-AMS). In case of conducting two-phase LES, these interfacial momentum exchange terms need to be modelled in terms of the resolved quantities of the flow or filtered variables while taking into account the effect of unresolved fluctuating on sub-grid scale. It should be mentioned that most of the reported work on two-phase or three-phase LES has overlooked or neglected the unresolved sub-grid scale contributions as how to model these terms remain very challengeable from perspective of both theoretically and experimentally. Several previous studies have also indicated the important role played by the turbulent terms of the interfacial momentum transfer on the bubble dynamics, in particular, the turbulent term related to the added mass force which has proved to be effective in improving the phase distribution prediction in many vertical multiphase flows e.g. bubbly mixing layer (Ayed et al., 2007), air-lift (Atiya et al., 2011), and vertical

liquid-liquid pipe flows (Rezig et al., 2017). In Eulerian-Lagrangian LES modelling of bubble column bubbly flows, different turbulent dispersion terms of particles in Lagrange approach were studied and compared by Lain and Grillo (Laín and Grillo, 2007). Sommerfeld *et al.* considered the bubble-induced liquid velocity fluctuation as a combination of contribution from the previous time step and another random function generated by Wiener procedure (Sommerfeld, 1993). The formulation of Langevin's model for the liquid velocity increase from bubble makes it possible to capture some basic physics of bubble dispersion in general turbulent flows while maintaining simple mathematical manipulation of the stochastic model, avoiding some pitfalls and simplifying macroscopic relationship extraction. Hosoi and Yoshida proposed an advanced Euler/Euler dispersion model considering the liquid phase turbulent kinetic energy and bubble-induced turbulent kinetic energy to include the bubble-liquid phase interactions into account (Hosoi and Yoshida, 2010). The simulated bubble volume fraction profile at outlet has good agreement with experiments. But the consistency becomes poor in the near-wall region and central region of the bubble column.

Due to the bubble's dynamic response to the surrounding carrier phase, the bubble mass centre changes with its entrainment in the bubble column, which leads to bubble wobbling. Sommerfeld *et al.* considered the bubble oscillations and tumbling motion which has been quantitatively analysed using the point-mass approximation and implementing the sub-grid-scale-turbulence modulation due to bubbles movement in LES-Euler/Lagrange calculations by accounting for drag, transverse lift,

added mass, wall forces (Sommerfeld et al., 2018). Although turbulence dispersion force has been neglected in their work, they have considered the impact of bubble fluctuations in the coupled SGS-bubble motion model, which has proved to be effective in the prediction of the bubble lateral migration. In particular, they have implemented the effect of the bubble eccentricity through Euler/Langrange modelling approach. To consider the similar bubble dynamic motion using Euler/Euler LES modelling approach, one may interpret that the interactions between bubble and the surrounding turbulent eddies give rise to the bubble deformation in case of no bubble coalescence or break-up taking place as shown in Figure 1. This can be further explained by the surface of bubbles dynamically deforming due to the action of surrounding eddies and large amount of adjacent and anisotropic small eddies stretching or squeezing bubbles, leading to the fluctuation of bubble mass-centre accordingly. Thus, the interphase forces acting on the dispersed phase are strongly affected by interactions between the bubbles and the turbulent shear caused by nearby turbulent eddies, and these interfacial momentum transfer have to be properly implemented in the sub-grid scale LES.

In general, all these numerical studies mentioned have partially highlighted the likely effect of the turbulent interfacial terms on the bubble dynamics. Without including the turbulent contribution from SGS-TDF and SGS-AMS, the axial momentum balance in the main flow direction of the bubble column bubbly flow is principally controlled by the buoyancy force, which results in the bubble axial rel-

ative velocities close to the terminal velocities of the bubbles in still liquid. However, this is not consistent with many experimental observations in bubble column for bubbles rising up in both the core region and near-wall region of the bubble column (Sommerfeld and Broder, 2009, Deen et al., 2001, Buwa and Ranade, 2002, Mudde et al., 1997, Rzehak et al., 2017, Kulkarni et al., 2007). In particular, the experimental data of the bubble columns reported by Sommerfeld *et al.* (2018) indicates an inconsistency of the predicted liquid phase velocity profiles with the experimental ones, especially in the strong sheared zone near the bubble column wall, so that the precise prediction on the interfacial mass transfer is also influenced and the bubble dynamics is not correctly indicated.

In the present study, the effects of adoption of the spatial filtering to the interfacial momentum exchange terms on the turbulent dispersion and added mass stress in bubble column bubbly flows are studied. By taking both phase velocity fluctuations and bubble volume fraction fluctuations into account, the spatial filtering of the drag force and added mass force terms will give rise to the extra terms proportional to the area density slip velocity correlation i.e., turbulent dispersion, and to the correlation of bubble volume fraction and gradient of SGS stress. On the basis of employing the SGS eddy diffusivity hypothesis, the SGS-TDF and SGS-AMS will be used to mimic the turbulent dispersion effect in the framework of Euler/Euler two-fluid model approach, revealing the bubble dynamics in the bubble column. In our modified SGS Smagorinsky model, the modified SGS eddy viscosity $\nu_T$accounting for the bubble dynamic response to the turbulent eddies induced shear has also been

implemented into the SGS-TDF term (Long et al., 2020). This chapter is organised as follows. Section 2 will present the mathematical modelling and the numerical method for bubble column bubbly flow, in particular describing the terms of SGS-TDF and SGS-AMS. The numerical results when considering the effect of SGS-TDF and SGS-AMS forces on bubble entrainment by turbulent eddies will be summarised and discussed in Section 3, concentrating on the results of various statistics involving the bubble volume fraction distribution, both bubble and liquid phase velocity profiles, turbulent kinetic energy spectra and related overall interfacial mass transfer together with the implication for turbulent dispersion that may partially play a role in giving rise to bubble cluster oscillation and wobbling in the bubble column. The main conclusions are given in Section 4.

2. MATHEMATICAL MODELLING AND NUMERICAL METHODS

2.1 Governing equations

The two-fluid model based LES modelling has been adopted in the present study. This requires the application of spatial filtering to mass and momentum conservation equations. It is assumed that both the continuous liquid phase and dispersed bubble phase are modelled as two interpenetrating continuums. The large-scale length turbulent eddies in bubble column bubbly flow will be resolved while the unresolved SGS fluctuations by small eddies will be modelled. Though the mass transfer between the carrier and dispersed phase will be accounted, the bubbly flow in the bubble column is assumed to be adiabatic. By applying the phase weighted

filtering to mass and momentum conservation equations, the governing equations can be written as

$$\frac{\partial}{\partial t}(\rho_k \alpha_k) + \nabla \cdot (\alpha_k \rho_k \boldsymbol{u}_k) = 0 \tag{4-1}$$

$$\frac{\partial}{\partial t}(\alpha_k \rho_k \boldsymbol{u}_k) + \nabla \cdot (\alpha_k \rho_k \boldsymbol{u}_k \boldsymbol{u}_k) = -\nabla \cdot (\alpha_k \boldsymbol{\tau}_k) - \alpha_k \nabla p + \alpha_k \rho_k g + \boldsymbol{M}_{F,k} \,. \tag{4-2}$$

In Equations (4-1) and (4-2), α_k is the filtered void fraction of phase *k*, defined by averaging the phase-indicator function (Drew and Passman, 2006). *k* signifies the component, liquid or bubbles with k=G for gas phase and k=L for liquid. Velocities in Equations (4-1) and (4-2), $\boldsymbol{u}_k$ is the filtered velocity vector for phase *k* in grid scale, given as $\widetilde{\boldsymbol{u}}_k = \boldsymbol{u}_k + u'_k$. Here $\widetilde{\boldsymbol{u}}_k$ is the instantaneous velocity and $\boldsymbol{u}'_k$ stands for the sub-grid scale (SGS) velocity, which needs to be modelled. The terms on the right-hand side of Equation (4-2) respectively represent the stress, the pressure gradient, gravity and the filtered interphase momentum exchange, which arises from the actions of the interphase forces. The stress term is expressed as Equation (4-3), given by

$$\tau_k = -\mu_{eff}\left(\nabla \boldsymbol{u}_k + (\nabla \mathbf{u}_\mathrm{k})^T - \frac{2}{3} I (\nabla \cdot \boldsymbol{u}_k)\right) \tag{4-3}$$

where μ_{eff} is the effective viscosity of the liquid phase, which may be assumed to be composed of three contributions; the molecular viscosity, the turbulent eddy viscosity and an extra term to model bubble induced turbulence as shown by Equation (4-4),

$$\mu_{eff} = \mu_{L,L} + \mu_{T,L} + \mu_{BI,L} . \tag{4-4}$$

The extra viscosity due to the bubble induced turbulence is now usually modelled based on Sato's model, which is given by

$$\mu_{BI,L} = \rho_L C_{\mu,BI} \alpha_G d_B |\boldsymbol{u}_G - \boldsymbol{u}_L| . \tag{4-5}$$

However, as will be discussed later in this section, this viscosity due to the bubble induced turbulence may also be contributed by the relative bubble dynamic response to those turbulent eddies that have equivalent or slightly larger length scale and entrapped the bubbles (Long et al., 2020, Bhole et al., 2008). The filtered momentum exchange term can be classified as different contributions from the interphase forces, which are defined by

$$\boldsymbol{M}_{F,L} = -\boldsymbol{M}_{F,G} = \boldsymbol{M}_{D,L} + M_{L,L} + \boldsymbol{M}_{AM,L} + \boldsymbol{M}_{TD,L} + \boldsymbol{M}_{AMS,L} \tag{4-6}$$

where the terms on the right-hand side of Equation (4-6) are interphase forces acting on the bubbles that caused by the filtered drag, lift and added mass plus turbulence dispersion and so-called added mass stress. The formulations of the filtered drag, lift and added mass forces employed in the Euler/Euler LES modelling are summarised in Table 1.

Table 1 Interphase force closure.

Forces	Expressions
Drag	$\boldsymbol{M}_{D,L} = \frac{3}{4}\alpha_G \rho_L \frac{C_D}{d_B}\lvert\boldsymbol{u}_G - \boldsymbol{u_L}\rvert(\boldsymbol{u}_G - \boldsymbol{u_L}),$ $C_D = \frac{2}{3}E_O^{\frac{1}{2}}, E_0 = \frac{g\Delta\rho d_B^2}{\sigma}$
Lift	$\boldsymbol{M}_{L,L} = \rho_L C_L(\boldsymbol{u}_B - \boldsymbol{u}_L) \times (\nabla \times \boldsymbol{u}_L),$ $C_L = \begin{cases} min[0.288tanh(0.121Re_B), f(E_O')\,] & E_O' \le 4 \\ f(E_O') & 4 < E_O' < 10 \\ -0.29 & E_O' > 10 \end{cases}$ $E_O' = \frac{g(\rho_l - \rho_g)d_h^2}{\sigma}, d_h = d(1 + 0.163E_O'^{0.757})^{1/3}$
Added mass	$\boldsymbol{M}_{AM,L} = \alpha_G \rho_L C_{AM}\left(\frac{D\boldsymbol{u}_G}{Dt} - \frac{D\boldsymbol{u}_L}{Dt}\right)$

The turbulent dispersion term $\boldsymbol{M}_{TD,L}$ can be obtained phase-weighted filtering the instantaneous interphase drag force term. The mechanism responsible for bubble acceleration due to the liquid phase velocity fluctuations is strongly associated with

the turbulent dispersion. The attention is restricted here to the consequence of the filtering of the drag force and added mass force. The interphase drag force can then be specified to be proportional to slip velocity and area density,

$$\widetilde{\boldsymbol{M}}_D = \frac{1}{8}\tilde{C}_D\tilde{A}_{GL}\rho_G|\widetilde{\boldsymbol{u}}_G - \widetilde{\boldsymbol{u}}_L|(\widetilde{\boldsymbol{u}}_G - \widetilde{\boldsymbol{u}}_L) \tag{4-7}$$

where the bubble area density is given by

$$\tilde{A}_{GL} = \frac{6\widetilde{\alpha}_G}{d_B}. \tag{4-8}$$

Taking the spatial filtering for Equation (4-7) by accounting for velocity fluctuations and area density fluctuations, Equation (4-9) is obtained,

$$\boldsymbol{M}_D = \boldsymbol{M}_{D,L} + \boldsymbol{M}_{TD,L} = \frac{1}{8}C_D A_{GL}\rho_G|\boldsymbol{u}_G - \boldsymbol{u}_L|(\boldsymbol{u}_G - \boldsymbol{u}_L) + \frac{1}{8}C_D\rho_G|\boldsymbol{u}_G - \boldsymbol{u}_L|\overline{A'_{GL}(\boldsymbol{u}'_G - \boldsymbol{u}'_L)} \tag{4-9}$$

where the drag coefficient and bubble diameter have been assumed to remain unchanged and the effect of the spatial filtering on the drag coefficient can be neglected. It can be seen from Equation (4-9) that the filtering the interfacial drag force gives rise to the filtered drag term and the term proportional to the area density-slip-velocity correlation $\frac{1}{8}C_D\rho_G|\boldsymbol{u}_G - \boldsymbol{u}_L|\overline{A'_{GL}(\boldsymbol{u}'_G - \boldsymbol{u}'_L)}$, so-called the turbulent dispersion force (SGS-TDF). If this correlation is modelled by using the SGS eddy diffusivity hypothesis, this is given by

$$\frac{1}{8}C_D\rho_G|\boldsymbol{u}_G-\boldsymbol{u}_L|\overline{A'_{GL}(\boldsymbol{u}'_G-\boldsymbol{u}'_L)}=\frac{1}{8}C_D\rho_G|\boldsymbol{u}_G-\boldsymbol{u}_L|\left(\frac{\nu_{SGS,G}}{\sigma_{SGS,G}}-\frac{\nu_{SGS,L}}{\sigma_{SGS,L}}\right)\frac{\nabla\overline{A_{GL}}}{\overline{A_{GL}}}$$

(4-10)

where $\overline{A'_{\mathrm{k}}\boldsymbol{u}'_{\mathrm{k}}}$ reflects the effect of turbulent eddies interaction with bubbles on the change of bubble interface area, caused by turbulent eddy fluctuations characterised by the fluctuating velocities. $\nu_{SGS,k}$ is the SGS turbulent kinematic viscosity and $\sigma_{SGS,L}$ denotes the SGS turbulent Schmidt number in terms of the interfacial area density. $\sigma_{SGS,L}$ = 0.9 has been used in the present study. By analogy with the eddy diffusivity hypothesis, the relationship between the bubble surface area density fluctuation and SGS relative velocities can be specified in the format of relationship between volume fraction and fluctuation velocity and modelled with aid of Equation (4-8), which is given by

$$\frac{\overline{A'_{GL}(\boldsymbol{u}'_G-\boldsymbol{u}'_L)}}{\overline{A_{GL}}}=\frac{\overline{\alpha'_G(\boldsymbol{u}'_G-\boldsymbol{u}'_L)}}{\overline{\alpha_G}}$$

(4-11)

Thus, the turbulent dispersion term can be simplified and expressed as

$$\boldsymbol{M}_{TD,L}=\frac{3}{4}\rho_G\frac{C_D}{d_G}|\boldsymbol{u}_G-\boldsymbol{u}_L|\left(\frac{\overline{\alpha'_G u'_G}}{\alpha_G}-\frac{\overline{\alpha'_L u'_L}}{\alpha_L}\right)=\frac{3}{4}\rho_G\frac{C_D}{d_G}|\boldsymbol{u}_G-\boldsymbol{u}_L|\frac{\nu_{SGS}}{\sigma_{SGS}}\left(\frac{\nabla\alpha_G}{\alpha_G}-\frac{\nabla\alpha_L}{\alpha_L}\right).$$

(4-12)

Since $\alpha_L+\alpha_G=1$ in this two-phase flow system and $\nabla\alpha_L+\nabla\alpha_G=0$, this would yield Equation (4-13):

$$\boldsymbol{M}_{TD,L}=-\frac{3}{4}\rho_G\frac{C_D}{d_G}|\boldsymbol{u}_G-\boldsymbol{u}_L|\frac{\nu_{SGS}}{\sigma_{SGS}}\left(\frac{1}{\alpha_L}+\frac{1}{\alpha_G}\right)\nabla\alpha_G\,.$$

(4-13)

As mentioned earlier, the bubble oscillation in the bubble column bubbly flow can be thought as a result of the interactions between bubbles and the surrounding turbulent eddies in the frame of Eulerian-Eulerian modelling, leading to the deformation of the bubble shapes if bubbles are not subjected to coalescence and break-up. Consequently, the bubble groups are observed to be wobbling along the height of the bubble column. Following the previous work of Long *et al.* (2020) by considering bubble dynamic response to the turbulent eddies that interact with or hit on the bubbles, the liquid-phase turbulence eddy viscosity can be modified as the sum from the filtered turbulent shear and dynamic SGS eddy viscosities, which can be written as,

$$\mu_{T,L} = \rho_L (C_s \Delta)^2 |S| (1 + \mathrm{C_b} \alpha_G \frac{\lambda}{d_B} \left(\frac{1}{1 + St_{SGS}} \right)^{\frac{3}{2}}) \tag{4-14}$$

where λ represents the different turbulent length scales in the range between the integral and Kolmogorov scales ($L>\lambda>\eta$), *Cs* is a model constant, *S* is the characteristic filtered rate of strain tensor and St_{SGS} is the non-dimensional Stokes number expressed as $St_{SGS} = \frac{\tau_{\mathrm{bubble}}}{\tau_{L,SGS}}$. Here, the bubble response time scale can be estimated using $\tau_{\mathrm{bubble}} = \frac{4(\rho_G + 0.5\rho_L) d_B^2}{3\mu_L C_D Re_B}$. Bubble Reynolds number $\mathrm{Re}_{B,max} = \frac{\rho_L d_B u_{slip}}{\mu_L} \approx 714.95$ in this chapter. The characteristic time of turbulent eddies in sub-grid scale can be estimated by $\tau_{L,SGS} = \Delta / \boldsymbol{u}'_{\mathrm{L,SGS}}$, where $\Delta = \left(\Delta_i \Delta_j \Delta_k\right)^{1/3}$ is the filter width and $\mathrm{u}'_{\mathrm{L,SGS}}$ stands for the liquid fluctuation velocity in the local grid. That $\lambda \sim \Delta$ is

assumed as the filter length scale is usually to fall into the range of inertia subrange wave length based on the turbulent kinetic energy spectrum. Thus, the turbulent dispersion force considering turbulent eddies interaction with bubbles, which may give rise to the bubble deformation or oscillation in bubble column bubbly flow can be calculated by

$$\boldsymbol{M}_{TD,L} = C_{TD}\frac{3}{4}\rho_G\alpha_G\frac{C_D}{d_G}|\boldsymbol{u}_G - \boldsymbol{u}_L|\frac{(C_S\Delta)^2|S|\left(1+C_b\alpha_G\frac{\Delta}{d_B}\left(\frac{1}{1+St_{SGS}}\right)^{\frac{3}{2}}\right)}{\sigma_A}\left(\frac{1}{\alpha_L}+\frac{1}{\alpha_G}\right)\nabla\alpha_L \tag{4-15}$$

It can be seen that the effect of sub-grid scale bubble induced turbulence on the turbulent dispersion force has been indicated in Equation (4-15). Thus Equation (4-15) is implemented into the present Euler/Euler LES simulations. For simplicity, Equation (4-15) is referred to as the modified sub-grid turbulent dispersion force model (SGS-TDF) hereafter.

As shown in Figure 4-1, the filtering of the instantaneous added mass force will also result in the mean and turbulent contributions in SGS scale when taking the filtering to the instantaneous added mass force, which can be expressed as:

$$\overline{\chi_G\widetilde{\boldsymbol{M}}_{AM,L}} = \alpha_G\left(\boldsymbol{M}_{\boldsymbol{AM,L}}^{\boldsymbol{filtered}} + \boldsymbol{M}_{\boldsymbol{AMS}}^{\boldsymbol{T}}\right) \tag{4-21}$$

which can be approximately written as

$$\overline{\chi_G \widetilde{\boldsymbol{M}}_{AM,L}} = \alpha_G \rho_L C_{AM} \left(\frac{\partial \boldsymbol{u}_L}{\partial t} + \boldsymbol{u}_L \cdot \nabla \boldsymbol{u}_L - \frac{\partial \boldsymbol{u}_G}{\partial t} + \boldsymbol{u}_G \cdot \nabla \boldsymbol{u}_G \right)$$

$$+\rho_L C_{AM} \left(\nabla \cdot \left(\alpha_G \overline{\boldsymbol{u}'_{L,i} \boldsymbol{u}'_{L,J}} \right) - \nabla \cdot \left(\alpha_G \overline{\boldsymbol{u}'_{G,i} \boldsymbol{u}'_{G,J}} \right) \right) \quad (4\text{-}22)$$

It should be noted that the consequence of applying spatial filtering to the added mass force would deal with the correlations such as $\boldsymbol{u}'_{ki} \cdot \nabla \boldsymbol{u}'_{\mathrm{kj}}$ as indicated in the second part of the right-side of Equation (4-22), which functions like the Reynolds stress but also correlates with the local bubble volume fractions. It is referred to as the SGS added mass stress (SGS-AMS). With employing the eddy diffusivity hypothesis, the SGS added mass stress (SGS-AMS) can be formulated, which can be written as

$$\mathbf{M}_{\mathrm{AMS}} = \alpha_G \rho_L C_{AM} \left(\frac{\nabla \cdot (\alpha_L \boldsymbol{\tau}_L)}{\alpha_L \rho_L} - \frac{\nabla \cdot (\alpha_G \boldsymbol{\tau}_G)}{\alpha_G \rho_G} \right) \quad (4\text{-}23)$$

where $\boldsymbol{\tau}_L$ and $\boldsymbol{\tau}_G$ are defined by $\boldsymbol{u}'_{L,i} \boldsymbol{u}'_{L,j}$ and $\boldsymbol{u}'_{G,i} \boldsymbol{u}'_{G,j}$, respectively. As the bubbles are subjected to the interactions with the eddies, it would be expected that the SGS-AMS force will also have a significant impact on the bubble dynamics and interfacial mass transfer between the bubbles and liquid phase.

2.2 Numerical modelling

The proposed SGS turbulent dispersion and added mass stress models were tested by comparing the simulation results with the detailed experimental data as reported by Sommerfeld *et al.* (2018) and the author's experiment using the PIV. Both the

modelled circular bubble column and the actual bubble column used in the experiments have an internal diameter of 140 mm, which was filled with a liquid level height of 0.65m. The experimental bubble column has a gas sparger that contains 50 evenly distributed capillaries at 0.4 mm in diameter, injecting the gas from the annular region within 100 mm in diameter. The gas flow rate was controlled by maintaining 160 L/H, corresponding to a superficial velocity of 2.89E-3 m/s and averaged bubble volume fraction of 1.26% with the number-averaged bubble diameter of 2.55 mm. In the simulation, the number weighted bubble size distribution (BSD) among the entire bulk phase obtained in the experiment was adopted to account for the actual bubble size change. In the previous studies on bubble column bubbly flow, a Gaussian distribution of the BSD at the bubble column inlet area was assumed for various configuration of bubble distributors or spargers and applied for different superficial velocity conditions (Polli et al., 2002). Polli *et al.* (2002) suggested to use the following empirical correlation for estimation of the bubble size distribution at the gas distributor,

$$\mathrm{f_i} = q \cdot \exp\left(-\frac{(d_{Bi}-\bar{d})^2}{\left(\gamma^p d_{Bi,min}^3\right)^{2/3}}\right) \tag{4-24}$$

where, i denotes the i-th class of bubble size division, f represents the bubble volume fraction of the i-th class of bubbles and d_{Bi} stands for the bubble diameter. $\bar{d}_B$ denotes the bubble mean diameter, p and q are the coefficients that can be adjusted to ensure the requirement $\sum_{i=1}^{n} f_i = 1.$ γ stands for the volume increment ratio. In general, the original BSD must be related to the quantity and the diameter of the

sparger capillaries, properties of the carrier phase and superficial velocities. In trial simulations, it was found that the use of the correlation between f_i and $\bar{d}_B$ together with γ may be much more efficient. After considering the condition of the gas aerator used in the experimental set-up and the correlations suggested for the inlet superficial velocity and the averaged BSD in the previous studies (Kulkarni et al., 2004, Bhole et al., 2008, Yang and Xiao, 2017, Polli et al., 2002), the BSD adopted at the inlet based on the experimental set-up of bubble column in the simulations as shown in Figure 4-2 was used to specified for the mean diameter of the bubbles in the present LES simulation. It should be noted here that the bubbles may coalescence with other bubbles or break up, this may give rise to bubbles of different diameters, shapes and velocities. Considering bubble volume fraction for the present study $\alpha_G < 0.04$, the bubble number density transport may be more appropriately used to describe the bubble size distribution if bubbles move with small collision, negligible breakup and coalescence rates (Pourtousi et al., 2015), given by

$$\frac{\partial n}{\partial t} + \nabla \cdot (\boldsymbol{u}_G \mathrm{n}) = 0. \tag{4-25}$$

The Sauter mean diameter can then be obtained by

$$d_{G32} = \left(\frac{6\alpha_G}{\pi n}\right)^{1/3}. \tag{4-26}$$

As the local bubble equivalent diameter is the same order of the SGS grid scales, therefore, the bubble size can be characterised with the 0-th moment of the bubble

size distribution i.e., only taking the local mean bubble diameter, i.e. specification of one equivalent bubble diameter rather than a range of bubble sizes. This approach requires much less computational effort and offers a surprisingly good agreement with available experimental data in comparison with other ways for evaluating bubble sizes such as the adoption of population balance model (PBM) (Huang et al., 2018).

ANSYS CFX 18.0 with complied CCL was employed for Euler/Euler LES modelling in the present study with the boundary conditions specified as described below. At inlet, a mass flow rate was specified, which is corresponding to the experimental conditions used Sommerfeld *et al.* (2018) and the author's experiment, and the volume fraction for each phase is specified as: $\alpha_L = 0, \alpha_G = 1$. At the top surface of the reactor, a pressure-constant boundary i.e., relative pressure being specified to be 0, was given. A non-slip condition was applied to the inner wall of the bubble column. A central-differencing discretisation scheme was used for convective and diffusive terms in the momentum equations, while a second-order backward Euler scheme is employed regarding to the discretization algorithm for the transient term in all of the simulations. The mesh set-up for the current LES modelling is illustrated in Figure 4-3. The mesh set-up for the bubble column was satisfied the condition that the cell size of Δz^+=100 in the main flow direction and Δr^+=5 in the radial direction with a growth rate of 1.2. With caution and from the perspective of the computational cost, $\bar{d}_B/\Delta = 0.6375$ in the core-region was used in the current Eulerian-Eulerian LES modelling. This grid resolution adopted in the LES simulation

for bubbly flow is considered to be reasonably close to Milelli's limit (Milelli, 2002). By using this mesh set-up, the control volume cell is large enough to contain the information of bubbles and fine enough to resolve large scale turbulence. The mesh set-up with 95,400 cells has been used throughout all the calculations.

3. RESULTS AND DISCUSSION

With and without considering the modified turbulent dispersion and added mass stress force models, the bubbly flows in the bubble column as shown in Figure 4-2 have been investigated using the Euler/Euler LES approach, by adopting the mean bubble diameter $\bar{d}_B = 2.55mm$ coupled with the use of MUSIG model but with the fitted BSD that has been experimentally obtained for the bubble column sparger inlet. In the LES simulation, the time step δt_E was chosen in terms of CFL criterion, $\min\left(\frac{|\boldsymbol{u}_L|\delta t_E}{\Delta}, \frac{|\boldsymbol{u}_G - \boldsymbol{u}_L|\delta t_E}{\Delta}\right)$<1.0, varying from 0.0005 s to 0.001s for capturing the transient behaviour of turbulent eddy evolution in the bubble column. The simulations were run to last for 100 seconds while the instantaneous velocities at given positions were monitored and recorded during the calculation process. In order to obtain those parameters related to bubble velocity, liquid velocity, bubble volume fraction and turbulence statistical characteristics, the time average was taken over a period of 50 seconds after the bubbly flow large eddy patterns have been well established and this takes about 5 periods of large eddy fluctuation in the bubble column.

3.1 Effects of accounting for the turbulent dispersion and added mass stress in LES on bubble transport

To highlight the importance of the turbulent dispersion and added mass stress in

affecting the bubble transport in Eulerian-Eulerian LES modelling, the results obtained by using our modified SGS-TDF and SGS-AMS models are also compared with those using Euler/Lagrange LES simulation (Sommerfeld et al., 2018) and experimental data as shown in Figures 4-4 and 4-5. In Figure 4-4, the time-averaged bubble axial velocity profiles predicted by using the modified and standard turbulent dispersion force models at height z=0.325m are illustrated. The experimental results reported and the Eulerian-Lagrangian simulation results carried out by Sommerfeld *et al.* (2018) are also presented for comparison. According to their Euler/Lagrange simulation, the interfacial forces such as drag, wall lubrication, lift, buoyancy, added mass forces are accounted. Our Euler/Euler LES simulation has employed the forces that include the time averaged drag, lift, buoyancy, added mass forces together with the use of the modified SGS-TDF and SGS-AMS and taken the bubble induced turbulence into account (Cases 2: D+L+AM+SGS-TDF and Case 3: D+L+AM+SGS-TDF+SGS-AMS). Since the standard turbulent dispersion force is modified with the consideration of bubble response to eddies, the result obtained for Case 2 can be therefore compared with Case A of Sommerfeld *et al.* (2018). In addition, an additional factor with bubble shape change, i.e. the ratio of the long axis to short axis of the bubble, for bubble oscillation was considered in their simulation (Case B), whose effect can be compared with Case 3 in the present study. It can be seen from figures that the Euler/Euler LES by implementing either the modified SGS-TDF force or SGS-AMS models (Cases 2 and 3) performs better than the simple use of the momentum exchange terms, drag, lift and added mass forces (Cases 1), for prediction of both liquid and bubble velocity profiles.

When restricting the attention to the results using the MUSIG approach, the predicted bubble and liquid axial velocity profiles (Cases 2 and 3) are found to be good agreement with the experimental data as reported by Sommerfeld *et al.* (2018). The bubble axial velocity profile predicted by neglecting the SGS-TDF and SGS-AMS contributions shows an apparent difference from the experimental result with over-prediction of the bubble axial velocity in the central core region but under-prediction of its value nearing the bubble column wall. This clearly demonstrates that the inclusion of the modified SGS-TDF and SGS-AMS in the LES simulation has a remarkable influence on the bubble radial dispersion. It can be seen from Figure 4-5 that the liquid flows upward in the central region but has a descending flow in the vicinity of the wall, well consistent with the experimental observation. The position of flow reversal occurrence is clearly seen to take place at a radial location of around r/R=0.9. It should be noted that the consistency of Euler/Euler LES modelling results on predicted liquid phase axial velocity and bubble volume fraction profiles (see Figure 4-6) compared with the experimental data are also improved in both the central region and near-wall region of the bubble column. This may be attributed to the inclusion of the modified SGS-TDF and SGS-AMS models to be effectively modulate the bubble lateral dispersion in the LES simulation, consequently giving rise to a better estimation of the bubble volume fraction gradient and a better prediction of the turbulent shear stress acting on the bubbles. Based on the comparison with Euler/Lagrange LES results (Case B) of Sommerfeld *et al.* (2018), it has been shown that our Euler/Euler LES coupled with the modified SGS-TDF

and SGS-AMS models can deliver consistent results for bubble dynamics when comparing with the experimental data.

Figure 4-6 shows the time-averaged radial bubble volume fraction distribution obtained by using the standard SGS-TDF (Case 1), the modified SGS-TDF (Case 2) and the modified SGS-TDF plus SGS-AMS models (Case 3), compared with the Euler/Lagrange LES simulation results reported by Muniz and Sommerfeld (2020). It is worth mentioning that the adoption of the bubble dynamic model has significantly improved the simulation results that were well matched the experimental data in their work. Two dash lines represents the predicted bubble volume fraction with (blue) and without (dark blue) bubble dynamics model. The prediction of bubble volume fraction profiles can be used as an indicator to assess whether the proposed TDF and AMS models are working properly. It can be observed from Figure 4-5 that the predicted profiles by using the modified SGS-TDF model and the modified SGS-TDF and SGS-AMS are consistent with their predicted velocity profiles, especially for the case that the SGS-AMS model is implemented into the modelling. Compared to the one without using the standard SGS-TDF model, a noticeable improvement was found especially in the near wall region though the magnitude of contribution from the turbulent dispersion force predicted using the modified SGS-TDF and SGS-AMS is still small. The fact that the results obtained by considering the fluctuating $\overline{\alpha_k' \boldsymbol{u}_k'}$ and $\nabla \cdot \left(\alpha_G \overline{\boldsymbol{u}_{L,i}' \boldsymbol{u}_{L,J}'}\right)$ with dynamic response to surrounding eddies are improved and are better consistent with the experimental results highlights the need for inclusion of the SGS-TDF and SGS-AMS for properly modelling

bubble dispersion especially bubble radial migration in the bubble column bubbly flow. To indicate the effect of inclusion of the SGS-TDF and SGS-AMS on modelling bubble group dynamics, the temporal evolution of the location of the maximum bubble volume fraction $\alpha_{G,max}$ at the cutting plane at z=325mm and the FFT of liquid axial velocity fluctuation at the given point, obtained by using both the modified SGS-TDF and SGS-AMS models are shown in Figure 4-7 and Figure 4-8, respectively. Figure 4-7 depicts the trajectory of the $\alpha_{G,max}$ offset position evolution. It can be seen clearly from the figure that the bubble group movement in the bubble column oscillates with the time regularly during the sampling time, and approximately 5 iterations are observed. A good agreement in the bubble oscillation period (around 10s per POP) and amplitude is found in each position of plume (POP). Such phenomenon can be explained by the good balance in considering the modified terms and shows the accuracy in using the proposed models. Such oscillation also affects the liquid axial velocity fluctuation, likely indicating the effect of inclusion of the models on large eddy entrainment as evidenced by Figure 4-8. The maximum amplitude is found at $f = 0.09994$ Hz which can be converted into a period of time t=10.0006s. It can be cautiously claimed that the bubble lateral dispersion effect may be highly associated with the bubble oscillations as the filtered turbulent eddy fluctuations bring out the bubble surface deformation so that its mas centre changes with time (see Figure 4-1).

3.2 Quantification of SGS-turbulent dispersion force and added mass stress contributions and effect on bubble dynamics

The filtered eddy fluctuation induced turbulent dispersion force term related to $\overline{A_{\mathrm{k}}'\boldsymbol{u}_{\mathrm{k}}'}$ can be regarded as the correlation between the SGS area density fluctuation and SGS relative velocities. With the eddy diffusivity hypothesis, the following relation can be specified by Equation (4-27)

$$\overline{\frac{A_{GL}'(\boldsymbol{u}_G'-\boldsymbol{u}_L')}{\overline{A_{GL}}}} = \overline{\frac{\alpha_G'(\boldsymbol{u}_G'-\boldsymbol{u}_L')}{\overline{\alpha_G}}}. \tag{4-27}$$

Equation (4-27) has utilised the assumption that the bubble size is unchanged. If this constraint is released, Equation (4-27) can be approximated:

$$\overline{\frac{\alpha_G'(\boldsymbol{u}_G'-\boldsymbol{u}_L')}{\overline{\alpha_G}}} \approx \overline{\frac{(A_{GL}d_B)'(\boldsymbol{u}_G'-\boldsymbol{u}_L')}{\overline{(A_{GL}d_B)}}} \tag{4-28}$$

In the bubble column fact, the bubbles would change their shapes in the duration of their transport, implying the variations in the interfacial area and equivalent bubble size. Thus, Equation (4-28) represents the behaviour of instantaneous bubble shape variations in the bubble column. In order to characterise the effect of the contributions from SGS-TDF and SGS-AMS on turbulent dispersion, the ratios of cross-sectional averaged SGS-TDF and total added mass force to the overall sum of drag, lift and added mass forces at different cross-sections along the height of the bubble

column have been obtained. The cross-sectional averaged SGS-TDF and SGS-AMS at a given height are obtained by the following averaging method.

$$\boldsymbol{M}_{TD,L}(\mathrm{z}) = \frac{1}{\pi R^2}\int_0^{2\pi}\int_0^{R}\left[C_{TD}\,\frac{3}{4}\rho_G\alpha_G\,\frac{C_D}{d_G}\,|\boldsymbol{u}_G - \boldsymbol{u}_L|\,\frac{(C_s\Delta)^2|S|\left(1+C_b\alpha_G\frac{\lambda}{d}\left(\frac{1}{1+St_{SGS}}\right)^{\frac{3}{2}}\right)}{\sigma_A}\left(\frac{1}{\alpha_L}+\frac{1}{\alpha_G}\right)\nabla\alpha_L\right]rdrd\theta \tag{4-29}$$

$$\boldsymbol{M}_{AMS,L}(\mathrm{z}) = \frac{1}{\pi R^2}\int_0^{2\pi}\int_0^{R}\left[\alpha_{\mathrm{G}}\rho_{\mathrm{L}}\mathrm{C}_{\mathrm{AM}}\left(\frac{\nabla\cdot(\alpha_{\mathrm{L}}\boldsymbol{\tau}_{\mathbf{L}})}{\alpha_{\mathrm{L}}\rho_{\mathrm{L}}}-\frac{\nabla\cdot(\alpha_{\mathrm{G}}\boldsymbol{\tau}_{\mathrm{G}})}{\alpha_{\mathrm{G}}\rho_{\mathrm{G}}}\right)\right]rdrd\theta \tag{4-30}$$

Figure 4-9 shows the distribution of SGS-AMS and SGS-TDF terms obtained from the LES at different height in the bubble column together with the bubble volume fraction gradient and shear strain rate distribution from H=0.1-0.6m at t=100s. Figure 4-10 shows the quantification of the ratio of the cross-sectional averaged SGS-TDF to the sum of drag, lift and added mass forces along the bubble column height. By comparing the magnitude in relation to the contribution from drag, lift and added mass forces, it can be seen from Figure 4-10 that along the height, the ratio can reach around 12% but gradually decreases with the height. The decrease in the ratio of the SGS-turbulent dispersion force to the overall contribution from drag, lift and added mass forces along the column height reveals that the bubble lateral dispersion is highly affected by the turbulent dispersion force. It can influence the prediction of the behaviour of bubble group oscillations in the bubble column. In the bottom region of the bubble column, the shear turbulence induced by recircula-

tion large turbulent eddies gives a stronger liquid velocity fluctuations, thus corresponding to a stronger SGS-TDF which might promote the bubble group oscillations. It is worth noting that as bubble dynamic response to the turbulent eddy fluctuation, the ratio for the case of using the modified SGS-TDF slightly increases comparing to the simulation using the standard case (Case 1), which further indicates the effect of the modified SGS-TDF term on bubble lateral dispersion. In terms of the ratio of total added mass force to the sum of the averaged drag, lift and added mass forces, the magnitude of the ratio can also reach 9% in the lower part of the bubble column but follows the same trend as the ratio of SGS-TDF to the sum of drag, lift and added mass forces as shown in Figure 4-11. Apparently, high correlation of the bubble dynamics with the bubble dispersion does exist while the effect of the turbulent dispersion force SGS-TDF and added mass stress SGS-AMS on bubble group oscillation is evidenced by a larger ratio of SGS-TDF to the sum of drag, lift and added mass forces as shown in Figure 4-9. According to most of previously reported studies, the drag force can take around 60%-80% of all the considered interfacial forces (Muniz and Sommerfeld, 2020). Thus, the present study has highlighted the importance of the contributions of SGS-TDF and SGS-AMS in the LES modelling of bubble column bubbly flow. A closer observation on the contours of the instantaneous bubble volume fraction gradient and the shear strain rate distribution at different height shown in Figure 4-9 indicates that the SGS-AMS force is much dependent upon the instantaneous bubble volume fraction

gradient and turbulent shear strain rates both in the radial and axial directions. Considering the simplifications for bubble column bubbly flows, the bubble phase momentum balance can be approximately written as:

$$0 \approx -\nabla \cdot (\alpha_G \boldsymbol{\tau}_k) - \alpha_G \nabla p + \alpha_G \rho_G \boldsymbol{g} + \frac{3}{4}\rho_G \frac{C_D}{d_G}|\boldsymbol{u}_G - \boldsymbol{u}_L|(\boldsymbol{u}_G - \boldsymbol{u}_L) + C_{TD}\frac{3}{4}\rho_G \alpha_G \frac{C_D}{d_G}|\boldsymbol{u}_G - \boldsymbol{u}_L| \frac{(C_S\Delta)^2|S|\left(1+C_b\alpha_G\frac{\Delta}{d_B}\left(\frac{1}{1+St_{SGS}}\right)^{\frac{3}{2}}\right)}{\sigma_A}\left(\frac{1}{\alpha_L} + \frac{1}{\alpha_G}\right)\nabla\alpha_L + \alpha_G \rho_L C_{AM}\left(\frac{\nabla\cdot(\alpha_L\boldsymbol{\tau}_L)}{\alpha_L\rho_L} - \frac{\nabla\cdot(\alpha_G\boldsymbol{\tau}_G)}{\alpha_G\rho_G}\right) \quad (4\text{-}31)$$

It should be noted that when bubble column bubbly flow is entering the sub-steady status, the lift force is relatively weak while the added mass force contribution is also weak. Thus, it can be seen from the force balance (Equation (4-31)) that the effect of the turbulent dispersion and added mass stress on the bubble relative velocity is significant, explaining why these two terms needs to be included in the LES modelling of bubble column bubbly flows.

3.3 Effects of inclusion of turbulent dispersion and added mass stress on turbulent kinetic energy spectra and estimation of interfacial mass transfer coefficient

In order to assess the impact of inclusion of SGS-TDF and SGS-AMS models on the calculation of the turbulent kinetic energy of the liquid phase, the one-dimensional LES-filtered turbulent kinetic energy power spectral densities (PSD) $E_{11}(\kappa)$ obtained for Cases 1, 2 and 3 are presented in Figure 4-12. The liquid axial turbulent velocity is monitored at the centre of the cross section at z = 0.325 m. The turbulent

energy spectrum is obtained by taking the Fast Fourier Transform (FFT) of the time correlation of axial turbulent velocity fluctuations based on the Welch method (Welch, 1967). As can be seen from Figure 4-12, the PSD predicted by using the modified SGS-TDF and SGS-AMS models can be still approximated and described by using Pope's model spectrum but considering the bubble volume fraction influence and the relation between one-dimensional and three-dimensional spectrum, defined by

$$E_{11}(\kappa_{11}) = \int_{\kappa_{11}}^{\infty} \frac{E(\kappa)}{\kappa}\left(1 - \frac{\kappa_1^2}{\kappa^2}\right) d\kappa$$

$$= \int_{\kappa_{11}}^{\infty} \frac{C(1-\alpha_G)\varepsilon^{2/3}\kappa^{=5/3}\left[\frac{\kappa L}{\sqrt{(\kappa L)^2 + C_L}}\right]^{\frac{5}{3}+p_0} exp\left[-\beta\left\{\left[(\kappa\eta)^4 + C_\eta^4\right]^{1/4} - C_\eta\right\}\right]}{\kappa}\left(1 - \frac{\kappa_1^2}{\kappa^2}\right) d\kappa \tag{4-32}$$

in which η is the Kolmogorov micro-scale and L is the integral scale, characterising the large eddy size. The Kolmogorov constant C is normally set equal to 1.5(Pope, 2001), but the value for C was found to be around 1.65 in the present work. The parameter values C_L and C_η are calculated from the below integral constraints based on the spectrum obtained by the LES, which satisfy:

$$k = \int_0^{\infty} E(\kappa) d\kappa \tag{4-33}$$

and

$$\varepsilon = \int_0^\infty 2\nu\kappa^2 E(\kappa) d\kappa \tag{4-34}$$

The parameters β and p_0 are found to be equal to 5.2 and 2.0, respectively. The use of the modified SGS-TDF and SGS-AMS models gives a -5/3 scaling in smaller wave number zone while presents a -3 scaling law measured based on the wave number κ_1 larger than the typical wave number characterized by the equivalent bubble size, i.e. $\kappa_B = \frac{2\pi}{d_B} \approx 2464\ m^{-1}$. It can be seen from Figure 4-12(c) that the transition for different scaling laws in $E_{11}(\kappa)$ takes place in the wave number at about $\kappa_1 \approx 2500$ m^{-1}, where the left of the transition location shows the -5/3 slope while the right side of the transition give rise to the -3 scaling, clearly indicating the feature of feeding of bubble induced turbulence to the turbulent kinetic energy. This -3 scaling finding are also demonstrated by existing experimental work as well as DNSs (Prakash et al., 2016, Mercado et al., 2010, Murai et al., 2000, Bouche et al., 2014, Riboux et al., 2010, Bunner and Tryggvason, 2003, Riboux et al., 2013, Roghair et al., 2011, Sugiyama et al., 2001). For the present case, this may indicate that the turbulence due to the bubble wake induced turbulence is fed into the liquid shear turbulence at the wave number around *2500* m^{-1}, close to the representative bubble wave number. The kinetic energy power spectral density of the liquid axial liquid velocities, predicted by Case 1 and 2at the middle point at *z*= 0.325m are also shown in Figure 4-12(a) and 12(b), respectively, for cases with and without using the modified SGS-TDF and SGS-AMS models. The wavenumber that the change in slope after the -3 scaling law occurs is marked as K_c in three cases. It seemed that one can observe the existence of -3 scaling following the -5/3 scaling law for

the spectrums obtained from all the cases with or without using the modified SGS-TDF and SGS-AMS models in the LES simulations. However, the width of the -3 scaling law in the spectrum for Case 3, i.e using both the modified SGS-TDF and SGS-AMS, is much wider than the other two cases, further highlighting the effect of modified terms on SGS turbulent motion ahead of dissipation range.

Since the modified SGS models that have taken the turbulence kinetic energy contribution from BIT and bubble interaction with the turbulence eddies into account, the relative slip velocity between bubbles and liquid together with the local turbulent energy dissipation rate play significant roles in estimating the value of interfacial mass transfer coefficient k_L. The eddy cell model proposed by Lamont and Scott (Lamont and Scott, 1970) indicated that the very small scale of the turbulent eddies play significant roles in the mass transfer and these motions lead to a sophisticate viscosity. They suggested that the surface renewal rate as the mass transfer indicator can be estimated as

$$k_L \propto D_L^{1/2} \left(\frac{\varepsilon_L}{\nu}\right)^{1/4} \tag{4-35}$$

where D_L is liquid mass diffusivity of liquid phase, ε_L is the local turbulence dissipation rate. It can be assumed that the local total turbulence dissipation rate by considering the bubble-eddy interactions can be expressed as $\varepsilon_L = \varepsilon + \varepsilon_B =$

$\varepsilon\left(1+\mathrm{C_b}\overline{\alpha_G}\frac{\lambda}{\mathrm{d}}\left(\frac{1}{1+St_{SGS}}\right)^{\frac{3}{2}}\right)=2\nu\int_0^{\infty}\kappa^2\,E(\kappa)d\kappa$. The influences of bubbles' dynamic responses to the surrounding liquid and inclusion of the SGS-TDF and SGS-AMS models in the LES on the liquid turbulent kinetic energy spectrum has been illustrated in Figure 4-12 and Equation (4-35), and can be used for estimation for k_L based on the eddy cell model, which can be expressed as

$$k_L \propto D_L^{1/2}\left(\frac{\varepsilon\left(1+\mathrm{C_b}\overline{\alpha_G}\frac{\lambda}{\mathrm{d}}\left(\frac{1}{1+St_{SGS}}\right)^{\frac{3}{2}}\right)}{\nu}\right)^{1/4} \propto D_L^{1/2}\left(\frac{2\nu\int_0^{\infty}\kappa^2E(\kappa)d\kappa}{\nu}\right)^{1/4} \tag{4-36}$$

Equation (4-36) shows that k_L is related to the turbulent kinetic energy integrated from the energy spectrum shown in Figure 4-12. As shown in Figure 4-13, a higher volumetric mass transfer coefficient at the cross-section z=325 mm was found when applying both the SGS-TDF and SGS-AMS models. It seems that ignorance of the SGS-TDF and SGS-AMS will result in underestimation of the mass transfer coefficient. It can also be seen from Figure 4-13 that there exist two peaks in the mass transfer coefficient radial distribution, likely associated with the gradient of turbulent shear strain distribution. This phenomenon is well demonstrated by Figure 4-14, where the volumetric mass transfer coefficient contours obtained at different height with and without using both the SGS-TDF and SGS-AMS models are compared. Therefore, by employing both the modified SGS-TDF and SGS-AMS models in the LES modelling, the distribution behavior of mass transfer characterized by $k_L a$ inside the bubble column can be better analyzed.

3.4 Analysis of spatial correlation between local bubble volume fraction and shear strain rate

In order to assess the effect of accounting the SGS-AMS on the evolution of turbulent eddy structural behaviour in the bubble column, the correlation between the local bubble volume fraction fluctuation and the added mass stress was assessed. As the SGS-AMS can be modelled by the product of the eddy viscosity and the filtered shear strain rates which can describe the shear caused by the turbulent eddies hitting on the bubbles, it can be expected that such evaluation would give a quantitative description of the effect of the SGS turbulent eddies on the bubble transport in the bubble column. The shear strain rate tensor $\boldsymbol{S}_{ij}$ is defined by $\boldsymbol{S}_{ij} = \frac{1}{2}\left(\frac{\partial \boldsymbol{u}_{Li}}{\partial x_j} + \frac{\partial \boldsymbol{u}_{Lj}}{\partial x_i}\right)$ and can be decomposed into a filtered and a fluctuation$\boldsymbol{S}_{ij} = \overline{\boldsymbol{S}}_{ij} + \boldsymbol{S}'_{ij}$. The correlation for $\alpha_L\overline{\boldsymbol{u}'_{L,i}\boldsymbol{u}'_{L,J}}$, which characterises the SGS-AMS evolution, thus can be written as

$$(C_s\Delta)^2\left|\bar{S}_{ij}\right|C_b\alpha_G\frac{\lambda}{d_B}\left(\frac{1}{1+St_{SGS}}\right)^{\frac{3}{2}}\overline{\boldsymbol{S}}_{ij}$$

It is expected that the interactions between the bubbles and the surrounding turbulent eddies in SGS scale in the bubble column would noticeably affect the bubble entrainment while this interaction has been accounted for in the SGS-AMS model. The following spatial correlation between the local bubble volume fraction and shear strain rate fluctuation to characterise the interaction of bubbles with SGS turbulent eddies along the axial height of the bubble column can be proposed and defined by

$$R_{\alpha_G \bar{S}_{ij}}(\Delta h) = \frac{\overline{\alpha'_G(h_0)|\bar{S}'_{IJ}(h_0+\Delta h)|}}{\sqrt{\alpha'^2_G(h_0)}\sqrt{\overline{|\bar{S}'^2_{ij}(h_0)|}}} \tag{4-37}$$

where Equation (4-36), α'_G and $\boldsymbol{S}_{ij}$' are defined by

$$\alpha'_G(z) = \alpha_G(z) - \frac{1}{h}\int_0^h \alpha_G(z)dz\,, \tag{4-38}$$

$$\bar{S}'_{ij}(z) = \bar{S}_{ij}(z) - \frac{1}{h}\int_0^h \bar{S}_{ij}(z)dz \tag{4-39}$$

Figure 4-15 shows the iso-surfaces of bubble volume fraction and local liquid shear strain rate distribution in the bubble column at t =100s. Figure 4-16 presents the spatial correlation coefficient $R_{\alpha_G \bar{S}_{ij}}(\Delta h)$ along the centreline at different axial height from Δh = 0 to Δh = 0.325m of the bubble column. It can be seen from the figure that along the centreline, higher value of bubble volume fraction, is always accompanied by larger variations in the correlation coefficient $R_{\alpha_G \bar{S}_{ij}}(\Delta h)$ along the height. This can be interpreted as the consequence of bubble entrainment being strongly affected by those turbulent eddies that are in the forehead region around the rising bubbles, which give rise to the local shear strain fluctuation around the spatially filtered shear strain rate along the height of the bubble column. Such turbulence induced shear strain rate change strongly affect the entrainment of the bubbles, characterised by the local bubble volume fraction fluctuations as can be seen from Figure 4-16. This again indicates that the added mass stress SGS-AMS has a significant effect on the prediction of bubble dispersion in the LES modelling.

4. CONCLUSIONS

Euler/Euler Large Eddy Simulation of the bubbly flow in the bubble column with consideration of the SGS turbulent dispersion and added mass stress forces has been conducted. The transient turbulent bubbly flow patterns and bubble dynamics are captured. The time-averaged bubble velocity, bubble volume fraction profiles and the turbulent kinetic energy spectrum obtained from the LES modelling were compared with the experimental data. The main concluding remarks are summarized as follows:

1) Bubble dynamics in the bubble column can be captures by using the adequate SGS-TDF and SGS-AMS models in Eulerian-Eulerian LES modelling, when mimicking the bubble transport in the bubble column. It has been demonstrated clearly that by using Euler/Euler large-eddy simulations (LES) modelling with considering the effect of bubble-eddy interactions on the SGS turbulent dispersion and added mass stress models, the improvement on the prediction of bubble dynamics was apparent based on the bubble axial velocity and bubble volume fraction profiles. This can imply that the modified SGS-TDF and SGS-AMS models may play an equivalent role in indicating the bubble fluctuating motion predicted by using Euler/Lagrange LES modelling approach but with the stochastic dispersion model (Sommerfeld et al., 2018).

2) The cross-sectional averaged absolute ratios of SGS-TDF force to the time averaged drag force and SGS-AMS force to the time averaged added mass force along

the height of the bubble column are found to be around 5%-10% with the higher percentage taking place in the lower part of the column. This indicates that modelling of the bubble dispersion, especially bubble lateral dispersion is highly influenced by use of SGS-TDF and SGS-AMS models. Both SGS-TDF and SGS-AMS play an important role in radial re-distribution of bubble volume fraction profiles with the SGS-TDF having more influences in the radial direction while SGS-AMS having more influences in the main flow direction.

3) The turbulent kinetic energy spectrum obtained from the Euler/Euler LES modelling for the axial liquid velocity at the given locations by using the combination of the modified SGS-TDF and SGS-AMS models has shown that the turbulent kinetic energy spectrum in the bubble column still presents a -5/3 scaling law followed by an approximate -3 scaling law in the slope of the spectrum, this is very likely attributed to the lower bubble volume fraction bubbly flow in the bubble column. For those turbulent eddies with the wavenumber being smaller than the characteristic wavenumber based on the bubble size, a -5/3 scaling law was observed, but a -3 scaling law was observed for the wavenumber being larger than the characteristic wavenumber. This demonstrates that the effect of bubble induced turbulence on the energy cascade mainly takes place in the region of high wavenumbers, where the turbulence may quickly be dissipated. The transition location for the slope in the turbulent kinetic spectrum obtained using the modified SGS turbulent dispersion and SGS-AFS models for the cases in the present study occurs

at about $\kappa = 2500\ m^{-1}$, which is close to the characteristic wavenumber of the transported bubbles $\kappa_B = 2464\ m^{-1}$. Additionally, a wider range of -3 scaling law is found with the consideration of SGS-TDF and SGS-AMS models, which demonstrates the good estimation of sub-grid scale turbulent motion before dissipation range by using the modified model.

4) The turbulent diffusion effects due to the contributions from the turbulent dispersion and the added mass stress forces include the correlations of the extra eddy viscosity related to bubble dynamic response to the turbulent eddies with the local bubble volume fraction gradient and the local bubble volume fraction related to the turbulent shear stresses gradients in the liquid and in the bubble phases. The numerical results show clearly that the two terms have complementary effects on the bubbles dynamics and on the bubble volume fraction distribution phenomenon. The simultaneous consideration of the two terms in the interfacial momentum transfer, allows an adequate prediction of the relative velocity reduction and inversion of bubble transport in the region near the bubble column wall. The better prediction of the bubble volume fraction distribution and the turbulent shear induced and bubble induced turbulence stresses acting on the bubbles are of importance for determination of the other interfacial forces and have a significant impact on the interfacial mass transfer.

REFERENCES

ATIYA, M. A., RAHMAN, A. M. & ABD AL-JABBAR, A. 2011. Simulation of oxygen mass transfer in an internal loop airlift reactor with axial dispersion model. *Al-Khwarizmi Engineering Journal,* 7**,** 61-75.

AYED, H., CHAHED, J. & ROIG, V. 2007. Hydrodynamics and mass transfer in a turbulent buoyant bubbly shear layer. *AIChE Journal,* 53**,** 2742-2753.

BURNS, A. D., FRANK, T., HAMILL, I. & SHI, J.-M. The Favre averaged drag model for turbulent dispersion in Eulerian multi-phase flows. 5th International Conference on Multiphase Flow, ICMF, 2004. ICMF, 1-17.

BUWA, V. V. & RANADE, V. V. 2002. Dynamics of gas–liquid flow in a rectangular bubble column: experiments and single/multi-group CFD simulations. *Chemical Engineering Science,* 57**,** 4715-4736.

DARMANA, D. 2006. *On the multiscale modelling of hydrodynamics, mass transfer and chemical reactions in bubble columns.* PhD Thesis, University of Twente.

DEEN, N. G., SOLBERG, T. & HJERTAGER, B. H. 2001. Large eddy simulation of the gas–liquid flow in a square cross-sectioned bubble column. *Chemical Engineering Science,* 56**,** 6341-6349.

DHOTRE, M., NICENO, B. & SMITH, B. 2008. Large eddy simulation of a bubble column using dynamic sub-grid scale model. *Chemical Engineering Journal,* 136**,** 337-348.

DHOTRE, M., SMITH, B. & NICENO, B. 2007. CFD simulation of bubbly flows: Random dispersion model. *Chemical Engineering Science,* 62**,** 7140-7150.

FARD, M. G., STIRIBA, Y., GOURICH, B., VIAL, C. & GRAU, F. X. 2020. Euler-Euler large eddy simulations of the gas–liquid flow in a cylindrical bubble column. *Nuclear Engineering and Design,* 369**,** 110823.

HOSOI, H. & YOSHIDA, H. Model development of turbulent dispersion force for advanced two-fluid model in consideration of bubble-liquid phase interactions. International Conference on Nuclear Engineering, 2010. 565-571.

KULKARNI, A., EKAMBARA, K. & JOSHI, J. 2007. On the development of flow pattern in a bubble column reactor: experiments and CFD. *Chemical Engineering Science,* 62**,** 1049-1072.

LAÍN, S. & GRILLO, C. 2007. Comparison of turbulent particle dispersion models in turbulent shear flows. *Brazilian Journal of Chemical Engineering,* 24**,** 351-363.

LAVIÉVILLE, J., MÉRIGOUX, N., GUINGO, M., BAUDRY, C. & MIMOUNI, S. 2017. A generalized turbulent dispersion model for bubbly flow numerical simulation in NEPTUNE_CFD. *Nuclear Engineering and Design,* 312**,** 284-293.

LONG, S., YANG, J., HUANG, X., LI, G., SHI, W., SOMMERFELD, M. & YANG, X. 2020. Large-eddy simulation of gas–liquid two-phase flow in a bubble column reactor using a modified sub-grid scale model with the consideration of bubble-eddy interaction. *International Journal of Heat and Mass Transfer,* 161**,** 120240.

MA, T., ZIEGENHEIN, T., LUCAS, D., KREPPER, E. & FRÖHLICH, J. 2015. Euler–Euler large eddy simulations for dispersed turbulent bubbly flows. *International Journal of Heat and Fluid Flow,* 56**,** 51-59.

MUDDE, R., GROEN, J. & VAN DEN AKKER, H. 1997. Liquid velocity field in a bubble column: LDA experiments. *Chemical Engineering Science,* 52**,** 4217-4224.

NIČENO, B., BOUCKER, M. & SMITH, B. 2008a. Euler-Euler Large Eddy Simulation of a Square Cross-Sectional Bubble Column Using the Neptune_CFD Code. *Science and Technology of Nuclear Installations,* 2009.

NIČENO, B., DHOTRE, M. & DEEN, N. 2008b. One-equation sub-grid scale (SGS) modelling for Euler–Euler large eddy simulation (EELES) of dispersed bubbly flow. *Chemical Engineering Science,* 63**,** 3923-3931.

REZIG, M., BELLAKHAL, G. & CHAHED, J. 2017. Phase distribution in dispersed liquid–liquid flow in vertical pipe: Mean and turbulent contributions of interfacial force. *AIChE Journal,* 63**,** 4214-4223.

RZEHAK, R., KRAUß, M., KOVÁTS, P. & ZÄHRINGER, K. 2017. Fluid dynamics in a bubble column: New experiments and simulations. *International Journal of Multiphase Flow,* 89**,** 299-312.

SOMMERFELD, M. Some open questions and inconsistencies of Lagrangian particle dispersion models. Proc. of 9th Symp. on Turbulent Shear Flows, 1993.

SOMMERFELD, M. & BRODER, D. 2009. Analysis of hydrodynamics and microstructure in a bubble column by planar shadow image velocimetry. *Industrial & Engineering Chemistry Research,* 48**,** 330-340.

SOMMERFELD, M., MUNIZ, M. & REICHARDT, T. 2018. On the importance of modelling bubble dynamics for point-mass numerical calculations of bubble columns. *Journal of Chemical Engineering of Japan,* 51**,** 301-317.

TABIB, M. V., ROY, S. A. & JOSHI, J. B. 2008. CFD simulation of bubble column—an analysis of interphase forces and turbulence models. *Chemical Engineering Journal,* 139**,** 589-614.

ZHANG, D., DEEN, N. G. & KUIPERS, J. 2009. Euler− Euler modeling of flow, mass transfer, and chemical reaction in a bubble column. *Industrial & Engineering Chemistry Research,* 48**,** 47-57.

FIGURES

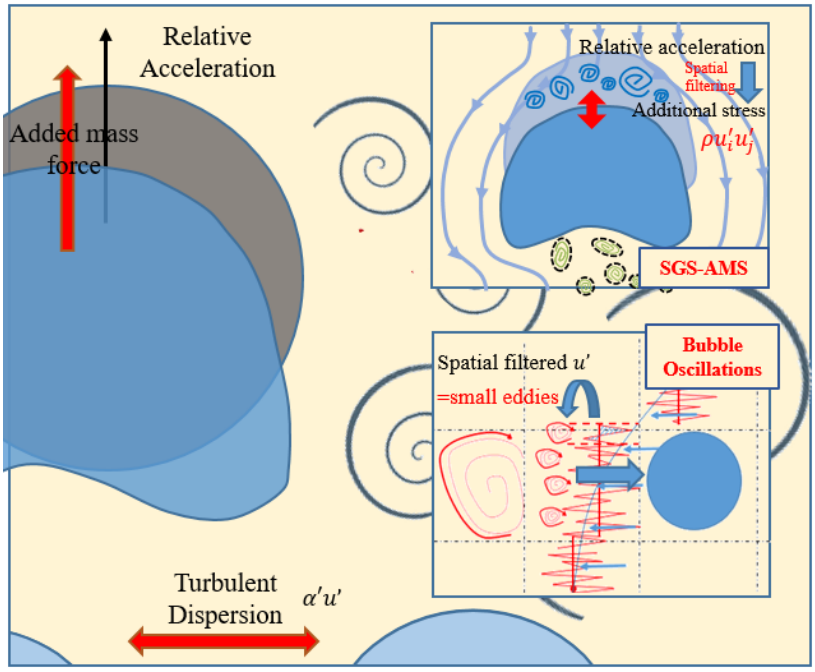

4- 1 Schematic of contribution from SGS-TDF and SGS-AMS in bubbly flow.

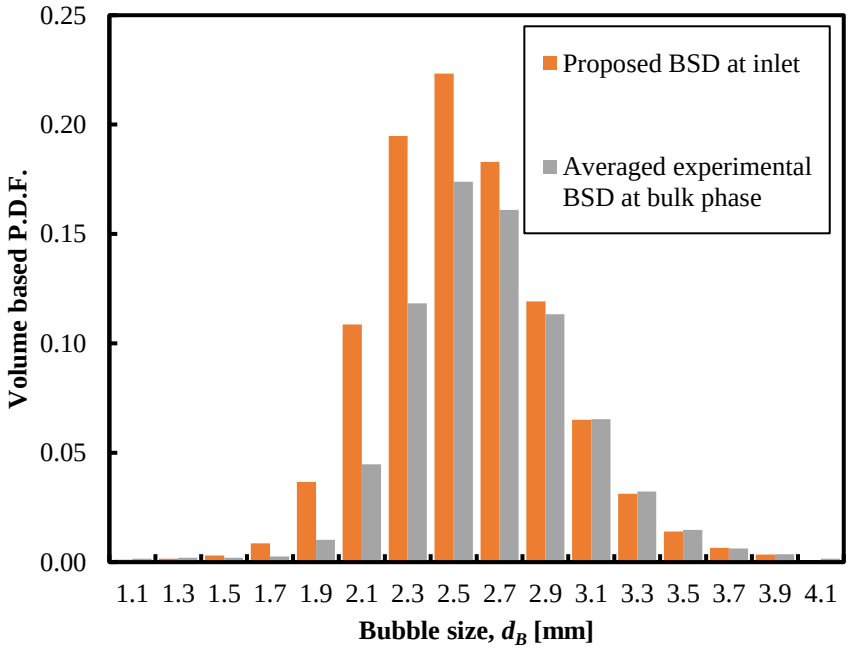

Figure 4- 2 Comparison of domain-averaged BSD and the adjusted BSD employed in the present LES simulation.

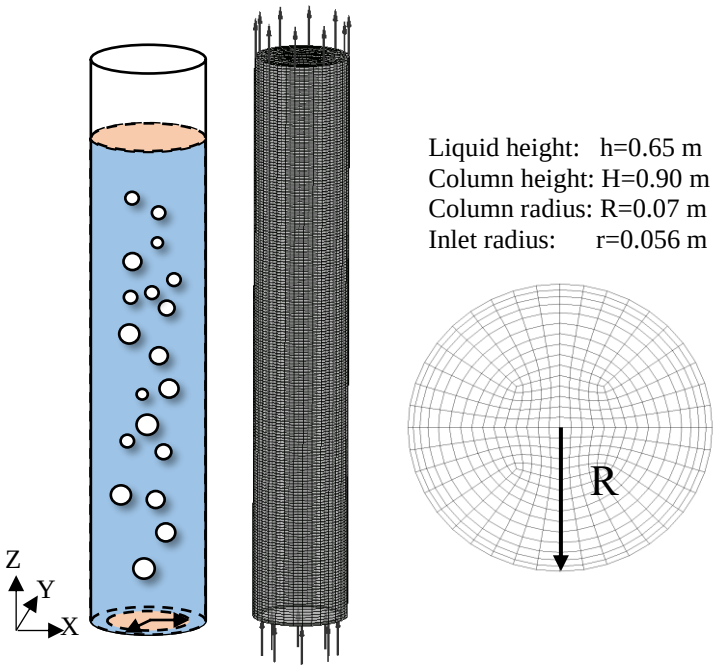

Figure 4- 3 Mesh set-up in the bubble column for LES modelling.

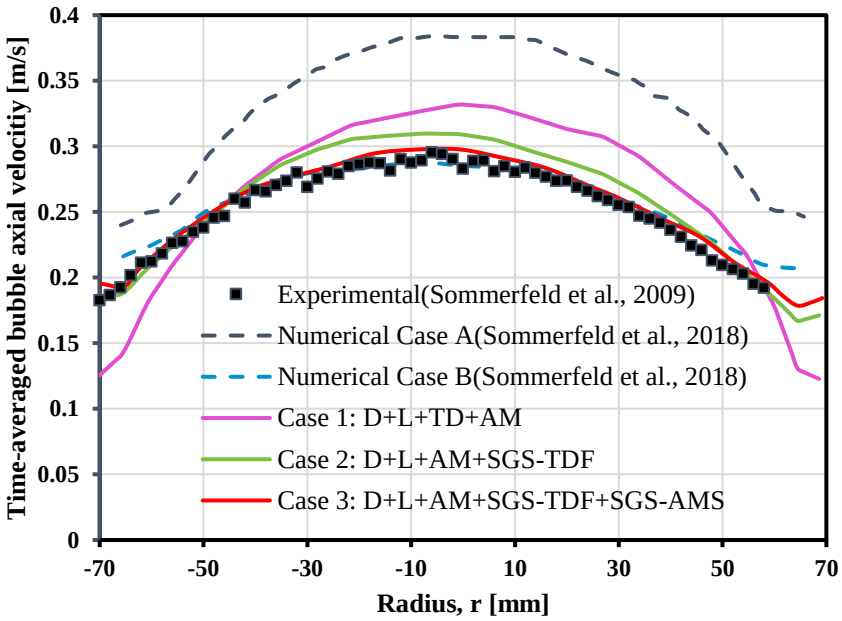

Figure 4- 4 Comparison of time-averaged bubble axial velocity distribution at z=325mm by using three models with experimental and numerical data obtained from Sommerfeld *et al*. (Dot: experimental data (2009); Dash: E-L simulation data

(2018) (Case A: all forces; Case B: all forces and bubble dynamic model); Solid: E-E simulation results in present case(Pink: conventional drag, lift, turbulent dispersion and added mass force; Green: pink with the modification on SGS turbulent dispersion; Red: pink with the modification on SGS turbulent dispersion and SGS added mass).

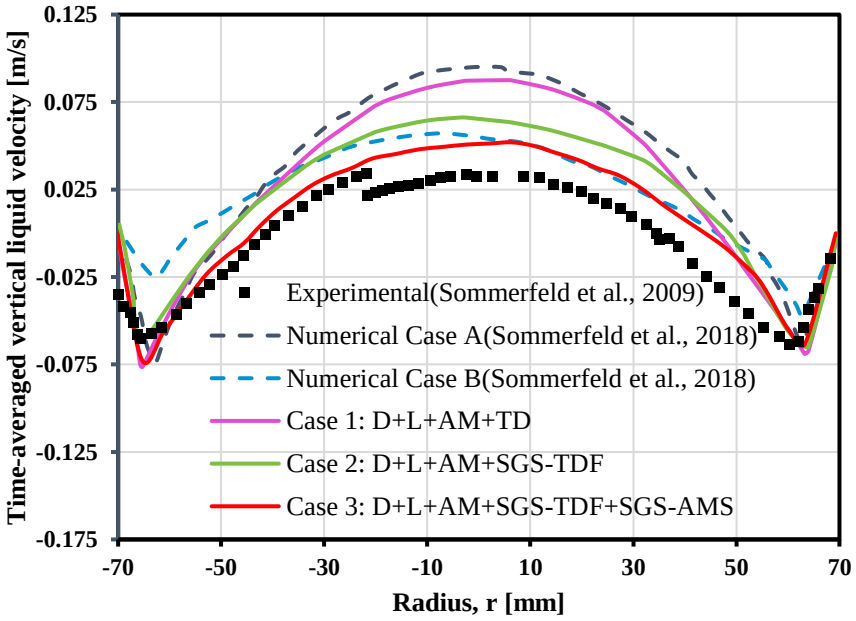

Figure 4- 5 Comparison of time-averaged liquid axial velocity distribution at z=325mm by using three models with experimental and numerical data obtained from Sommerfeld *et al* (2009, 2018).

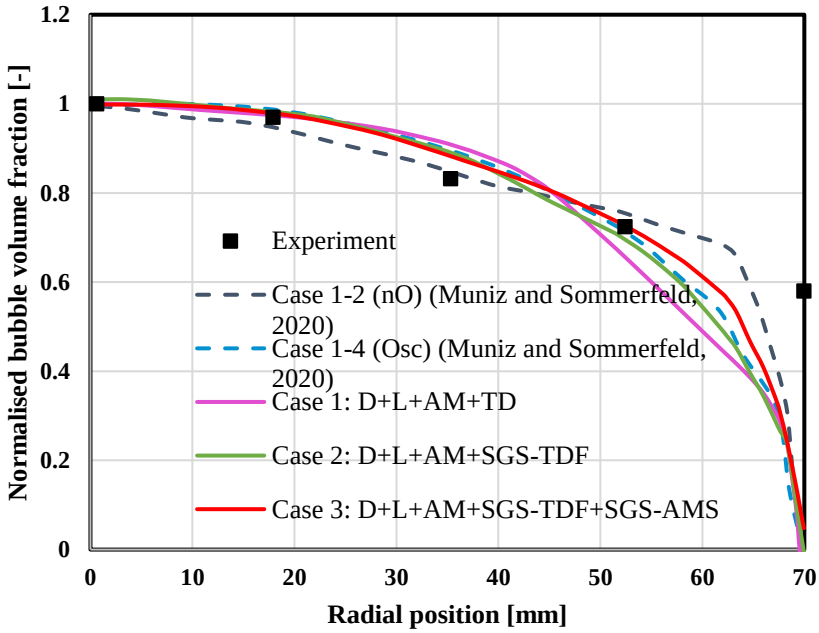

Figure 4- 6 Comparison of time-averaged normalized bubble volume fraction distribution at z=325mm by using three models with experimental and numerical data obtained from Sommerfeld *et al*. (2009, 2020)

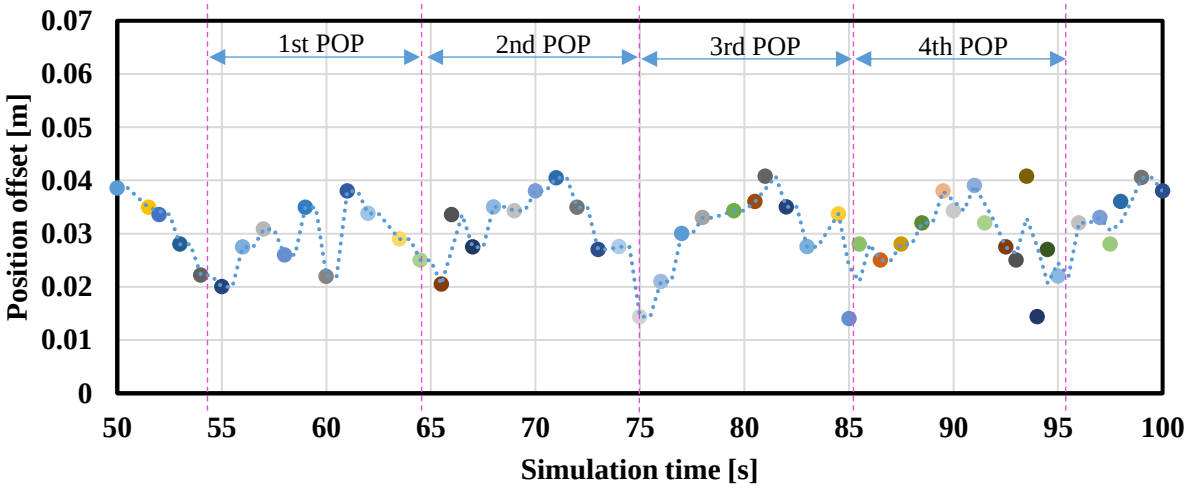

Figure 4- 7 Temporal evolution of the location of the maximum bubble volume fraction $\alpha_{G,max}$ at the cutting plane of the bubble column at z=325mm, obtained by using both the modified SGS-TDF and SGS-AMS models (Case 3).

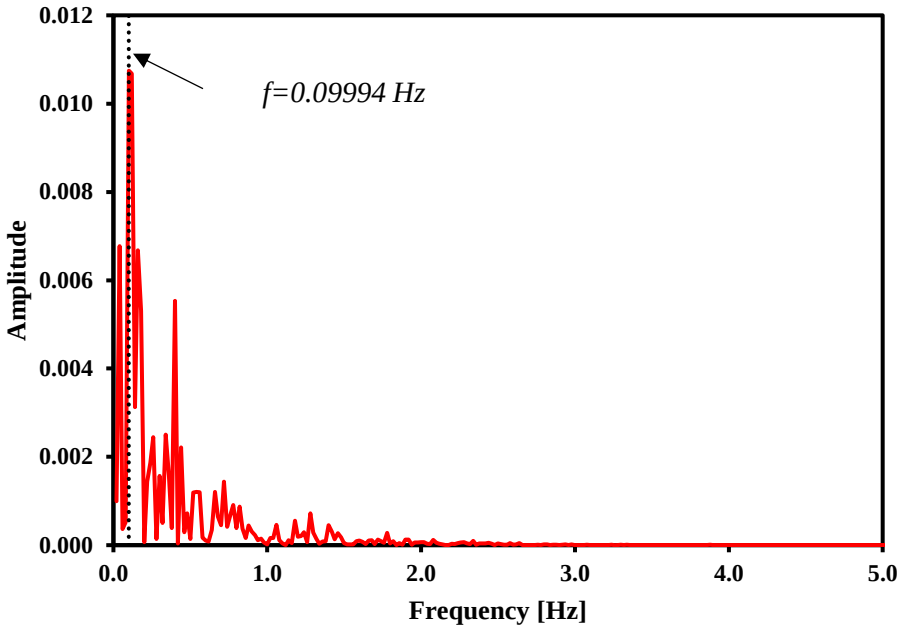

Figure 4- 8 FFT of liquid axial velocity fluctuation obtained at middle point at z=325mm.

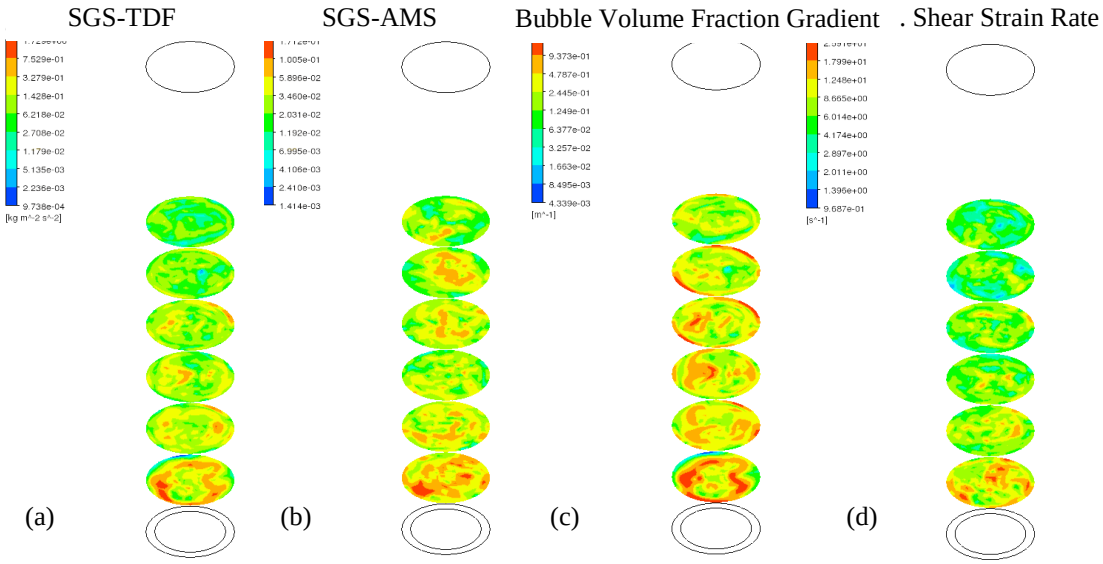

Figure 4- 9 Distribution of (a) SGS-TDF; (b) SGS-AMS; (c) bubble volume fraction gradient; (d) liquid phase shear strain rate at different height from H=0.1-0.6m at t=100s in Case 3.

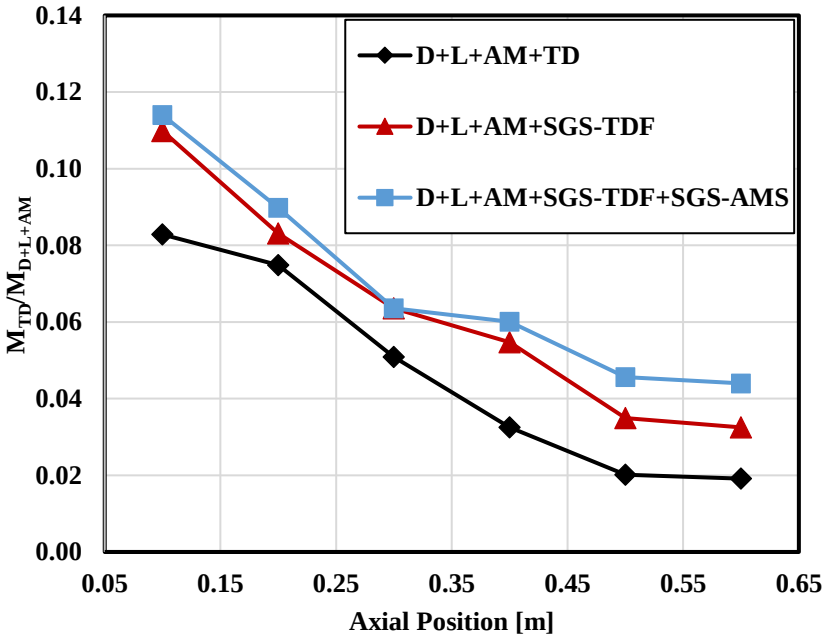

Figure 4- 10 Quantification of SGS turbulent dispersion force (TDF) contribution: cross-sectional averaged TDF over the sum of drag, lift and added mass force ratio along the bubble column height H=0.1-0.6m.

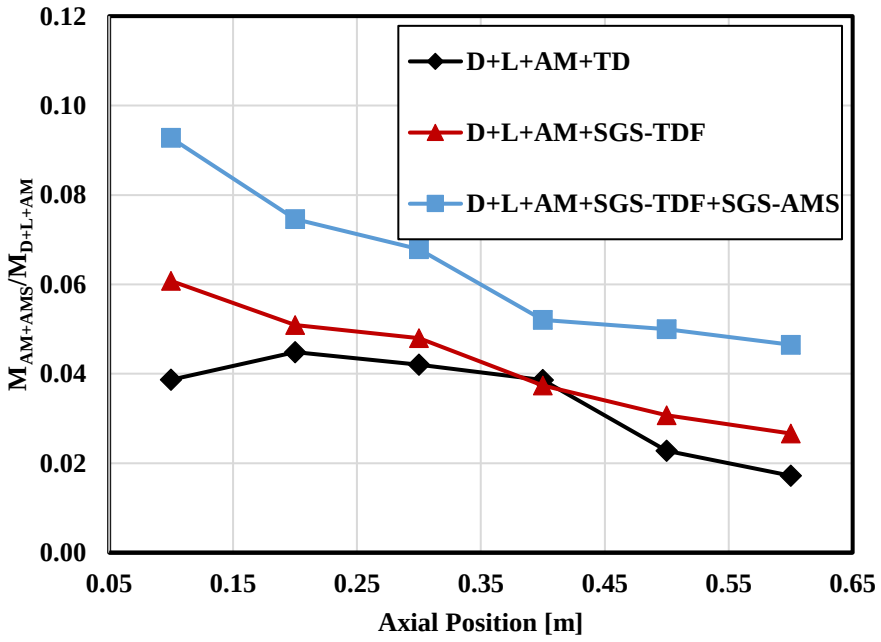

Figure 4- 11 Quantification of total added mass force (AM) contribution: cross-sectional averaged AM over the sum of drag, lift and added mass force ratio along the bubble column height H=0.1-0.6m.

(a)

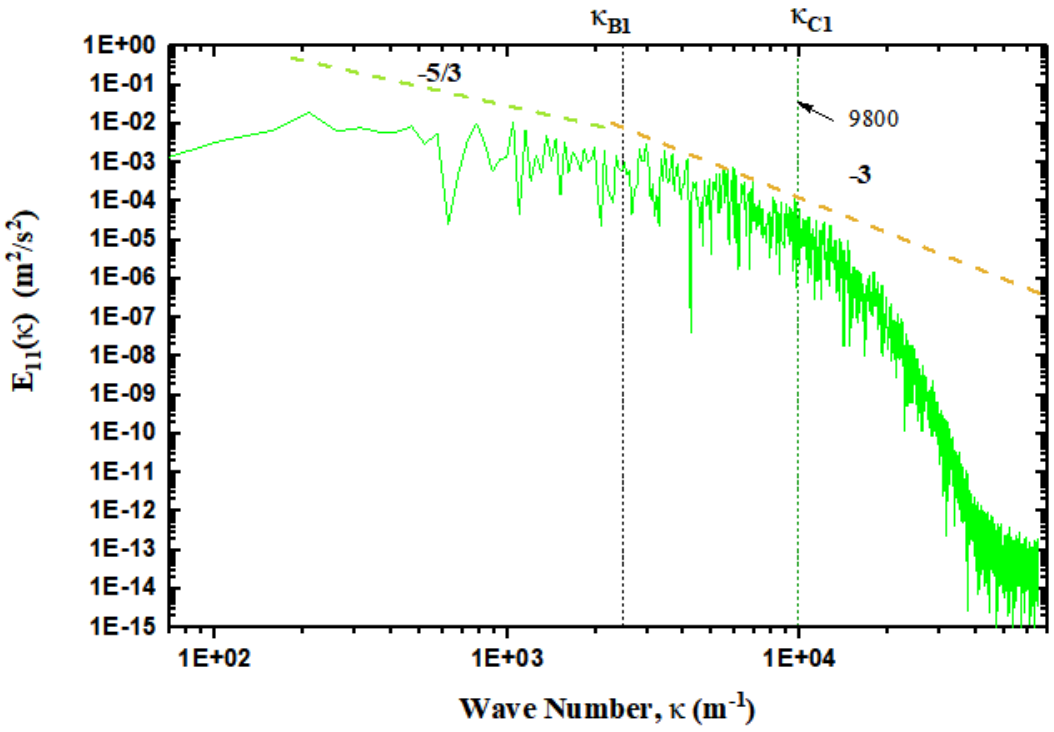
κB1
κC1
-5/3
9800
-3
E11(κ) (m²/s²)
Wave Number, κ (m⁻¹)
1E+00
1E-01
1E-02
1E-03
1E-04
1E-05
1E-06
1E-07
1E-08
1E-09
1E-10
1E-11
1E-12
1E-13
1E-14
1E-15
1E+02
1E+03
1E+04

(b)

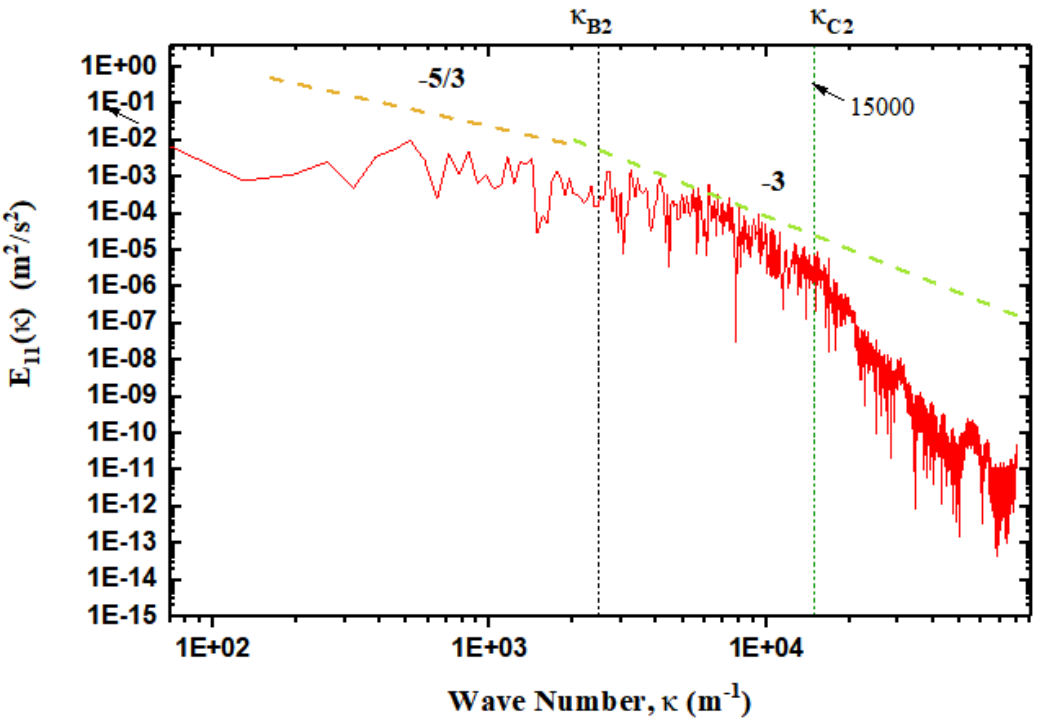
κB2
κC2
-5/3
15000
-3
E11(κ) (m²/s²)
Wave Number, κ (m⁻¹)
1E+00
1E-01
1E-02
1E-03
1E-04
1E-05
1E-06
1E-07
1E-08
1E-09
1E-10
1E-11
1E-12
1E-13
1E-14
1E-15
1E+02
1E+03
1E+04

(c)

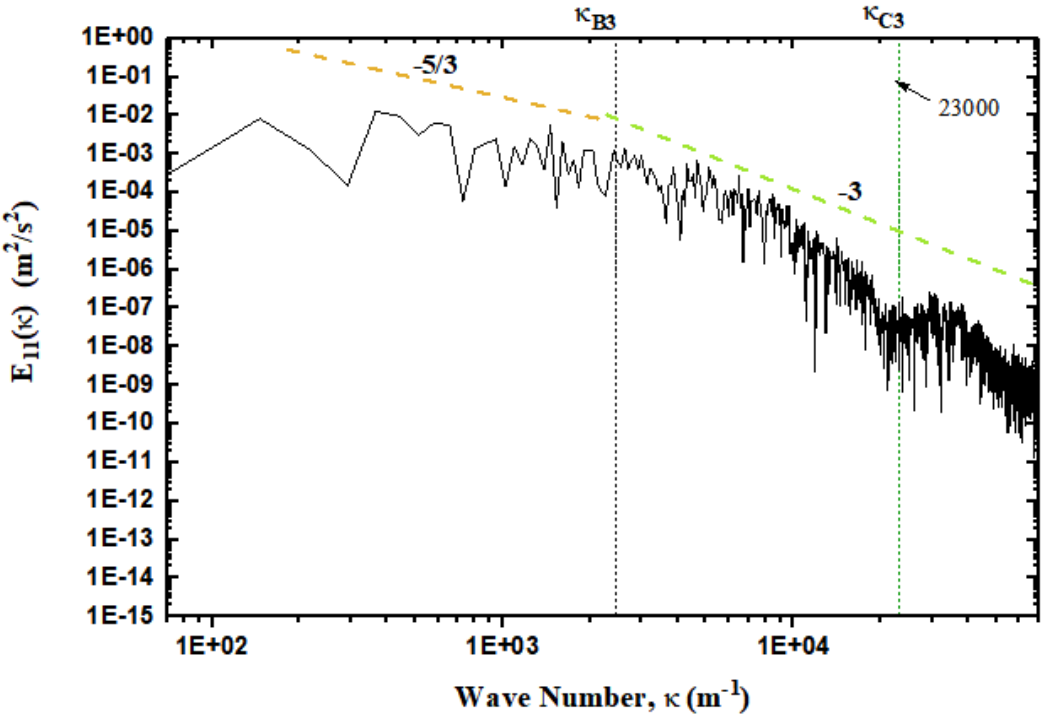

Figure 4- 12 Predicted turbulent kinetic energy spectrum of liquid axial velocity at middle point at z=325mm by using (a) case 1: D+L+AM+TD; (b) case 2: D+L+AM+SGS-TDF; (c) case 2: D+L+AM+SGS-TDF+SGS-AMS.

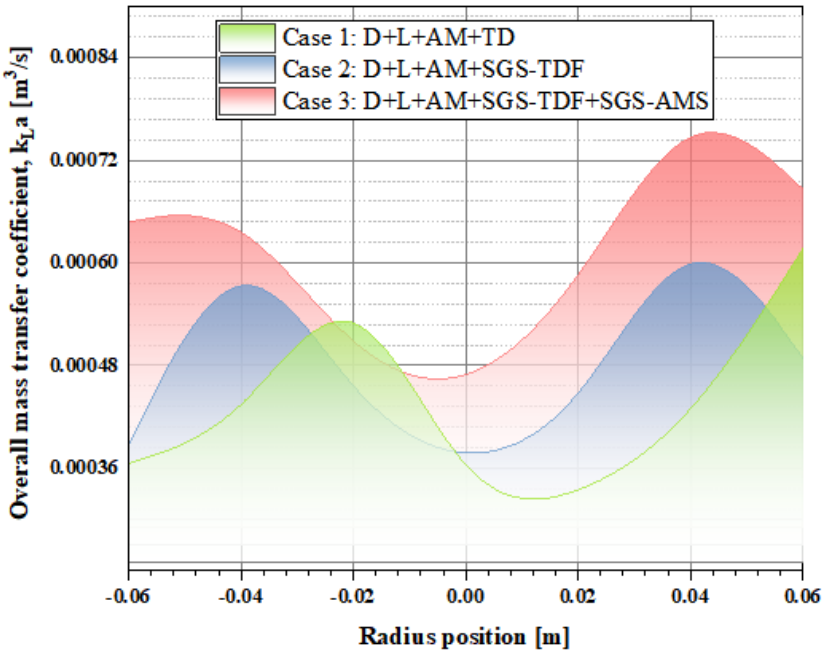

Figure 4- 13 Estimated volumetric mass transfer coefficient radio distribution at z=325mm.

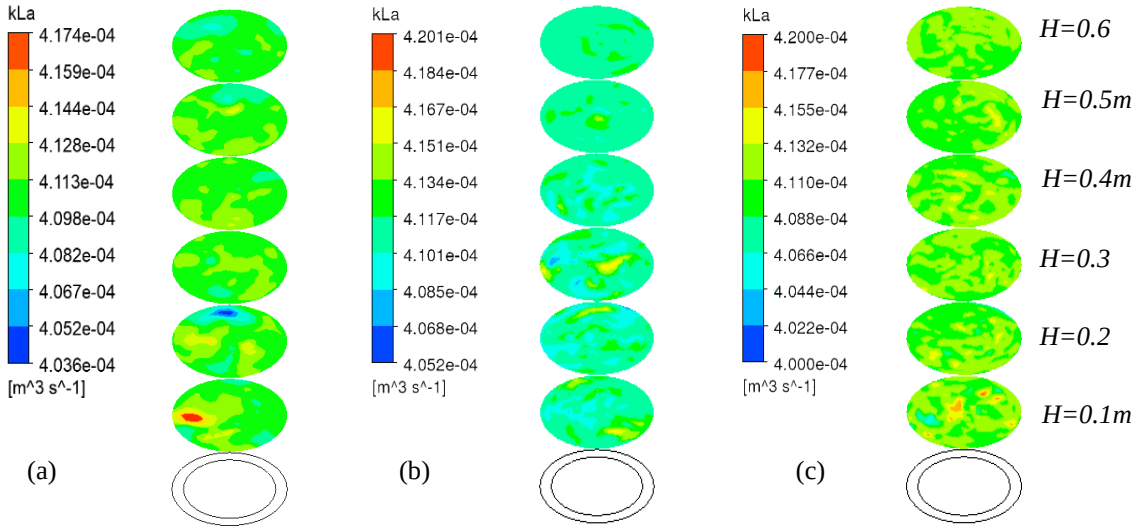

Figure 4- 14 Calculated volumetric mass transfer coefficient $\mathbf{k_l a}$ contour along column by using (a) case 1: D+L+AM+TD; (b) case 2: D+L+AM+SGS-TDF; (c) case 2: D+L+AM+SGS-TDF+SGS-AMS.

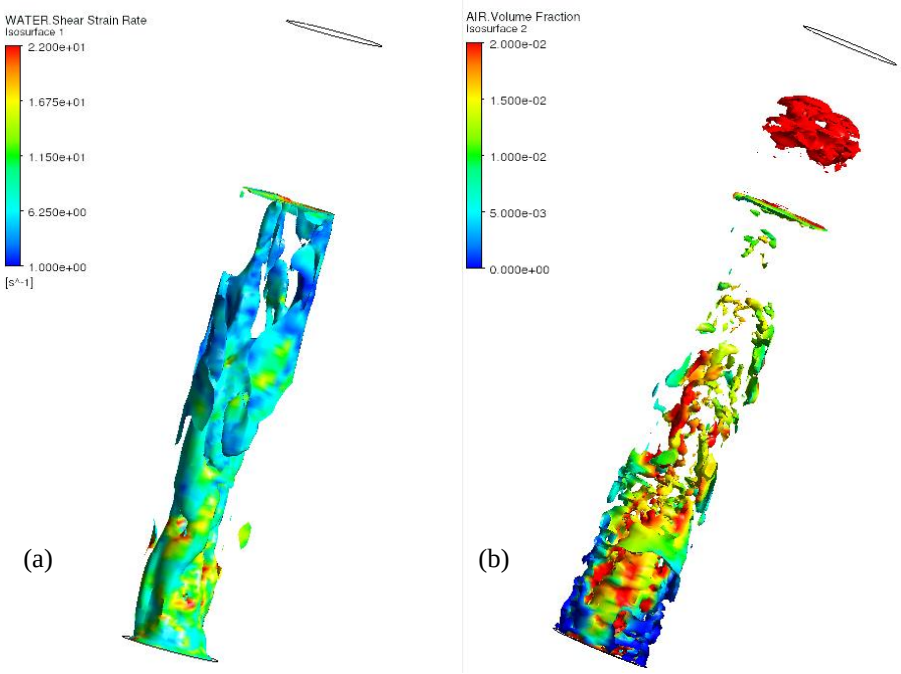

Figure 4- 15 Iso-surfaces of (a) bubble volume fraction $\boldsymbol{\alpha_B = 0.016}$ colored by local water shear strain rate and (b) water shear strain rate $\boldsymbol{S_{ij,L} = 10\ s^{-1}}$e , colored by local bubble volume fraction at t =100s.

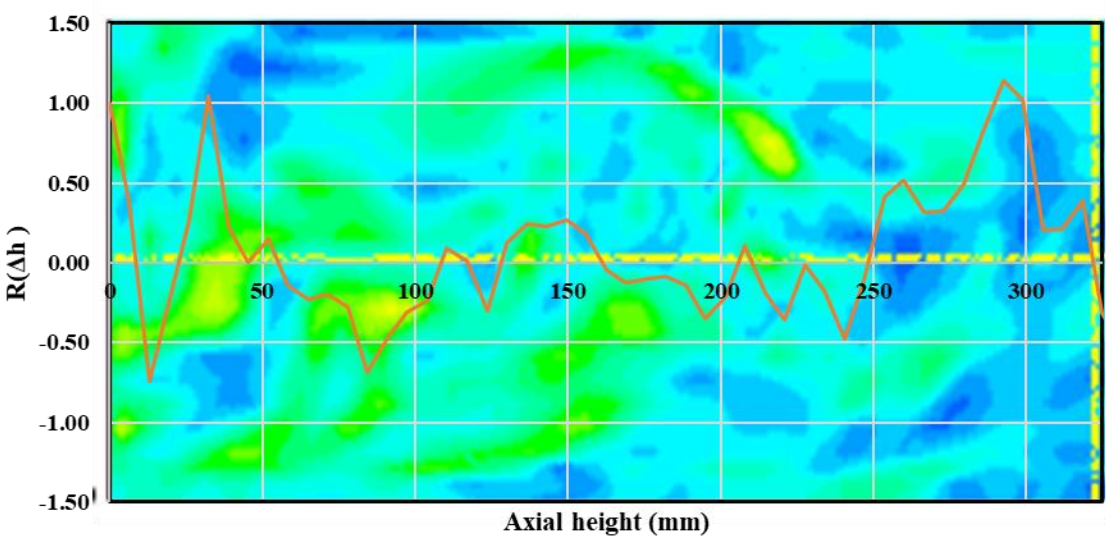

Figure 4- 16 Spatial correlation coefficient $\boldsymbol{R_{\alpha_G \bar{S}_{ij}}(\Delta h)}$ along the height of the bubble column from z=0 to z=325mm. The background was superimposed with the contours of instantaneous liquid phase shear strain rate at X=0, YZ-Plane.

CHAPTER 5: EULER/EULER LARGE EDDY SIMULATION OF BUBBLY FLOW IN BUBBLE COLUMNS UNDER CO_2 CHEMISORPTION CONDITIONS

SUMMARY

In Chapter 3 and 4, the influences of the modified sub-grid scale (SGS) turbulent dispersion force (TDF) and SGS added mass stress force (AMS) in LES simulation on momentum transfer occurring in bubble column bubbly flows have been investigated. The deformation of bubble shape and bubble oscillation in the transport, caused by strong interaction between the bubbles and the surrounding turbulent eddies have been implicitly considered in the modified SGS-TDF and SGS-AMS models while the bubble dispersion can be better predicted using such models when comparing with the only use of conventional interphase force models. Although the modified SGS-TDF and SGS-AMS models have shown good capabilities in evaluating the velocity and bubble volume fraction profiles for bubble column bubbly flows, the effect of implementation of such models in LES simulation on the mass transfer in bubble column bubbly flow, characterised by CO_2 adsorption process, has not been assessed yet, to the best knowledge of the author of this thesis. As the turbulent eddies in the surroundings of bubbles interact strongly with the rising bubbles in bubble column bubbly flow, such interaction will bring out the change in interfacial areas between the bubbles and carrier fluid, consequently leading to

the changes in the interfacial mass transfer. When employing large eddy simulation for modelling bubbly flow coupled with the chemisorption process, the SGS filtered velocity fluctuations of liquid phase can be interpreted as the turbulent eddies that continuously hit the surfaces of bubbles, causing bubble deformation and variation of the bubble interfacial areas, which gives rise to the turbulent dispersion and added mass stress forces. This chapter will demonstrate through Euler/Euler large-eddy simulations (LES) that by considering the turbulent dispersion force (SGS-TDF) and added mass stress (SGS-AMS) in LES simulation of a reactive bubble column reactor bubbly flow under CO2 chemisorption condition, the bubble dynamics and mass transfer can be better indicated, which leads to significant improvements in the prediction of bubble lateral dispersion and the interfacial mass transfer. The SGS-TDF and SGS-AMS arisen from the filtering were modelled by coupling with the modified SGS eddy viscosity to reflect the effect of bubble response to the turbulent eddies on the eddy viscosity and eddy mass diffusivity. A comprehensive assessment of the effects of these additional filtered stress terms on the time-averaged velocity and bubble volume fraction profiles, flow patterns, mass transfer and the pH variation in bubble column CO_2 chemisorption bubbly flow was made. In the meantime, the corresponding turbulent kinetic energy and species concentration spectra were obtained.

1. INTRODUCTION

Various carbon-neutralisation technologies have been intensively discussed in recent years. A typical example is CO_2 absorption or recycling in aqueous NaOH

using bubble column. It has been widely recognised that the adoption of bubble column reactors is effective for CO_2 chemisorption due to their simple structures and high interfacial contact areas that can give high mass and heat transfer rates. However, the chemisorption process in the bubble column involves complex phenomena with the interfacial mass transfer, chemical reactions and hydrodynamics being strongly coupled and numerical simulation of such reactive gas-liquid two-phase flow in the bubble column remaining a challenge (Figure 5-2). The key issue lies in a suitable modelling method for air volume fraction, volumetric mass transfer coefficient, interfacial area concentration, equivalent bubble diameter, enhancement factor and reaction rate constant. At present, two approaches to numerical computations of gas-liquid two-phase flows are employed: the two-fluid approach (Euler/Euler method) where both phases are treated as a continuum (Sokolichin and Eigenberger, 1994; Mudde and Simonin, 1999), and the Euler/Lagrange approach in which the fluid phase is treated as a continuum while the disperse phase involving a large number of bubbles is traced through the previously calculated flow field by taking into account relevant fluid forces. The two-fluid approach (Euler/Euler method) allows for efficient numerical computations of large and industrial scale processes such as bubble columns, but strong approximations and sophisticated closures are usually required for accurately describing the phase interaction.

Both the Euler/Euler (E-E) and Euler/Lagrange (E-L) approaches have been used to describe the chemisorption process of carbon dioxide in bubble columns (Jain *et al.*, 2015, Gruber *et al.*, 2015, Márquez *et al.*, 1999, Bauer and Eigenberger, 2001,

Darmana *et al.,* 2005, Darmana *et al.,* 2007, Zhang *et al*., 2009, Taborda and Sommerfeld, 2021, Krauβ and Rzehak, 2017, Krauß and Rzehak, 2018, Taborda *et al*., 2021, Jia and Zhang, 2017, Hlawitschka *et al*., 2016, Kováts *et al.*, 2018). For the Euler/Lagrange approach, Darmana *et al.* (2007) used a discrete bubble model to simulate the CO_2 absorption in aqueous NaOH in the frame of E-L LES. Their simulation results indicated that the overall mass transfer rate was underestimated compared with the experimental data. The pioneering experimental and modelling work carried out by Darmana *et al.* was recovered by many other researchers (Taborda and Sommerfeld, 2021, Krauβ and Rzehak, 2017, Hlawitschka *et al*., 2017, Buffo *et al*., 2017, Zhang *et al*., 2009). Taborda and Sommerfeld (2021) studied the effect of bubble dynamic model initially proposed by Sommerfeld *et al.* (2018) on the mass transfer during the CO_2 chemisorption, indicating that the mass transfer in CO_2 chemisorption can be better predicted by accurate estimation of the surface area of bubbles through considering bubble oscillation behaviour in the bubble column. After comparing with three different cases, they revealed that the case with consideration of the bubble oscillations and full dynamic model can deliver better results being consistent with the experimental data. While using the Euler/Euler modelling approach, Chen (2012) conducted a simulation on the carbon dioxide recycling process by considering four absorption systems in the bubble column. They indicated that the factors that have the impact on the mass transfer coefficient can be sequentially identified by the pH value, the concentration of CO_2, the temperature and the introduced gas-flow rate. The mass transfer enhancement factor in their model had to be adjusted based on the experiments reported by

Fleischer's group in order to achieve the better prediction results. It should be noted here that the enhancement factor plays an important role in evaluating the efficiency of the mass transfer for the reactive flows. The effect on the mass transfer using different enhancement factor models has been assessed in detail by Krauβ and Rzehak (2017). The authors have proposed a simplified expression of the enhancement factor model which has shown to be more reasonable after comparing the simulation results. Furthermore, an engineering calculation applicable model which well expresses the chemisorption reaction between CO_2 and the water apart from OH^- was implemented into their Euler/Euler modelling (Krauß and Rzehak, 2018). However, the time-dependent change of the pH value was not well reflected in their work, which may be attributed to the fact that the coupling between the hydrodynamics and chemisorption reaction dynamics is still not well addressed. In addition, the mass transfer occurs in the region where the species concentration differences (Figure 5-2), and is highly related to the estimation of the mass transfer coefficient and local interfacial area density. The bubble size variation will be directly influenced by the local interfacial area density. The effect of bubble size distribution at the inlet of the reactive bubble column on bubble dynamics was discussed by Hlawitschka *et al.* (2017) who conducted E-E simulation of the reactive bubble column and compared the modelling results with their experimental data. They found that the change in the bubble size was not significantly affected by the reaction, and the predicted concentration distribution was overestimated for the region of top 1/3 of the bubble column. The adoption of the population balance model for accounting

the bubble size changes taking the likely bubble coalescence and break-up was conducted by Buffo *et al.* (2017) in their E-E two-fluid model simulations. They have reported that a generally similar trend and consistency with the experimental results on bubble volume fraction profiles but they had to employ an inlet bubble size distribution that has a standard deviation of 15% to the measured mean experimental value. Zhang *et al.* (2009) conducted the E-E LES by incorporating the bubble number density model, revealing the coupling between the shear turbulence and mass transfer in the bubble column.

The correct prediction of the mass transfer in bubble columns is highly dependent upon both the turbulence modelling of shear turbulence and the description of the bubble-induced turbulence. The RANS (Reynolds averaged Navier-Stokes) modelling approaches have been widely used in conjunction with a turbulence model such as k-ε or k-ω. The turbulence models for describing the bubble-induced turbulence (BIT) have also been analysed by Zhang *et al.* (2006), showing that no major differences existed when including the BIT. However, the impact on the mass transfer by the BIT was not assessed in these previous studies. It should be mentioned that a more recent work of Magolan *et al.*, (2019) considered the BIT-correlations but has indicated the existence of remarkable differences in the computed turbulent kinetic energy for the formulations considered. As large eddy simulations (LES) are increasingly being used for the calculation of bubbly flows, it has been accepted that the fine turbulent structures can be described by comparatively simple models, e.g. the use of Smagorinsky model (Deen *et al.*, 2001; Darmana *et al.*, 2005; Göz

et al., 2006; Hu and Celik, 2008; Radl and Khinast, 2010; Sungkorn *et al.*, 2011), and the effects on the transfer process can be better evaluated. For Euler/Euler two-fluid LES modelling, the turbulence vortex structures are resolved up to the filter width, corresponding approximately to the grid size, and thus the bubble transport by these vortices is resolved. Most of the cases employing such LES modelling have neglected the influence of the fine structure turbulence (SGS: sub-grid scale) on the bubble motion and the effect of the entrained bubbles on the SGS (Radl and Khinast, 2010) since their contribution to the energy of the fluid fluctuation is comparatively low. However, as indicated in the review article by Dhotre *et al.* (2013), the use of LES for disperse bubbly flows can correctly reproduce the turbulent kinetic energy only when modelling bubble-induced turbulence (BIT) is conducted. This has clearly indicated consideration of the BIT has a decisive influence on the mass transfer and a subsequent chemical reaction in the bubble column.

From the available research, the effects of consideration of turbulent dispersion and added mass stress on the interfacial mass transfer in the Euler/Euler LES modelling of bubble column bubbly flow are rarely discussed, i.e., the term $\nabla \cdot (\alpha_k \boldsymbol{\tau_k})$. The appearance of the additional added mass stress is the consequence when filtering one of the interphase forces, the added mass force. The present work will particularly assess the impact of including the added mass stress in the LES modelling on the mass transfer of the CO_2 chemisorption in the bubble column. In addition, since the range of the bubble size in the chemisorption process in the present study falls into the integral turbulent length scale (Taylor length scale ~ 4 mm) and inertia sub-

range, the effects of such interaction between the bubbles and the surrounding eddies on the eddy effective diffusivity will be taken into account. This chapter will be organised as follows. Section 2 presents the mathematical modelling used in present work and related formula derived for those modified terms that will be particularly addressed. The numerical set-ups for the validation of the Euler/Euler LES modelling of CO_2 chemisorption reactive bubbly flow are described in Section 3 while Section 4 presents the predicted results obtained from E-E LES modelling by employing the three different mass transfer models together with the comparisons with the available experimental work plus the detailed discussion. The conclusions reached from the present study are given in Section 5. Two appendices are also provided with the correlations for reaction kinetics and physico-chemical properties that were used in the study and the empirical expression based on the fitting for the enhancement factor of an instantaneous irreversible second order reaction.

2. MATHEMATICAL MODELLING

2.1 Governing equations

The two-fluid model based on the Euler/Euler LES turbulence modelling was adopted in this work. It was assumed that each fluid (or phase) is treated as a continuum in any size of domain under consideration while both phases share the domain and can interpenetrate as they are transported within it. The Eulerian modelling frame work employs the phasic function of presence to account for the space occupation by either the liquid or bubbles. This allows the mass and momentum

transport equations for each phase to be directly derived by applying LES filtering. In this LES model, each parameter φ is characterised as the combination of the part $\tilde{\varphi}$ that needs to be resolved during the filtering process and the unresolved part φ' that needs to be modelled by using the SGS model for closure. For convenience, the tilde symbol "~" will be dropped hereafter. The phase filtered conservation equations for continuity and momentum can then be written as

$$\frac{\partial}{\partial t}(\alpha_k \rho_k) + \nabla \cdot (\alpha_k \rho_k \boldsymbol{u}_k) = \dot{m}_k \tag{5-1}$$

$$\frac{\partial}{\partial t}(\alpha_k \rho_k \boldsymbol{u}_k) + \nabla \cdot (\alpha_k \rho_k \boldsymbol{u}_k \boldsymbol{u}_k) = -\alpha_k \nabla p_k - \nabla \cdot (\alpha_k \rho_k \tau_k) + \alpha_k \rho_k \boldsymbol{g} + \boldsymbol{M}_k \tag{5-2}$$

where index $k = G,\ L$ stands for the gas (bubble) and liquid, respectively, $\boldsymbol{u}_k$ refers to the local instantaneous velocity vector and α_k stands for the volume fraction satisfying $\alpha_G + \alpha_L = 1$. On the left-hand side of Equation (5-1), the terms represent the change rate of the phasic mass and transport due to advection. The term on the right-hand side indicates the mass transfer occurred between phases, which is given by

$$\dot{m}_L = -\dot{m}_G = \dot{m}^{CO_2} \tag{5-3}$$

where the carbon dioxide chemisorption process is concerned. The terms on the right-hand side of Equation (5-2) represent the stresses due to viscous and turbulent shear, the pressure gradient, gravity and the filtered momentum exchange between

the phases, caused by the actions of the interface forces, respectively. The stress term of phase *k* can be expressed as:

$$\tau_k = -\mu_k^{eff}\left\{(\nabla \boldsymbol{u}_k + (\nabla \boldsymbol{u}_k)^T) - \frac{2}{3} I(\nabla \cdot \boldsymbol{u}_k)\right\} \quad (5\text{-}4)$$

where μ_L^{eff} is the effective viscosity for the carrier phase, which is assumed to be composed of the contributions from the molecular viscosity μ_L, the shear induced turbulence viscosity μ_T and the extra viscosity due to bubble-induced turbulence μ_{BI}, given by

$$\mu_L^{eff} = \mu_{L,L} + \mu_{T,L} + \mu_{BI,L} \, . \quad (5\text{-}5)$$

The viscosity due to the bubble induced turbulence can be modelled following the work of Sato and Sekoguchi (1975), which is given by Equation (5-6),

$$\mu_{BI,L} = \rho_L C_{\mu,BI} \alpha_G d_B |\boldsymbol{u}_G - \boldsymbol{u}_L| \quad (5\text{-}6)$$

The shear-induced turbulence viscosity can be modelled using the Smagorinsky SGS model (Smagorinsky, 1963)

$$\mu_{T,L} = \rho_L (C_s \Delta)^2 |S| \quad (5\text{-}7)$$

where C_s is the model constant and takes a value of 0.1 in the present study. The SGS filtering length scale Δ takes the value based on the grid control volume as $\Delta =$

$(V_{cell})^{\frac{1}{3}}$. For estimating the effective viscosity of gas phase, Equation (5-8) is adopted.

$$\mu_G^{eff} = \frac{\rho_G}{\rho_L}\mu_L^{eff} \tag{5-8}$$

In the present LES model, large eddies with the length scale being greater than the filter size are directly resolved while those small eddies with the size smaller than the filter size are modelled using the SGS model. It thus can be imagined that the eddies smaller than $\Delta = (V_{cell})^{\frac{1}{3}}$ will give rise to the local fluctuations, implying the potential impact on the interfacial mass transfer when the bubbles are entrained in the bubble column. If no coalescence and breakup is assumed with the condition of low bubble volume fraction, $\alpha_G < 5\%$, the shape of bubbles are more likely to be spherical or ellipsoidal with little occurrence of breakup and coalescence (Talvy *et al*., 2007, Colombet *et al.*, 2011). In such case, the bubble number density can be defined by Equation (5-9):

$$\frac{\partial n}{\partial t} + \nabla \cdot (\boldsymbol{u}_G n) = 0\,. \tag{5-9}$$

Therefore, the interfacial mass transfer occurred between phases would subsequently give rise to the bubble size change as the bubble equivalent size variation can be associate with the zero-th moment of bubble size distribution (BSD) through $d_{32} = \left(\frac{6\alpha_G}{\pi n}\right)^{\frac{1}{3}}$. As the size of the bubbles and their surrounding turbulence eddies

are different, the bubbles will not respond immediately to the fluctuations of the eddies. Considering the bubble response to the eddies and the interaction between bubbles and eddies with a Stokes number, defined by $St_{SGS} = \frac{\tau_{\text{bubble}}}{\tau_{L,SGS}}$, the Smagorinksy model of sub-grid eddy viscosity can be modified based on the correlation between the fluctuating velocities of the bubbles and liquid in terms of the turbulent eddies with the length scales falling into the inertia subrange (Kruis and Kusters, 1997), expressed by Equation (5-10):

$$\frac{\boldsymbol{u}_G^{'2}}{\boldsymbol{u}_L^{'2}} = \frac{1}{1+St}. \tag{5-10}$$

When Equation (5-10) is implemented into the sub-grid scale, the relationship can be replaced by $\frac{\boldsymbol{u}_G'^2}{\boldsymbol{u}_{L,SGS}'^2} = \frac{1}{1+St_{SGS}}$. The bubble response time scale was proposed by Sommerfeld *et al.* (2018), $\tau_{\text{bubble}} = \frac{4(\rho_G+0.5\rho_L)d_B^2}{3\mu_L C_D Re_B}$. The SGS turbulent eddy turn over time can be estimated by $\tau_{L,SGS} = \Delta/\boldsymbol{u}'_{\text{L,SGS}}$. As $u_L'^2 \sim (\lambda\varepsilon)^{2/3}$, the modified SGS fluctuation velocity can be expressed as Equation (5-11):

$$\boldsymbol{u}'_{\boldsymbol{L,SGS}} \sim \left(\frac{1}{1+St_{SGS}}\right)^{\frac{1}{2}} (\lambda\varepsilon)^{\frac{1}{3}} \left(\frac{1}{C_D}\right)^{\frac{1}{3}} \left(\frac{\rho_B + C_{AM}\rho_L}{\rho_L}\right)^{\frac{1}{3}}. \tag{5-11}$$

The turbulence dissipation due to the bubbles corresponds to the inertial subrange can be assumed that mainly occurs when the eddy integral scale λ approximately equals Δ and the dissipation can be estimated by Equation (5-12):

$$-\tau_{ij}\overline{S_{ij}}|_G \sim \rho_L C_D \left(\frac{\rho_L}{\rho_B}\right)\frac{\boldsymbol{u_\lambda^3}}{d_B}\overline{\alpha_G} = C_b \rho_L \varepsilon \alpha_G \frac{\lambda}{d_B}\left(\frac{1}{1+St_{SGS}}\right)^{\frac{3}{2}}. \quad (5\text{-}12)$$

It was found from the trial simulation that a value of C_b = 0.7 would be suitable. The total turbulence dissipation due to liquid phase shear induced turbulence and the turbulence due to bubble response to SGS eddies can be estimated by

$$-\tau_{ij}S_{ij} = \rho_L \varepsilon \left(1 + \mathrm{C_b}\alpha_G \frac{\lambda}{d_B}\left(\frac{1}{1+St_{SGS}}\right)^{\frac{3}{2}}\right). \quad (5\text{-}13)$$

By employing the eddy viscosity model, the liquid-phase turbulence coupled with the modified SGS viscosity can be written as

$$\mu_{T,L} = \rho_L (C_s \Delta)^2 |S| \left[1 + C_b \alpha_G \frac{\Delta}{d_B}\left(\frac{1}{1+St_{SGS}}\right)^{3/2}\right] \quad (5\text{-}14)$$

and will be implemented into our LES modelling.

2.2 Interfacial momentum exchange modelling

In Euler/Euler LES modelling of bubbly flows, the total interfacial force arising as the action of the interfacial momentum exchange between the two phases is usually characterised by the contributions from several independent physical effects so that the interfacial force $\boldsymbol{M}_F$ can be written as

$$\boldsymbol{M}_{F,L} = -\boldsymbol{M}_{F,G} = \boldsymbol{M}_{D,L} + \boldsymbol{M}_{L,L} + \boldsymbol{M}_{TD,L} + \boldsymbol{M}_{AM,L} \quad . \tag{5-15}$$

The forces indicated in Equation (5-15) represent the contributions from the inter-phase drag force, lift force, added mass force and turbulent dispersion force. These forces have been obtained by using the phase weighted filtering. The drag force is due to the resistance experienced by the bubble transport in the liquid. Both viscous and turbulent stresses generate the skin drag and pressure distribution around the moving bubbles gives rise to the form drag, especially when the boundary layer on the bubble surface separates to generate the bubble wakes. The lift force arises from the net effect of pressure and stress acting on the surfaces of the bubbles, which are strongly associated with the averaged shear gradient acting on the bubbles and the orientation of slip velocity. The turbulent dispersion force can be regarded as the turbulent diffusion of the dispersed phase by those turbulent eddies that are strongly interact with the bubbles. For LES modelling of the gas–liquid system, the contri-bution from the added mass force has to be considered. Most of recent work on LES modelling of bubbly flows have included this force (Lain, 2009; Zhang *et al.*, 2006; Dhotre *et al.,* 2008; Fard *et al.,* 2020). However, in the case of large eddy simulation, there would be an additional force at the SGS level, i.e., added mass

stress (SGS-AMS), when filtering the added mass force term in addition to the turbulent dispersion force. An attempt is made in the present study to take account of sub-grid-scale added mass stress which will be discussed in this section (Figure 5-2). The interphase momentum transfer due to drag force is given by

$$\boldsymbol{M}_{D,L} = \frac{3}{4}\alpha_G \rho_L \frac{C_D}{d_B}|\boldsymbol{u}_G - \boldsymbol{u}_L|(\boldsymbol{u}_G - \boldsymbol{u}_L)\,. \tag{5-16}$$

The drag coefficient for closure is the correlation proposed by Tomiyama (2004),

$$\mathrm{C_D} = \max\left[min\left[\frac{16}{Re}(1 + 0.15Re^{0.687}), \frac{16}{Re}\right], \frac{8}{3}\frac{\ddot{E}o}{\ddot{E}o+4}\right] \tag{5-17}$$

where the Eötvos number $E_0 = \frac{g\Delta\rho d_B^2}{\sigma}$ is the ratio of the bubble buoyancy force to the surface tension. The lift force acting on bubbles can be estimated by

$$\boldsymbol{M}_{L,L} = \rho_L C_L(\boldsymbol{u}_B - \boldsymbol{u}_L) \times (\nabla \times \boldsymbol{u}_L)$$

$$C_L = \begin{cases} min[0.288tanh(0.121Re_B), f(E_O')\,] & E_O' \le 4 \\ f(E_O') & 4 < E_O' < 10 \\ -0.29 & E_O' > 10 \end{cases} \tag{5-18}$$

where Re_B is the bubble Reynolds number measured based on the equivalent bubble diameter in case of deformed bubbles being concerned and $E_O' =$

$\frac{g(\rho_l-\rho_g)d_h^2}{\sigma}, d_h = d(1+0.163E_O'^{0.757})^{1/3}$. The filtered added mass force can be estimated using Equation (5-19), where the added mass coefficient C_{AM} takes the value of 0.5.

$$\boldsymbol{M}_{AM,L} = \alpha_G \rho_L C_{AM}\left(\frac{D\boldsymbol{u}_G}{Dt} - \frac{D\boldsymbol{u}_L}{Dt}\right) \tag{5-19}$$

After employing spatial filtering to the drag force, the turbulent dispersion force can be obtained using the eddy viscosity hypothesis, which is given by

$$\boldsymbol{M}_{TD,L} = C_{TD}\frac{3\alpha_G}{4}\frac{\rho_L}{d_B}(\boldsymbol{u_L}-\boldsymbol{u_G})\frac{\nu_t}{\sigma_{TD}}\left(\frac{\nabla\alpha_L}{\alpha_L}-\frac{\nabla\alpha_G}{\alpha_G}\right). \tag{5-20}$$

As shown in Figure 5-1, the turbulent fluctuations due to the phase weighted filtering can be imagined as the eddies acting on the bubble surfaces. When taking the filtering to the instantaneous added mass force, the filtering of the force will result in the mean and turbulent contributions:

$$\overline{\chi_G \boldsymbol{M}_{AM}} = \alpha_G\left(\boldsymbol{M}_{\boldsymbol{AM}}^{\boldsymbol{filtered}} + \boldsymbol{M}_{\boldsymbol{AMS}}^{\boldsymbol{T}}\right) \tag{5-21}$$

which can be approximately written as

$$\begin{aligned}\overline{\chi_G \boldsymbol{M}_{AM}} = {} & \alpha_G\rho_L C_{AM}\left(\frac{\partial \boldsymbol{u}_L}{\partial t} + \boldsymbol{u}_L\cdot\nabla\boldsymbol{u}_L - \frac{\partial \boldsymbol{u}_G}{\partial t} + \boldsymbol{u}_G\cdot\nabla\boldsymbol{u}_G\right) \\ & +\rho_L C_{AM}\left(\nabla\cdot\left(\alpha_G\overline{\boldsymbol{u}'_{L,i}\boldsymbol{u}'_{L,j}}\right) - \nabla\cdot\left(\alpha_G\overline{\boldsymbol{u}'_{G,i}\boldsymbol{u}'_{G,j}}\right)\right).\end{aligned} \tag{5-22}$$

It should be noted that the consequence of applying spatial filtering to the added mass force would deal with the correlation $u'_{ki} \cdot \nabla u'_{kj}$ as indicated in the second part of the right-side of Equation (5-22), which functions like the Reynolds stress but also correlates with the local bubble volume fraction fluctuation. It is referred to as the SGS added mass stress (SGS-AMS). By employing the eddy diffusivity hypothesis, the SGS added mass stress (SGS-AMS) can be formulated, which can be given by

$$\mathbf{M}_{\mathrm{AMS}} = \alpha_{\mathrm{G}}\rho_{\mathrm{L}}C_{\mathrm{AM}}\left(\frac{\nabla\cdot(\alpha_{\mathrm{L}}\boldsymbol{\tau}_{\mathbf{L}})}{\alpha_{\mathrm{L}}\rho_{\mathrm{L}}} - \frac{\nabla\cdot(\alpha_{\mathrm{G}}\boldsymbol{\tau}_{\mathrm{G}})}{\alpha_{\mathrm{G}}\rho_{\mathrm{G}}}\right) \tag{5-23}$$

where $\boldsymbol{\tau}_L$ and $\boldsymbol{\tau}_G$ are defined by $\boldsymbol{u}'_{L,i}\boldsymbol{u}'_{L,j}$ and $\boldsymbol{u}'_{G,i}\boldsymbol{u}'_{G,j}$, respectively. As the bubbles are subjected to the eddy fluctuations, it can be expected that the SGS-AMS force will have a significant impact on the interfacial mass transfer between the bubbles and liquid phase and this effect will be discussed in Section 4.

2.3 Chemisorption process description and the involved interfacial mass transfer

Generally two reactions can be assumed to take place in chemisorption of carbon dioxide bubbles in the NaOH solution using the bubble column reactor. Firstly, there is a physical absorption of CO_2 from gas phase to liquid,

$$\mathrm{CO}_2(g) \rightarrow CO_2(aq) \tag{5-24}$$

in which two reversible reactions simultaneously take place, described by

$$CO_2(aq) + OH^- \underset{k_{1-}}{\overset{k_{1+}}{\rightleftharpoons}} HCO_3^- \tag{5-25}$$

$$HCO_3^- + OH^- \underset{k_{2-}}{\overset{k_{2+}}{\rightleftharpoons}} CO_3^{2-} + H_2O\ . \tag{5-26}$$

The reaction rates can be evaluated by

$$\mathrm{R}_{1+} = k_{1+}\,[CO_2(aq)][OH^-] \tag{5-27}$$

$$\mathrm{R}_{1-} = k_{1-}\,[HCO_3^-] \tag{5-28}$$

$$\mathrm{R}_{2+} = k_{2+}\,[HCO_3^-][OH^-] \tag{5-29}$$

$$\mathrm{R}_{2-} = k_{2-}\left[CO_3^{2-}\right] \tag{5-30}$$

where $k_{\mathrm{i}\pm}$ represents the reaction rate constant for the above reversible reactions, $i = 1, 2$ denote the first and second reaction, respectively, while "+" and "–" stand for the forward and backward reaction separately. The detailed estimation process of the reaction rate constant can be found in the Appendix. The interfacial mass transfer occurring in the above-mentioned chemisorption process can be described by using the mass fraction Y^j of each species j in the liquid mixture and the species transport equation for the liquid phase is given by

$$\frac{\partial}{\partial t}\left(\alpha_L \rho_L Y^j\right) + \nabla \cdot \left(\alpha_L \rho_L Y^j \boldsymbol{u}_k\right) = \nabla \cdot \left(\alpha_L \rho_L D^j_{L,eff} \nabla Y^j\right) + \dot{m}^j + \alpha S^j \qquad (5\text{-}31)$$

where $D^j_{L,eff}$ is the liquid phase effective diffusivity. As the eddy turbulent fluctuations will have a significant impact on the interfacial mass transfer for bubble size which have an equivalent size of the SGS grid and falls into the inertia subrange, the mass effective diffusivity that takes the eddy turbulent diffusivity into account can be expressed as

$$D^j_{eff} = D^j_0 + \frac{(C_s\Delta)^2|S|\left(1+\mathrm{C_b}\alpha_G\frac{\Delta}{\mathrm{d}}\left(\frac{1}{1+St_{SGS}}\right)^{\frac{3}{2}}\right)}{\rho Sc_t} \qquad (5\text{-}32)$$

where Sc_t is the turbulent Schmidt number. The relationship between the molecular diffusivity of carbon dioxide in water adopts the one proposed by Ratcliff and Holdcroft (1963), given by

$$D^{CO_2} = 2.35 \times 10^{-6} exp^{(-2119/T)} \qquad (5\text{-}33)$$

$$\mathrm{D}^{\mathrm{j}}_0 = \mathrm{D}^{\mathrm{I}}_0 \left(\frac{T}{T^I} - 1\right)^{\gamma^I}. \qquad (5\text{-}34)$$

The mass transfer rate of species CO2 from bubbles to the liquid can be defined as

$$\dot{m}^j = k_L a E \rho_L \left(Y_L^{j*} - Y_L^j\right) \qquad , \quad j = \mathrm{CO_2\ (aq)} \qquad (5\text{-}35)$$

where k_L is the mass transfer coefficient for liquid side CO_2, $k_L = \frac{ShD_{CO_2}}{d_B}$. The interfacial area concentration can be estimated by $a = 6\alpha_G/d_B$ if the bubbles are assumed to be spherical. The correlation which relates the mass fraction of CO_2(aq) for both sides of the bubble surface can be written as Equation (5-36) by using the henry constant and the equivalent mass fraction of aqueous carbon dioxide in the liquid side can be thus defined as

$$Y^* = H^{CO_2} \frac{\rho_L}{\rho_G} Y_G^{CO_2} \tag{5-36}$$

where the solubility of CO_2 in water, characterised by Henry constant H^{CO_2}applies to the condition that the solute concentration is low. It should be pointed out that the use of the ratio of the CO_2 concentration in the liquid to the CO_2 concentration in the gas at equilibrium is appropriate from perspective point of view of the numerical simulation. For the estimation of Henry constant H^{CO_2}, Versteeg and van Swaaij (1988) have proposed a correlation for the temperature dependency of pure water based on their own experimental data, given by

$$H^{CO_2} = 3.59 \times 10^{-7} RT exp^{2044/T} . \tag{5-37}$$

The interfacial mass transfer occurred can be characterised by the overall mass transfer coefficient, k_L, which can be obtained from the following Sherwood number correlations for bubbles that are dependent on Reynolds and Schmidt numbers (Lochiel and Calderbank 1964; Brauer 1981; Bird *et al.* 2006). For non-spherical

bubbles, the correlation is derived by accounting for the stochastic deformations of the interface caused by turbulent eddy fluctuations acting on the bubble surface. The overall mass transfer coefficient estimation in the present work is based on Equation (5-38):

$$Sh = \frac{k_L d_B}{D_{CO_2}} = 2 + 0.015\mathrm{Sc}^{0.7}\mathrm{Re}^{0.89}\,. \tag{5-38}$$

The interfacial mass transfer is also influenced by the pH value of the solute. Such an effect is usually accounted for by introducing the enhancement factor. The enhancement factor dependency on pH value was investigated by Fleisher *et al.* (1996) who have replicated the same experiment on CO_2 chemisorption in NaOH solution as done by Darmana *et al.* (2007). They revealed that the chemical reactions in CO_2 chemisorption has an influence on the absorption process. They proposed the enhancement factor which can be estimated by the following expression given by Equation (5-39):

$$\mathrm{E} = \begin{cases} 1241.3Y^{OH^-} + 1.0069, & if\ Y^{OH^-} \geq 1.8 \times 10^{-6} \\ 1, & if\ Y^{OH^-} < 1.8 \times 10^{-6}\,. \end{cases} \tag{5-39}$$

Thus, using Equation (5-31) coupled with Equations (5-32)-(5-39), the mass fraction distributions of each species, $Y^{\mathrm{CO}_2}, Y^{{CO_3}^{2-}}, Y^{{HCO_3}^-}, Y^{OH^-}$ and $Y^{\mathrm{CO}_2 l}$ can be obtained using the modified LES SGS model.

3. NUMERICAL SIMULATION

The modified LES models proposed in the present study were validated by comparing with the experimental data carried out by Darmana *et al.* (2005; 2007) and our own experimental data, herein referred to as Case 1, Case 2 and Case 3. The schematics of the configurations of three bubble columns studied in this work are illustrated in Figure 5-3. In the LES modelling, the reference position of the coordinates was chosen to be the centre of the cross-section at the bottom of the bubble columns. The columns in three cases were assumed to be filled with a NaOH solution with the given liquid level. The gas aerator in case 1 was located at the centre of the bottom plane of the reactor via 21 needles within a 5mm square pitch. Air or carbon dioxide was injected to the system via a perforated plate with 40 holes evenly distributed at a 6.25mm square plate for Case 2. While for Case 3, the gas was introduced into the column via a capillary gas sparger equipped with 13 needles with an inner diameter of 0.57 mm. The detailed information is listed in Table 5-1.

Table 5- 1 Geometry parameters and the experimental conditions of the three bubble columns.

	Liquid height (m)	Initial pH	Superficial velocity (mm/s)	Inlet area $W_{in} \times D_{in}$ (mm×mm) / R_{in} (mm)	Width W, depth D or radius R_{bcr} and height of column H (mm)	Initial bubble diameter (mm)
Case 1	1	12.5	7	30×10	200, 30, 1200	5.5
Case 2	0.45	12	4.9	30×30	150, 150, 550	4

Case 3	1.4	12.5	5	40	50, 1400	5.5

The initial bubble sizes adopted in the LES modelling were 5.5mm (Case 1, 3) and 4 mm (Case 2), combined with the use of bubble number density equation to compute the bubble size, which is essential factor in calculating the related coefficients in evaluating the interfacial mass transfer. Bubble Reynolds number $Re_{B,max} = \frac{\rho_L d_B u_{slip}}{\mu_L} \approx 1542.04\ (Case\ 1,3)\ and\ 1121.48\ (Case\ 2)$ in this chapter. The simulation domains for the three cases were partitioned with the computational grids of $d_B/\Delta \approx 0.733$ for Case 1, 0.727 for Case 2 and 0.675 for Case 3 in the central region of the bubble columns with a growth rate of 1.2 from the walls, which satisfy the constraints suggested by Milelli's criterion for bubbly flows using Euler/Euler two-fluid LES modelling. The mesh set-ups with 48,000, 49,500 and 52,920 mesh cells were adopted for three cases, respectively. In order to clearly illustrate the impact from the chemisorption process on the hydrodynamics in the bubble column bubbly flows, nitrogen was assumed to be injected into the column at the beginning and CO_2 was then supplied. Similarly, the LES simulation also adopted the procedure with N_2 being supplied without chemical reaction for the first 20 seconds of the simulation and the solutions of the species transport equations being turned on afterwards, which were continued for 50 seconds for Case 1 and 250 seconds for both Case 2 and Case 3. The simulation results obtained by the LES during the given time interval were collected for time averaging. To better capture the transient dynamics of the turbulent eddy development in the bubble columns, the time step adopted in the simulation was chosen in terms of the CFL criteria, i.e.,

$\min(\frac{|\boldsymbol{u}_L|\delta t_E}{\Delta}, \frac{|\boldsymbol{u}_G - \boldsymbol{u}_L|\delta t_E}{\Delta}) < 1.0$, but was gradually increased from 0.0005 to 0.001 seconds. In the LES simulations, the contact between the liquid phase and the bubble column wall was set as a no-slip condition, whereas a free-slip condition was used for the dispersed phase with the assumption of minimal direct contact between the bubbles and the walls. The turbulent wall function with assuming a smooth wall of the bubble column was utilized to eliminate the requirement to resolve the viscous sublayer for a very small y^+. Constant relative static pressure ($P_{rel} = 0$) was used for the outlet at the top of the bubble columns. At the inlet, the normal gas superficial velocity and mass fraction were specified according to the experimental gas superficial velocities and the gas fluxes. The mass fractions were computed by analysing five species transport equations for $CO_2(aq), CO_3^{2-}, HCO_3^-, OH^-$ and H_2O. To initialise the LES simulation, the mass fraction of OH- in liquid phase in the bubble columns was calculated from the given pH while the rest related species mass fractions $Y_{CO2,L}, Y_{HCO_3^-,L}$ and , $Y_{CO_3^{2-}}$ were set to 1×10^{-50}. H_2O was set as the constrained species obeying $\sum_{i=1}^{N} Y_{i,L} = 0$.

4. RESULTS AND DISCUSSION

In order to validate the reliability of the proposed modified SGS-ADM model coupled with the consideration the effect of the modification by bubbles dynamic response to the surrounding eddies on the bubble induced turbulence eddy diffusivity, the LES simulations were conducted for both rectangular (Cases 1 and 2) and cylindrical (Case 3) bubble columns based on the experimental data as reported by Darmana *et al.* (2005, 2007)) and the experiments conducted in our research team.

Corresponding to each experimental case, the simulations were conducted by including (a) conventional turbulent dispersion and mean added mass forces (hereafter referred to as Model A); (b) the modified SGS turbulent dispersion (SGS-TDF) and mean added mass forces with coefficient C_{AM}=0.5 (hereafter referred to as Model B) and (c) the modified SGS turbulent dispersion (SGS-TDF) and the SGS added mass stress force (SGS-AMS) (hereafter referred to as Model C). In the following subsections, the overall mass transfer in the CO_2 chemisorption process will be comprehensively discussed, focusing on the influences of accounting for the added mass stress force term arisen as the consequence of spatial filtering on the interfacial mass transfer, time-averaged velocities, bubble volume fraction profiles, liquid phase turbulent kinetic energy spectrum and the species concentration spectrum.

4.1 Effect of SGS-AMS on CO2 chemisorption process

The time history of the species concentration and pH variation obtained by including the SGS-AMS in the LES modelling are compared with the two experimental cases reported from Darmana *et al.* (2007). The time-dependent predicted pH and species concentration profiles acquired at middle point of z = 980mm using three different models A, B and C are shown in Figure 5-4. In the figure, dot lines represent the predicted concentration by using the standard force model (Case 1-Model A), dash-dot lines stand for the profile using the standard added mass force model and modified SGS-TDF (Case 1- Model B), while the dashed lines are the one with modified SGS-TDF and SGS-AMS (Case1- Model C). Generally, the predicted

species concentration evolution and the pH value variation obtained in three LES simulations with and without the modifications are in good agreement with the experimental data. During the bubble rising-up, CO_2 may be physically dissolved into the liquid across the interface, leading to an increase in CO_2 (aq) concentration. As a result, this process triggers the chemical reactions in the liquid phase. It can be seen from Figure 5-4 that for the first 75 seconds of simulation time, carbonate is accumulated during the fast consumption of hydroxyl ions, where the dissolved CO_2 are fully interacting. This phenomenon is well reflected by the apparent change in slope of pH curve. The products are carried by the large circulation among the bubble column to the top region as well as the downwards recirculation near the wall region. When the initial OH^- is totally consumed, the carbonate concentration reaches the maximum and begins to drop, the bicarbonate concentration starts to increase until the initial concentration of hydroxide ions reached. At the same time, the aqueous carbon dioxide starts to store since all of the hydroxide has been used. By comparison, the simulation results predicted by the model without including the SGS-AMS modification have an obvious delay in the species concentration variation when the same reaction rate constant, mass transfer coefficient were used. A faster reaction was found when using the SGS-TDF and SGS-AMS models (Model C) while the use of the SGS-TDF and SGS-AMS without modifying the eddy viscosity (Model B) predicts a reaction with the rate which lies in the predicted reaction rates by using Model A and Model C. This phenomenon indicates that the influence of the modification is well reflected in the mass diffusivity estimation when solving the transport equation. By considering the SGS-TDF and SGS-AMS, the

dispersion of the bubbles in transverse or radial direction may be better estimated and bubble cluster wobbling which can lead to a longer residence time. Also, the inclusion of the SGS-AMS term in the LES modelling seemed to yield a better estimation for momentum exchange due to those turbulent eddies in the zones characterised by added mass surrounding the bubbles, giving rise to a higher interfacial mass transfer rate, consequently leading to the predictions for an earlier dissolution and stimulating the following reactions. Thus, the predicted concentration profiles by employing the Model C clearly have a closer trend to the experimental data. This reveals an important fact that the contribution of the filtered SGS-AMS to the interfacial mass transfer when using the LES modelling approach cannot be neglected.

For Case 2, the evolution of domain-averaged pH and CO_3^{2-}concentration predicted by employing three models A, B and C were also compared with the LES simulation results reported by Zhang *et al.* (2009) as shown in Figure 5-5. The productions of CO_3^{2-} predicted by our three approaches are similar to their results but a faster reaction progress can be observed when employing both filtered TDF and AMS models. It was also found that when neglecting the contributions from the SGS-TDF and SGS-AMS (Model A), the predicted reaction progress has a significant delay and reaches the equilibrium much later.

Apart from the results for Cases 1 and 2, similar finding was also observed in the case of cylindrical bubble column (Case 3). The pH-value time history was predicted by using the three models as well, which is shown in Figure 5-6. It can be seen from the Figure that by using the modified models (Case 3- Model B and Model C), the predictions are remarkably improved with a better performances comparing to the results obtained without considering the contribution of the SGS-TDF and SGS-AMS. It should be noted that the slope of the pH time history curve changes with the time evolution, which is caused by the shift in equilibrium of the first reaction mechanism in terms of the bicarbonate expressed in Equations (5-25) and (5-26). It seems that applying Model B and Model C, an improvement in predicting the reaction progress is strongly evidenced with better prediction being achieved using Model C.

4.2 Effect of inclusion of SGS-TDF and SGS-AMS on hydrodynamics

The better performance of adopting the SGS-TDF and SGS-AMS models (Model C) in the predicted species concentration evolution may be attributed to a better description of the bubble dispersion and liquid shear stress so that the bubble residence time in the bubble column can be better predicted. To assess this speculation, the time-averaged bubble axial velocity at z = 750mm predicted by using the three models are compared with the experimental results, as shown in Figure 5-7. The time-averaged bubble axial velocity is calculated based on the following relationship:

$$\bar{u}_B(r) = \frac{1}{N\Delta t}\sum_{i=1}^{N} \boldsymbol{u_{Bi}}(r,t)\Delta t\ .$$

For the non-reactive case, one can observe that there are not significant differences in the magnitude of the maximum averaged velocity using the three models but the large difference can be observed in the positions away from the central in the radial distribution. Nevertheless, for the reactive case with CO_2 injected, it can be seen from the Figure 5-7 that a good agreement with the experimental data is attained for the Model B and Model C. For the simulation conducted without considering the SGS-TDF and SGS-AMS, the bubble axial velocity seems to be much over-predicted for Model A, implying that the lateral bubble distribution being not well described due to the underestimated lateral bubble dispersion. Consequently, the higher bubble volume fraction in the core region will induce higher bubble rising velocity so that an overestimation of the bubble axial velocity takes place. However, when considering the effect of SGS-TDF and SGS-AMS, a decrease in the bubble axial velocity is found, giving rise to an adequate estimation of the bubble axial velocity distribution in the transverse direction. The comparisons using the three models clearly indicates that the SGS-AMS plays an important role in the bubble dispersion and bubble dynamics.

Figure 5-8 depicts the predicted time-averaged laterally bubble axial velocity distribution at L/D = 7 for the non-reactive case with injection of N_2, comparing with the experimental data (Damara *et al.*, 2007, 2009). To better consider the effect of the cross-section of the bubble columns (Model A, B and C) on the hydrodynamics, the bubble lateral velocity profiles are obtained by the following average method,

$$u_{B,z} = \frac{1}{DW}\int_0^{D/2}\int_0^{W/2}\left(\frac{1}{T_N - T_0}\int_{T_0}^{T_N} u_B(r,t)dt\right)dxdy$$

where T_0 and T_N are the start and end times of sampling from the LES modelling simulation, which take T_0-T_N = 250s in the time averaging. It can be found from the Figure 5-that the higher bubble axial velocity in the center region is predicted (Case 3- Model A), which has a maximum value of 0.42 m/s at the axis. The maximum averaged bubble axial velocity predicted for Case 3- Model B and Case 3- Model C has respective 4.707% and 7.693% reductions compared with the case of using Model A, which is more consistent with the experimental data. However, the prediction performance becomes poorer in the region 0.95 < r/R < 1.0, which may be attributed to the conflict between of mesh refinement in the LES modelling and Milelli's limitation for two-fluid bubbly flow simulation. Although the relative smaller bubbles are more likely to be pushed towards the wall due to actions from the lateral dispersion and lift force, a finer mesh near wall region required by LES ($5 < \Delta r^+ < 30$) still lead to a less than 1 mm grid imposed at the wall boundary, which will affect the accuracy of the LES modelling results. This remains to be resolved in further studies using the two-fluid LES modelling for bubbly flow problems.

The local bubble size distribution has a significant impact on the hydrodynamics and overall interfacial mass transfer in the bubble column bubbly flows. To assess the effect of LES modelling implementing the SGS-TDF and SGS-AMS terms on the interfacial mass transfer in the bubble column, the cross-sectional averaged and time-averaged bubble mean Sauter diameter variation along the height for Case 2

is shown in Figure 5-9. It can be seen from the Figure 5-that similar trends for bubble mean Sauter diameter variation are observed for all the models A, B and C, i.e., the bubble diameter decreases with the increase in the axial height. However, comparisons of all three models with the experimental data reported by Darmana *et al.* (2009) are not well matched in the beginning part of bubble injection into the bubble column who found that the bubbles close to the injection region $z < 0.4$ m frequently cluster in the centre zone, giving rise to a drawback in detection of accurate bubble diameter in the experiments. As the bubbles rise up, the influence from the large induced eddies by the four corners of the rectangular reactor becomes weaker and the bubble size measurement may become more reliable, especially when $z > 0.4$ m. Without any modification to the conventional TDF and AMF models, a small reduction in bubble diameter is found as comparing with the simulation result reported by Darmana *et al.* (2009). After taking the SGS-TDF bubble dispersion into account, it can be seen from the Figure 5-that a steady decline in the predicted equivalent diameter was identified in our LES simulation. Consistent with the bubble axial velocity prediction results, the implementation of the SGS-TDF gives a better bubble lateral dispersion estimation, resulting in a higher bubble volume fraction gradient in core region corresponding to the higher species concentration gradient and thus higher interfacial mass transfer. It should be noted that a closer consistency in the simulation and experimental data using model C is achieved especially for the region in higher part of the bubble column. This may be explained by the modification on the term related to eddy viscosity and the turbulent dispersion, i.e.,

$$\frac{C_b \alpha_G \frac{\Delta}{d} \left(\frac{1}{1 + St_{SGS}}\right)^{\frac{3}{2}}}{\sigma_{TD}} \frac{\nabla \alpha_G}{\alpha_G}$$

where the association between the bubble diameter and the local bubble volume fraction can be identified. Thus, the higher the axial height from the gas sparger, the larger of a difference between the simulation results and the experimental observation without modification. Furthermore, when using Model C, the correlation of turbulent eddy fluctuation induced shear and local bubble volume fraction for the bubbles $\frac{\nabla \cdot (\alpha_k \boldsymbol{\tau_k})}{\alpha_k \rho_k}$ would give rise to the local bubble volume fraction change, implying that the bubble diameter may be affected and this would be reflected in the estimation of the bubble Reynolds number, $\mathrm{Re_b} = |u_G - u_l| d_B \rho_L / \mu_L$. Based on the correlation proposed by Brauer (1978), the overall interfacial mass transfer rate will be enhanced.

4.3 Effect of inclusion of SGS-TDF and SGS-AMS on bubble dynamics

Figure 5-10 shows the instantaneous velocity vector highlighted by the local air volume fraction at different time steps with the results predicted using Model A, B and C from left to right. The transient meandering behaviour of the rising bubble group wobbling is captured using the proposed models. It can be seen from the Figure 5-10 that relative higher bubble volume fraction takes place in the central region of the bubble column, indicating that the bubble transport is significantly affected by the large turbulent eddies and the bubbles are entrapped by these large

eddies to form the meandering phenomena. It can be seen from the snapshots that the colours are weaken in the region close to the bubble column wall, which implies fewer bubbles being existed or lower bubble volume fraction, when using Model A. However, the spread of bubbles is apparently evidenced when employing Model C in the modelling. Even when using Model B without considering the SGS-AMS, the lateral bubble dispersion can be observed as a result of considering the SGS-TDF.

To highlight the species concentration evolution in the chemisorption reaction process, the contours of CO_2 concentration and pH value in the X-Z cutting plane through the bubble column are displayed in Figure 5-11 by using Model C for several time instants. It can be seen from the figure that at the beginning of the chemisorption process, only traceable amounts of dissolved CO_2 were detected over the whole region of the liquid solution in the bubble column, which gives out a slow reaction. At this point, the pH value of the liquid is obviously to indicate alkali-like, and very minor variations were noticed over time intervals less than 50 seconds (see also Figure 5-6). As a result of the reactions, the distribution of the pH value appears to be more homogeneous than the CO_2 distribution does. As the mass transfer progresses, the hydroxide is quickly consumed and the pH-value is further reduced (see Figure 5-6). Due to the restraint of the bubble column cross-sectional shape, bubbly flow at $z < 0.4$ H in the bubble column exists for the large recirculation vortices around the bottom corner of the bubble column, which results in poor interfacial mass transfer while a better interfacial mass transfer occurs in the upper

region of the bubble column. With the chemisorption reaction process continuing, the bubbly flow patterns in the bubble column become dynamically stable for the period of 50 to 100 seconds. At 150 seconds, the dissolved CO_2 is found to be well distributed in the liquid NaOH solution and the predicted pH value throughout the bubble column distributes uniformly.

The instantaneous bubble locations observed from Darmana's *et al.* work (2007) are shown in Figure 5-12 as a qualitative contrast to the contours by the present LES simulation for Case 2 using Model C. In Figure 5-12, the illustrations from the left to right are the instantaneous bubble locations, the predicted bubble volume fraction, the iso-surfaces of bubble volume fraction of 0.03, the bubble velocity, the liquid velocity and the pH-values, respectively. The bubble volume fraction contours clearly show the bubble group being wobbling and exhibiting the trace of "S" shape, which matches the experimental observation. The gradient of gas hold-up near the wall, on the other hand, is higher in the simulation than in the experiment. As the chemisorption process is going on, the bubble volume fraction profiles steadily reduce the magnitude with increase of the height. It can be also seen from Figure 5-12 that the pH variance is coupled with the dissolved CO_2 distribution and large turbulent eddy evolution.

4.4 Turbulent liquid kinetic energy spectrum and chemical species concentration spectrum

The turbulent kinetic energy power energy spectrum based on the axial liquid velocity fluctuations obtained at the centreline of the bubble column at Z = 0.75H are shown in Figure 5-13(a). The predicted axial liquid velocity fluctuations were converted to a format of two-point correlation based on time development. The power spectrum density per frequency was then obtained by taking the Fast Fourier Transform of the time-correlation. To have a deeper analysis of the power energy spectrum, the bubble representative frequency was also estimated for Case 2- Model C as reported by Prakash *et al.* (2016), which is given by

$$f_B = \frac{U_r}{2\pi d_B} = 5.79 \text{ Hz}\,.$$

Thus, it can be thought that the bubble induced turbulence energy was fed into in the system with the above induced eddy frequency. Following Risso and Ellinggsen (2002), the typical wave number can be estimated by

$$\kappa_B = \frac{2\pi}{\lambda_B} = \frac{2\pi f_B}{u_{mean}} = 143.2269 \text{ m}^{-1}\,.$$

As revealed by the accessible experimental studies or DNS simulation data (Sathe *et al*., 2013, Lucas et al., 2001, Prakash et al., 2016) the turbulence generated in bubble column bubbly flow can be characterized by the composition of the shear turbulence induced by the liquid velocity gradient and the bubble-induced turbu-

lence (BIT). The appearance of -5/3 scaling on the turbulent kinetic energy spectrum is very likely the effort of liquid phase shear turbulence but homogenised by the bubbles while the occurrence of -3 scaling is the result of bubble induced turbulence (BIT). It should be noted that in a recent work of LES modelling bubble column bubbly flow (Liu and Li, 2018), a -25/3 scaling law was identified and the authors attributed it to the contribution from the BIT. As can be seen from Figure 5-13(a), there exists an obvious transition in the slope of the predicted energy spectrum $E_{11}(\kappa)$ at around $\kappa_{B1} \approx 125\ m^{-1}$. For the wavenumber smaller than κ_{B1}, the -5/3 scaling which is located in the inertial sub-range is well recovered while for the wavenumber greater than the representative wavenumber corresponding to the bubble size, the slope was found to approach -3, being consistent with the experimental observations reported previously by other researchers (Murai *et al*., 2000; Sugiyama *et al.,* 2001; Bouche *et al*., 2014; Mendez-Diaz *et al*., 2013; Mercado *et al*., 2010; Riboux *et al*., 2010; Bunner and Tryggvason, 2003; Riboux *et al*., 2013; Roghair *et al*., 2011). It is believed that this effect can be partially described by consideration of the modified SGS-TDF and SGS-AMS terms in the LES modelling. It is cautiously mentioned that the bubble induced turbulence due to the rising bubble wakes may decay quite rapidly prior to the onset of turbulence spectral transfer. Pope (2000) also noted that the major mechanism in the energy cascade ($l < l_{EI}$) is the kinetic energy transfer to successively smaller scales (shear and bubble-induced viscosity dominants) and viscous dissipation (molecular viscosity dominants) where l_{EI} denotes the turbulence length scale between anisotropic large eddies and isotropic tiny eddies. Thus, the bubble induced turbulence energy will

not participate in the kinetic energy transferring in larger length scales associated with low wave numbers instead it will contribute to the turbulent kinetic energy transfer from the wave numbers associated with higher eddy frequencies. These eddies that are strongly related to the bubble size contributes to the turbulent dissipation in the higher frequency range as Lance and Bataille (1993) pointed out.

As can be seen from Figure 5-13(b), the cut-off length scale in our LES modelling of the species concentration spectrum is slightly larger than the wavenumber of order $\left(\frac{\epsilon}{\nu^3}\right)^{-\frac{1}{4}}$ while the Kolmogorov scale, $\eta \equiv \left(\frac{\nu^3}{\varepsilon}\right)^{\frac{1}{4}}$, estimated for case 2 is around 0.9149mm. According to the work reported by Lundgren (Lundgren, 1985), the -1 slope transition region could be found in the predicted species mass fraction spectrum, following a -5/3 Kolmogorov scaling law in the inertia subrange. In the present work, the species concentration fluctuations of OH^- and aqueous CO_2 at z = 0.75 H of the centreline of the bubble column are traced in the LES modelling. After applying two-point correlation and Fourier fast transformation, the concentration density spectrum was obtained as shown in Figure 5-13(b). It can be seen from the Figure 5-that a clear -5/3 scaling law is found in the inertia subrange, corresponding to $\kappa < 1/\Delta_{\text{cutoff}}$ and an approximate -1 scaling law is recovered after this transition position. This further supports the argument that the mass transfer occurring in CO_2 chemisorption process in the bubble column is strongly affected by the turbulent eddies acting on the bubble surfaces as schematically indicated in Figure 5-1. The wavenumber corresponding to the transition point in the species concentration spectrum right seemed to correspond to the thickness of the liquid

film enclosing the bubbles. Another interesting point needs to be noted that a transition in the scaling for $E_{Co2(aq)}(\kappa)$ takes place at around $\kappa_2 \approx 100\, m^{-1}$, where the wavelength is slightly larger than κ_B. This may indicate that a slower chemisorption occurs when the bubbles are entrapped by a similar or relatively larger eddy following a fast process when the CO_2 gas penetrates across the bubble surface to enter the surrounding liquid film hit by far too small turbulent eddies. The transition for $E_{OH^-}(\kappa)$ to take place at around $\kappa_3 \approx 40\, m^{-1}$ indicates that the reaction process $CO_2(aq) + OH^- \underset{k_{1-}}{\overset{k_{1+}}{\rightleftharpoons}} HCO_3^-$ finally reaches an equilibrium in the entire domain of the bubble column with the size of the largest eddies being the order of bubble column diameter.

5. CONCLUSIONS

Euler/Euler LES simulations of the carbon dioxide chemisorption in the sodium hydroxide solution in three different size bubble columns with low volume fractions were conducted using three different momentum exchange modelling models, i.e., A- conventional force models; B- modified SGS-TDF model; C- modified SGS-TDF and SGS-AMS models. The influences of considering the terms of SGS-TDF and SGS-AMS on the interfacial mass transfer of chemisorption process were assessed in the LES modelling. The bubble dynamic response to the turbulent eddies was also considered through the modification in the turbulent eddy viscosity and the mass eddy diffusivity. In the meantime, the bubble number density model was also used in the LES modelling of the mass transfer. The LES simulations using

the three models have been conducted based on the two rectangular and one cylindrical bubble column experimental cases. The main conclusions reached as the results of the present study can be summarised as follows:

(1) The LES simulation for prediction of the evolution of the species concentration and pH-value using the joint models of SGS-TDF and SGS-AMS (Model C) yields a similar degree of agreement with the experimental data. An apparent delay in the chemisorption reaction progress was found when using the models without considering the SGS-AMS modification. A possible explanation for this noticeable difference can be attributed to the fact that the model excluding the SGS-TDF and SGS-AMS (Model A) gives the poor estimation of the bubble lateral dispersion, resulting in an over-prediction of bubble volume fraction in the central region of the bubble column and interfacial mass transfer. The corresponding bubble dynamics in the core region would lead to a shorter bubble residence time, which may reduce the interfacial mass transfer across the phases, causing a delayed consumption on the hydroxide.

(2) The predicted time-averaged axial bubble velocity profiles in the lateral and radial directions for three models were compared with the experimental and the simulations conducted by other researchers. Quantitatively, a good agreement overall with the experimental data with N_2 supplied and with CO_2 supplied was obtained. However, the predicted distribution of the bubble axial velocities by considering the SGS-TDF and SGS-AMS (Model C) in the core region of the bubble columns

was found to be lower than the ones using the models (Model A and Model B), which was more consistent with the experimental data, indicating the necessity of considering the SGS-AMS for an accurate description of bubble dispersion and bubble dynamics in the bubble columns. It should be noted that the consistency for the predicted bubble velocity profiles compared with the experimental data become poorer at the near-wall region, which needs further investigation on how the LES modelling with SGS-TDF and SGS-AMS models can implement the Milelli's criterion for mesh requirement.

(3) The cross-sectional averaged and time-averaged equivalent bubble diameter along the axial height of the bubble columns exhibits a stepped reduction trend as measured from the gas sparger. It was found that such predicted a bubble diameter change along the height has a smaller deviation from the experimental data when considering both SGS-TDF and SGS-AMS (Model C) in the LES model However, the bubble size was still overestimated and this may require the effect of the anisotropic SGS-Reynolds stress in the LES model to be considered.

(4) The turbulent kinetic energy spectrum and the concentration spectrum of hydroxide and aqueous CO_2 obtained in the LES modelling still present a typical -5/3 scaling and -3 scaling laws for the former while the transition position in the slope was found to be close to the estimated representative bubble wavenumber. This indicates that the bubble induced turbulence only contributes the interfacial mass transfer with those eddy length scale smaller than the equivalent bubble size. For

the species concentration spectrum, the typical -5/3 scaling law was also identified with the eddies falling into the inertial sub-range, following by a scaling which approaches -1 while the transition cut-off length scale was found to be slightly smaller than the Kolmogorov scale η, which is consistent with the work reported by Lundgren (1985). The mechanism of the CO_2 chemisorption related to the inter-facial mass transfer as reflected from the concentration spectrum indicates that the turbulent eddies with the size smaller than the equivalent bubble diameter have a major impact on the interfacial mass transfer, again affirming the importance of SGS-TDF and SGS-AMS.

REFERENCES

BAUER, M., & EIGENBERGER, G. (2001). Multiscale modeling of hydrodynam-ics, mass transfer and reaction in bubble column reactors. *Chemical Engineering Science*, ***56***(3), 1067-1074.

BIRD, R. B., STEWART, W. E., & LIGHTFOOT, E. N. (2006). *Transport phe-nomena* (Vol. 1). John Wiley & Sons.

BOUCHE, E., ROIG, V., RISSO, F., & BILLET, A. M. (2014). Homogeneous swarm of high-Reynolds-number bubbles rising within a thin gap. Part 2. Liquid dynamics. *Journal of Fluid Mechanics*, **758**, 508-521.

BRAUER, F., & SOUDACK, A. C. (1981). Constant-rate stocking of predator-prey systems. *Journal of Mathematical Biology*, **11**(1), 1-14.

BRAUER, H. (1978). Unsteady state mass transfer through the interface of spherical particles—I: Physical and mathematical description of the mass-transfer problem. *International Journal of Heat and Mass Transfer*, **21**(4), 445-453.

BUFFO, A., VANNI, M., & MARCHISIO, D. L. (2017). Simulation of a reacting gas–liquid bubbly flow with CFD and PBM: Validation with experiments. *Applied Mathematical Modelling*, **44**, 43-60.

BUNNER, B., & TRYGGVASON, G. (2003). Effect of bubble deformation on the properties of bubbly flows. *Journal of Fluid Mechanics*, **495**, 77-118.

CHEN, P. C. (2012). Absorption of carbon dioxide in a bubble-column scrubber. *Greenhouse Gases-Capturing, Utilization and Reduction*, 95-112.

COLOMBET, D., LEGENDRE, D., COCKX, A., GUIRAUD, P., RISSO, F., DANIEL, C., & GALINAT, S. (2011). Experimental study of mass transfer in a dense bubble swarm. *Chemical Engineering Science*, **66**(14), 3432-3440.

DARMANA, D., DEEN, N. G., & KUIPERS, J. A. M. (2005). Detailed modeling of hydrodynamics, mass transfer and chemical reactions in a bubble column using a discrete bubble model. *Chemical Engineering Science*, **60**(12), 3383-3404.

DARMANA, D., HENKET, R. L. B., DEEN, N. G., & KUIPERS, J. A. M. (2007). Detailed modelling of hydrodynamics, mass transfer and chemical reactions in a bubble column using a discrete bubble model: Chemisorption of CO2 into NaOH solution, numerical and experimental study. *Chemical Engineering Science*, **62**(9), 2556-2575.

DHOTRE, M. T., DEEN, N. G., NICENO, B., KHAN, Z., & JOSHI, J. B. (2013). Large eddy simulation for dispersed bubbly flows: a review. *International Journal of Chemical Engineering*, 2013.

EDWARDS, T. J., MAURER, G., NEWMAN, J., & PRAUSNITZ, J. M. (1978). Vapor-liquid equilibria in multicomponent aqueous solutions of volatile weak electrolytes. *AIChE Journal*, **24**(6), 966-976.

EIGEN, M. (1954). Methods for investigation of ionic reactions in aqueous solutions with half-times as short as 10–9 sec. Application to neutralization and hydrolysis reactions. *Discussions of the Faraday Society*, **17**, 194-205.

FARD, M. G., STIRIBA, Y., GOURICH, B., VIAL, C., & GRAU, F. X. (2020). Euler-Euler large eddy simulations of the gas–liquid flow in a cylindrical bubble column. *Nuclear Engineering and Design*, **369**, 110823.

GÖZ, M. F., SOMMERFELD, M., & LAÍN, S. (2006). Instabilities in Lagrangian tracking of bubbles and particles in two-phase flow. *AIChE journal*, **52**(2), 469-477.

GRUBER, M. C., RADL, S., & KHINAST, J. G. (2015). Rigorous modeling of CO_2 absorption and chemisorption: The influence of bubble coalescence and breakage. *Chemical Engineering Science*, **137**, 188-204.

HIKITA, H., ASAI, S., & TAKATSUKA, T. (1976). Absorption of carbon dioxide into aqueous sodium hydroxide and sodium carbonate-bicarbonate solutions. *Chemical Engineering Journal*, **11**(2), 131-141.

HLAWITSCHKA, M. W., DREFENSTEDT, S., & BART, H. J. (2016). Local analysis of CO2 chemisorption in a rectangular bubble column using a multiphase Euler-Euler CFD code. *Chemical Engineering & Process Technology Journal*, ***7***(3).

HLAWITSCHKA, M. W., KOVÁTS, P., ZÄHRINGER, K., & BART, H. J. (2017). Simulation and experimental validation of reactive bubble column reactors. *Chemical Engineering Science*, **170**, 306-319.

HU, G., & CELIK, I. (2008). Eulerian–Lagrangian based large-eddy simulation of a partially aerated flat bubble column. *Chemical Engineering Science*, **63**(1), 253-271.

JAIN, D., KUIPERS, J. A. M., & DEEN, N. G. (2015). Numerical modeling of carbon dioxide chemisorption in sodium hydroxide solution in a micro-structured bubble column. *Chemical Engineering Science*, **137**, 685-696.

JIA, H. W., & ZHANG, P. (2017). Mass transfer of a rising spherical bubble in the contaminated solution with chemical reaction and volume change. *International Journal of Heat and Mass Transfer*, **110**, 43-57.

KOLMOGOROV, A. N. (1991). The local structure of turbulence in incompressible viscous fluid for very large Reynolds numbers. *Proceedings of the Royal Society of London. Series A: Mathematical and Physical Sciences* **434**(1890): 9-13.

KOVÁTS, P., THÉVENIN, D., & ZÄHRINGER, K. (2018). Characterizing fluid dynamics in a bubble column aimed for the determination of reactive mass transfer. *Heat and Mass Transfer*, **54**(2), 453-461.

KRAUß, M., & RZEHAK, R. (2018). Reactive absorption of CO2 in NaOH: An Euler-Euler simulation study. *Chemical Engineering Science*, **181**, 199-214.

KRAUB, M., & RZEHAK, R. (2017). Reactive absorption of CO2 in NaOH: Detailed study of enhancement factor models. *Chemical Engineering Science*, **166**, 193-209.

LIU, Z., & LI, B. (2018). Scale-adaptive analysis of Euler-Euler large eddy simulation for laboratory scale dispersed bubbly flows. *Chemical Engineering Journal*, **338**, 465-477.

LOCHIEL, A. C., & CALDERBANK, P. H. (1964). Mass transfer in the continuous phase around axisymmetric bodies of revolution. *Chemical Engineering Science*, **19**(7), 471-484.

LONG, S., YANG, J., HUANG, X., LI, G., SHI, W., SOMMERFELD, M., & YANG, X. (2020). Large-eddy simulation of gas–liquid two-phase flow in a bubble column reactor using a modified sub-grid scale model with the consideration of bubble-eddy interaction. *International Journal of Heat and Mass Transfer*, **161**, 120240.

LUCAS, D., KREPPER, E., & PRASSER, H. M. (2001). Prediction of radial gas profiles in vertical pipe flow on the basis of bubble size distribution. *International Journal of Thermal Sciences*, **40**(3), 217-225.

LUNDGREN, T. S. (1985). The concentration spectrum of the product of a fast bimolecular reaction. *Chemical Engineering Science*, **40**(9), 1641-1652.

MÁRQUEZ, M. A., AMEND, R. J., CARBONELL, R. G., SÁEZ, A. E., & ROBERTS, G. W. (1999). Hydrodynamics of gas-lift reactors with a fast, liquid-phase reaction. *Chemical Engineering Science*, **54**(13-14), 2263-2271.

MENDEZ-DIAZ, S., SERRANO-GARCIA, J. C., ZENIT, R., & HERNANDEZ-CORDERO, J. A. (2013). Power spectral distributions of pseudo-turbulent bubbly flows. *Physics of Fluids*, **25**(4), 043303.

MERCADO, J. M., GOMEZ, D. C., VAN GILS, D., SUN, C., & LOHSE, D. (2010). On bubble clustering and energy spectra in pseudo-turbulence. *Journal of Fluid Mechanics*, **650**, 287-306.

MILELLI, M. (2002). A numerical analysis of confined turbulent bubble plumes, ETH Zurich.

MUDDE, R. F., & SIMONIN, O. (1999). Two-and three-dimensional simulations of a bubble plume using a two-fluid model. *Chemical Engineering Science*, **54**(21), 5061-5069.

MURAI, Y., KITAGAWA, A., SONG, X. Q., OHTA, J., & YAMAMOTO, F. (2000). Inverse Energy Cascade Structure of Turbulence in a Bubble Flow: Numerical Analysis Using Eulerian-Lagrangian Model Equations. *JSME International Journal Series B Fluids and Thermal Engineering*, **43**(2), 197-205.

POHORECKI, R., & MONIUK, W. (1988). Kinetics of reaction between carbon dioxide and hydroxyl ions in aqueous electrolyte solutions. *Chemical Engineering Science*, **43**(7), 1677-1684.

PRAKASH, V. N., MERCADO, J. M., VAN WIJNGAARDEN, L., MANCILLA, E., TAGAWA, Y., LOHSE, D., & SUN, C. (2016). Energy spectra in turbulent bubbly flows. *Journal of Fluid Mechanics*, ***791***, 174-190.

RADL, S., & KHINAST, J. G. (2010). Multiphase flow and mixing in dilute bubble swarms. *AIChE journal*, **56**(9), 2421-2445.

RATCLIFF, G. A., & HOLDCROFT, J. G. (1963). Diffusivities of gases in aqueous electrolyte solutions. *Transactions of the Institution of Chemical Engineers*, **41**(10), 315-319.

RIBOUX, G., LEGENDRE, D., & RISSO, F. (2013). A model of bubble-induced turbulence based on large-scale wake interactions. *Journal of Fluid Mechanics*, **719**, 362-387.

RIBOUX, G., RISSO, F., & LEGENDRE, D. (2010). Experimental characterization of the agitation generated by bubbles rising at high Reynolds number. *Journal of Fluid Mechanics*, **643**, 509-539.

RISSO, F., & ELLINGSEN, K. (2002). Velocity fluctuations in a homogeneous dilute dispersion of high-Reynolds-number rising bubbles. *Journal of Fluid Mechanics*, **453**, 395-410.

ROGHAIR, I., MERCADO, J. M., ANNALAND, M. V. S., KUIPERS, H., SUN, C., & LOHSE, D. (2011). Energy spectra and bubble velocity distributions in pseudo-turbulence: Numerical simulations vs. experiments. *International Journal of Multiphase Flow*, **37**(9), 1093-1098.

SATHE, M., JOSHI, J., & EVANS, G. (2013). Characterization of turbulence in rectangular bubble column. *Chemical Engineering Science*, ***100***, 52-68.

SATO, Y., & SEKOGUCHI, K. (1975). Liquid velocity distribution in two-phase bubble flow. *International Journal of Multiphase Flow*, ***2***(1), 79-95.

SMAGORINSKY, J. (1963). General circulation experiments with the primitive equations: I. The basic experiment. *Monthly weather review*, **91**(3), 99-164.

SOKOLICHIN, A., & EIGENBERGER, G. (1994). Gas—liquid flow in bubble columns and loop reactors: Part I. Detailed modelling and numerical simulation. *Chemical Engineering Science*, **49**(24), 5735-5746.

SOMMERFELD, M., MUNIZ, M., & REICHARDT, T. (2018). On the importance of modelling bubble dynamics for point-mass numerical calculations of bubble columns. *Journal of Chemical Engineering of Japan*, **51**(4), 301-317.

SUGIYAMA, K., TAKAGI, S., & MATSUMOTO, Y. (2001). Multi-scale analysis of bubbly flows. *Computer methods in applied Mechanics and Engineering*, **191**(6-7), 689-704.

SUNGKORN, R., DERKSEN, J. J., & KHINAST, J. G. (2011). Modeling of turbulent gas–liquid bubbly flows using stochastic Lagrangian model and lattice-Boltzmann scheme. *Chemical Engineering Science*, **66**(12), 2745-2757.

TABORDA, M. A., & SOMMERFELD, M. (2021). Reactive LES-Euler/Lagrange modelling of bubble columns considering effects of bubble dynamics. *Chemical Engineering Journal*, **407**, 127222.

TABORDA, M. A., KIPPING, R., HAMPEL, U., & SOMMERFELD, M. (2021). Advanced analysis of bubble columns: Comparison of Euler/Lagrange simulations and experiments under CO2 chemisorption conditions. *Chemical Engineering Research and Design*, **170**, 389-405.

TALVY, S., COCKX, A., & LINÉ, A. (2007). Modeling of oxygen mass transfer in a gas–liquid airlift reactor. *AIChE Journal*, **53**(2), 316-326.

TOMIYAMA, A. (2004). Drag, lift and virtual mass forces acting on a single bubble. 3rd Int. Symp. Two-Phase Flow Modeling and Experimentation Pisa.

TSONOPOULOS, C., COULSON, D. M., & INMAN, L. B. (1976). Ionization constants of water pollutants. *Journal of Chemical and Engineering Data*, **21**(2), 190-193.

ZHANG, D., DEEN, N. G., & KUIPERS, J. A. M. (2006). Numerical simulation of the dynamic flow behavior in a bubble column: a study of closures for turbulence and interface forces. *Chemical Engineering Science*, **61**(23), 7593-7608.

ZHANG, D., DEEN, N. G., & KUIPERS, J. A. M. (2009). Euler− Euler modeling of flow, mass transfer, and chemical reaction in a bubble column. *Industrial & Engineering Chemistry Research*, **48**(1), 47-57.

APPENDIX

Reaction rate

The correlation between the first reaction's forward rate constant with the ionic strength has been suggested by Pohorecki and Moniuk (1988) who have employed a laminar jet technique to obtain,

$$\log\left(\frac{k_{1+}}{k_{1+}^{\infty}}\right) = 0.221\,\frac{I}{[kmol\,m^{-3}]} - 0.016\,\frac{I^2}{[kmol^2\,m^{-6}]} \qquad \text{(A1)}$$

where the temperature relevant (suitable in the range of 291-314K) reaction rate constant [$m^3\ kmol^{-1}\ s^{-1}$] at an infinitely ionic dilution is shown as,

$$log(k_{1+}^{\infty}) = 11.895 - 2382\,\frac{[K]}{T} \qquad \text{(A2)}$$

In terms of the ionic strength, I, it is defined by

$$I = \frac{1}{2}\left(c_L^{Na^+} Z_{Na^+}^2 + c_L^{OH^-} Z_{OH^-}^2 + c_L^{HCO_3^-} Z_{HCO_3^-}^2 + c_L^{CO_3^{2-}} Z_{CO_3^{2-}}^2\right) \qquad \text{(A3)}$$

where the valences Z of each dissolved ions are $Z_{Na^+} = 1, Z_{OH^-} = Z_{HCO_3^-} = -1, Z_{CO_3^{2-}} = -2$. The first reaction, described by Equation (5-17), occurs in conjunction with water's auto-dissociation, $H_2O \rightleftharpoons H^+ + OH^-$. As a result, the equilibrium constant K_w of water ionization is required. Tsonopoulos *et al.* (1976) proposed the following equation to describe K_w's temperature dependence:

$$K_w = c_L^{H^+} c_L^{OH^-} = 10^{\left(-\frac{5839.5[K]}{T} + 22.4773\log\left(\frac{T}{[K]}\right) - 61.2062\right)}. \qquad \text{(A4)}$$

With consideration of the water auto-dissociation, the equilibrium constant K_3 is expressed by the following empirical relationship as proposed by Edwards *et al.* (1978):

$$K_3 = \frac{c_L^{HCO_3^-} c_L^{H^+}}{c_L^{CO_2}} = \exp\left(-\frac{12092.1[K]}{T} - 36.786 \ln\left(\frac{T}{[K]}\right) + 235.482\right). \quad \text{(A5)}$$

Thus, the backward reaction rate constant of the first reaction can be expressed as,

$$k_{1-} = \frac{K_W}{K_3} k_{1+}. \quad \text{(A6)}$$

According to Eigen (1954), the forward reaction rate constant k_{2+} for the second reaction (Equation (5-19)) is in the order of 10^{10}– 10^{11} m^3 $kmol^{-1}$ s^{-1} with the proton transferring. Darmana *et al.* (2007) demonstrate that a substantially lower number can be used as long as this reaction stays significantly faster than other, most notably $k_{2+} \gg k_{1+}$. $k_{2+} = 10^6 m^3$ $kmol^{-1}$ s^{-1} is set with unaffected results. According to Hikita *et al.* (1976), the equilibrium constant K_2 of the second reaction is determined as the ratio:

$$K_2 = \frac{k_{2+}}{k_{2-}} \quad \text{(A7)}$$

where,

$$\log K_2 = log k_{2\infty} + \frac{1.01\sqrt{c_L^{Na^+}}}{1+1.27\sqrt{c_L^{Na^+}}} + 0.125 c_L^{Na^+} \quad \text{(A8)}$$

$$log k_{2\infty} = \frac{1568.94}{T} + 0.4134 - 0.00673T. \quad \text{(A9)}$$

	D_0^I $\cdot 10^9$ $(m^2\ s^{-1})$	T^I (K)	γ^I
OH^-	*26.65*	*216.5*	*11.658*
HCO_3^-	*7.016*	*204*	*2.394*
Na^+	*5.391*	*209.7*	*1.619*
CO_3^{2-}	*5.447*	*210.3*	*2.193*

Regarding the turbulent viscosity ν_t as defined in Equation (5-20), the modification on the shear turbulent eddy viscosity has been done by Long et al. (2020), in which the bubble dynamic response to surrounding eddies in sub-grid scale has been considered,

$$\nu_{t,SGS} = (C_s \Delta)^2 \mid S \mid \left[1 + C_b \overline{\alpha}_G \frac{\Delta}{d_B} \left(\frac{1}{1 + St_{SGS}} \right)^{3/2} \right]. \quad \text{(A10)}$$

The species source terms due to reactions is summarised below,

$$S^{OH^-} = (\mathrm{R}_{1-} - \mathrm{R}_{1+} + \mathrm{R}_{2-} - \mathrm{R}_{2+}) M^{OH^-} \quad \text{(A11)}$$

$$S^{HCO_3^-} = (\mathrm{R}_{1+} - \mathrm{R}_{1-} + \mathrm{R}_{2-} - \mathrm{R}_{2+}) M^{HCO_3^-} \quad \text{(A12)}$$

$$S^{CO_3^{2-}} = (\mathrm{R}_{2+} - \mathrm{R}_{2-}) M^{CO_3^{2-}} \quad \text{(A13)}$$

$$S^{CO_2(aq)} = (\mathrm{R}_{1-} - \mathrm{R}_{1+}) M^{CO_2} . \quad \text{(A14)}$$

It is noted that $\sum_j Y_L^j = 1$, $\sum_j \alpha S_L^j = 0$ need to be followed for mass conservation.

FIGURES

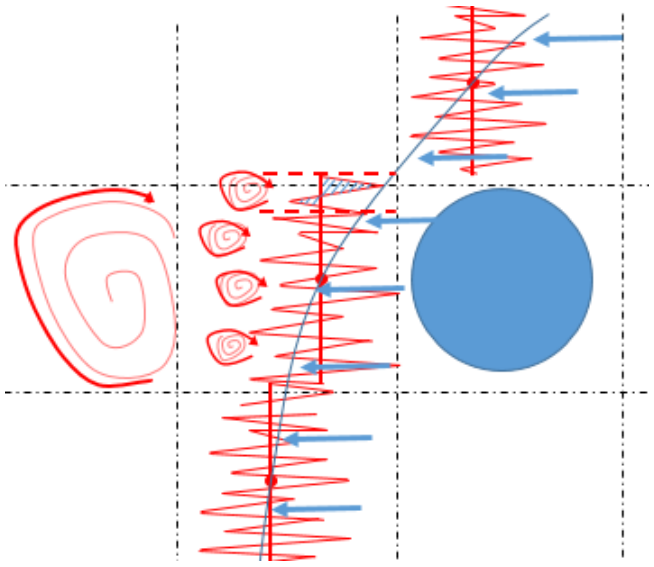

Figure 5- 1 Schematic of turbulent eddy fluctuations around the bubbles using the LES spatial filtering in bubble column bubbly flows.

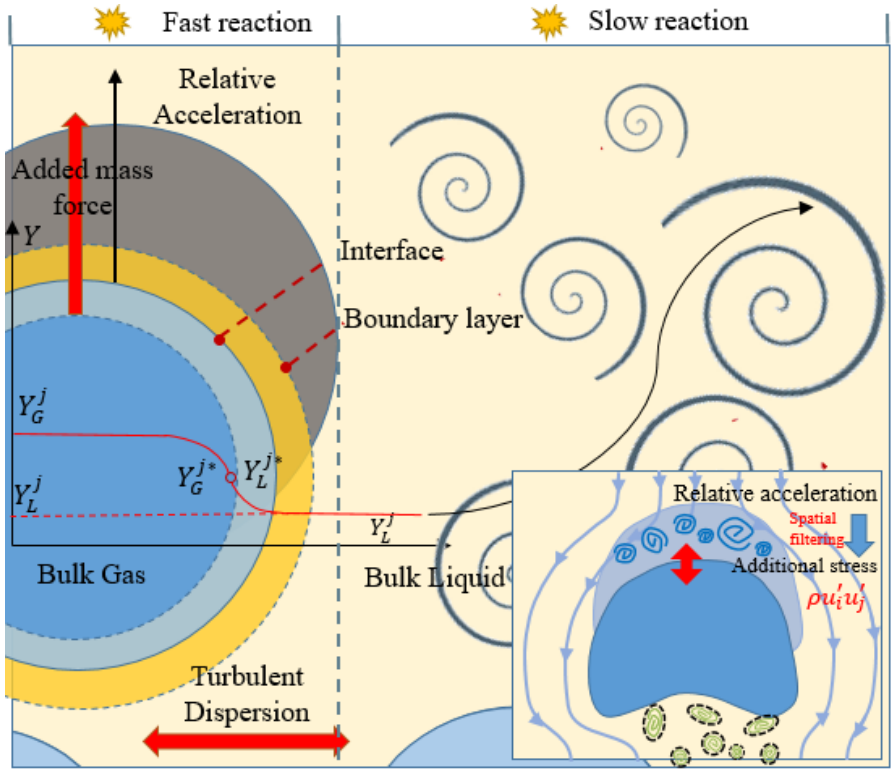

Figure 5- 2 Schematic diagram of the mass transfer between the rising-up bubble and the surrounding liquid phase (NaOH solution) in the bubble column.

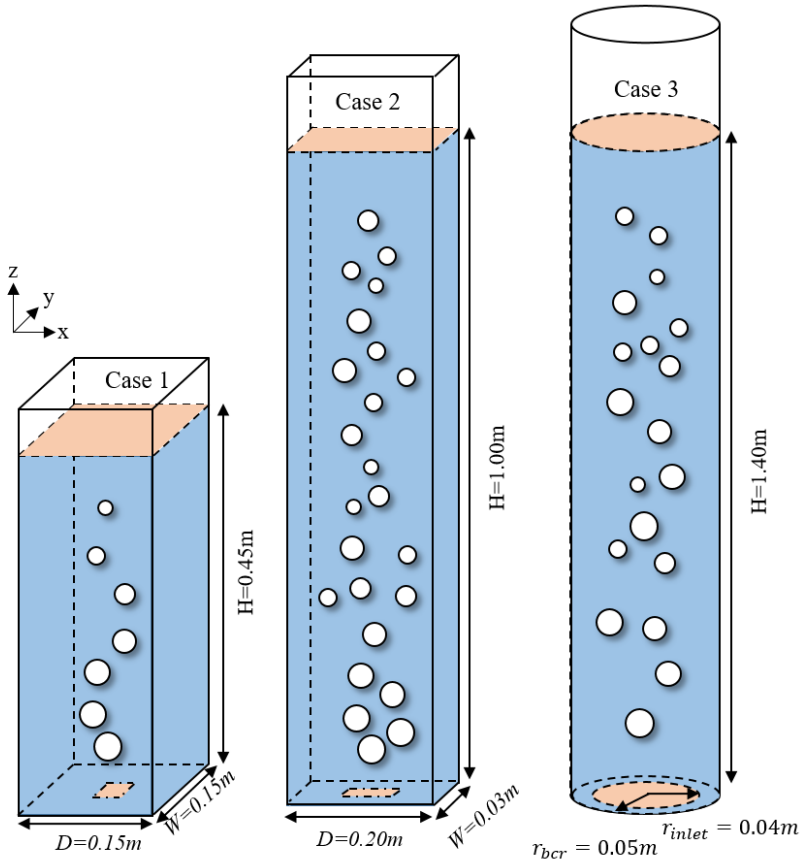

Figure 5- 3 Schematic diagrams of the experimental set-up of the three reactive bubble column reactors.

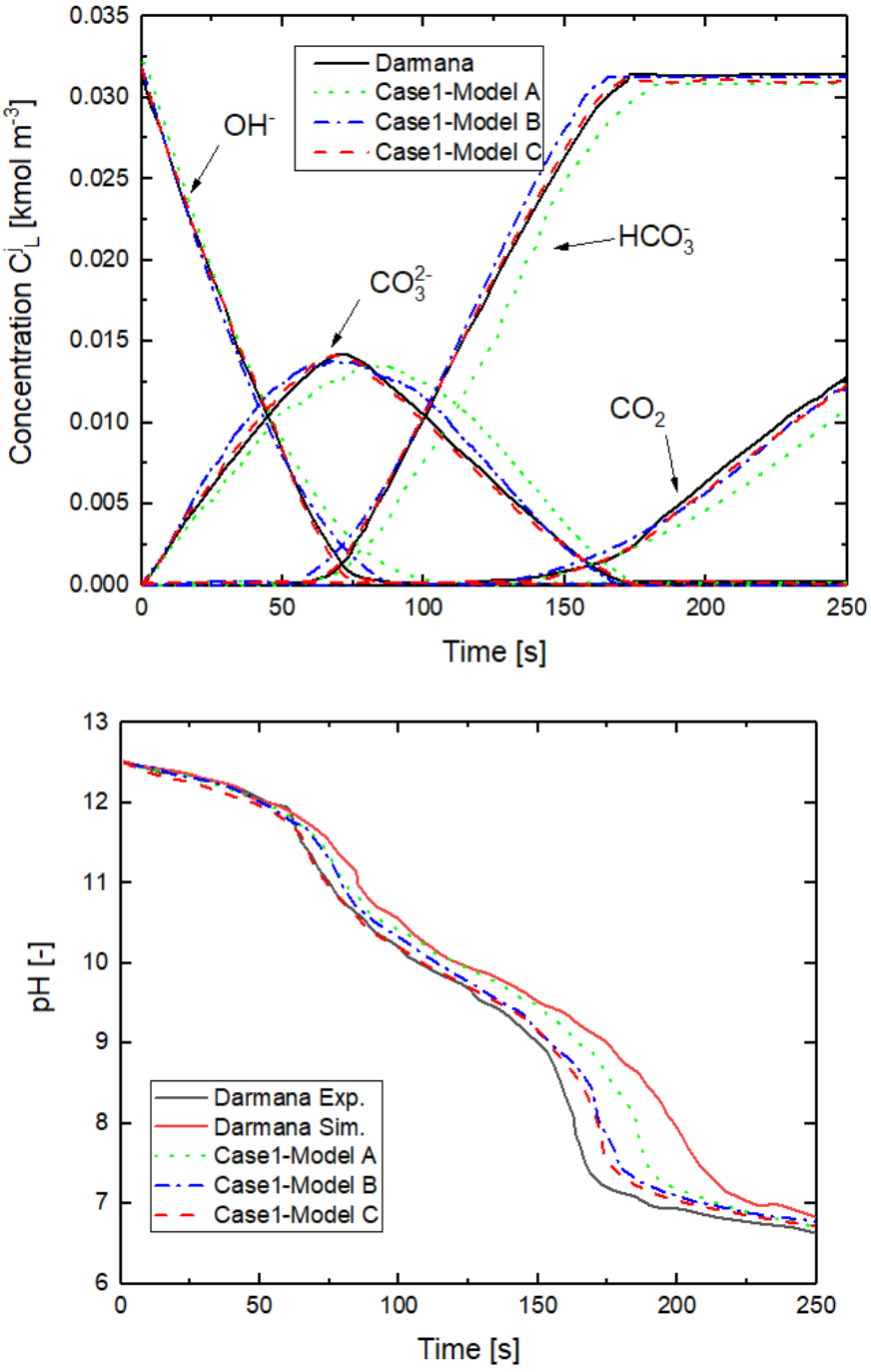

Figure 5- 4 Time history of the predicted local species concentrations compared with the measured experimental data of Darmana *et al.* (solid line).

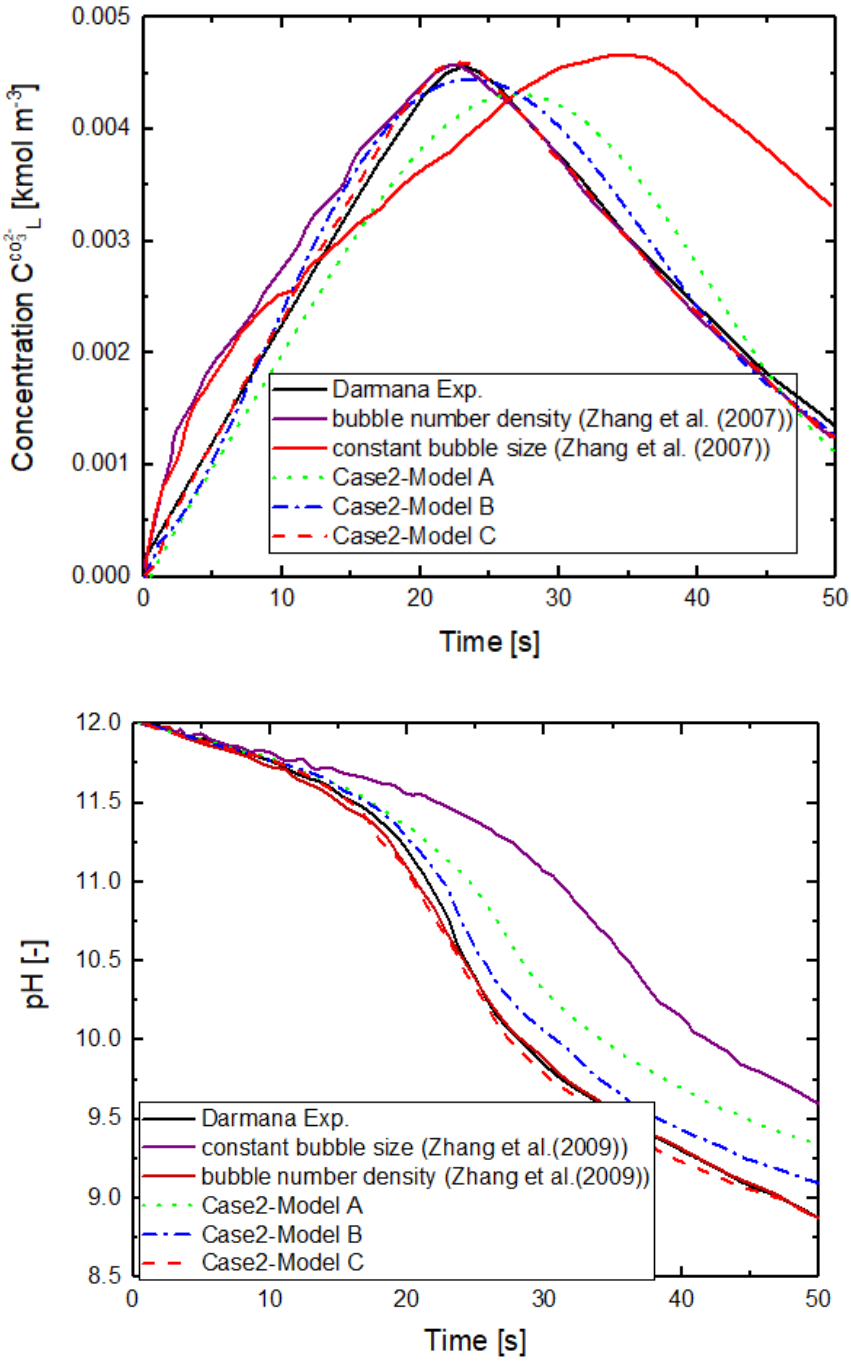

Figure 5- 5 Time history of predicted domain-averaged $\mathbf{CO_3^{2-}}$ concentration and pH-value at middle point at z = 980 mm.

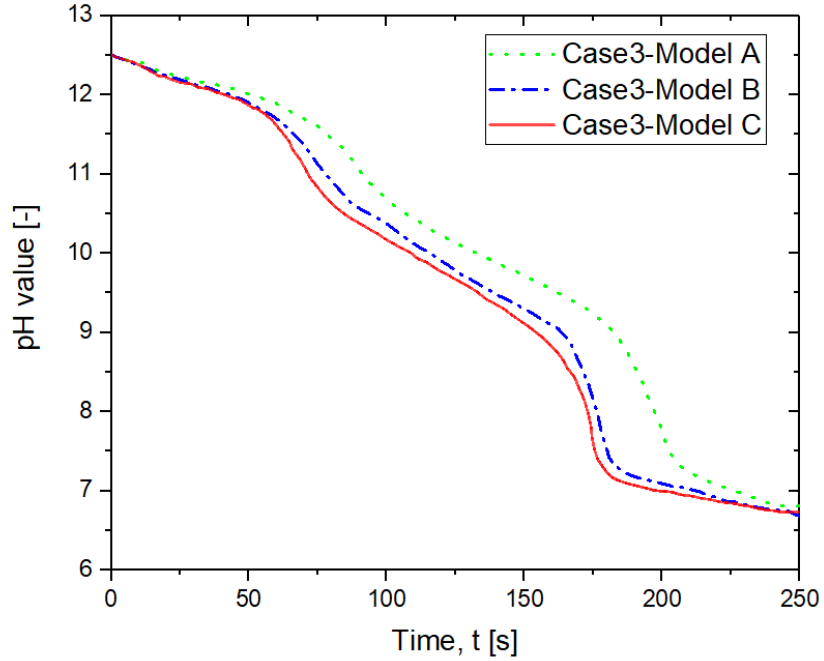

Figure 5- 6 Time history of predicted pH-value at middle point at H/D = 1.

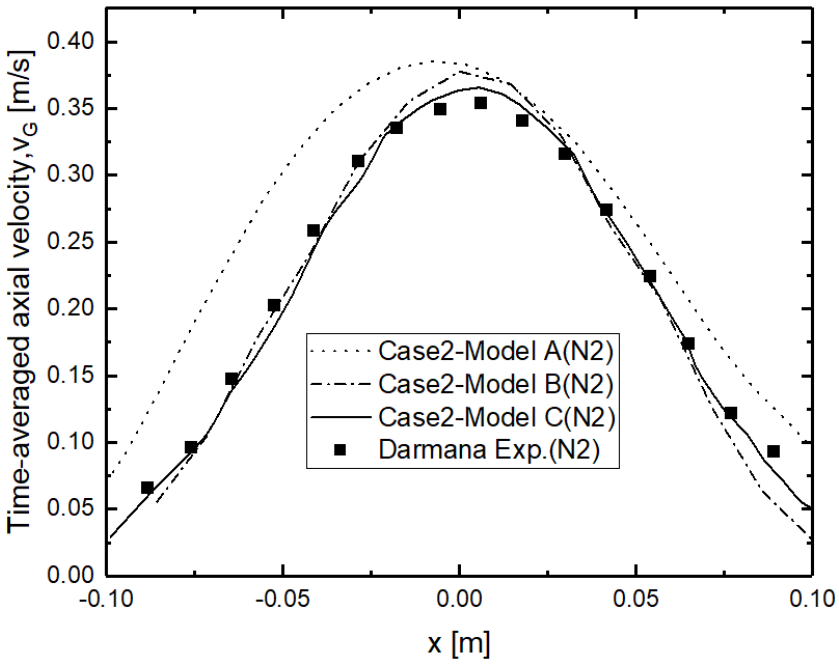

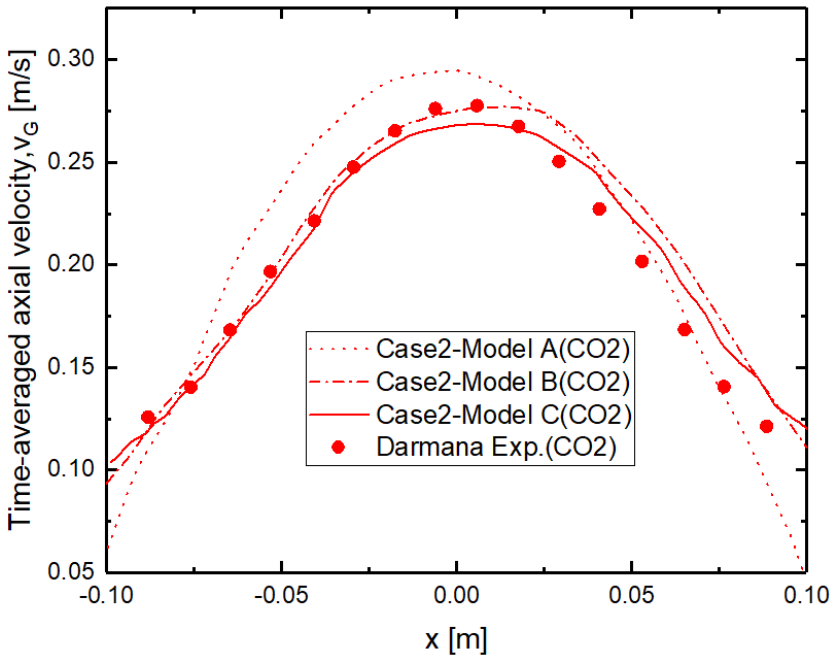

Figure 5- 7 Time-averaged radial distribution of axial bubble velocity at z = 750 mm (a) with $\mathbf{N_2}$ supplied (b) with $\mathbf{CO_2}$ supplied.

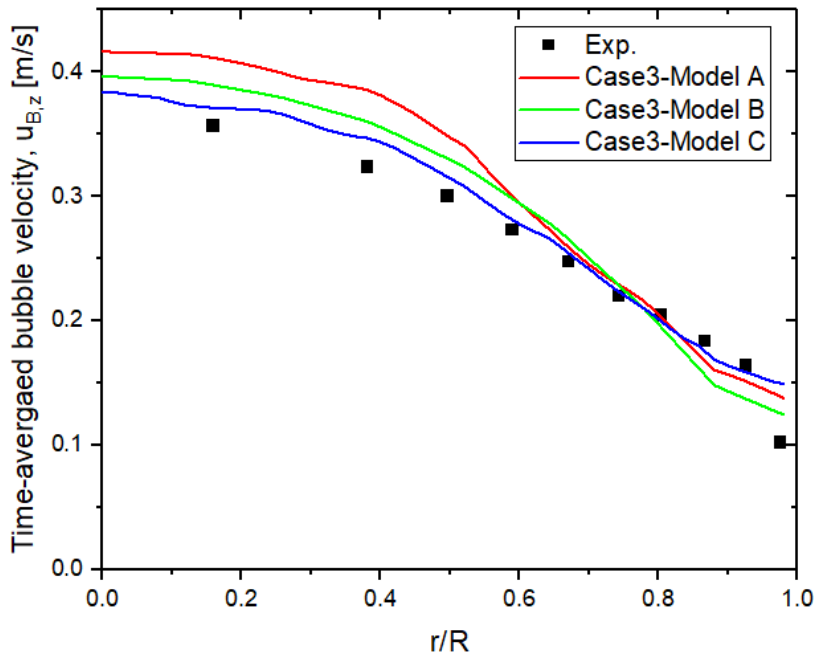

Figure 5- 8 Time-averaged bubble axial velocity at middle point at H/D = 7.

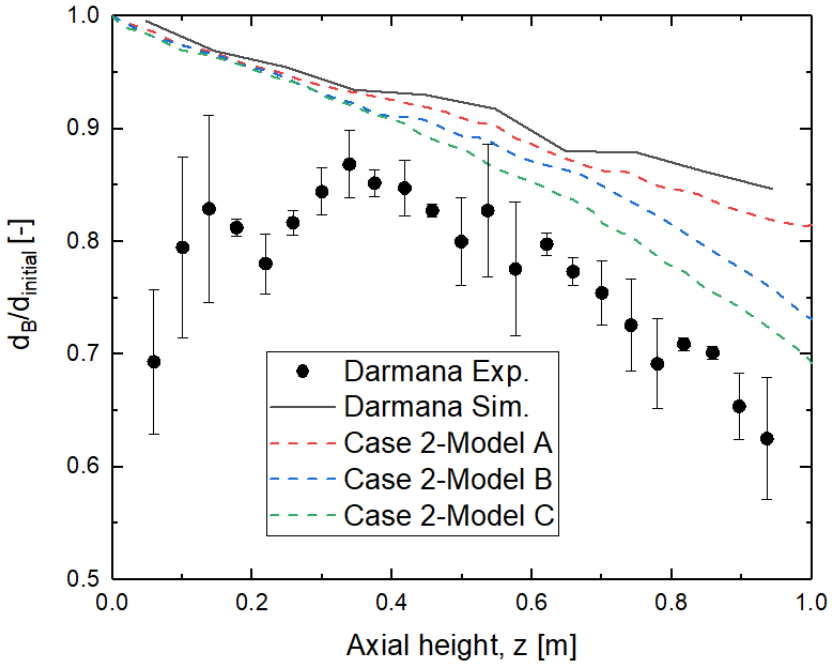

Figure 5- 10 Variation of cross-sectional averaged and time-averaged equivalent dimensionless bubble along the axial height of the bubble column.

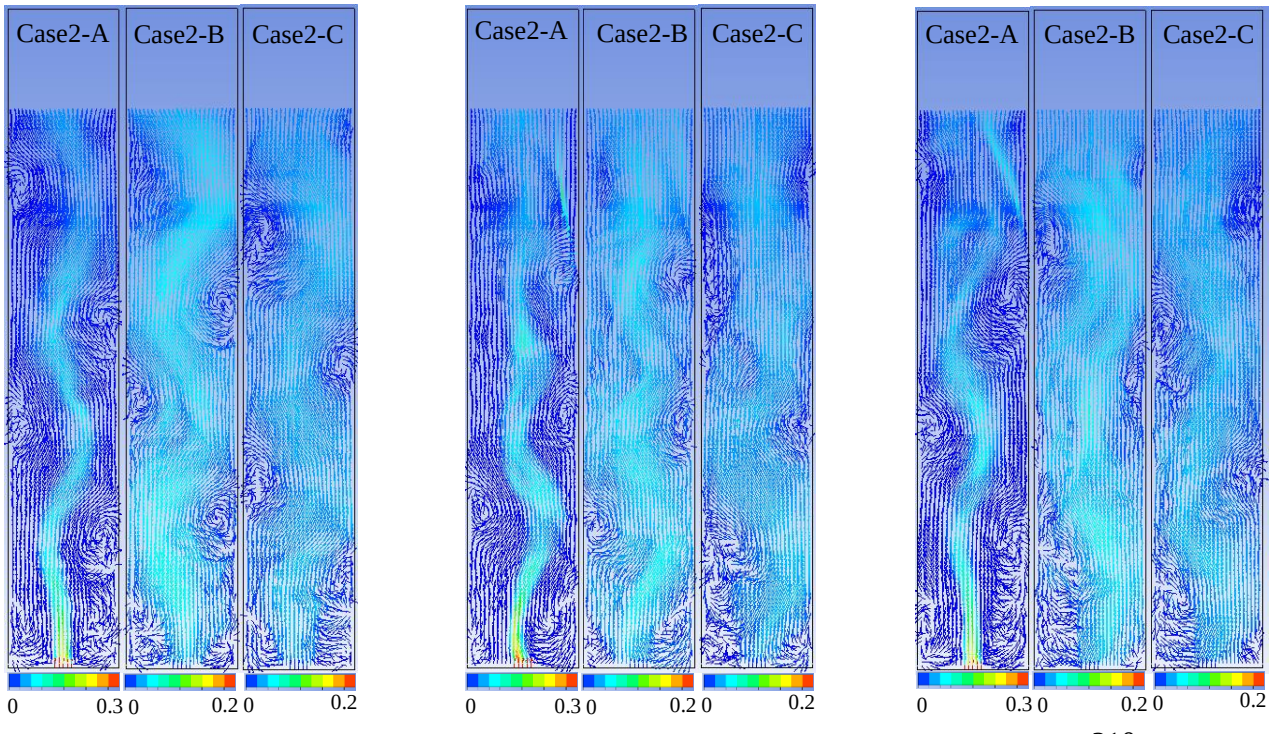

Figure 5- 9 Snapshots of instantaneous bubble velocity distribution in the X-Z cutting plane (y = 0) at three different time instants.

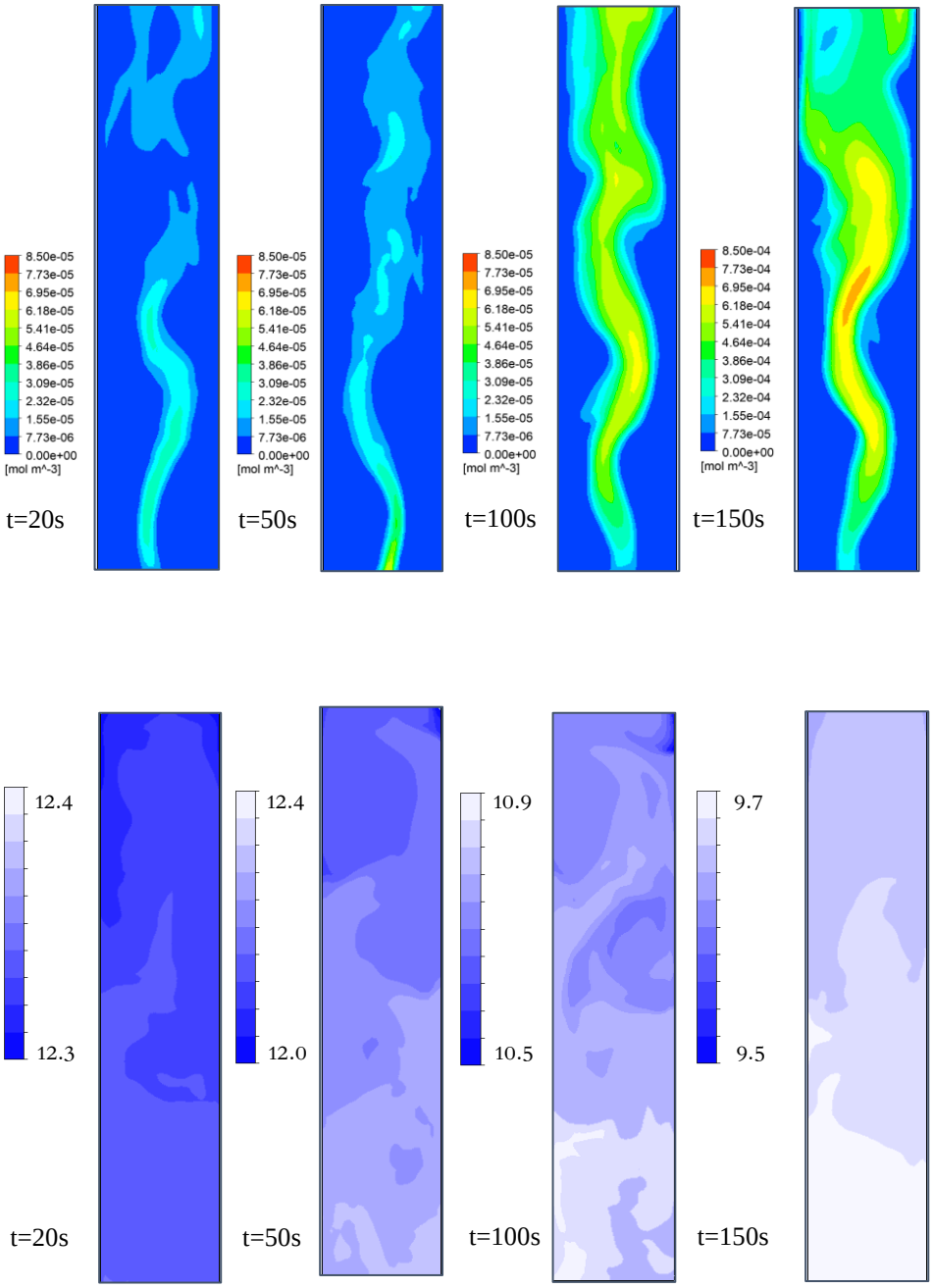

Figure 5- 11 Instantaneous contours of (a) CO_2 molar concentration and (b) pH-values in the X-Z cutting plane (y = 0) (Case 2-C).

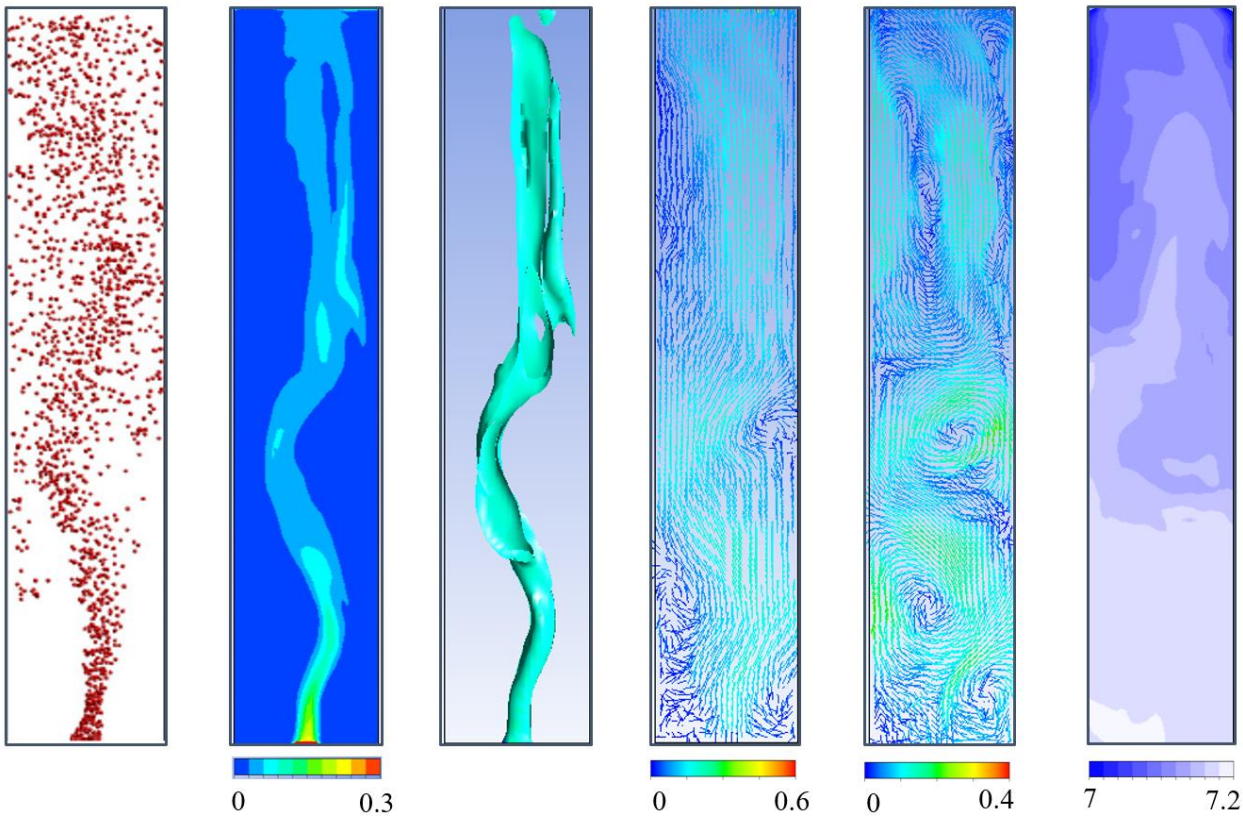

Figure 5- 12 Instantaneous (a) bubble position according to Darmana *et al.* (2007); (b) predicted corresponding air volume fraction; (c) iso-surface of $\boldsymbol{\alpha_{Gas} = 0.03}$ (d) gas phase velocity vector field; (e) liquid phase velocity vector field (f)pH value of XZ plane at y = 0.

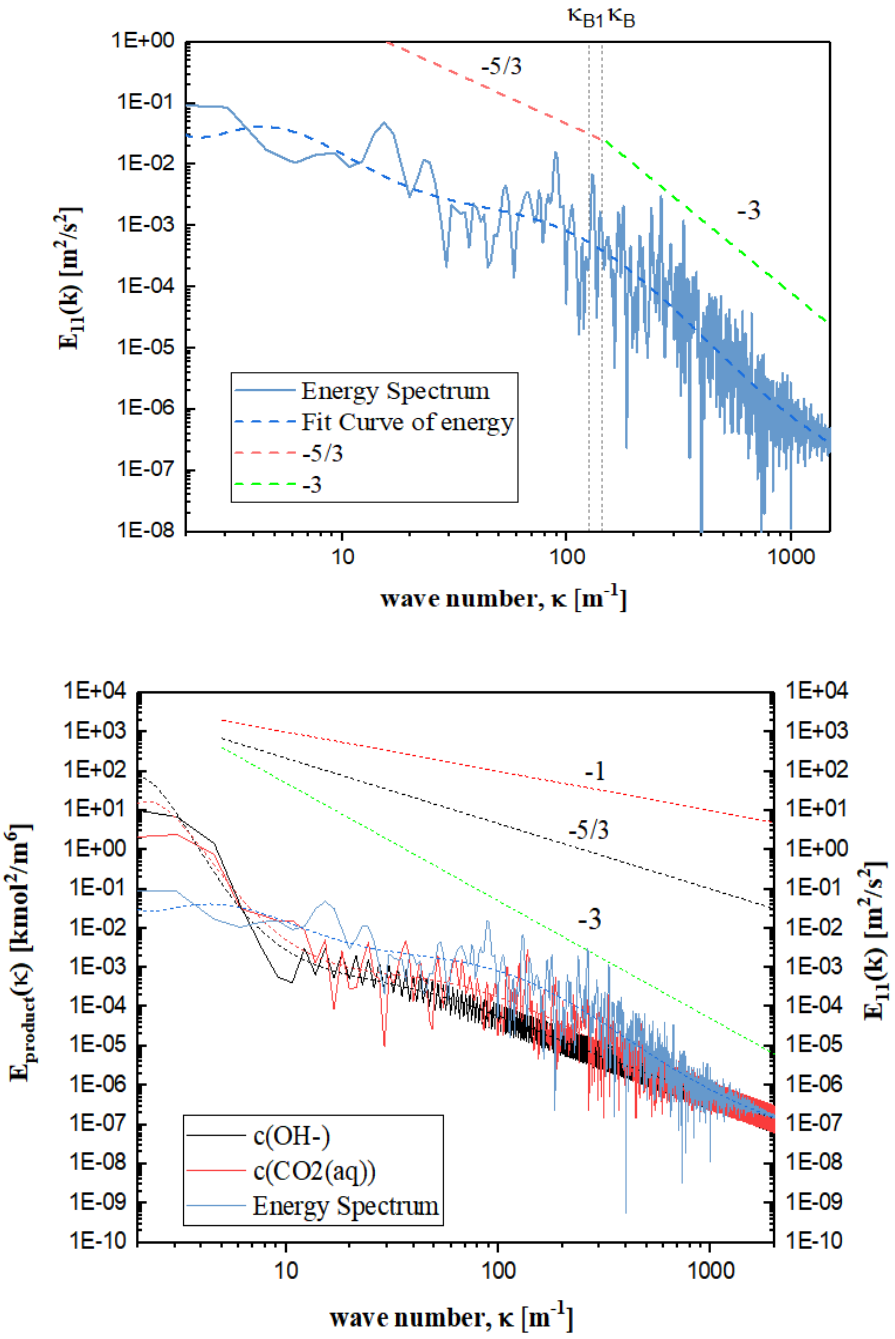

Figure 5- 13 Concentration spectrums of hydroxide ions and aqueous CO_2 and liquid turbulent axial velocity spectrum obtained at the centreline of the bubble column at z = 0.5 H

CHAPTER 6: EFFECTS OF SUB-GRID SCALE BUBBLE-EDDY AND PARTICLE-EDDY INTERACTIONS ON GAS-SOLID-LIQUID THREE-PHASE FLOW IN A SLURRY BUBBLE COLUMN

SUMMARY

In Chapter 2, the effect of the consideration of bubble dynamic responses to the surrounding eddies in eddy viscosity model on predicting the bubble column bubbly flow has been investigated. It has been demonstrated that the use of the modified turbulent eddy viscosity model is capable of capturing the transient behaviour of the gas-liquid two-phase flow in bubble column when adopting two-fluid Euler/Euler large eddy simulation. Comparing to the use of the standard SGS model, the performance of prediction of momentum and mass transfer in bubble column bubbly flow has been implemented, highlighting the importance of the inclusion of bubble-eddy interactions. As for gas-liquid-solid three-phase flows in slurry bubble column reactors, the relative velocity fluctuations between the eddies and smaller particles (compared with the bubble size) may be also strong, which will give rise to the modulation on the turbulent eddy viscosity in SGS model. This interaction has been rarely addressed in the work of Euler/Euler LES simulation. This chapter will attempt to investigate the effect of inclusion of SGS bubble-eddy and particle-eddy interactions in turbulent eddy viscosity model on gas-solid-liquid three-phase

flows in slurry bubble columns. The modified SGS eddy viscosity model, which considers bubble and solid particle dynamic response to SGS turbulent eddies through introduction of the Stokes numbers for bubble and solid particles, is proposed. With consideration of the bubble and solid particle responses to the eddies, Eulerian-Eulerian LES of gas-liquid-solid three-phase flow in a slurry column is conducted. Based on the comparison of the simulation results using the modified SGS model with those using the standard SGS model without the modification, also with the literature reported experimental data, the hydrodynamics and bubble dynamics can be better predicted by using the modified SGS model. The use of the modified SGS eddy viscosity model in Euler/Euler LES for gas-liquid-solid three phase flow in bubble column was found to be able to deliver a better performance in predicting the shear turbulence in the near wall region, especially for the gas hold-up gradient and liquid shear strain rate. The typical -5/3 Kolmogorov and -3 scaling laws for bubbly column bubbly flows can be still identified in the turbulent kinetic energy spectrum obtained for gas-liquid-solid particle three-phase slurry flow in bubble columns but the turbulent kinetic energy corresponding to the higher wave number region was found to be enhanced due to the modulation caused by particle-eddy interactions. This finding further demonstrates the necessity of considering the SGS relative velocity fluctuations in the modified Smagorinsky's SGS model in Euler/Euler LES modelling.

1. INTRODUCTION

Slurry bubble column reactors (SBCR), comparing with the traditional tubular fixed-bed reactors, have the following advantages: (1) Good heat and mass transfer performance, which can be operated under almost isothermal condition; (2) Small size catalyst particles that can be added, which yields high production rate; (3) Relative low pressure drop in the bubble column; (4) Simple structure and low operating costs. Because of the above-mentioned advantages, slurry bubble column reactors have been widely used in the coal chemical, petrochemical, pharmaceutical and environmental industries. Despite the structure simplicity of the SBCRs, multiphase hydrodynamics in such reactors remains intricate, involving dynamic mesoscale or coherent structures such as large-scale circulation, bubble-scale oscillations, bubble-induced turbulence and particle-induced turbulence together with their dynamic responses to the induced liquid flow in the SBCR (Chen et al., 1994; Li et al., 2013; Yano et al., 1999; Roghair et al., 2013; An et al., 2020). In the presence of solid particles, bubble dynamics and gas-liquid flow characteristics would become more difficult for numerical simulation (Kara et al., 1982; Hölzer and Sommerfeld, 2008; Mokhtari and Chaouki, 2021). The accurate modelling of the hydrodynamics of slurry liquid phase and bubble behaviours in slurry bubble column reactors remains highly challengeable.

The flow characteristics of the gas-liquid-solid three-phase flow in the SBCRs were also experimentally investigated in previous studies, it has been found from the experiments that the gas hold-up decreases with increasing particle concentration after the introduction of solid particles (An et al., 2020, Li and Prakash, 1997). Sada

et al (1984) have indicated that the hydrodynamic behaviour in a SBCR at solid phase particle concentrations less than 5 vol.% is essentially the same as that of a gas-liquid two-phase flow in a bubble column in the absence of particles. Kato et al. (1973) and Rabha et al. (2013a, 2013b) suggested based on their experiment that the particle concentration has a greater influence on the overall gas hold-up and bubble size distribution. With the addition of solid phase particles, the state of the rising bubbles would change accordingly. Prakash et al. (2019, 2020) and Li & Prakash (1997) concluded that when the particle concentration increases, the viscosity of the slurry phase increases accompanying by increase in the bubble size. Krishna et al. (1997) studied the effect of particle concentration on the respective gas hold-up for cases of large and small bubbles and revealed that as the particle concentration increases, the gas hold-up of large bubbles increases while decreasing for small bubbles. Prakah et al. (2020) also found that the rise velocities of large bubbles increase and those of small bubbles decrease as the particle concentration increases. Gandhi et al. (1999) studied the hydrodynamics of gas-liquid-solid flow in the SBCR and they found that when the apparent gas velocity is relatively low, the effect of particle concentration on the gas hold-up is actually small, which corresponds to the flow to be either in homogeneous or in transition states. They believed that the solid concentration might play a significant role when the apparent gas velocity is relatively high, in particular for the flow to be in the Churn-turbulent state. They thus proposed that the higher the particle concentration, the weaker the settling tendency of the particles.

Existence of solid particles in gas-liquid-solid three-phase flow also have a significant effect on the formation of turbulence in the liquid carrier phase, though such effect is not yet understood and remains an open subject for further study (Zhang et al., 2021). The majority of researchers have believed that the large particles may exacerbate liquid carrier-phase turbulence, whereas small particles may dampen the liquid carrier phase turbulence (Tanaka and Eaton, 2010). Troshko and Zdravistch (2009) adopted the attenuated turbulent dissipation rate to compute the average turbulent kinetic energy of turbulent eddies in a breakage efficiency model. This Chapter will attempt to use a rational step-by-step approach for analysing the solid particle effects and to develop a modified Smagorinsky's SGS model for Euler/Euler LES of gas-liquid-solid three-phase slurry bubble column flows. As the effect of the attenuation on the size distribution of bubbles caused by the solid particles is still unclear, this Chapter would focus on and consider the particle effect in the proposed SGS eddy viscosity model. By implementing the proposed modified SGS eddy viscosity model into the LES simulation, the gas hold-up, velocity profiles, shear strain rate distribution at different distance from the wall and the liquid phase turbulent kinetic energy spectrum at given position will be evaluated by comparing the simulation results with the experimental data reported in the literature. The mathematical modelling used in present work and numerical simulation set-up are presented in Section 2. Section 3 will give the predicted results from Euler/Euler LES modeling using the modified SGS eddy viscosity model with and without the modification together with the discussion on these results. The main conclusions as the output from this Chapter are summarized in Section 4.

2. MATHEMATICAL MODELLING AND NUMERICAL METHODS

2.1 Mathematical modelling

The Eulerian-Eulerian two-fluid model is used in which slurry phase is regarded as continuous phase and gas phase is treated as dispersed phase. The slurry phase is represented as a pseudo-homogeneous phase made up of liquid and solid particles. This model offers the advantage of lower processing costs and adequate simulation resolutions comparing to DNS or Eulerian-Lagrangian approaches. In this Eulerian-Eulerian LES model, each parameter φ is characterised as the combination of the part $\tilde{\varphi}$ that needs to be resolved during the filtering process and the unresolved part φ' that needs to be modelled by using the SGS model for closure. For convenience, the tilde symbol "~" will be dropped hereafter. Since most of the equations related to momentum transfer among the bubble column are highlighted in detail in Chapter 2 to 5, the equations will not be repeated and summarized in Table 6-1.

Table 6- 1 Mathematical models used in this chapter

Governing equations	
$\frac{\partial}{\partial t}(\alpha_k \rho_k) + \nabla \cdot (\alpha_k \rho_k \boldsymbol{u}_k) = \dot{m}_k$	(6-1)
$\frac{\partial}{\partial t}(\alpha_k \rho_k \boldsymbol{u}_k) + \nabla \cdot (\alpha_k \rho_k \boldsymbol{u}_k \boldsymbol{u}_k) = -\alpha_k \nabla p_k - \nabla \cdot (\alpha_k \rho_k \tau_k) + \alpha_k \rho_k \boldsymbol{g} + \boldsymbol{M}_k$	(6-2)
$\tau_k = -\mu_{eff}\left(\nabla \boldsymbol{u}_k + (\nabla \mathbf{u}_\mathrm{k})^T - \frac{2}{3} I(\nabla \cdot \boldsymbol{u}_k)\right)$	(6-3)

$$\mu_{eff} = \mu_{L,L} + \mu_{T,L} + \mu_{BI,L}. \quad (6\text{-}4)$$

$$\mu_{BI,L} = \rho_L C_{\mu,BI} \alpha_G d_B |\boldsymbol{u}_G - \boldsymbol{u}_L|. \quad (6\text{-}5)$$

Force models

$$\boldsymbol{M}_{D,L} = \frac{3}{4}\alpha_G \rho_L \frac{C_D}{d_B} |\boldsymbol{u}_G - \boldsymbol{u_L}|(\boldsymbol{u}_G - \boldsymbol{u_L}) \quad (6\text{-}6)$$

$$\mathrm{C_D} = max\left(\frac{24}{Re_B}(1 + 0.15 \cdot Re_B^{0.687}), 0.44\right) \quad (6\text{-}7)$$

$$\boldsymbol{M}_{L,L} = \rho_L C_L (\boldsymbol{u}_B - \boldsymbol{u}_L) \times (\nabla \times \boldsymbol{u}_L) \quad (6\text{-}8)$$

$$C_L = \begin{cases} min[0.288tanh(0.121Re_B), f(E_O')\,] & E_O' \le 4 \\ f(E_O') & 4 < E_O' < 10 \\ -0.29 & E_O' > 10 \end{cases} \quad (6\text{-}9)$$

$$\boldsymbol{M}_{AM,L} = \alpha_G \rho_L C_{AM} \left(\frac{D\boldsymbol{u}_G}{Dt} - \frac{D\boldsymbol{u}_L}{Dt}\right) \quad (6\text{-}10)$$

$$\boldsymbol{M}_{TD,L} = C_{TD} \frac{3\alpha_G}{4} \frac{\rho_L}{d_B} (\boldsymbol{u_L} - \boldsymbol{u_G}) \frac{\nu_t}{\sigma_{TD}} \left(\frac{\nabla \alpha_L}{\alpha_L} - \frac{\nabla \alpha_G}{\alpha_G}\right) \quad (6\text{-}11)$$

A slurry phase was used in this simulation to represent the mixing of liquid and solid. In order to determine whether the mixture could be simplified to a pseudo-homogeneous phase before running the simulation, a criterion was proposed by Koide et al. (1983) to determine whether particles could be totally suspended under the operating conditions. They discovered that as gas velocity rose under constant solid loading, particles were steadily fluidized and the reactor pressure difference would gradually reached maximum and kept unchanged. At a maximum solid loading of 10%, the superficial velocity (0.01 m/s) used in this chapter is higher than the critical limit of 0.063 m/s. Consequently, the slurry phase of the mixture of

liquid and solid can be assumed. The corresponding formulas related to above calculation are listed in Table 6-2. According to the literatures on the correlations of slurry density and viscosity based on Einstein equation (Tsuchiya et al., 1997, Einstein, 1906, Prakash and Majumder, 2020), the related physical properties of different particle loading used in this work are shown in Table 6-2.

Table 6- 2 Physical properties of the slurry phase

Solid volume fraction (α_S)	Density [kg m^{-3}]	Viscosity [mPa s]
0	998.2	1
10	1138.4	1.21

Calculation process- Critical velocity

$$\frac{\mathrm{U_{critical}}}{U_\infty} = 0.801\left(\frac{\rho_s-\rho_l}{\rho_l}\right)^{0.6} C_s^{0.146}\left(\frac{\sqrt{dg}}{U_\infty}\right)^{0.24}\left(1+807\left(\frac{g\mu^4}{\rho_l\sigma^3}\right)^{0.578}\right)\left(1 - 1.2\left(1-\frac{d_t}{d_R}\right)\text{^}0.0301\left(\frac{d^2 g\rho_l}{\sigma}\right)^{0.559}\right)$$

$$U_\infty = \frac{gd^2(\rho_s-\rho_l)}{18\mu}$$

Calculation process- slurry density and viscosity

$$\rho_{\mathrm{slurry}} = \rho_l(1-C_s)+\rho_s C_s$$

$$\mu_{\mathrm{slurry}} = \mu_l exp\left(\frac{KC_s}{1-\frac{C_s}{C_{sc}}}\right)$$

$$\mathrm{K} = \{2.9 - 1.6tanh[0.3(9-10^2U_\infty)]\}/\emptyset$$

$$\mathrm{C_{sc}} = \{1.3 - 0.1tanh[0.5(10-10^2U_\infty)]\}\mathrm{C_{s0}}$$

The slurry viscosity correlation was proved to be applicable for a wide range of solid holdup (d_B > 5 mm). ∅ is the particle sphericity and C_{s0} is the solid holdup at incipient fluidization state, and model parameters K is 1.581 and C_{sc} is 0.6 in this chapter.

Based on the aforementioned improvements in the prediction of hydrodynamics and mass transfer using the modified SGS turbulent eddy viscosity in Euler/Euler LES reported in Chapter 2, where the turbulent shear eddy viscosity has included the modification of bubble-eddy dynamic response in gas-liquid two-phase flow in bubble columns, the shear turbulent eddy viscosity due to SGS relative velocity fluctuation was proposed (Long et al., 2020), given by

$$\nu_{t,SGS} = (C_s \Delta)^2 \mid S \mid \left[1 + C_b \overline{\alpha}_G \frac{\Delta}{d_B} \left(\frac{1}{1 + St_{SGS}} \right)^{3/2} \right]. \quad (6\text{-}12)$$

Following the modelling approach used to derive Equation 6-12, the dynamic response of particles to the surrounding turbulent eddies can be also considered by introducing sub-grid scale particle phase Stokes numbers in the shear turbulence eddy viscosity for the modified Smagorinsky's SGS model. The SGS eddy viscosity model of liquid-phase turbulence in which considers the joint modulation from liquid turbulence scale and solid concentration effects can be thus written as

$$\nu_{t,SGS} = (C_s \Delta)^2 \mid S \mid \left[1 + C_b \alpha_G \frac{\Delta}{d_B} \left(\frac{1}{1 + St_{B,SGS}} \right)^{3/2} + C_p \alpha_S \frac{\Delta}{d_P} \left(\frac{1}{1 + St_{P,SGS}} \right)^{3/2} \right] \quad (6\text{-}13)$$

where *Cs* is the Smagorinsky constant and *S* represents the characteristic resolved strain rate tensor, the bubble response time scale is calculated as $\tau_{\text{bubble}} = \frac{4(\rho_G + 0.5\rho_L) d_B^2}{3\mu_L C_D Re_B}$, Bubble Reynolds number $Re_{B,max} = \frac{\rho_L d_B u_{slip}}{\mu_L} \approx 2250.9$ in this chapter. the SGS turbulent eddy turn over time can be estimated by $\tau_{L,SGS} = \Delta / \boldsymbol{u}'_{\text{L,SGS}}$. α_S is the particle bulk solid volume fraction, the particle SGS stokes

number $St_{P,SGS}$ is given by $\frac{\rho_p d_p^2}{18\rho_L \nu \tau_{L,SGS}}$. Δ is the filter scale in the large eddy simulation.

2.2 Numerical simulation

The modified LES SGS model proposed in the present study was validated by comparing with the experimental data carried out by Tyagi and Buwa (2017). A quasi-2D SBCR (X 0.2m× Y 0.04m× Z 1.4m) was employed which used a three-phase system of air, water, and glass beads (ρ= 2400 kg/m^3, d_s = 250 μm) as benchmarks for our simulation. The gas was sparged via 50 holes perforated plate with 1mm inner diameter, the gas inlet is simplified as a rectangular inlet located at the bottom of the reactor. In the current investigation, Euler/Euler LES modeling was carried out using ANSYS CFX 18.0 and the boundary conditions listed below. The inlet condition of gas superficial velocity of 0.1 m/s was used which is same with the experimental set-up, and the volume fractions for each phase were defined as: α_{slurry}=0, α_G=1. Relative pressure was specified to be zero at the reactor's top surface by means of a pressure-constant boundary. The bubble column's wall was set with a non-slip condition. Convective and diffusive terms in the momentum equations were discretized using a central-differencing discretization scheme; transient terms were discretized using a second-order backward Euler scheme. According to the PDF of the bubble size distribution reported by Tyagi and Buwa (2017) and An et al. (2020), an equivalent bubble diameter of 12 mm was used in the simulation. The simulation domain was partitioned with the computational grids of $d_B/\Delta \approx$

0.8 in the central region of the bubble columns with a growth rate of 1.2 from the walls, which satisfy the constraints suggested by Milelli's criterion ($0.66<d_B/\Delta<0.833$) for bubbly flows using Euler/Euler two-fluid LES modelling.

3. RESULTS AND DISCUSSION

The gas-liquid-solid three-phase flow in bubble column was simulated using a constant time step size of 0.001 s, which is smaller than the time scale corresponding to the eddies that have Taylor integral length scale. Due to the transient nature of the turbulent flow in the bubble column, the simulation was run for 80 seconds and the data used for statistics were collected for the final 40 seconds when the flow in the SBCR was found to be steady. The following sub-sections present the simulation results and findings together with brief discussion.

3.1 Effect of the proposed SGS model on hydrodynamics and bubble dynamics

Figure 6-1 presents the instantaneous liquid velocity vectors at different time step. At t=1.5s, it can be seen that the injected bubble is rising up in the bubble column. At t=2s, the bubble reaches the upper liquid surface, and a large-scale circulation can be found with the liquid phase descending in the near-wall region. After t=2.4s, a number of large eddies starts to oscillate throughout the bubble column with the time developing. The transient behaviour of the liquid phase can be clearly captured by using the modified LES eddy viscosity model.

Figure 6-2 shows the time averaged radial distributions of gas hold-up. The time-averaged gas hold-up is obtained by using the following expression:

$$\alpha_{Gcross}(H) = \frac{1}{\pi R^2}\int_0^R \left(\frac{1}{T_1 - T_0}\int_{T_0}^{T_1} \alpha_G(r, H, t)dt\right) 2\pi r dr \qquad (6\text{-}14)$$

where T_0 and T_1 are the beginning and end time for sampling. The predicted time-averaged gas hold-up by using the standard and modified SGS eddy viscosity model are compared with the experimental data reported by Tyagi and Buwa (2017), and the CFD-PBM simulation (k-ε model) reported by An et al. (2020). For the solid-free system, the gas hold-up profile predicted by using both the standard and modified SGS model shows a good agreement with the experimental data, as shown in Figure 6-2(a). A slightly better consistency was found by using the modified SGS model. It is interesting to note that the trends of the predicted gas hold-up using the standard LES model and that of An et al. look similar but An's et al result has apparently overestimated the gas hold-up radial distribution. They have attributed the overestimation in gas hold-up profile to the inappropriate modelling of bubble-induced turbulence in their work. With increase in the solid particle volume fraction, their results become even worse as can be seen from Figure 6-2(b). With the presence of solid particles, our LES simulation results (using the modified SGS model) show consistent with the gas hold-up profile based on the experimental data. As can be seen from Figure 6-2(b), the predicted gas hold-up profile obtained by using the modified SGS model may give a better estimation for the gradient of local gas hold-up in the region between X=0.05 and X=0.1, which will lead to a better

estimation of turbulent dispersion force, contributing to a better prediction of gas hold-up profile. This implies that consideration of the particle-eddy interactions in the SGS turbulent eddy viscosity will increase the predicted shear stresses in the near wall region of bubble column so that the overestimation of the gas hold-up can be avoided.

The time-averaged bubble and liquid axial velocities are predicted, as shown in figure 6-3 and 6-4. It can be observed that, the difference in the predicted profile by using the standard SGS model at both $\alpha_S = 0$ and $\alpha_S = 0$ can be hardly distinguished. For the bubbly flow system, a decrease in the central region and increase in the near-wall region is observed in the profile predicted by the modified SGS model (green line) compared with the one without modification. While in the particle-laden system, a further reduction is found accompanied by a more flatten curve near the wall. This further indicates that the additional eddy viscosity term in Equation 6-13 related to the particle-eddy interaction cannot be neglected and it can modulate the 'two-way coupling behaviour' between phases, consequently giving rise to a better estimation of the void fraction gradient and a better prediction of the dispersed phase's lateral migrations.

3.2 Qualification of the modified SGS model's effect on shear strain rate

After comparing the gas hold-up and bubble and liquid phase velocity profiles with the standard model, it is observed that the modified SGS model can have a better estimation of the dispersed phase's lateral migration. In order to further validate this observation, the shear strain rate at three different location along the X-axis are

compared and shown in Figure 6-5. Three points are located in the centre of the bubble column (Point 1: X=0 m), the central region (Point 2: X=0.06 m) and the vicinity of the wall (Point 3: X=0.09 m), respectively. In both bubbly flow and gas-liquid-solid three phase flow, an overall increase in the liquid shear strain rate is observed with the use of the modified SGS model. Gandhi et al. (1999) investigated the radial distribution of the solid volume fraction at various solid loadings and claimed that increasing the solid volume fraction results in an increase in the solid volume fraction at the near wall region. Due to the rapid rise of big bubbles in the column center, more solid particles accumulate towards the column walls. When the attention is restricted to point 3, a noticeable difference between the case$\alpha_S = 0\%$ and $\alpha_S = 10\%$ is found. This may attribute to the small diameter particles are more likely transferred to the wall, the relative motions between particles and surrounding eddies are strong due to the high concentration of the particles in the near-wall region, thus the real condition can be well reflected.

3.3 Investigation of power spectra of solid concentration fluctuation and liquid velocity fluctuation

To determine how the turbulent fluctuations in the bubble column are affected by the presence of solid particles, the effect of α_S and the inclusion of the particle-eddy dynamic responses on the power spectra of the gas hold-up fluctuations are shown in Figure 6-6. According to the previous experimental work of the measurement of local α'_G, the flow can be characterized as the combination of meandering bubble plume with the low frequency α'_G (0-1 Hz) and the bubble swarm with high

frequency α'_G (1-10 Hz) (Tyagi and Buwa, 2017, Mudde and Simonin, 1999, Vial et al., 2000). With an increase in α_S from 0 to 20% vol. fraction, it was discovered by Tyagi and Buwa that the frequency of local α'_G produced by bubble swarms increased as α_S increased, whereas the frequency caused by meandering plume motion decreased (i.e., column-scale oscillations) as α_S increased due to the formation of large bubbles/slugs as a result of the addition of solid particles. In Figure 6-6 (a) and (b), the coexistence of the low frequency meandering bubble plume and the high frequency bubble swarm oscillations are found in the simulation using standard SGS model, without noticeable differences. With the increase of α_S, the decrease in low frequency motion shifting to an increase in the higher frequency motions is found by using the modified SGS model, corroborating the finding of Tyagi and Buwa (2017). With the inclusion of the additional eddy viscosity considering the particle-eddy interactions, grid scale oscillation can be well captured, further supporting the importance of these two terms in the LES modelling of bubble column three-phase flow.

In order to assess the impact of inclusion of the modified SGS model on the calculation of the turbulent kinetic energy of the liquid phase, the one-dimensional LES-filtered turbulent kinetic energy power spectral densities (PSD) $E_{11}(\kappa)$ obtained for $\alpha_S = 10\%$ are presented in Figure 6-7. It can be seen that the use of the modified SGS models gives a -5/3 scaling in smaller wave number zone while presents a -3 scaling law measured based on the wave number κ_1 larger than the typical wave

number characterized by the equivalent bubble size, i.e. $\kappa_B = \frac{2\pi}{d_B} \approx 502.65\ m^{-1}$. It can be seen from Figure 6-7 that the transition for different scaling laws in $E_{11}(\kappa)$ takes place in the wave number at about $\kappa_1 \approx 450\ m^{-1}$, where the left of the transition location shows the -5/3 slope while the right side of the transition give rise to the -3 scaling, clearly indicating the feature of feeding of bubble induced turbulence to the turbulent kinetic energy. However, the turning point of the one using standard SGS model approximately appears at a higher value away from κ_B. In addition, a rise in the slope of $E_{11}(\kappa)$ is found at $\kappa_C \approx 1200\ m^{-1}$ when using the modified SGS model. The following phenomenological picture can be used to qualitatively explain these observations. Large eddy structures in gas-liquid-solid three phase flow have less energy than they do in bubbly flow, because they are disturbed by the finite-size particles that drag the surrounding fluid in their direction. Simultaneously, particles induced new eddies in their downstream path, increasing their frequency in the flow and thus increasing the energy of the high wave numbers. The similar findings can be also found in the recent literatures (Sayed et al., 2022, Gupta et al., 2018). Thus it can be revealed that the relative motion of the particle and surrounding eddies can be highlighted by using the proposed SGS model and its importance on modulating the liquid phase turbulence cannot be neglected.

4. CONCLUSIONS

Eulerian-Eulerian LES simulations of gas-liquid-solid three-phase flow at $\alpha_S = 0$ and 10% in a bubble column have been conducted. The simulations have taken into

account the effects of local solid particle loading, bubble volume fraction and bubble and solid particle dynamic responses to the surrounding eddies in the modified Smagorinsky's SGS model as reflected in the turbulent SGS eddy viscosity. It has been demonstrated that the implementation of the proposed modified SGS turbulent eddy viscosity in Euler/Euler LES effectively catches up the modified contributions from eddy solid particle interaction and bubble-eddy interaction to the liquid-phase shear turbulence as indicated by the predicted turbulent kinetic energy spectrum and predicted gas hold-up and liquid velocity profiles for gas-liquid-solid particle three-phase slurry flow in a bubble column. The main concluding remarks are summarized as follows:

1) The hydrodynamics and bubble dynamics, i.e., transient behaviours, gas hold-up profile, bubble and liquid velocities distribution can be well predicted by using the LES SGS model with the modified SGS eddy viscosity model. The simulation results obtained by using the modified Smagorinsky's SGS model were found to be better consist with the experimental data available from the literature. The inclusion of bubble-eddy interaction and particle-eddy interaction in the SGS turbulent eddy viscosity for gas-liquid-particle slurry three-phase flow can improve the estimation of shear turbulence viscosity in Euler/Euler LES.

2) The time-averaged liquid phase shear strain rate obtained at X=0, 0.06 and 0.09m was obtained by employing the standard and modified SGS model. It was found that a noticeable increase in the predicted shear strain rate in the vicinity of the wall by using the modified SGS model comparing with that by using the standard SGS

model. This indicates that the modified SGS model can effectively capture the particle response to SGS turbulent fluctuations, highlighting the importance of consideration of the particle-eddy dynamic response in the shear turbulent eddy viscosity estimation in LES.

3) The local α'_G power spectral density predicted by using the modified SGS model shows a significant enhancement in high frequency scale, which demonstrates that sub-grid scale bubble and particles oscillations were successfully considered. The turbulent kinetic energy spectrum obtained from the present LES modelling still presents a typical -5/3 scaling and -3 scaling laws while the transition position in the slope was found to be close to the estimated representative bubble wavenumber, which demonstrates the good estimation of sub-grid scale turbulent eddy motion which mainly takes place in the wavelength close to the bubble size by using the modified SGS eddy viscosity model. An increased turbulent kinetic energy at high wave number corresponding to the particle size scale was also identified, indicating that the proposed modified SGS turbulent eddy viscosity model plays a key role in modulating the liquid phase turbulence and the relative velocity fluctuations due to the solid particle response to the surrounding SGS eddies cannot be overlooked.

REFERENCES

AN, M., GUAN, X. & YANG, N. 2020. Modeling the effects of solid particles in CFD-PBM simulation of slurry bubble columns. *Chemical Engineering Science,* 223**,** 115743.

CHEN, R., REESE, J. & FAN, L. S. 1994. Flow structure in a three-dimensional bubble column and three-phase fluidized bed. *AIChE Journal,* 40**,** 1093-1104.

EINSTEIN, A. 1906. A new determination of molecular dimensions. *Annuals of Physics,* 19**,** 289-306.

GANDHI, B., PRAKASH, A. & BERGOUGNOU, M. 1999. Hydrodynamic behavior of slurry bubble column at high solids concentrations. *Powder Technology,* 103**,** 80-94.

GUPTA, A., CLERCX, H. & TOSCHI, F. 2018. Effect of particle shape on fluid statistics and particle dynamics in turbulent pipe flow. *The European Physical Journal E,* 41**,** 1-15.

HÖLZER, A. & SOMMERFELD, M. 2008. New simple correlation formula for the drag coefficient of non-spherical particles. *Powder Technology,* 184**,** 361-365.

KARA, S., KELKAR, B. G., SHAH, Y. T. & CARR, N. L. 1982. Hydrodynamics and axial mixing in a three-phase bubble column. *Industrial & Engineering Chemistry Process Design and Development,* 21**,** 584-594.

KATO, Y., A, N., KAGO, T., FUKUDA, T. & TANAKA, S. 1973. Gas holdup and over-all volumetric absorption-coefficient in bubble columns with

suspended solid particles-absorption rate of oxygen by an aqueous-solution of sodium sulfite. *International Chemical Engineering,* 13**,** 562-567.

KOIDE, K., TAKAZAWA, A., KOMURA, M. & MATSUNAGA, H. 1984. Gas holdup and volumetric liquid-phase mass transfer coefficient in solid-suspended bubble columns. *Journal of Chemical Engineering of Japan,* 17**,** 459-466.

KOIDE, K., YASUDA, T., IWAMOTO, S. & FUKUDA, E. 1983. Critical gas velocity required for complete suspension of solid particles in solid-suspended bubble columns. *Journal of Chemical Engineering of Japan,* 16**,** 7-12.

KRISHNA, R., DE SWART, J. W., ELLENBERGER, J., MARTINA, G. B. & MARETTO, C. 1997. Gas holdup in slurry bubble columns: effect of column diameter and slurry concentrations. *AIChE Journal,* 43**,** 311-316.

LI, H. & PRAKASH, A. 1997. Heat transfer and hydrodynamics in a three-phase slurry bubble column. *Industrial & Engineering Chemistry Research,* 36**,** 4688-4694.

LI, W.-L., ZHONG, W.-Q., JIN, B.-S., XIAO, R. & HE, T.-T. 2013. Flow regime identification in a three-phase bubble column based on statistical, Hurst, Hilbert–Huang transform and Shannon entropy analysis. *Chemical Engineering Science,* 102**,** 474-485.

LONG, S., YANG, J., HUANG, X., LI, G., SHI, W., SOMMERFELD, M. & YANG, X. 2020. Large-eddy simulation of gas–liquid two-phase flow in a bubble column reactor using a modified sub-grid scale model with the

consideration of bubble-eddy interaction. *International Journal of Heat and Mass Transfer,* 161**,** 120240.

LUO, X., LEE, D., LAU, R., YANG, G. & FAN, L. S. 1999. Maximum stable bubble size and gas holdup in high‐pressure slurry bubble columns. *AIChE Journal,* 45**,** 665-680.

MOKHTARI, M. & CHAOUKI, J. 2021. Effect of solid loading and particle size on the phase holdup distribution and bubble behaviour in a pilot-scale slurry bubble column. *Chemical Engineering Science,* 243**,** 116732.

MUDDE, R. F. & SIMONIN, O. 1999. Two-and three-dimensional simulations of a bubble plume using a two-fluid model. *Chemical Engineering Science,* 54**,** 5061-5069.

PRAKASH, A., MARGARITIS, A., LI, H. & BERGOUGNOU, M. 2001. Hydrodynamics and local heat transfer measurements in a bubble column with suspension of yeast. *Biochemical Engineering Journal,* 9**,** 155-163.

PRAKASH, R., MAJUMDER, S.K., SINGH, A., 2019. Particle-laden bubble size and its distribution in microstructured bubbling bed in the presence and absence of a surface active agent. *Ind. Eng. Chem. Res*. 58 (8), 3499–3522.

PRAKASH, R. & MAJUMDER, S. K. 2020. Effect of particle size and concentration on bubble size distribution and aspect ratio in a counter-current microstructured bubble column. *Journal of Industrial and Engineering Chemistry,* 90**,** 105-116.

RABHA, S., SCHUBERT, M., HAMPEL, U., 2013a. Intrinsic flow behavior in a slurry bubble column: a study on the effect of particle size. *Chemical Engineering Science.* 93, 401–411.

RABHA, S., SCHUBERT, M., WAGNER, M., LUCAS, D., HAMPEL, U., 2013b. Bubble size and radial gas hold-up distributions in a slurry bubble column using ultrafast electron beam X-ray tomography. *AIChE Journal*. 59 (5), 1709–1722.

ROGHAIR, I., BALTUSSEN, M., ANNALAND, M. V. S. & KUIPERS, J. 2013. Direct numerical simulations of the drag force of bi-disperse bubble swarms. *Chemical Engineering Science,* 95**,** 48-53.

SADA, E., KATOH, S., YOSHII, H., YAMANISHI, T. & NAKANISHI, A. 1984. Performance of the gas bubble column in molten salt systems. *Industrial & Engineering Chemistry Process Design and Development,* 23**,** 151-154.

SAYED, M. A., DEHBI, A., NICENO, B. & MIKITYUK, K. 2022. Particle subgrid scale modeling in hybrid RANS/LES of turbulent channel flow at low to moderate Reynolds number. *Powder Technology,* 397**,** 117013.

TANAKA, T. & EATON, J. K. 2010. Sub-Kolmogorov resolution partical image velocimetry measurements of particle-laden forced turbulence. *Journal of Fluid Mechanics,* 643**,** 177-206.

TROSHKO, A. A. & ZDRAVISTCH, F. 2009. CFD modeling of slurry bubble column reactors for Fisher–Tropsch synthesis. *Chemical Engineering Science,* 64**,** 892-903.

TSUCHIYA, K., FURUMOTO, A., FAN, L.-S. & ZHANG, J. 1997. Suspension viscosity and bubble rise velocity in liquid-solid fluidized beds. *Chemical Engineering Science,* 52**,** 3053-3066.

TYAGI, P. & BUWA, V. V. 2017. Dense gas–liquid–solid flow in a slurry bubble column: Measurements of dynamic characteristics, gas volume fraction and bubble size distribution. *Chemical Engineering Science,* 173**,** 346-362.

VIAL, C., CAMARASA, E., PONCIN, S., WILD, G., MIDOUX, N. & BOUILLARD, J. 2000. Study of hydrodynamic behaviour in bubble columns and external loop airlift reactors through analysis of pressure fluctuations. *Chemical Engineering Science,* 55**,** 2957-2973.

YANO, T., KURAMOTO, K., TSUTSUMI, A., OTAWARA, K. & SHIGAKI, Y. 1999. Scale-up effects in nonlinear dynamics of three-phase reactors. *Chemical Engineering Science,* 54**,** 5259-5263.

ZHANG, H., GUO, Z., WANG, Y., SHEN, X. & WANG, T. 2021. Effect of particles on hydrodynamics and mass transfer in a slurry bubble column: Correlation of experimental data. *Authorea Preprints*.

FIGURES

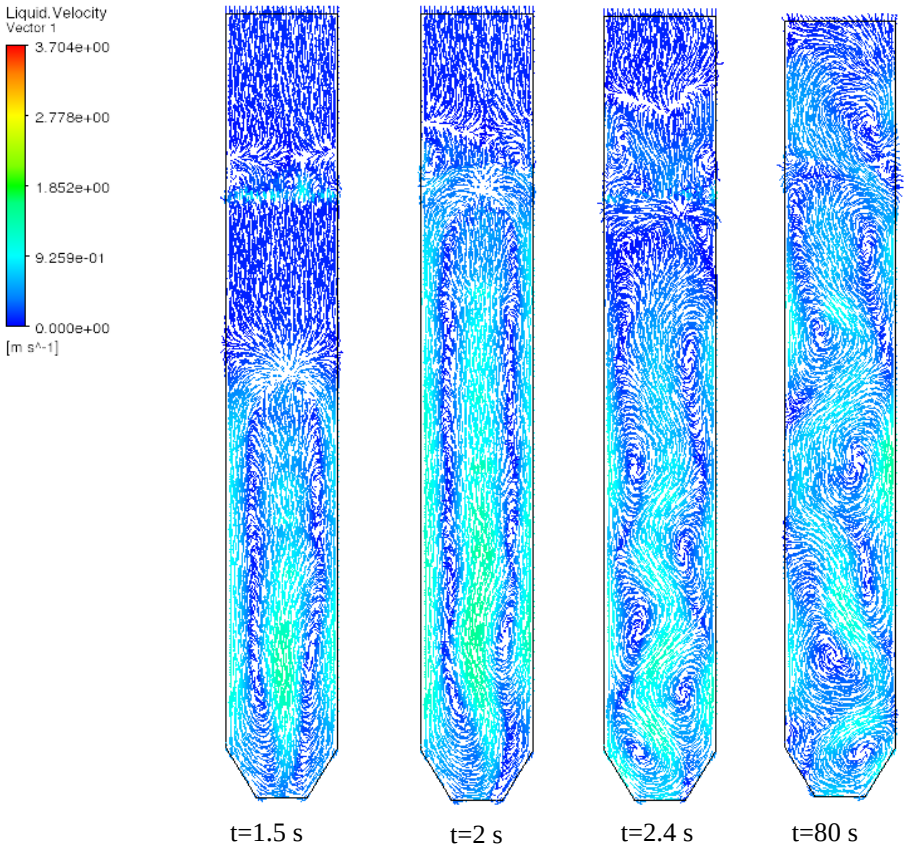

Figure 6- 1 Transient captured liquid velocity vector at XY-plane at different time step.

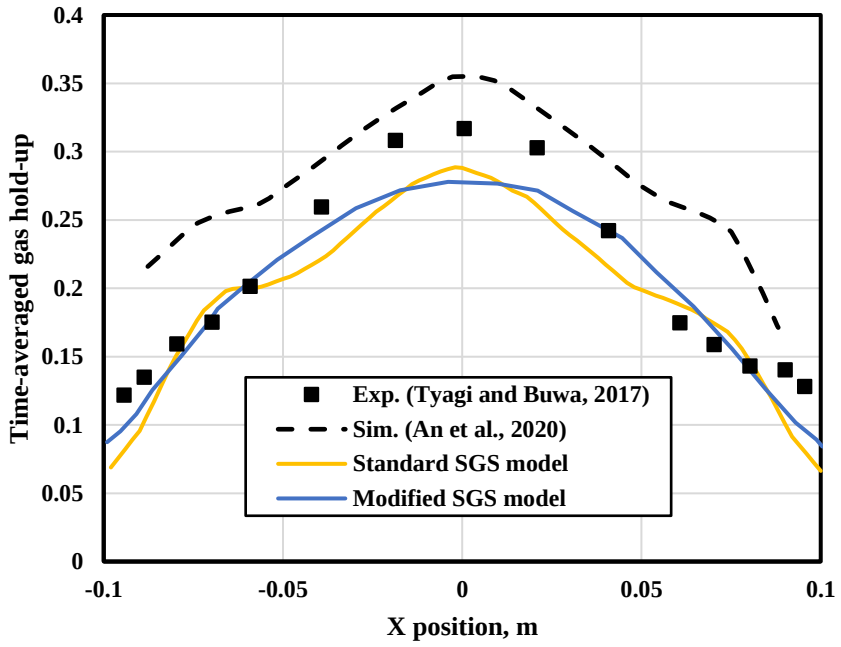

(a)

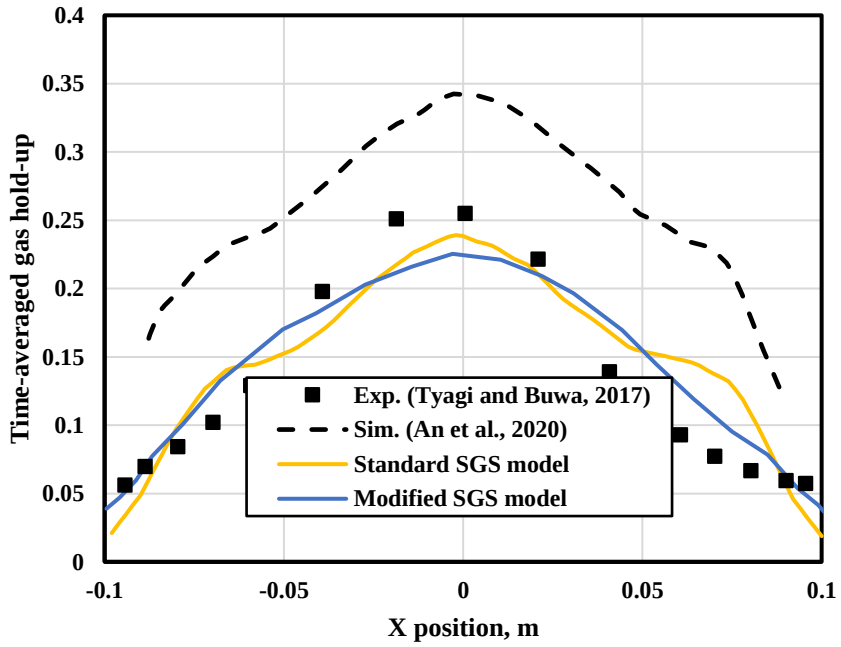

(b)

Figure 6- 2 Predicted time-averaged gas hold-up radial distribution at (a) $\boldsymbol{\alpha_S = 0}$; and (b$\boldsymbol{\alpha_S = 10}$%).

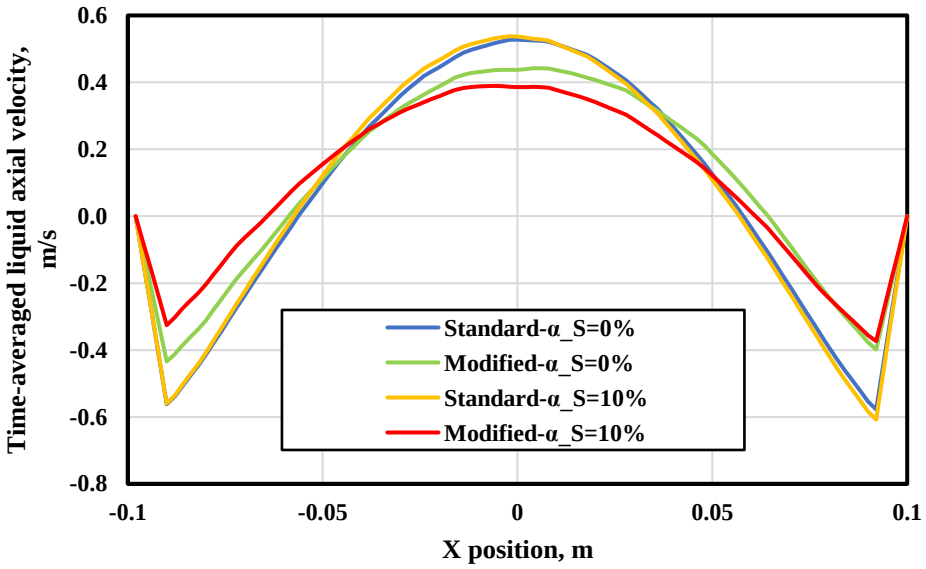

Figure 6- 3 Predicted radial distribution of the time-averaged liquid axial velocity at $\boldsymbol{\alpha_S = 0}$ and $\boldsymbol{\alpha_S = 10\%}$ by using different eddy viscosity model.

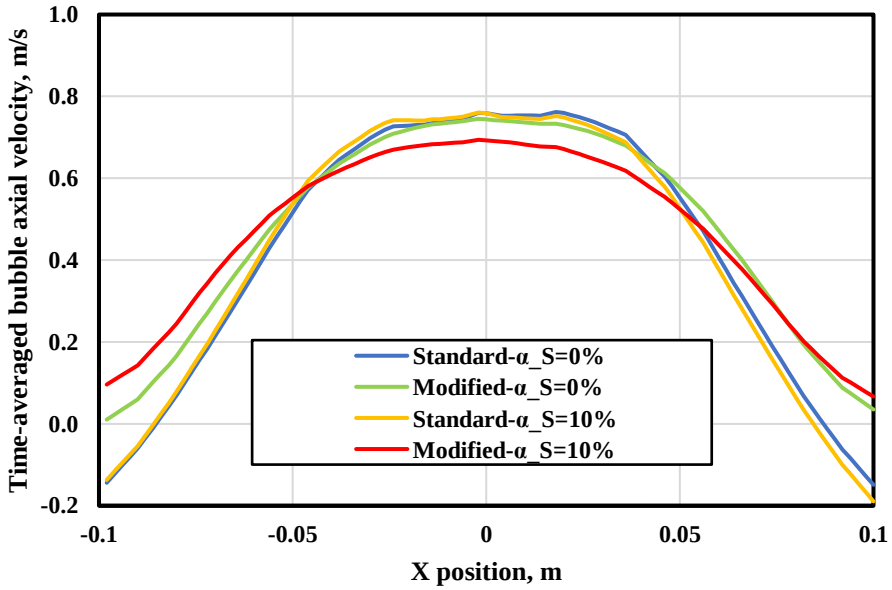

Figure 6- 4 Predicted radial distribution of the time-averaged bubble axial velocity at $\boldsymbol{\alpha_S = 0}$ and $\boldsymbol{\alpha_S = 10\%}$ by using different eddy viscosity model.

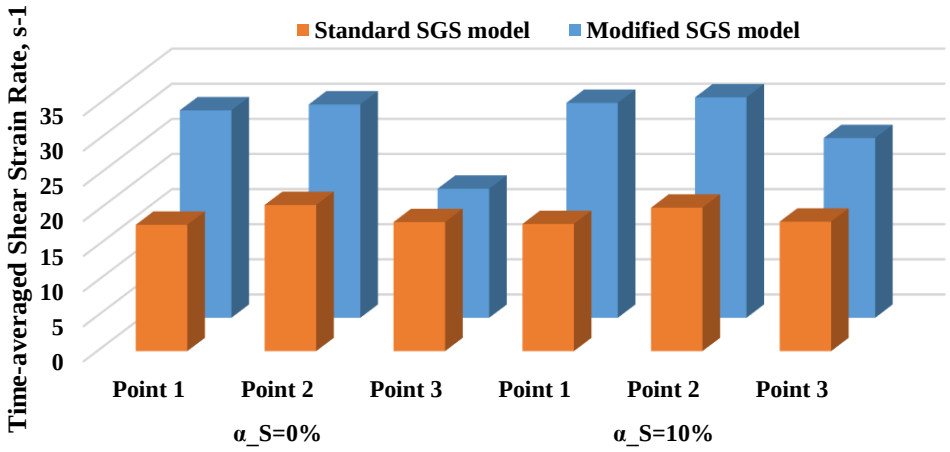

Figure 6- 5 Time-averaged liquid phase shear strain rate at $\boldsymbol{\alpha_S = 0}$ and $\boldsymbol{\alpha_S = 10}\%$ by using different eddy viscosity model. (Point 1: X=0 m; Point 2: X=0.06 m; Point 3: X=0.09 m. Y=0. Z=0.765 m)

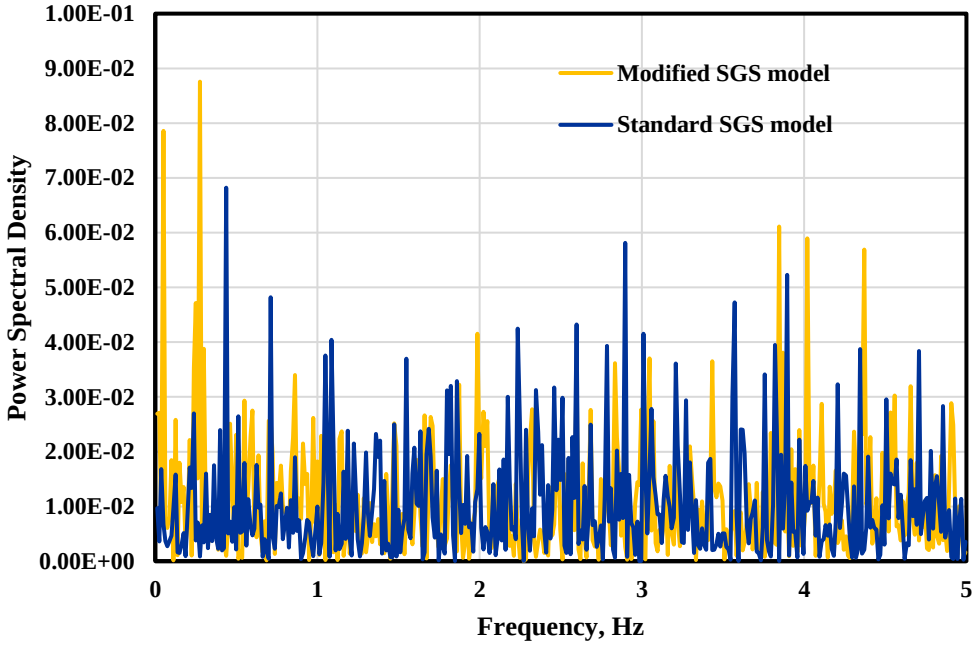

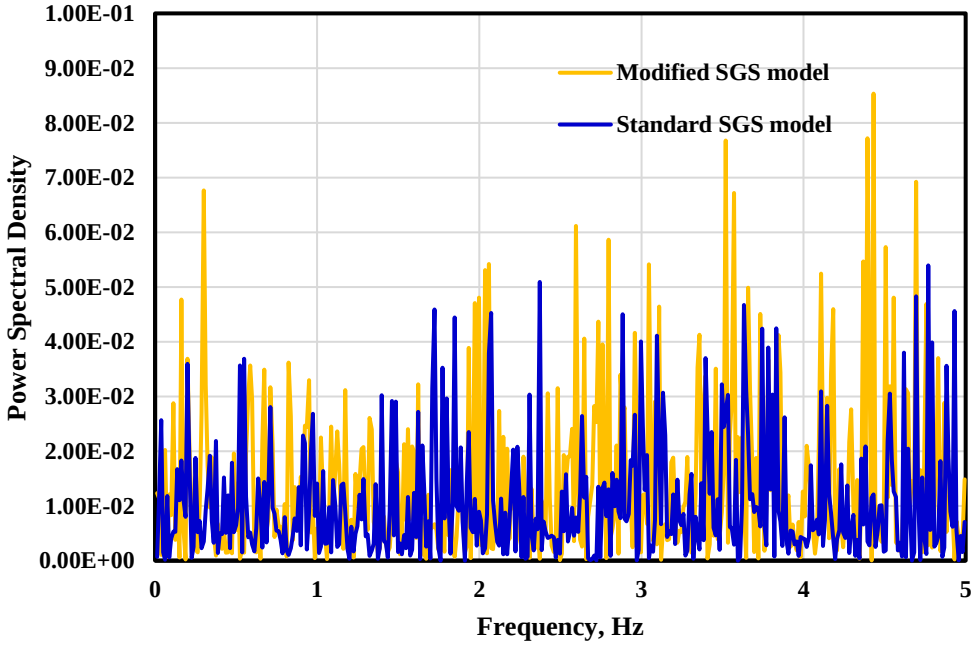

Figure 6- 6 Power spectra of gas volume fraction fluctuations by using different SGS eddy viscosity models: (a)$\alpha_S = 0$; (b)$\alpha_S = 10$ at X=0, Y=0, Z=0.765m.

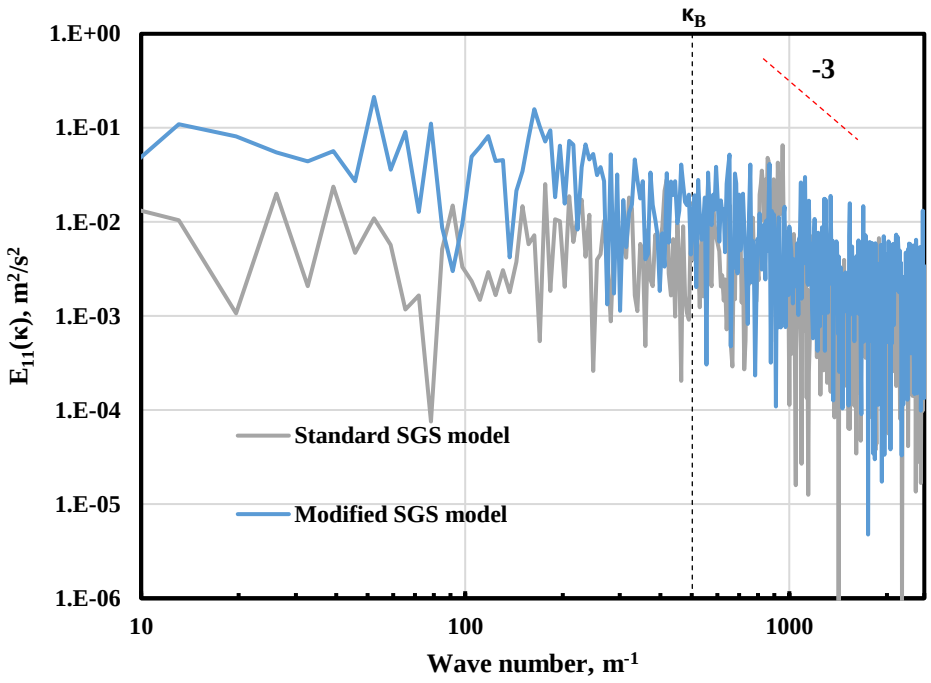

Figure 6- 7 Turbulent kinetic energy spectra of liquid axial velocity fluctuation at X=0, Y=0, Z=0.765m.

CHAPTER 7:

RECAPITULATION AND RECOMMENDATIONS

1. LARGE EDDY SIMULATION MODELLING OF BUBBLE COLUMN GAS-LIQUID TWO-PHASE BUBBLY FLOW AND GAS-SOLID-LIQUID THREE-PHASE FLOW

The aims of this PhD project are to investigate bubble column bubbly flow and bubble column three-phase flow using Euler/Euler large eddy simulation (LES) approach, focusing on LES sub-grid-scale (SGS) modelling which implements the modifications of the dynamic responses of the rising bubbles and solid particles to their surrounding turbulent eddies into the SGS models for modelling the gas-liquid two-phase and gas-solid-liquid three-phase flows in bubble column reactors. Current status of LES modelling of two or three-phase flows in bubble columns together with the corresponding experimental studies has been comprehensively reviewed in Chapter 1. As two or three phase flows in bubble column reactors involve complicated transport phenomena such as strong interactions between bubbles and turbulent eddies, solid particles modification on turbulent eddies, the couplin between the interfacial mass transfer and momentum transfer, the hydrodynamics and mass transfer involved cannot be predicted using LES with the standard Smagorinsky SGS model without considering the aforementioned couplings and modifications, especially when the interfacial force closures based

on spatial-filtering are concerned. Although several eddy viscosity models and SGS interfacial forces models have been proposed and successfully implemented into LES of multiphase flows in bubble column reactors in the frame of Eulerian-Eulerian approach in the previous studies, it still remains very challengeable by using the Euler/Euler LES for accurate predicting those important parameters for multiphase flows in the bubble columns such as liquid velocities, bubble volume fraction, turbulent kinetic energy spectrum, species concentration spectrum, modified force models contribution and flow patterns, particularly when comparing the simulation results with the existing experimental data available from the open literature. The present PhD project has attempted to consider the effects of SGS bubble-eddy interaction in bubble column bubbly flows, bubble-eddy and particle-eddy interactions in slurry bubble column, and SGS turbulent dispersion and SGS added mass stress force terms on both the hydrodynamics and mass transfer (e.g. take CO_2 adsorption in a reactive bubble column as the example). By employing the proposed models in the Euler/Euler LES modelling as reported from Chapter 2 to Chapter 6, it has been clearly demonstrated that the predictions of those important parameters either in bubble column bubbly flows or three-phase flow in slurry bubble column have been significantly improved.

The main concluding remarks are summarised as follows:

i. The standard LES SGS Smagorinsky eddy viscosity model was modified in Chapter 2, with the introduction of dynamic SGS Stokes number to include the effect of bubble dynamic responses to surrounding eddies. The proposed model is successfully implemented into Euler/Euler LES bubbly

flow in bubble column simulation. The grid independency, predicted bubble and liquid axial velocity, gas hold-up and liquid turbulent kinetic energy spectrum have been examined and compared with the standard model and the existing experimental data as reported in the open literature. The extra SGS eddy viscosity due to bubble response to the turbulent eddies, which has been overlooked in all previous studies on multiphase flow LES modelling, has been considered by the modified SGS eddy viscosity model.

ii. Unlike the utilisation of ensemble-averaged interfacial force closures in RANS modelling, SGS spatial filtering process gives rise to the extra terms the turbulent dispersion force and added mass stress force in the interfacial momentum exchane terms in the filtered momentum equation for Euler/Euler LES approach. In Chapter 3, a spatial filtered SGS turbulent dispersion force model (SGS-TDF) was proposed, which implicitly takes the bubble shape variation into account. The modified SGS-TDF model was implemented into Euler/Euler LES modelling of bubble column bubbly flows. The flow structures, bubble dynamics, the SGS-TDF force lateral and axial contribution together with the turbulent kinetic energy spectrum have been assessed when using the proposed SGS-TDF model and have been compared with those simulations without implementing the modified SGS-TDF model.

iii. As the consequence of LES spatial filtering process, the additionally generated term in interfacial momentum exchanes, which may have signicant impact on bubble dynamics or bubble transport in bubble column,

would be the added mass stress force (SGS-AMS), as carefully discussed in Chapter 4. Three different model combinations have been trialed in Euler/Euler LES simulations based on the conditions of the actual experimental bubble column. Such interphase force model combinations that were tested in the LES modelling are (1) drag + lift + added mass + conventional TDF; (2) drag + lift + added mass + modified SGS-TDF and (3) drag + lift + added mass + modified SGS-TDF + SGS-AMS. The contributions from these spatial filtered modelled terms were evaluated. It has been revealed from the simulation results that by including the modified SGS-TDF and SGS-AMS models in the simulation, hydrodynamics involved in bubble column bubbly flow can be better captured when comparing with the experimental data, implicitly mimicing the bubble oscillation dynamics as exposed by Sommerfeld et al. (2018) using Euler/Lagrange LES modelling.

iv. As the turbulent eddies in the regions of the front of the rising bubbles strongly interact with bubbles (characterised by added mass) and generate local fluctuation, it can be expected that considertion of the SGS-AMS and SGS-TDF will have an important effect on the interfacil mass transfer occurring in the bubble column. Subsequently, the impact of inclusion of the proposed SGS-AMS and SGS-TDF models in Euler/Euler LES modelling on the mass transfer of CO_2 chemisorption in a reactive bubble column reactor has been assessed and discussed in Chapter 5. The proposed models have shown obvious advantages in predicting the time evaluation of

species concentration in the CO_2 chemisorption process and pH curve when comparing with the LES simulation for only utilizing the standard models. Furthermore, the reaction mechanism of CO_2 chemisorption in the bubble column can be clearly observed from the predicted species concentration spectrum. It was found from the predicted species concentration spectrum that there still exists a typical -5/3 scaling following by an approximate -1 scaling in the slope change in the spectrum.

v. Based on the significant improvement in the prediction of hydrodynamics and mass transfer in Chapter 2 by modifying the shear eddy viscosity considering the bubble-eddy dynamic response in gas-liquid two-phase flow in bubble columns, the more complex gas-liquid-solid three phase flow in slurry bubble columns has been investigated in Chapter 6. A modified eddy viscosity model including the effects of local solid particle loading and bubble volume fraction and bubble and solid particle dynamic responses to surrounding eddies has been proposed. The gas hold-up and velocity distributions, shear strain rate at different distance to the war, local α'_G power spectra and turbulent kinetic energy spectrum have been comprehensively studied by comparing the simulation using two SGS eddy viscosity models with and without modification.

The specific realisations of the aforementioned claims are illustrated thoroughly in the following section.

2. SPECIFIC REALISATIONS

In Chapter 2, the proposed bubble induced turbulence eddy viscosity model that takes the bubble response to the turbulent eddies into account was validated using two experimental bubble column bubbly flow cases reported in the open literature with bubble column internal diameter being 0.1m and 0.15m, respectively. It has been demonstrated that the Euler/Euler LES simulation in conjuction with the use of the modified SGS model delivers much improvements on the predicted gas volume fraction and liquid velocity profiles, being better consistent with the experimental results than those when only using the standard Smagorinsky SGS model. LES Simulation of gas-liquid flow in the bubble column reactor has been carried out using the modified SGS model, which has taken the bubble-eddy interaction into account. The results of LES simulations clearly indicate that by employing the modified SGS model with consideration of Stokes number, the bubble entrainment transient behaviour in the cylindrical bubble column that was observed in the experimental work can be reasonably captured. The effect of the modified SGS model on the velocity profile and gas hold-up is also demonstrated by the simulation. The findings from the work are also coincided with the available DNS studies and validated by those corresponding bubble column experiments. By adopting the eddy cell model, the volumetric mass transfer coefficient in the bubble column based on Euler/Euler LES simulation coupled with the modified SGS model can be accurately estimated, which has shown much more improvement in

the prediction of the interfacial mass transfer between the bubbles and liquid than that using the conventional SGS model.

In Chapter 3, the inlet bubble size distribution (BSD) model was implemented into the LES simulation considering the condition of the actual experimental gas distributor used in the bubble column while the correlation of gas superficial velocity and domain-averaged BSD was obtained. Compared with the simulation results using only simple mono bubble diameter, the velocity profiles predicted by adopting the adjusted MUSIG model were found to be better agreed with the experimental data. It was clearly demonstrated that by using Euler/Euler large-eddy simulations (LES) modelling and taking into account the effect of bubble-eddy interaction on the SGS turbulent dispersion model, the bubble dynamics in bubble column bubbly flow can be still captured without using Euler/Lagrange LES modelling. This imples that Euler/Euler LES modelling when implementing the modified SGS turbulent dispersion model performs an equivalent role in disclosing the bubble fluctuation motion predicted by employing the Euler/Lagrange LES modelling approach, but with the stochastic dispersion model. This Chapter particularly presents a few cases through Euler/Euler large-eddy simulations (LES) modelling to demonstrate that the turbulent dispersion of bubbles can be used to effectively indicate the effect of turbulent eddies on bubble dynamics, in particular the bubble cluster oscillations, which leads to remarkable improvements in the prediction of bubble lateral dispersion behaviour. The use of spatially filtered-averaging to model the $\overline{(\alpha_k' u_k')}$ term related to turbulent bubble dispersion is proposed with a modification on SGS eddy viscosity to reflect turbulent dispersion due to bubble

induced turbulence. It was found that by using the proposed model, the time-averaged LES modelled bubble velocities and bubble volume fraction profiles are in good agreement with the experimental data while the turbulent kinetic energy spectrum obtained at the location on the centreline of the bubble column still exhibits the conventional -5/3 scaling for shear induced turbulence and -3 scaling in slope for bubble induced turbulence.

Euler/Euler LES simulation on bubble column bubbly flow, treating the interfacial momentun exchange terms with and without considerin the proposed SGS-TDF and SGS-AMS, was conducted and validated by the bubble column experimental results in Chapter 4. The chapter particularly assess the impact of inclusion of the SGS-AMS term in the LES modelling on bubble dispersion in the bubble column bubbly flows. It can be postulated that the turbulent eddies in the fronts of the rising bubbles in the bubble column would generate local fluctuations while such fluctuations would significantly affect the bubble transport and dispersion, leading to the bubble continuous deformation and bubble oscillation accordingly. When applying the LES for modelling bubbly flows, most of the existing studies usually just consider the interfacial momentum exchange terms contributed from the drag and non-drag forces that are modelled as the lift force, added mass force and turbulent dispersion force. These forces are expressed in terms of the resolved quantities of the flow (mean or filtered variables) but this treatment approach may underestimate the effect of unresolved SGS fluctuations on the bubble dispersion. Chapter 4 further demonstrates that bubble dynamics in the bubble column bubbly

flows can be captured by using the adequate SGS-TDF and SGS-AMS models in Eulerian-Eulerian LES modelling when mimicking the bubble transport in the bubble column. By using Euler/Euler large-eddy simulations (LES) modelling with considering the effect of bubble-eddy interactions on the SGS turbulent dispersion and added mass stress models, the improvement on the prediction of bubble dynamics was apparent based on the bubble axial velocity and bubble volume fraction profiles. This may indicate that the use of modified SGS-TDF model in conjuction with SGS-AMS model in Euler/Euler LES simulation can effectively mimic the bubble fluctuating motion as predicted by using Euler/Lagrange LES modelling approach. A spatial correlation between the local bubble volume faction and liquid shear strain rate was proposed, which is used to reveal the effect of sub-grid scale turbulent fluctuation on bubble transport in the bubble column.

In order to further investigate the impact of consideration of the SGS-AMS and SGS-TDF terms on the prediction of the interfacial mass transfer, the Euler/Euler LES simulation of absorption of carbon dioxide in aqueous NaOH in two rectangular and one cylindrical bubble column were conducted in Chapter 5. When the identical reaction rate constant and mass transfer coefficient are utilized, the simulation results predicted by utilizing the model without modification have shown an obvious delay in the species concentration variation. This indicates that inclusion of the proposed SGS-AMS model in LES may be sensitive in quantitatively predicting the species concentration time evolution. Using the proposed SGS-ADF and SGS-TDF models, the predicted turbulent kinetic energy

power spectrum has recovered the -5/3 and -3 scaling laws. When analyzing the species concentration spectrum of OH^- and aqueous CO_2 at a given point, a -1 scaling law following the classical -5/3 Kolmogorov scaling was identified. OH- was found to evolve in the CO_2 chemisorption process in both fast and slow reaction period (Taylor to Integral turbulent scale). It was also revealed from the species concentration spectrum that those turbulent eddies with the size smaller than the bubble diameter have a significant effect on the interfacial mass transfer, reinforcing the necessity of inclusion of the SGS-TDF and SGS-AMS in Euler/Euler LES modelling of bubble column bubbly flows, especially when the interfacial mass transfer is concerned.

The effects of the bubble-eddy and particle-eddy SGS dynamic responses in the Euler/Euler LES of the gas-liquid-solid three-phase flow in slurry bubble columns were investigated in Chapter 6. The implementation of the modified SGS shear eddy viscosity model successfully revealed the influence of solid particles and bubbles on the liquid-phase turbulence energy spectrum and their modulation patterns on the liquid-phase turbulence. The hydrodynamics and bubble dynamics, i.e., transient behaviours, gas hold-up profile, bubble and liquid velocities distribution can be well predicted by using the LES SGS model with the modified SGS eddy viscosity model. The inclusion of bubble-eddy interaction and particle-eddy interaction in the SGS turbulent eddy viscosity for gas-liquid-particle slurry three-phase flow can improve the estimation of shear turbulence viscosity in Euler/Euler LES. By using the conventional and modified SGS model, the time-averaged liquid phase shear strain rate were also compared at X=0, 0.06, and 0.09. It is discovered

that utilizing the modified SGS model results in a noticeable improvement in the vicinity of the wall, whereas the change is not visible when using the conventional model. The local α'_G power spectrum predicted by the improved SGS model showed a significant increase in high frequency scale, demonstrating that sub-grid size bubble and particle oscillation were successfully considered. It was also discovered in the turbulent kinetic energy spectrum, emphasizing the relative velocity fluctuations of the particle and the surrounding eddies can be well evaluated in the SGS eddy viscosity model. Furthermore, the transition in the slope of the typical -5/3 and -3 scaling law in the energy spectrum was close to the estimated representative bubble wavenumber, demonstrating the good estimation of sub-grid scale turbulent eddy motion which mainly takes place in the wavelength close to the bubble size by using the modified SGS eddy viscosity model.

3. RECOMMENDATIONS FOR FUTURE WORK

This PhD project have investigated bubble column bubbly flow and bubble column three-phase flow using Euler/Euler large eddy simulation (LES) approach, focusing on LES sub-grid-scale (SGS) modelling with the consideration of the modifications of the dynamic responses of the rising bubbles and solid particles to their surrounding turbulent eddies on the SGS eddy viscosity model and the influences of the sub-grid scale fluctuation between phases due to the filtering on correct description of the interfacial momentum exchange closures. Nevertheless, there are still a number of issues that need to be further addressed in order to fully understand

the nature and effects of bubble-induced turbulence, bubble-eddy interaction and modification on the liquid sheassuesr turbulence caused by the introduction large solid particles on Euler/Euler LES modelling of multiphase flows and mass transfer in the bubble columns. To the best of the author's knowledge, these issues can be classified as follows:

i. Since this PhD project has concentrated on the use of Euler/Euler LES modelling for prediction of multiphase flow and mass transfer in bubble column reactors, one of the unavoidable problems encountered when conducting the simulations is how to appropriately compromise between the near-wall grid size requirement for running the LES and satisfication of the grid criterion proposed by Milelli (2002) for bubbly flows. As the resolution requirements using Euler/Euler LES for modelling bubble column bybbly flow are typically restricted by $\Delta r^{+} \sim 5 - 30,\ \Delta z^{+} \sim 40$, this means that the grid size used in the simulation will be obviously contradicted with the requirement that the grid size should be larger than the bubble size so that the simulation results of Euler/Euler LES modelling can be trusted and reliable. As the scaling of the Re number in the near wall region can be simplified by using wall function with increasing y^{+} for larger Re, the adopted wall function should contain the influence of the bubbles. However, such wall function coupling with the local bubble volume fraction, which can be used for Euler/Euler LES modelling in the near-wall treatment, is still unavailable. At present, Euler/Euler LES modelling coupled with using wall function does exist modelling error and it can impair the overall

accuracy of simulations. In order to circumvent the problem mentioned above, one may use the technique that ensures the accurate transfer of interfacial forces from a particle or bubble to the carrier fluid. Since the most important parameter which governs the two-way coupling is the local volume fraction of the disperse phase, a template-distribution based on the local bubble or solid volume fraction specified with a Gaussian filtering function can be used. By using the template filtering function, the finite volume particle or bubble which exists at an arbitrary position is distributed into surrounding grid cells. The local volume fraction, therefore, always varies continuously, whilst the particle or bubble is allow to be located inside a grid or across several cells. This approach may be resolving the grid requirement imposed by Euler/Euler LES modelling of bubble column bubbly flows. Further investigation is needed.

ii. According to the current work, both the liquid shear-induced turbulence and bubble-induced turbulence coexist and can be identified from the turbulence kinetic energy spectrum based on Euler/Euler LES simulations. It should be emphasised, however, that the -5/3 classical Kolmogorov law stands for liquid shear-induced turbulence while -3 scaling law represents the appearance of bubble-induced turbulence. They are only applicable to certain limited range of liquid turbulence in the actual power spectrum density (cut-off length in LES). Although the characteristic bubble frequency $f_B = u_{slip}/2\pi d_B$ which can be converted into the corresponding characteristic bubble wavenumber has been used to identify the

contributions from the turbulence induced by shear and bubbles on the tubulent kinetic energy spectrum, the distinction is still vague. Actually, the precise distinction is difficult to make due to the fact that the values may vary depending upon the relative motion between the preceding bubbles and the surrounding eddies. Additionally, the mechanism by which energy cascades from the integral (i.e. eddies in the scale of bubble column radius) to inertial sub-range (bubble scale) to the dissipation range remains unknown, thus complicating the assignment of these two types of turbulence. As a result, seeking a suitable SGS eddy viscosity which can be used to better model the SGS turbulent fluctuation would be beneficial to Euler/Euler LES modelling multiphase flow turbulence in the bubble column. It is thus proposed to apply the SGS kinetic energy and the viscous dissipation equations as closure relations in Euler/Euler LES modelling of the shear turbulence and bubble induced turbulence in bubble column bubbly flows.

iii. The studies on adoption of Euler/Euler LES for modelling three-phase slurry bubble column reactors are still rarely reported in the open literature. Although some promising results are obtained, a systematic understanding of how density difference in three-phase flows contributes to the interfacial forces closures is still lacking. The density difference of gas-liquid and solid-liquid may lead to significant difference in the directions of bubble and solid particle movements. As a result, seeking the proper drag force relationships which can reflect the interaction between the bubbles and solid

particles becomes necessary. The use of DNS for modelling a single rising bubble surrounding by several large solid particles but with different intervals in the liquid may give rise to the light to find such drag force models.

LIST OF PUBLICATIONS AND CONFERENCES

JOURNAL ARTICLES:

LONG, S., YANG, J., HUANG, X., LI, G., SHI, W., SOMMERFELD, M., & YANG, X. 2020. Large-eddy simulation of gas–liquid two-phase flow in a bubble column reactor using a modified sub-grid scale model with the consideration of bubble-eddy interaction. *International Journal of Heat and Mass Transfer*, *161*, 120240. (Chapter 2)

LONG, S., YANG, X., YANG, J., & SOMMERFELD, M. 2022. Euler/Euler Large eddy simulation of bubbly flow in bubble columns under CO2 chemisorption conditions. *Chemical Engineering Journal*, 445, 136654 (Chapter 5)

LONG, S., YANG, X., YANG, J., SHI, W., & SOMMERFELD, M., 2022. Large eddy simulation of bubble column bubbly flows by considering sub-grid scale turbulent dispersion effect on modulating bubble transport. *Chemical Engineering Science.* (Required review completed) (Chapter 3)

LONG, S., YANG, X., YANG, J., SOMMERFELD, M., & XUE, C. 2022. Large eddy simulation of bubble flow in bubble column reactor by considering turbulent diffusion effect and bubble oscillation. (Submitted to *Applied Thermal Engineering, VSI:HEFAT2021 special issue*) (Chapter 4)

SHI, W., LONG, S. YANG, X., & CAI, X. 2022. 计及气泡诱导与剪切湍流的气泡破碎、湍流相间扩散及传质模型[J]. *化工学报*, DOI: 10.11949/0438-1157.20220465.

CONFERENCE PROCEEDINGS AND PRESENTATIONS:

LONG, S., YANG, X., YANG, J., LI, G., & XUE, C. 2019. Large-Eddy Simulation of the Gas-Liquid Flow in a Cylindrical Bubble Column Reactor. *10th International Conference on Multiphase Flow*, Rio de Janeiro, Brazil, May 19 – 24.

LONG, S., YANG, X., YANG, J., LI, G., & XUE, C. 2019. Large-Eddy Simulation of Bubbly Flow in a Cylindrical Bubble Column Reactor. *14th International Conference on Heat Transfer, Fluid Mechanics and Thermodynamics*, Dublin, Ireland, July 22-24.

LONG, S., YANG, J., HUANG, X., LI, G., SHI, W., & YANG, X. 2019. 鼓泡塔反应器内气液两相流动考虑气泡-涡旋相互作用修正的亚格子模型的大涡模拟. *2019 中国化工年会*, 青岛, October 17-19.

SHI, W., LONG, S., YANG, J., HUANG, X., LI, G., & YANG, X. 2019. 气液鼓泡反应器 CFD 耦合群平衡模拟中考虑介尺度气泡诱导尾涡湍流作用的气泡聚并模型. *2019 中国化工年会*, 青岛, October 17-19.

LONG, S., YANG, X., YANG, J., & SOMMERFELD, M. 2021. Large Eddy Simulation modelling of CO2 chemisorption in bubble columns accounting the SGS turbulent dispersion and virtual mass stress. *13th International conference on mathematic in (Bio)chemical kinetics and engineering*, Shanghai, China, October 24-27. (Invited speech delivered by: Prof. Xiaogang Yang)

LONG, S., YANG, X., YANG, J., HUANG, X., & SOMMERFELD, M. 2021. Large eddy simulation of bubble flow in bubble column reactor by considering turbulent diffusion effect and bubble oscillation. *15th International Conference on Heat Transfer, Fluid Mechanics and Thermodynamics*, Amsterdam, Netherlands (Online), July 26-28. (Best Paper Award)